r-process nucleosynthesis: on the astrophysical conditions and the impact of nuclear physics input

r-Prozess Nukleosynthese: Über die astrophysikalischen Bedingungen und den Einfluss kernphysikalischer Modelle
Zur Erlangung des Grades eines Doktors der Naturwissenschaften (Dr. rer. nat.)
genehmigte Dissertation von M.Sc. Dirk Martin, geb. in Rüsselsheim
Tag der Einreichung: 07.02.2017, Tag der Prüfung: 29.05.2017

1. Gutachten: Prof. Dr. Almudena Arcones Segovia
2. Gutachten: Prof. Dr. Jochen Wambach

TECHNISCHE
UNIVERSITÄT
DARMSTADT

Fachbereich Physik
Institut für Kernphysik
Theoretische Astrophysik

r-process nucleosynthesis: on the astrophysical conditions and the impact of nuclear physics input
r-Prozess Nukleosynthese: Über die astrophysikalischen Bedingungen und den Einfluss kernphysikalischer Modelle

Genehmigte Dissertation von M.Sc. Dirk Martin, geb. in Rüsselsheim

1. Gutachten: Prof. Dr. Almudena Arcones Segovia
2. Gutachten: Prof. Dr. Jochen Wambach

Tag der Einreichung: 07.02.2017
Tag der Prüfung: 29.05.2017

Darmstadt 2017 — D 17

Bitte zitieren Sie dieses Dokument als:
URN: urn:nbn:de:tuda-tuprints-63017
URL: http://tuprints.ulb.tu-darmstadt.de/6301

Für meine Uroma Helene.

Abstract

The origin of the heaviest elements in our Universe is an unresolved mystery. We know that half of the elements heavier than iron are created by the rapid neutron capture process (r-process). The r-process requires an extremely neutron-rich environment as well as an explosive scenario. Naturally, the merger of a neutron star with another compact object provides suitable conditions. In particular, neutron star mergers present the most promising astrophysical site for the r-process.

In this thesis, we study the r-process nucleosynthesis in the material ejected from neutron star mergers from two sites. First, we compute the detailed r-process abundances for the different kinds of ejecta from these systems, probing the astrophysical conditions. Second, we determine the impact of the nuclear physics input on the final abundance yields.

For our comprehensive nucleosynthesis study, we use hydrodynamical conditions from recent astrophysical simulations of neutron star mergers in 3D. We calculate for the first time the mass-integrated nucleosynthesis yields of the dynamic ejecta and of the neutrino-driven wind. The separation of timescales allows a separate treatment of these two ejecta. We find that the dynamic ejecta carry a substantial neutron-rich component to produce a successful r-process. Since in all current simulations only an approximate neutrino treatment is computationally feasible, we explore the possible impact of weak reactions. In our post-processing procedure, we see a decrease in neutron-richness, such that a successful r-process to the heaviest elements can be prevented. For the subsequent neutrino-driven wind, we find that the nucleosynthesis yields depend sensitively on both the life time of the massive neutron star and the polar angle. Matter in excess of up to $9 \cdot 10^{-3} M_{\odot}$ becomes unbound until ~ 200 ms in the aftermath of the merger, similar the ejected mass from the dynamic ejecta. Here, electron fractions of $Y_e \approx 0.2-0.4$ lead to the production of mainly nuclei with mass numbers $A < 130$. This complements the yields from the earlier dynamic ejecta. We consider mixing scenarios with these two types of ejecta to explain the abundance pattern in r-process enriched metal-poor stars. Additionally, we calculate heating rates for the decay of the freshly produced radioactive isotopes. The resulting light curve, known as kilonova, peaks in the blue band after about four hours. Furthermore, high opacities due to heavy r-process nuclei in the dynamic ejecta lead to a second peak in the infrared after three to four days.

From the nuclear physics side, we investigate the impact of the nuclear physics input on the nucleosynthesis. Here, nuclear masses play a fundamental role in understanding how the heaviest elements are created in the r-process. Using masses obtained with six Skyrme energy density functionals that are based on different optimization protocols, we calculate neutron capture and photodissociation rates. We predict r-process nucleosynthesis yields in realistic astrophysical scenarios and determine for the first time systematic uncertainty bands for r-process abundances related to mass modeling. We find that features of the underlying microphysics make an imprint on abundances especially in the vicinity of neutron shell closures. Abundance peaks and troughs are reflected in the trends of neutron separation energy. Further advances in the nuclear theory and experiments, when linked to observations, will help in the understanding of astrophysical conditions in extreme r-process sites.

Cover picture: An artist's impression of two colliding neutron stars [1].

Zusammenfassung

Der Ursprung der schwersten Element in unserem Universum ist ein ungelöstes Rätsel. Wir wissen jedoch, dass etwa die Hälfte der Element, die schwerer als Eisen sind, im rapiden Neutroneneinfangprozess (r-Prozess) entstehen. Der r-Prozess läuft in explosiven Szenarien ab, die besonders neutronenreich sind. Naturgemäß bietet die Verschmelzung eines Neutronensterns mit einem anderen kompakten Objekt passende Bedingungen. Insbesondere stellt die Verschmelzung von zwei Neutronensternen die aussichtsreichste astrophysikalische Umgebung dar.

In dieser Arbeit studieren wir die r-Prozess Nukleosynthese in der Materie, die bei der Verschmelzung zweier Neutronensterne herausgeschleudert wird. Zunächst berechnen wir die detaillierten r-Prozess Häufigkeiten für die verschiedenen Arten von ausgestoßener Materie, um die astrophysikalischen Bedingungen zu ergründen. Danach bestimmen wir den Einfluss kernphysikalischer Modelle auf die endgültigen Häufigkeiten.

Für unsere umfassende Studie der Nukleosynthese nutzen wir hydrodynamische Profile aus den neusten Simulationen von der Verschmelzung zweier Neutronensterne in 3D. Wir berechnen erstmalig die mit der Masse gewichtete Nukleosynthese von dynamisch herausgeworfenem Material und dem neutrinogetriebenen Wind. Die zeitliche Trennung der beiden Auswürfe von Materie erlaubt es uns, diese getrennt zu behandeln. Unsere Ergebnisse zeigen, dass das dynamisch herausgeworfene Material eine hinreichend neutronenreiche Komponente besitzt, um zu einem erfolgreichen r-Prozess zu führen. Weiterhin untersuchen wir den Einfluss der schwachen Reaktionen, da alle derzeitigen Simulationen sämtliche Effekte aufgrund von Neutrinos nur genähert handhaben können. Bei dieser nachträglichen Verarbeitung der Simulationsdaten finden wir, dass das Material weniger neutronenreich wird. Dadurch kann ein erfolgreicher r-Prozess, der bis zu den schwersten Elementen hin reicht, verhindert werden. In dem darauffolgenden neutrinogetriebenen Wind zeigt sich, dass die Nukleosynthese stark von sowohl der Überlebensdauer des zentralen, massiven Neutronensterns als auch vom Betrachtungswinkel abhängt. Material mit einer Masse von $9 \cdot 10^{-3} M_{\odot}$ wird innerhalb der ersten ~ 200 ms nach der Verschmelzung der beiden Neutronensterne ausgestoßen. Dieser Wert ist dem des dynamisch herausgeworfenen Materials sehr ähnlich. Der relativ hohe Elektronenanteil $Y_{\mathrm{e}} \approx 0.2 - 0.4$ im neutrinogetriebenen Wind führt zu der vorwiegenden Produktion von Atomkernen mit Massenzahlen $A < 130$. Folglich ist die Nukleosynthese komplementär zu der von dynamisch herausgeworfenem Material. Wir betrachten mehrere Mischungsszenarien der beiden ausgestoßenen Arten von Material, um die Häufigkeitsverteilungen in metallarmen Sternen, die reich an r-Prozess Elementen sind, zu erklären. Weiterhin bestimmen wir die Heizraten für den Zerfall der produzierten radioaktiven Isotope. Die resultierende Lichtkurve, auch bekannt als Kilonova, erreicht nach vier Stunden ein Maximum im Bereich blauer Wellenlängen. Darüber hinaus führen die hohen Opazitäten aufgrund der schweren r-Prozess Atomkerne in dynamisch herausgeworfenem Material zu einem zweiten Maximum im Infraroten nach drei bis vier Tagen.

Ausgehend den kernphysikalischen Aspekten untersuchen wir, wie kernphysikalische Modelle die r-Prozess Nukleosynthese beeinflussen. Hierbei spielen die Massen der Atomkerne eine wichtige Rolle, um zu entschlüsseln, wie die Synthese schwerer Elemente abläuft. Wir verwenden sechs Sätze an Massen, die auf verschiedenen Optimierungsprotokollen im Rahmen der Skyrme Energiedichtefunktionaltheorie beruhen, um Neutroneneinfangraten und Photodissoziationsraten zu berechnen. Wir bestimmen die r-Prozess Nukleosynthese in realistischen astrophysikalischen Szenarien und ermitteln erstmals systematische Unsicherheitsbänder aufgrund der Modellierung von Kernmassen. Es stellt sich heraus, dass die Eigenschaften der zugrunde liegenden Mikrophysik einen Einfluss auf die r-Prozess Häufigkeiten haben. Dies zeigt sich insbesondere in der Nähe abgeschlossener Neutronenschalen. Die Häufigkeitsmaxima und -lücken spiegeln sich direkt in der Entwicklung der Neutronenseparationsenergie wider. Weitere Fortschritte in der Kernphysik, sowohl in der Theorie als auch im Experiment, werden in Kombination mit astronomischen Beobachtungen dabei helfen, die astrophysikalischen Bedingungen für den r-Prozess zu verstehen.

Contents

List of Figures

List of Tables

1 Introduction and motivation

Where does all the gold in the universe come from? And how was it created? The origin of the heavy elements, such as gold, is one of the outstanding questions in science [2]. Throughout the history of our universe, a ubiquitous process has given rise to about half of the elements heavier than iron. This is the so-called rapid neutron capture process (r-process). While its fundamental concept is known since the year 1957 [3], the astrophysical site has not been unambiguously identified yet. As the name suggests, the r-process occurs at extreme neutron densities in an explosive environment that get more than a hundred times hotter than the core of our sun. Clearly, neither the Earth nor even the core of our sun will ever provide the necessary conditions. These requirements can be met in astrophysical environments with neutron stars. The most promising host for the r-process is a neutron star merger, in which two of these compact remnants with the size of a big city collide and eject matter into the interstellar medium. Each of them carries about one and a half the mass of our sun, but is compressed so much that protons quickly capture electrons to form neutrons. A common comparison states that one teaspoon of neutron star material weighs more than all humans on Earth.

Coalescing neutron stars are a unique site in astrophysics. During their inspiral phase, a significant fraction of energy and angular momentum is emitted as gravitational waves (GWs). Thus, they are considered a major source of GW signals. More recently, these “ripples in spacetime” raised public attention. With an instrument so sensitive that it can measure lengths more accurate than one-thousandth the diameter of a proton [4], the LIGO collaboration succeeded in directly observing gravitational waves from a merger of two black holes [5]. Since the merger of two neutron stars is predicted to happen more often than the one of two black holes, the advent of gravitational wave detection brings us closer to an answer to the above questions after the origin of the heavy elements than ever before. Furthermore the merger of two neutron stars is the best candidate to explain short gamma-ray bursts (sGRBs). As mentioned before, they are the most promising scenario for the r-process. Extremely neutron-rich as well as explosive conditions favor the production of elements up to uranium via the rapid neutron capture process (r-process). The production of substantial mass fractions of radioactive material, r-process nuclei in particular, is suspected to lead to a long-term decay heating of the ejected material [6]. In fact, a near-infrared data point from the recently observed sGRB 130603B [7, 8] is interpreted as a first detection of a kilonova [9]. This is in excellent agreement with theoretical light curve calculations for an assumed ejected mass of several $10^{-2}\,M_\odot$ [10]. In the future, more events like this kilonova can become crucial in view of the long-anticipated discovery of GWs by the next generation of GW detectors.

Neutron star mergers feature at least three distinct channels for matter ejection. During a merger event, part of the total mass gets unbound by gravitational torques and hydrodynamic processes. These are the dynamic ejecta [11–14]. When the accretion disk expands, the recombination of free nuclei into alpha particles as well as the viscous heating release enough energy to evaporate matter from the accretion disk at late times [15, 16]. In addition to this, a smaller amount of mass is ejected in a neutrino-driven wind, similar to the one of a proto-neutron star, resulting from a core-collapse supernova. Here, the central remnant is a massive neutron star which is surrounded by a thick accretion disk. Gravitational binding energy is released in form of both neutrinos and anti-neutrinos with substantial luminosities of about 10^{53} erg/s and energies of $\sim 10-15$ MeV. Due to neutrino absorption, matter is driven away from the accretion disk [17, 18]. Every type of ejecta has different physical properties and thus a unique impact on the overall nucleosynthesis.

This work belongs to the field nuclear astrophysics, the interdisciplinary branch connecting nuclear physics and astrophysics. We combine the nuclear physics input and the astrophysical environments to give predictions on the r-process nucleosynthesis for heavy elements such as gold or europium. In this way, we contribute important pieces to the r-process puzzle (Fig. 1.1).

In order to study the r-process in neutron star mergers, one needs the results from detailed astrophysical simulations. From a theoretical point of view, the astrophysical candidates for the r-process are precious laboratories, because they provide extreme conditions, which are not realized on the Earth. However, the presence all four fundamental forces in these environments has posed a challenge for the modeling so far. This has only become possible now, as the increased computational power of supercomputers facilitates 3D simulations in general relativity. At the same time, the microphysics used in such simulations have improved, e.g., the neutrino reactions and the equation of state. Many exciting questions remain to be answered, for instance: How neutron-rich are the ejecta? What is the amount of ejected mass and how large is the event rate for neutron star mergers?

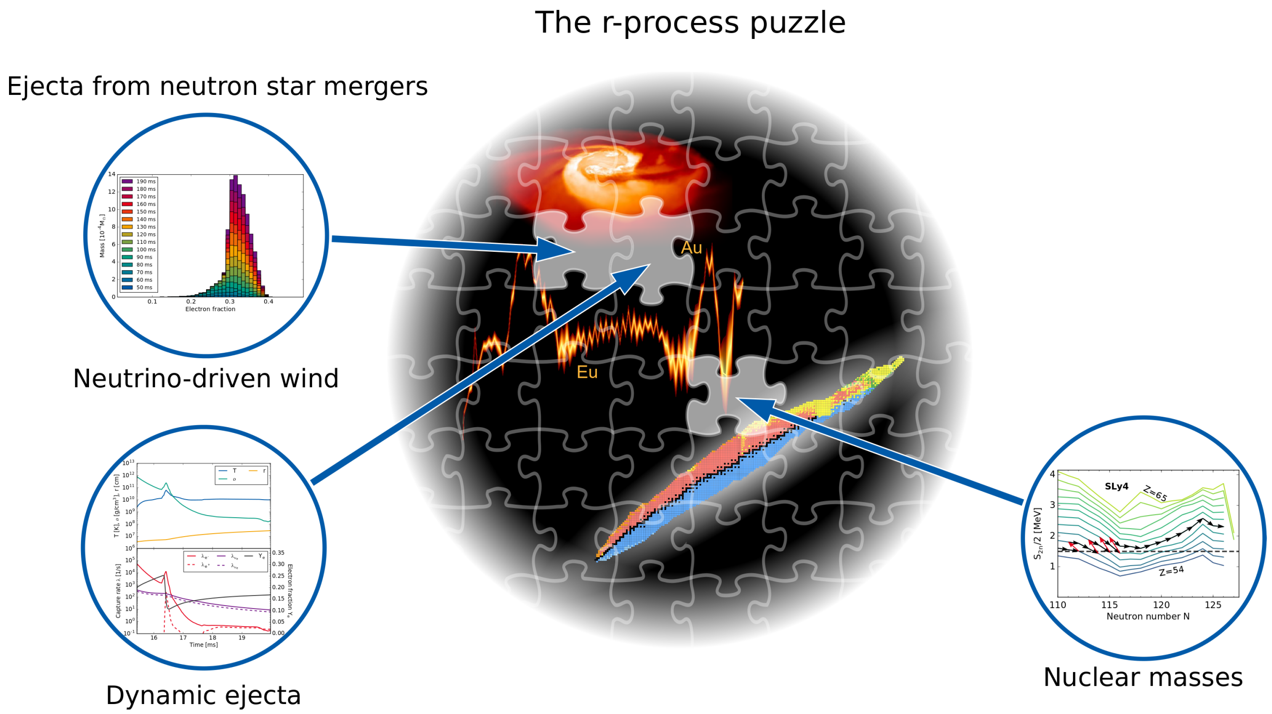

Figure 1.1: Schematic overview of this work. We determine the nucleosynthesis yields in the dynamic ejecta as well as the neutrino-driven wind from neutron star mergers, and study the impact of nuclear masses on the r-process. Our results contribute important pieces to the r-process puzzle.

Complementary to progress in hydrodynamical simulations, the nuclear physics provides information on how the heavy elements are created. From the nuclear physics perspective, the r-process involves nuclei consisting of many more neutrons than protons. These extremely neutron-rich nuclei are far from stability and thus decay radioactively on very short timescales. Currently, we know roughly 300 stable nuclei and there are about 3200 unstable nuclei [19] of which at least any property is identified. Since overall 7000 nuclei are estimated to exist [20], only few experimental information is available for neutron-rich nuclei participating in the r-process. Furthermore, theoretical models can be very uncertain because they rely on extrapolations that are prone to systematic errors. Current and future beam facilities, e.g., FAIR (Facility for Antiproton and Ion Research) in Germany, RIKEN in Japan, and FRIB (Facility for Rare Isotope Beams) in the USA, will be able to artificially produce and analyze the nuclei that occur as radioactive intermediate products in the formation of heavy elements.

We span the astrophysical framework in Ch. 2 by introducing the basic concepts of the r-process as well as the details on the possible sites. In Ch. 3, we give the foundations for the nuclear reactions and the nuclear reaction network that we use. Additionally, we define simplifying equilibria and a scheme to evolve the electron fraction. Chapter 4 deals with our results for the nucleosynthesis in ejected material from neutron star mergers, particularly in the dynamic ejecta and the neutrino-driven wind. To investigate different kinds of ejected material from neutron star mergers, we exploit their separation by timescales. The impact of nuclear physics input, particularly the one of nuclear masses, is presented in Ch. 5. In Ch. 6, we summarize our results and conclude with an outlook.

2 Astrophysical framework

In the following, we give an overview of the main processes that lead to the creation of all elements heavier than iron. Their imprints can be related to distinct features in the observed abundance distributions of our sun and old, metal-poor stars. Then, we discuss the astrophysical scenarios that are currently considered to contribute to different aspects of the r-process nucleosynthesis. Namely, we focus on the ejecta from core-collapse supernovae and neutron star mergers.

2.1 The origin of heavy elements

In the big bang, the lightest chemical elements were formed, which comprise most of the visible matter in our universe. These elements are hydrogen (^{1}H, $\sim 75\,\%$) and helium (^{4}He, $\sim 25\,\%$), with small contributions of ^{2}H, ^{3}He and lithium[1] [21]. Another portion of elements up to iron is created via nuclear fusion reactions in the course of stellar evolution, especially toward the end of a massive star's life (see Sect. 2.2.1). Since nuclei in the vicinity of iron possess the maximum binding energy per nucleon, any further charged particle mechanism is inhibited by the Coulomb barrier. In addition, a charged particle process, producing nuclei with higher nuclear charges, requires subsequently the larger temperatures the more the atomic number of an element increases. However, the need of rising temperatures is counteracted by the emergence of photodisintegration reactions that destroy the freshly produced nuclei very quickly.

Which processes create heavy elements, i.e., nuclei that are more massive than $A \gtrsim 60$? The formation of most of the elements beyond the iron peak must be driven by reactions that do not suffer the limitations mentioned before. Here, neutrons play a key role. Since neutron captures are not affected by Coulomb barriers, the corresponding cross sections are far less sensitive to temperature and they are nonnegligible even at low and moderate temperatures. Furthermore, beta decays are important to convert neutrons within nuclei into protons, in order to proceed toward heavier atomic numbers.

Additional hints are provided by the abundance distribution of the elements in our sun. This can be extracted from meteorite samples or observed in the solar spectrum [22, 23], shown in Fig. 2.1. It was realized by the authors of Ref. [3] in 1957 that several different mechanisms are needed to explain solar abundances. Particularly, the authors discovered that at least two different processes are necessary to shape the prominent double-peak structure in the vicinity of $A \sim 130$ and $A \sim 200$. The two processes are called the slow neutron capture process (s-process) and rapid neutron capture process (r-process). Each of the two processes is responsible for approximately half of the elements heavier than iron. Moreover, a rare p-process contributes very little to produce the less abundant neutron-deficient nuclides [24].

It is instructive to discuss the s- and the r-process in a simple schematic framework. At first glance, the success of each process is a competition between neutron captures and beta decays. Therefore, we generally distinguish them by relative timescales. The s-process is characterized by relatively low neutron densities $n_{\mathrm{n}} \sim 10^{8}\,\mathrm{cm}^{-3}$ [25]. Hence, beta decays happen on a shorter timescale than neutron capture reactions ($\tau_{(\mathrm{n},\gamma)} \gg \tau_{\beta}$) [26]. As a result, beta decays occur, before unstable nuclei can capture neutrons. Starting from a few seed nuclei, whose distribution depends on the previous history of the host event, heavier elements form by successive neutron capture. Since the beta decays win over the slow neutron captures, the nucleosynthesis path runs close to the valley of stability. Its end is marked by nuclei at $A = 209$, where further neutron capture can only produce unstable nuclei. The s-process path is marked by the green line in Fig. 2.2. Small neutron capture cross sections before the magic neutron numbers at $N = 50$, $N = 82$, and $N = 126$ enhance the abundances of strontium ($A = 88$), barium ($A = 138$), and lead ($A = 208$), respectively. This leads to large-A peaks of the distinct double peaks in the solar abundance pattern (see Fig. 2.1). As the s-process takes place close to stability, most of the properties of the involved nuclei are known [26].

At extremely high neutron densities $n_{\mathrm{n}} \gtrsim 10^{22}\,\mathrm{cm}^{-3}$ [27], neutrons are captured more rapidly than nuclei beta-decay ($\tau_{(\mathrm{n},\gamma)} \ll \tau_{\beta}$). In combination with a very short explosive scenario, many subsequent neutron captures lead to the production of short-lived nuclei far away from the valley of stability. This second case describes the r-process.

---

[1] Due to the large amounts of hydrogen and helium, astronomers tend to simply refer to elements with $Z > 2$ as metals.

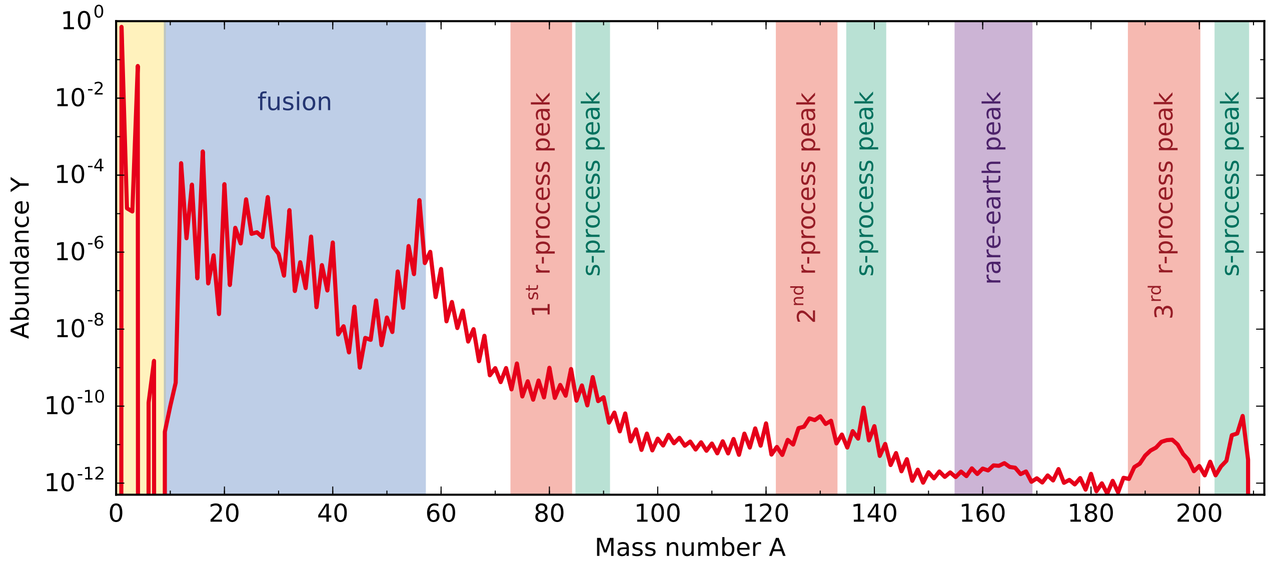

Figure 2.1: Solar abundances according to the various nucleosynthesis processes. The yellow region marks the elements created by the big bang. In the blue area, the elements that contribute to the fusion of elements up to the iron peak region. The regions in which the abundances pile up due to the s- and r-process are highlighted in green and red, respectively.

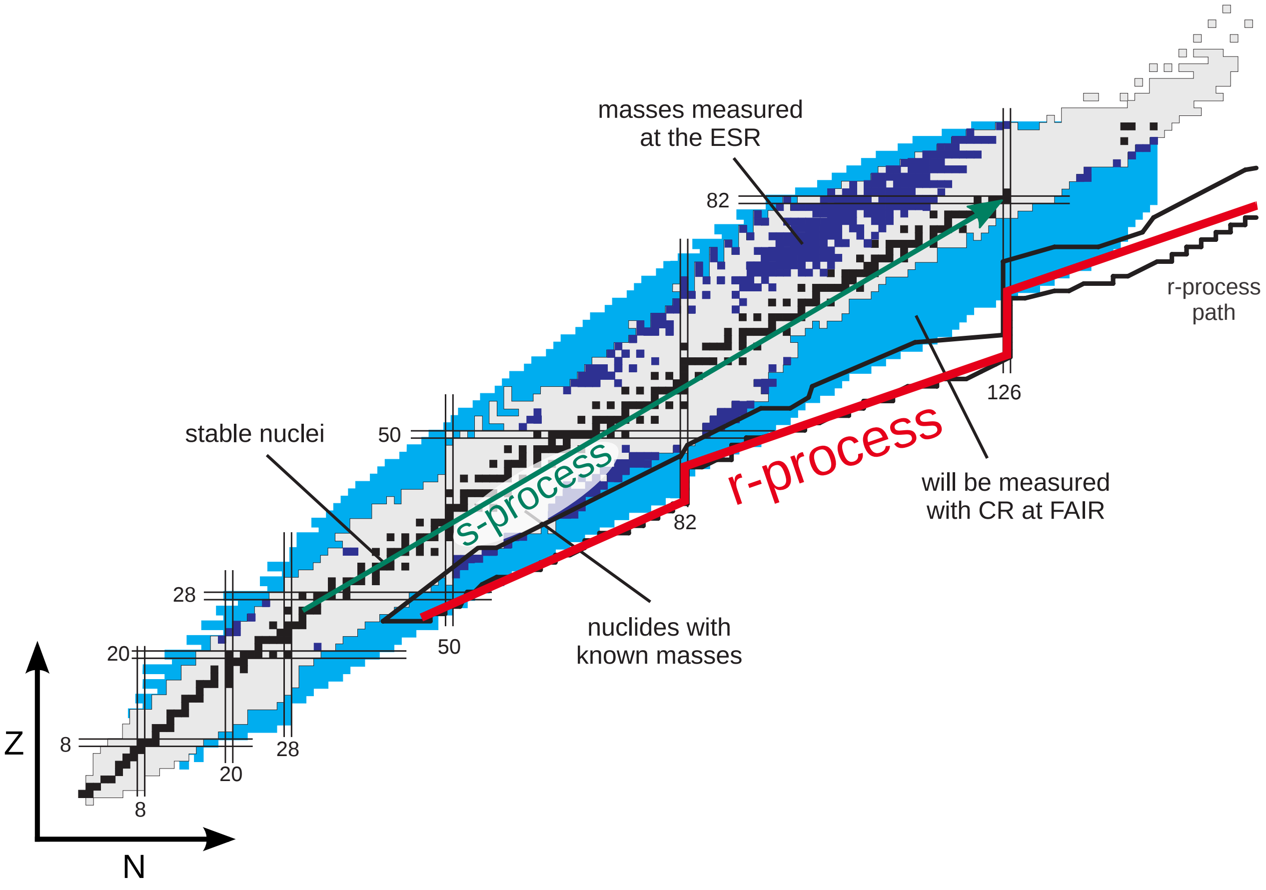

Figure 2.2: Paths of the s- and r-process in the nuclear chart. The s-process (thin green line) advances along the valley of stability, whereas the r-process (thick red line) extends to the most neutron-rich nuclei. The chart also shows stable nuclei (black), nuclei with known masses (gray), as well as nuclei that will be measured by the Electron Storage Ring (ESR, dark blue) and by Facility for Antiproton and Ion Research (FAIR, light blue). Courtesy of Yu. Litvinov.

Its schematic path is shown as a thick red line in Fig. 2.2. As can be seen, rapid neutron captures are the only way to overcome the elements in the lead region. Thus, the r-process creates all the uranium and thorium in the universe.

Let us take a step back and consider another aspect at high neutron densities. Typically, environments with high neutron fluxes exhibit also temperatures above $T \sim 1\,\text{GK}$. This gives rise to photodissociations that establish an (n,γ)—(γ,n) equilibrium. Under these circumstances, a steady-state can develop. This can be studied with the waiting point approximation [28]. For each nucleus along a given isotopic chain, the change in abundance (defined in Eq. (3.33)) due to photodissociations and neutron captures cancel each other:

$$\lambda_{(\gamma,\text{n})}\, Y(Z,A+1) - n_\text{n} \langle \sigma v \rangle_{(\text{n},\gamma)}\, Y(Z,A) = 0\,, \tag{2.1}$$

where $\lambda_{(\gamma,\text{n})}\, Y(Z,A+1)$ and $n_\text{n} \langle \sigma v \rangle_{(\text{n},\gamma)}\, Y(Z,A)$ incorporate the effects of photodissociations and neutron captures, respectively. Consequently, the system of differential equations (see Sect. 3.3) transforms into a system of ordinary equations. Using detailed balance, we can directly write down the ratio of the abundances for neighboring nuclei by relating their fundamental properties (see Sect. 3.1.3):

$$\frac{Y(Z,A+1)}{Y(Z,A)} = n_\text{n} \frac{G(Z,A+1)}{2G(Z,A)} \left(\frac{A+1}{A}\right)^{3/2} \left(\frac{2\pi(\hbar c)^2}{k_\text{B} T m_\text{u} c^2}\right)^{3/2} \exp\left(S_\text{n}(A+1)/[k_\text{B}T]\right)\,, \tag{2.2}$$

with the nuclear partition function $G(Z,A)$ and the neutron separation energy $S_\text{n}(A+1)$ of the more massive isotope. For every isotopic chain, the (n,γ)—(γ,n) equilibrium favors one nucleus to be produced predominantly. This nucleus is called waiting point nucleus, since the abundance flow waits for its decay to proceed to higher atomic numbers. When the waiting point nucleus decays, a beta-flow establishes between isotopic chains. The waiting point approximation is schematically presented in Fig. 2.3. In this simple picture, the r-process path is completely set by the neutron separation energy as a function of temperature and the neutron density of the environment. The neutron separation energy increases for nuclei closer to stability and decreases for nuclei closer to the drip line. The r-process path passes through the isotope close to the equilibrium value. For example, let us assume $Y(Z,A+1) \approx Y(Z,A)$ in Eq. (2.2). Neglecting the nuclear partition functions and taking $T = 1.25\,\text{GK}$, $n_\text{n} = 10^{22}\,\text{cm}^{-3}$, we arrive at $S_\text{n} \approx 3.0\,\text{MeV}$ [29]. This means that the r-process path is completely determined by nuclei with $S_\text{n} \approx 3.0\,\text{MeV}$ in every isotopic chain. Usually, the abundance maximum is attained by a nucleus with even neutron number, since pairing effects dramatically decrease the separation energy for unpaired neutrons.

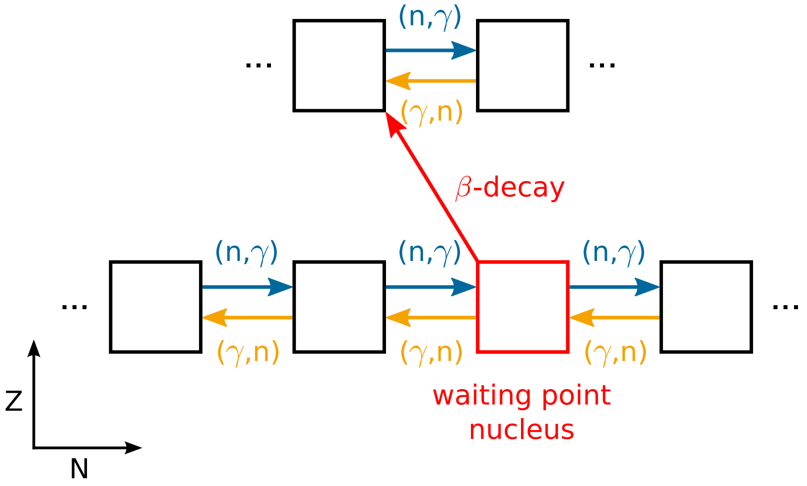

Figure 2.3: Waiting point approximation. During the (n,γ)—(γ,n) equilibrium, the production of one nucleus within an isotopic chain is favored with respect to a given temperature and neutron density. This nucleus is called waiting point nucleus, since the abundance flow waits for its decay to proceed.

The steady-state provides a sufficient description during (n,γ)—(γ,n) equilibrium [28, 30], similar as nuclear statistical equilibrium (NSE) does for high enough temperatures. As both temperature and neutron density eventually decrease with time, one needs to perform dynamical r-process calculations to follow the ongoing nucleosynthesis. How far the r-process reaches, depends on the initial neutron-to-seed ratio Y_n/Y_seed, i.e., the amount of neutrons that each seed nucleus[2] can capture. For seed nuclei with $A \sim 50$, a neutron-to-seed ratio of about $100 - 150$

---

[2] We call all nuclei with $A > 4$ seed nuclei.

is required to execute a successful r-process. The abundance peaks in the final nucleosynthesis pattern are due to the pile up at nuclei with magic neutron numbers. Here, the sudden drop of the neutron separation energy causes an abrupt quasi-(n,γ)—(γ,n) equilibrium. Accordingly, the abundance flow runs vertically along isotones in these regions. In contrast to the abundance peaks produced during the s-process, the r-process peaks are formed due to nuclei that are located far-off stability. Although they stem from shell closures at the neutron magic numbers $N = 50, 82, 126$, the r-process abundance peaks reside at lower mass numbers. Their positions are shown in Fig. 2.4. Throughout this work, we refer to them as first ($A \sim 80$), second ($A \sim 130$), and third ($A \sim 195$) r-process peak. In between the second and third peak, there is a peak for the abundances of rare-earth elements, correspondingly referred to as rare-earth peak. Up to now, the formation of this distinct feature remains unclear [31]. However, it is conjectured to be formed either by fission of super-heavy elements [32], or late-time neutron capture (see, e.g., Refs. [33, 34]). In the most extreme case, the extent of the r-process can reach the heaviest nuclei that decay by spontaneous, neutron-, or beta-induced fission. This happens around nuclei with mass numbers $A \approx 260$ and atomic numbers $Z \approx 94$ [35, 36]. The fission of such heavy nuclei leads to the creation of nuclei around the second peak. If the system maintains high neutron densities sufficiently long, the fission products continue to capture neutrons. Eventually, they have become super-heavy elements again (with $A \gtrsim 240$), leading to effective fission cycling [12, 13]. The r-process ends, when the neutrons are exhausted, such that the neutron density drops over orders of magnitude. Then, nuclei beta-decay to the valley of stability, forming final abundance pattern. Even though the neutron density vanishes fast, late neutrons play a role for the formation of distinct r-process features, in particular for the elements around the third r-process peak.

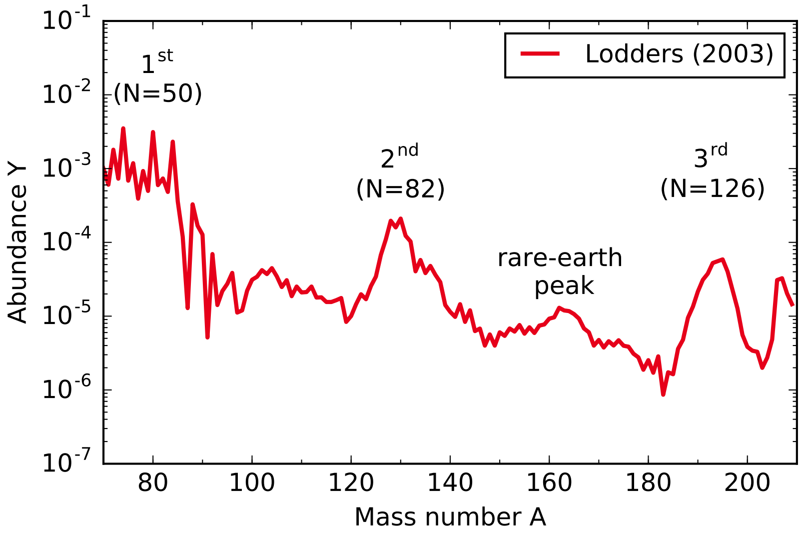

Figure 2.4: Solar residual abundances. After subtracting the s- and p-process abundances from the solar pattern, the remaining part is typically referred to as solar r-process. The distinct local maxima are attributed to the neutron shell closures, while the origin of the rare-earth peak is an unsettled question.

2.1.1 Observations of metal-poor stars

Apart from the abundance distribution of the chemical elements in our sun, we can get insights about the synthesis of heavy elements from metal-poor stars. These are very old stars in the Galactic halo, whose atmospheric metal content, the metallicity, is more than an order of magnitude lower than the solar metallicity. Historically, the iron abundance is used as a reference value for the metallicity and age of a star. The metallicity, [Fe/H], of a star is defined by the ratio

$$[\mathrm{Fe/H}] = \log_{10}(Y_{\mathrm{Fe}}/Y_{\mathrm{H}})_\star - \log_{10}(Y_{\mathrm{Fe}}/Y_{\mathrm{H}})_\odot , \qquad (2.3)$$

where $\star$ tags the abundance of the star and $\odot$ the one of the sun. The older a star is, the less iron enrichment had happened to the material in the time before the star formed. Thus, by observing stars with different metallicities, we can infer the history of the chemical enrichment of the Galaxy. In this way, it is possible on the one hand to pin down, how early r-process events must have taken place in the history of the universe. This is in particular important, when considering an astrophysical site as a potential host for the r-process. On the other hand, we can compare the elemental abundance patterns to investigate the amount of enrichment and the robustness of the r-process.

Figure 2.5(a) shows the abundances $\log \varepsilon(\mathrm{A}) = \log(Y_\mathrm{A}/Y_\mathrm{H}) + 12$ of six r-process enriched metal-poor stars with $[\mathrm{Fe/H}] \lesssim -2$ (four of them have even $[\mathrm{Fe/H}] \lesssim -3$). For comparison, the blue lines are the solar residual abundances, i.e., the pattern that remains after subtracting the s- and p-process abundances. They are scaled to the abundance of europium, which is almost exclusively produced by the r-process. Clearly, the r-process signatures can be observed in these stars. Especially the abundance pattern for heavy r-process elements ($56 < Z < 82$) is resembled remarkably well. This feature has led to the conclusion that the r-process that creates these elements must be robust, no matter where it occurs [37]. In contrast, the abundances vary for lighter heavy elements with $Z < 50$. The star to star scatter is shown in the plots of Figs. 2.5(b,c). Furthermore, some metal-poor stars are deficient in elements with $Z > 50$, while still being enriched in the lighter heavy elements [38]. This indicates that there must be more than just one r-process [39].

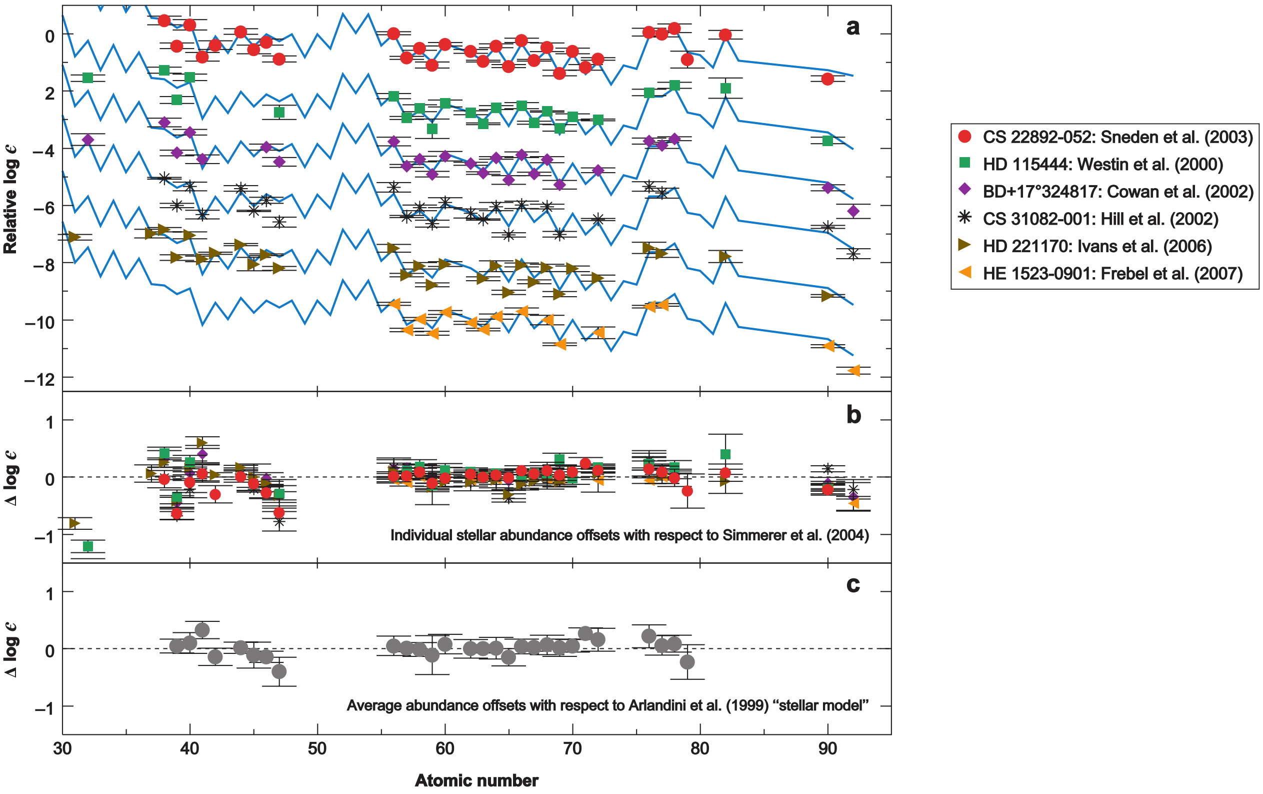

Figure 2.5: Abundances of six metal-poor stars. The top panel shows the elemental abundances of the stars compared to the solar abundances (blue line). The two lower panels demonstrate the deviations of the stellar abundances with respect to the values of Refs. [40, 41]. Adopted from Ref. [37].

Early Galactical chemical evolution studies indicated the need for a continuous source for r-process material [42, 43]. However, detections such as the one of live ^{244}Pu in deep-see reservoirs [44], and recent observations, e.g., a study of the ancient ultra-faint dwarf galaxy Reticulum II [45] hint toward a rare event. In the next sections, we shed light on the astrophysical background of these sites.

2.2 Core-collapse Supernovae

Core-collapse supernovae belong to the most powerful events in the universe. For a long time, the neutrino-driven wind from a proto-neutron star has been considered a possible host for the r-process. With an event rate of $\sim 10^{-2}\,\mathrm{yr}^{-1}\mathrm{galaxy}^{-1}$, core-collapse supernovae occur frequent enough to account for the observed r-process material. Moreover, core-collapse supernovae require stars with high masses that have an extremely short life, in contrast to low-mass stars, e.g., our sun. Thus, the comparably short delay after star formation, could explain the r-process enrichment of even the oldest, metal-poor stars in our Galaxy, the Milky Way.

Here, we introduce the core-collapse supernova and the subsequent neutrino-driven wind. We discuss their current challenges to provide suitable conditions for the r-process, and possible cure in terms of a rare kind of supernova that develops magneto-hydrodynamically driven jets.

2.2.1 Evolution of massive stars

Here, we give a concise description of the life of massive stars. For a detailed explanation see, e.g., Ref. [46].

For the most time of its life, a star produces internal pressure via hydrogen fusion to helium, preventing the gravitational collapse. Eventually, the helium nuclei in the center are more abundant than hydrogen and hydrogen burning does not create enough pressure any more to prevent gravitational contraction. This lets the central temperature climb to a critical limit, where helium gets ignited and the helium fusion to carbon in the triple-α reaction takes over in compensating the gravitational pressure. After these two burning stages, the subsequent evolution of the star depends very much on its mass. Stars with mass $M \lesssim 8\,M_\odot$ are not capable of developing high enough temperatures by further contraction to ignite another burning stage. Just like our sun, these stars ultimately end their lives as white dwarfs, stabilized by a degenerate electron gas. On the contrary, more massive stars ($M \gtrsim 8\,M_\odot$) undergo further hydrostatic burning stages that happen in a similar manner as the ones before. The ashes of the previous stage accumulate in the center, exhausting the fuel of the current stage. Thus, the star cannot withstand the gravitational pressure, raising central density and temperature. As soon as the core reaches high enough temperatures, the ashes become the fuel of the following burning phase. Gradually, the star develops a concentric shell structure. Each shell is characterized by the most abundant species, as shown in Fig. 2.6. From the outermost to the innermost shell, these elements are hydrogen, helium, carbon, neon, oxygen, and silicon. The inner core basically consists of iron that is produced by silicon burning, since no more fusion is energetically favorable from the iron region nuclei onwards. While the burning always occurs at the interfaces of the shells, the timescales, at which the fuels get exhausted, are steadily decreasing by up to several orders of magnitude from one shell to another toward the center. Due to the increasing Coulomb barriers of nuclei in the inner layers, the fusion of heavier nuclei is driven by alpha particle capture, and photodissociation reactions become more important, as do weak reactions.

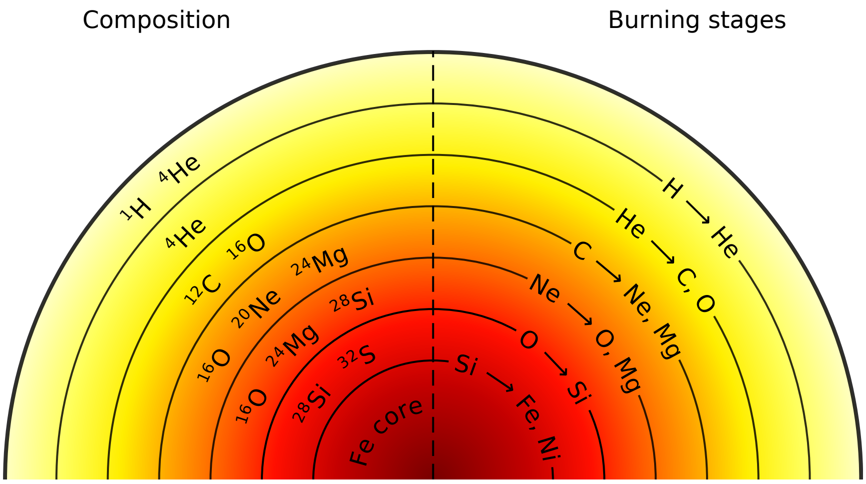

Figure 2.6: Burning stages in a massive star. By fusion reactions, more massive nuclei are formed at the inner interface of each layer. Each layer is identified by its most abundant species. In the final burning stage, silicon burns to iron, from which on no fusion reactions are energetically feasible. The size of the shells does not resemble their actual scale.

2.2.2 Collapse and explosion

At the end of their lifetime, stars with more than roughly $10\,M_\odot$ exhibit an onion-like structure, defined by the subsequent burning stages [46]. The stellar iron core continuously gains mass due to the silicon burning at its surface. As the creation of elements heavier than iron peak nuclei would rather cost than release energy, no outward pressure is exerted by fusion reactions any more. In addition, the large Coulomb barriers disfavor further charged particle reactions. Instead, the electron degeneracy pressure balances the gravitational pressure. This environment in the iron core is similar to the conditions in a white dwarf (as shown for the example of a $15\,M_\odot$ progenitor star in the middle upper corner of Fig. 2.7), where degenerate electrons support a mass up to the Chandrasekhar limit of about

$$M_{\mathrm{Ch}}|_{T=0} = 1.44\,M_\odot \left(\frac{Y_\mathrm{e}}{0.5}\right)^2 . \tag{2.4}$$

However, the temperature in the core is substantially higher ($\sim 10\,$GK) and the pressure generated by the electrons and ions supports even masses above the Chandrasekhar limit [47]. This delays the inevitable fate of the massive star only slightly. Soon, the ashes of the silicon burning increase the mass of the progressively contracting core so much that the electron degeneracy pressure is not capable of stabilizing it further: the collapse begins. Its description here follows to large extent Refs. [48, 49].

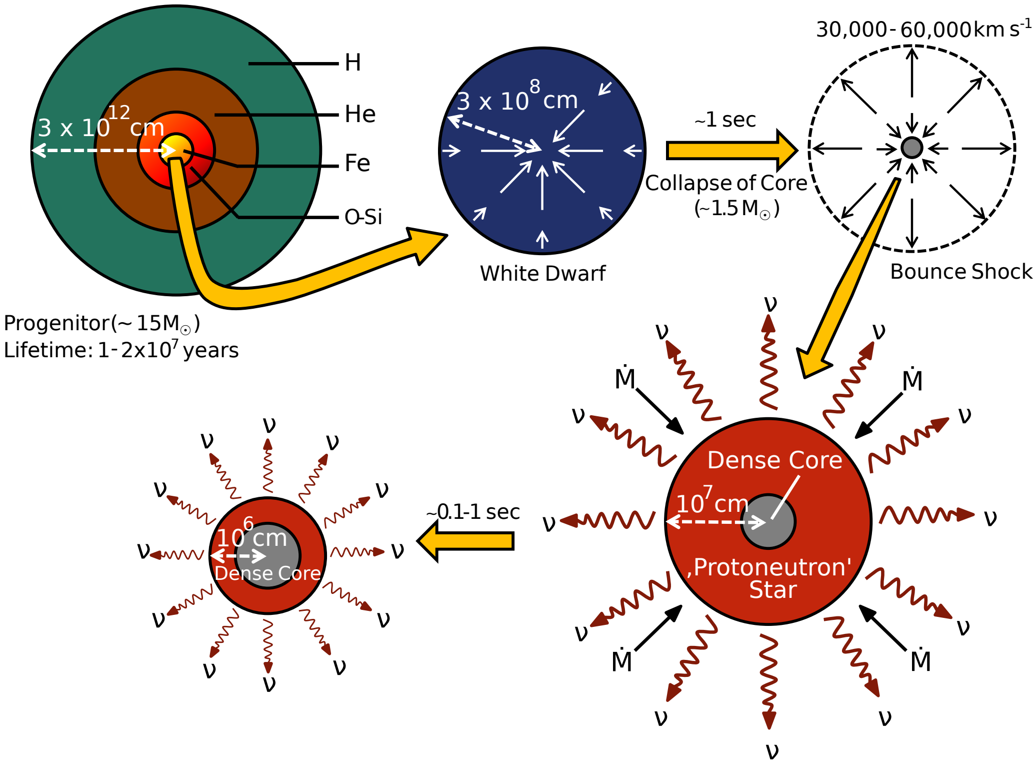

Figure 2.7: Schematic picture of a core-collapse supernova. Clockwise from the left upper corner: the inner iron core of a massive progenitor star collapses to a proto-neutron star that cools down by neutrino emission, and ends up as a neutron star. Courtesy of Ref. [50], and adapted from Ref. [47].

Due to the high density, the Fermi energy of the degenerate electrons is considerably higher than their rest mass energy, leading to copious electron captures. This decreases the electron degeneracy pressure and simultaneously creates neutrinos that escape from the core. For massive stars with at least $\sim 10\,M_\odot$, the temperature in the iron core is such high that photodissociation reactions play a major role for the destabilization. Photons disintegrate iron nuclei into alpha particles and nucleons. Not only does this drain energy, it also produces free protons that can capture electrons even faster than nuclei, because the electrons only have to overcome the neutron-proton mass difference $\Delta = 1.293\,$MeV. The subsequent neutrino emission speeds up the collapse of the core to even smaller radii, where increasing number of free protons captures electrons more rapidly. This self-reinforcing feedback loop shrinks the iron core from initially thousands of kilometers to tens of kilometers. The collapse proceeds on the free fall time scale

$$t_{\mathrm{ff}} \sim \frac{1}{\sqrt{G\rho}} \approx 0.1\,\mathrm{s}\,. \tag{2.5}$$

During the collapse, the interactions of neutrinos with matter become more and more important. When the central density exceeds 10^{12} g/cm^3 (see, e.g., Ref. [51]), the plasma is opaque even for neutrinos. Consequently, neutrinos interact more often with infalling matter, such that their diffusion time scale exceeds the free fall time scale. Hence, they are trapped [52], establishing a weak equilibrium.

As the central density continues to rise above nuclear saturation density ($\rho_{\text{nuc}} \approx 3 \cdot 10^{14}\,\text{g/cm}^3$), the collapse is abruptly hindered. The repulsive short-range part of the nuclear interaction prevents a further compression and therefore causes an outwards moving shock wave, the so-called bounce. In the beginning, it was believed that this shock wave completely disrupts the star and triggers the explosion. However, the bounce shock loses its energy via the dissociation of iron and nickel nuclei, while traveling through the outer core. Moreover, neutrinos can escape freely due to the lower density in the outer regions. At radii of roughly $r \sim 100\,\text{km}$, a standing shock is formed, as illustrated in the lower right part of Fig. 2.7.

How does the scenario turn from an implosion back into an explosion again? This is the famous supernova puzzle, which is a central unresolved problem in supernova theory [47]. It was realized early on that neutrinos provide a huge energy reservoir to be tapped for a successful explosion [53]. In the delayed neutrino-heating mechanism [54], neutrinos deposit energy just behind the shock. Although it is the most probable explanation and recent multi-D simulations explode successfully, the predicted explosion energies are somewhat lower than the observed ones [55–57]. Thus, different mechanisms were proposed to settle the issue, including effects from rotation, magnetic fields, phase transitions, and acoustic oscillations [58].

When the outgoing shock is revived finally, it repels the outer layers and triggers the explosion ultimately. While the shock moves through the outer layers, matter heats up and nuclei are formed during the explosive nucleosynthesis. The dominant reactions of explosive nucleosynthesis are alpha captures, forming nuclei up to the iron region if the temperatures are sufficiently high. During the explosion, extreme turbulences can lead to anisotropic mass ejection.

In the center of the system, the very hot and dense proto-neutron star cools down via neutrino emission. Eventually, it ends up as either neutron star or stellar black hole. The final fate of the remnant depends on the structure of the progenitor star. Recent studies show that there is neither a clean transition nor a monotonic dependence on the progenitor mass alone [59, 60]. However, the final fate can be directly related to the mass-infall rate $\dot{M}$ of the collapsing star and the electron neutrino luminosity of the accreting proto-neutron star [61].

2.2.3 Neutrino-driven winds from core-collapse supernovae

In the aftermath of a core-collapse supernova, the neutrino emission from the nascent proto-neutron star can unbind a substantial baryonic outflow, the so-called neutrino-driven wind [62]. Initially, matter above the proto-neutron star experiences sufficiently high temperatures to be in NSE. The abundances in NSE are dominated by nucleons and light nuclei up to alpha particles [63]. Due to the high fluxes, (anti)neutrinos start to deposit energy in the outer layers of the proto-neutron star at the so-called neutrino sphere. Thus, the neutrino energy is effectively absorbed and converted into kinetic energy of material, which starts to move outward. As the material expands, it cools down to $T \sim 8\,\text{GK}$. Descending from NSE, neutrons and protons start to form alpha particles in the alpha-rich freeze-out [64]. Furthermore, seed nuclei are formed in mainly charged particle reactions [65]. When the temperature has dropped to $T \sim 3\,\text{GK}$, matter is made up of free nucleons, alpha particles, and seed nuclei. From now on, the further nucleosynthesis path strongly depends on the three wind parameters that set the neutron-to-seed ratio $Y_{\text{n}}/Y_{\text{seed}}$ in the wind [65–67]: entropy per baryon S, expansion timescale τ, and electron fraction Y_{e}.

For radiation dominated environments, the entropy scales as $S \propto T^3/\rho$ [66]. With increasing temperature, and thus entropy, photodissociation reactions destroy seed nuclei and increase the neutron-to-seed ratio. Likewise, decreasing density results in declining many-body reaction rates, forming less seed nuclei.

The expansion timescale τ specifies how fast the material expands during the production of seed nuclei. It can be expressed as [68]

$$\tau = \left.\frac{r}{v}\right|_{T=0.5\,\text{MeV}}, \tag{2.6}$$

where r is the radius and v is the velocity. The faster the expansion, the less time remains to form seed nuclei. Typically, the expansion timescales are at the order of tens of milliseconds for the neutrino-driven wind.

The third parameter is the electron fraction Y_e, which is the ratio of electrons to baryons. It is changed by weak reactions, mainly electron neutrino and electron antineutrino captures on nucleons. Under the approximation that the environment is dominated by nucleons, the equilibrium electron fraction evolution in Eq. (3.90) is given by

$$Y_\mathrm{e,eq} \simeq \frac{\lambda_{\nu_\mathrm{e}}}{\lambda_{\nu_\mathrm{e}} + \lambda_{\bar{\nu}_\mathrm{e}}} = \frac{1}{1 + \frac{\lambda_{\bar{\nu}_\mathrm{e}}}{\lambda_{\nu_\mathrm{e}}}} = \left[1 + \frac{L_{\bar{\nu}_\mathrm{e}} \left(\epsilon_{\bar{\nu}_\mathrm{e}} - 2\Delta + 1.2\Delta^2 / \epsilon_{\bar{\nu}_\mathrm{e}} \right)}{L_{\nu_\mathrm{e}} \left(\epsilon_{\nu_\mathrm{e}} + 2\Delta + 1.2\Delta^2 / \epsilon_{\nu_\mathrm{e}} \right)} \right]^{-1} . \tag{2.7}$$

If we assume that the electron neutrino and antineutrino luminosities are equal, we find the ejecta to be proton-rich ($Y_\mathrm{e} > 0.5$) for $\epsilon_{\bar{\nu}_\mathrm{e}} - \epsilon_{\nu_\mathrm{e}} < 4\Delta$, and neutron-rich ($Y_\mathrm{e} < 0.5$) otherwise.

In summary, to obtain a successful r-process up to the heaviest elements, we need high entropies, short expansion timescales, and low electron fractions.

The neutrino-driven wind following a core-collapse supernovae was historically the favored production site. However, as the simulations have become more and more sophisticated, the conditions required for a successful r-process up to the heaviest elements have become unlikely [69–75].

Nevertheless, neutrino-driven winds can feature a variety of neutron-rich and proton-rich conditions, leading to the production of the lighter heavy elements up to silver [76]. Under neutron-rich conditions, alpha-capture reactions and especially (α, n)-reactions play a crucial role to form elements in the weak r-process [77]. On the contrary, proton-rich conditions enable the νp-process [78]. Both processes can contribute a combination of light s-, p-, and r-process nuclei.

2.2.4 Magneto-hydrodynamically driven supernovae

Even though neutrino-driven winds seem to be excluded, some rare core-collapse supernovae may plausibly contribute to the r-process [79–83]. Such a magneto-hydrodynamically driven (MHD) supernova relies on a different explosion mechanism than a typical core-collapse supernova.

At the end of its lifetime, the iron core of a differentially rotating massive star collapses. Then, the overall magnetic field strength increases as $B \propto \rho^{2/3}$ by the magnetorotational instability (e.g., Refs. [84, 85]), or according to the following mechanism [86]. Assuming flux conservation, the free energy in the differential rotation is consumed to wind up the poloidal component of the magnetic field. This builds up a toroidal component at the costs of simultaneous decrease of the rotational energy. Simultaneously, there is a strong amplification in magnetic pressure along the rotation axis, which can grow by already two orders of magnitude within the first 10 ms after core bounce. The magnetic pressure quickly exceeds the local gravitational pressure of the matter. Since the vertical component of the Lorentz force along the rotational axis points outward, matter gets accelerated toward the poles. Additionally, the horizontal component of the Lorentz force pushes the flow inward, thus confining the jet that pierces the stalled shock wave after core collapse. A bipolar jet outflow is launched. Due to the standing shock, the outer material is accreted and passes through the shock front, such that photons disintegrate nuclei into neutrons and protons. The inward moving matter reaches high densities and temperatures close to the proto-neutron star. In this environment, electron captures convert the free protons into neutrons, lowering the electron fraction. Moreover, the shape of the magnetic field forces the outflowing matter to move on spiraling trajectories that can be pictorially described as spring-shaped. As a consequence, the jet outflow remains longer in the hot and dense region directly above the proto-neutron star, where further electron captures take place prior to the ejection. On a short timescale, the jet drives out neutron-rich material that can undergo r-process nucleosynthesis.

It is estimated that 0.1 %—1 % of all core-collapse supernovae develop MHD jets. Similar to neutron star mergers, the jetlike supernovae pose rare events. Although not suffering the timescale argument of binary mergers, the unknown event rate and ejecta mass prevents jetlike supernova from unambiguously being the main r-process site.

2.3 Neutron star mergers

Today, binary neutron stars are the most promising scenario to explain the origin of heavy elements in the universe [11–13, 16, 18, 87–89]. Extremely neutron-rich as well as explosive conditions favor the production of elements up to uranium via the r-process in at least part of the ejecta.

In this section, we will first recap the astrophysical relevance of neutron star mergers. Then, we summarize the formation and coalescence of neutron star binaries. Finally, we characterize the variety of ejecta from neutron star mergers that are the central topic of this work.

2.3.1 Astrophysical relevance

Since the first detection of neutron star binaries, the merger of two neutron stars or a neutron star with a black hole has been realized as an ideal environment for r-process nucleosynthesis [90–92]. However, their contribution to the early Galaxy is still under discussion. Earlier work [43] disfavored them as dominant source of r-process in the early Galaxy, because of the presumed long coalescence time. In contrast, more recent studies are either more optimistic about their role [93] or actually favor them over supernovae as major production site, see for example the recent hydrodynamical studies of Refs. [94, 95]. Other models can explain the r-process abundances at all metallicities, solely based on the neutron star merger scenario [96]. Here, more work is clearly needed to settle the case (see Refs. [97, 98]).

In general, coalescing neutron stars are a unique laboratory in astrophysics. All fundamental forces in nature are involved in their underlying processes. As mentioned in the previous section, inspiraling neutron star binaries emit a significant fraction of energy and angular momentum as gravitational waves (GWs) during their inspiral phase. Thus, they are considered a major source of GW signals [99]. The recent measurements of GW signals from several binary black hole mergers [5, 100] has tremendously raised the excitement for the detection of GWs from binary neutron star mergers. The galactic merger rate is estimated to be $80.0^{+209.1}_{-66.1}$ events/Myr [101, 102]. For a detection with advanced LIGO at design sensitivity, this translates to a binary neutron star merger rate of $0.4-400$ events/yr (see table V of Ref. [103]).

Furthermore, they are the best candidate to explain short gamma-ray bursts (sGRBs) [104]. In fact, the idea that compact binary mergers could be the sources of the heaviest r-process elements has recently received strong support from an observed near-infrared excess in the aftermath of sGRBs [7, 8, 105, 106]. This emission has been interpreted as the detection of a “kilonova” [9] (sometimes referred to as “macronova”, cf. Ref. [107]). The kilonova is a transient that is powered by the radioactive decay of freshly synthesized r-process elements. Its temporal emergence and magnitude can be estimated from basic considerations [108]. Assuming spherical symmetry and radially expanding ejecta with $R = vt$, the diffusion timescale of photons

$$t_{\mathrm{diff}} \simeq \frac{R}{c}\tau = \frac{R}{c}\rho\kappa R = \frac{3M_{\mathrm{ej}}\kappa}{4\pi c v t}\,, \tag{2.8}$$

where the density ρ is averaged over the enclosed volume $4\pi R^3/3$, containing the total mass M_{ej} of the ejecta. κ is the opacity of the ejecta. Radiation eventually escapes after the expansion timescale, and setting $t = t_{\mathrm{diff}}$ [109], we obtain

$$t_{\mathrm{peak}} \simeq \left(\frac{3M_{\mathrm{ej}}\kappa}{4\pi v c}\right)^{1/2} \approx 8.4\,\mathrm{d}\left(\frac{M_{\mathrm{ej}}}{10^{-2}M_{\odot}}\right)^{1/2}\left(\frac{v}{0.1c}\right)^{-1/2}\left(\frac{\kappa}{10\ \mathrm{cm}^2/\mathrm{g}}\right)^{1/2}. \tag{2.9}$$

Since the kilonova is powered by the radioactive decay of r-process nuclei, we can estimate the peak luminosity from the heating rate $\dot{Q}(t) \approx 10^{10}\,\mathrm{erg}/(\mathrm{g\,s})\,M_{\mathrm{ej}}t_{\mathrm{day}}^{-1.2}$ [9]:

$$L_{\mathrm{peak}} \simeq \dot{Q}\left(t_{\mathrm{peak}}\right) \approx 1.5\cdot 10^{40}\mathrm{erg/s}\,. \tag{2.10}$$

In Eq. (2.10), we used $M_{\mathrm{ej}} = 10^{-2}\,M_{\odot}$, $v = 0.1c$, and $\kappa = 10\,\mathrm{cm}^2/\mathrm{g}$. This luminosity peak after only several days, and in the near-infrared – rather than after hours in the optical/UV as originally expected [6] – supports the view that the ejecta are made of very heavy r-process elements. The enrichment in actinides and lanthanides results in effective opacities that are orders of magnitude larger than those of supernovae [10, 110–112]. Therefore, photons are effectively trapped. They are released delayed, when the ejecta will have expanded, and thermal spectrum will have shifted to the infrared. This observation links for the first time compact binary mergers not only with sGRBs observationally, but also with the formation of very heavy elements. Such kilonovae are an important facet in the multi-messenger view of compact binary mergers [113, 114] and, since they emit quasi-isotropically, they may become crucial in assuring further direct GW detections by the next generation of GW detectors [115–118].

2.3.2 Neutron star binary systems

In spite of extensive searches, up to now only eight neutron star binary systems are known in the galactic disk (see, e.g., Ref. [119] and references therein). Their masses are arranged in pairs in Fig. 2.8, together with the overall error-weighted mean of $1.373\,M_{\odot}$. Binary systems of neutron stars are rare, since two massive stars needed to be

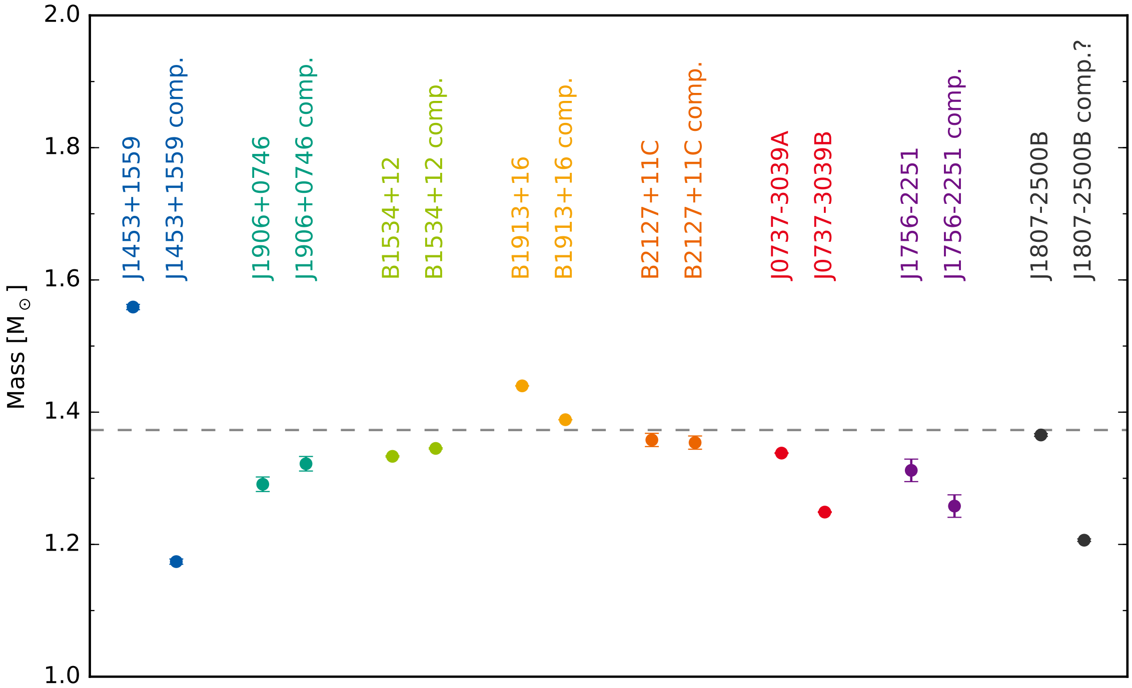

Figure 2.8: Overview of the masses for observed binary neutron stars. The masses are plotted with their 1σ error bar. The dashed gray line indicates the error-weighted mean of $1.373\,M_\odot$ for all observed masses so far. The data are taken from the compilation of Ref. [120].

close to each other, and explode in a supernova, while maintaining proximity. One possibility is that two neutron stars encounter each other dynamically in globular clusters (e.g., Ref. [121]). The standard formation scenario considers a twin system, with stars in the mass range from $8\,M_\odot$ to $25\,M_\odot$ [122, 123]. Stars in this mass interval are likely to be heavy enough to end their lives in a supernova, but sufficiently light to not collapse to a black hole. As pointed out in Sect. 2.2.2, the exact mass range is not well known and presumably discontinuous [59]. The more massive star, which is called the primary, passes the burning stages faster, and expands when it evolves toward a giant phase. As it bloats up, it can overflow its Roche lobe, transferring mass to the lower mass companion, i.e., the secondary. Reaching the end of its life time, the primary explodes in a core-collapse supernova and forms as a neutron star. Asymmetric explosions that kick the new born neutron star, lead to increased eccentricity and can destroy the binary. If the system survives the supernova explosion, the secondary is in the main sequence. At this stage, the secondary transfers mass to the neutron star. This causes the emission of X-rays. Leaving the main sequence, the secondary bloats up and engulfs the primary in a common envelope phase [124]. While the stars orbit each other in the envelope, they lose orbital energy by friction. Thus, the envelope evaporates, releasing angular momentum and energy from the binary system. The common envelope phase is critical in many ways. If the neutron star accretes too much mass from the envelope, it collapses to a black hole. On the other hand, if the orbital decay of the binary system happens too fast, the neutron star will merge with the secondary, before it has exploded. If neither of these scenarios is realized, the secondary explodes in a core-collapse supernova. Again, the system must survive the natal kick of the neutron star.

The problematic issue of getting a neutron star safely through the common envelope phase can be circumvented if both the initial stars have similar masses. Then, the secondary expands before the primary explodes. The common envelope phase takes place, before a neutron star is formed. Similar to the standard scenario, this variant ends with a close double neutron star system. However, the binary system must sustain two subsequent core-collapse supernovae.

Once formed, the neutron stars orbit around each other. In this inspiral phase, the orbital period continuously decreases by the emission of gravitational waves. The theory of general relativity predicts a decrease of the semi-major axis a as [122]

$$\frac{\mathrm{d}a}{\mathrm{d}t} = -\frac{64G^3 m_1 m_2 M}{5a^3c^5}\left(1-e^2\right)^{-7/2}\left(1+\frac{73}{24}e^2+\frac{37}{96}e^4\right), \tag{2.11}$$

where m_1 and m_2 are the masses of the neutron stars, and e is the eccentricity of the binary system. In addition to the shrinking of the relative separation, general relativistic effects reduce the eccentricity e by

$$\frac{\mathrm{d}e}{\mathrm{d}t} = -\frac{304 G^3 m_1 m_2 M}{15 a^4 c^5} \left(1-e^2\right)^{-5/2} \left(e + \frac{121}{304} e^3\right) . \tag{2.12}$$

Due to the strong dependence on the semi-major axis, a positive feedback loop is maintained: the emission of gravitational waves speeds up the inspiral that in turn enhances the energy emitted via gravitational waves, and so forth. Therefore, the orbit of the binary system is effectively circularized by emitting gravitational waves.

The inspiral timescale, on which the two neutron stars merge, is given by [125]

$$t_{\mathrm{inspiral}} \simeq 10^7\,\mathrm{yr} \left(\frac{P_{\mathrm{orb}}}{1\,\mathrm{h}}\right)^{8/3} \left(\frac{m_1+m_2}{M_\odot}\right)^{-2/3} \left(\frac{\mu}{M_\odot}\right)^{-1} (1-e^2)^{7/2} , \tag{2.13}$$

with the orbital period P_{orb}, the total mass $M = m_1 + m_2$ and the reduced mass $\mu = m_1 m_2/(m_1+m_2)$ of the system. Equation (2.13) implies that large masses and large eccentricity reduce the inspiral time.

The inspiral of two neutron stars was first observed for the Hulse-Taylor binary pulsar[3] PSR 1913+16 [126]. This was also the first indirect measurement of gravitational waves, for which Taylor & Hulse were awarded the Nobel prize in 1993. The short orbital period of 7.75 h makes it an invaluable laboratory to test several aspects of general relativity. Moreover, the neutron star binary J0737-3039A+B was detected in 2003 [127]. Here, both neutron stars are pulsars whose properties can be measured precisely. With an orbital period of just 2.45 h, their relative separation is even smaller, enhancing the general relativistic effects. In the future, these systems will help to carry out high-precision tests of general relativity in the limit of strong gravitational fields.

Ultimately, the initial separation distance has reduced so much that the coalescence phase commences. When the orbits are at the order of their radii, tidal interactions deform the neutron stars. Eventually, they touch and merge. Most of the material falls into the center to form a massive neutron star or black hole, depending on mass and rotation. In general, rotating neutron stars can support higher masses beyond the static limit prescribed by the Tolman-Oppenheimer-Volkoff equations [128, 129] for a given equation of state. Furthermore, the spiral arms form a thick accretion disk. After some time, the massive neutron star collapses to a black hole, because of viscosity as well as angular momentum transfer.

Similar to the proto-neutron star after a core-collapse supernova, the hot massive neutron star copiously emits neutrinos. However, there is a significant contribution from the fast rotation disk that is subject to turbulent motion, while being quickly accreted onto the central remnant. As the neutron-rich material captures positrons, the neutrino fluxes are dominated by mainly electron antineutrinos.

2.3.3 Channels of mass ejection

Neutron star mergers feature several distinct channels for matter ejection. A schematic overview of the ejecta from a neutron star merger event (in the absence of strong magnetic fields) is given in Fig. 2.9. Within milliseconds after the coalescence, part of the total mass gets unbound by gravitational torques and hydrodynamic processes. These are the dynamic ejecta that have long been recognized as a likely source of the heaviest r-process nuclei [11–14, 88, 130–133]. The dynamic ejecta have been found to consist of a cold “tidal component” that is launched via gravitational torques and a hotter “interaction component” that comes from the hydrodynamical interaction of the neutron stars. The overall amount of dynamic ejecta is in good agreement between different studies [114]. For given nuclear physics input, the dynamic ejecta yield a very robust, “strong r-process” [37] pattern due to efficient fission cycling [12–14, 89, 134–136]. This means that all merger events produce practically identical abundance patterns (for this type of ejecta), independent of the details of the merging system. The abundance pattern, however, shows some sensitivity to the resulting distribution of fission fragments and to the resulting beta-decay half lives [36, 136, 137]. In general, the properties of very neutron-rich nuclei involved in the r-process are subject to extreme extrapolations that impact the final abundances [138–141]. Chapter 5 deals with the influence of nuclear masses on the r-process pattern (see also Ref. [142]).

Recent studies in full GR [131, 143, 144] and in the conformal flatness approximation [14] agree that shocks are more important for the dynamic ejecta in the GR case, especially when a soft equation of state is used. This

---

[3] A pulsar is a neutron star whose symmetry axis of the dipolar magnetic field is inclined with respect to the rotation axis. This leads to a beamed emission of radiation, often compared to a lighthouse.

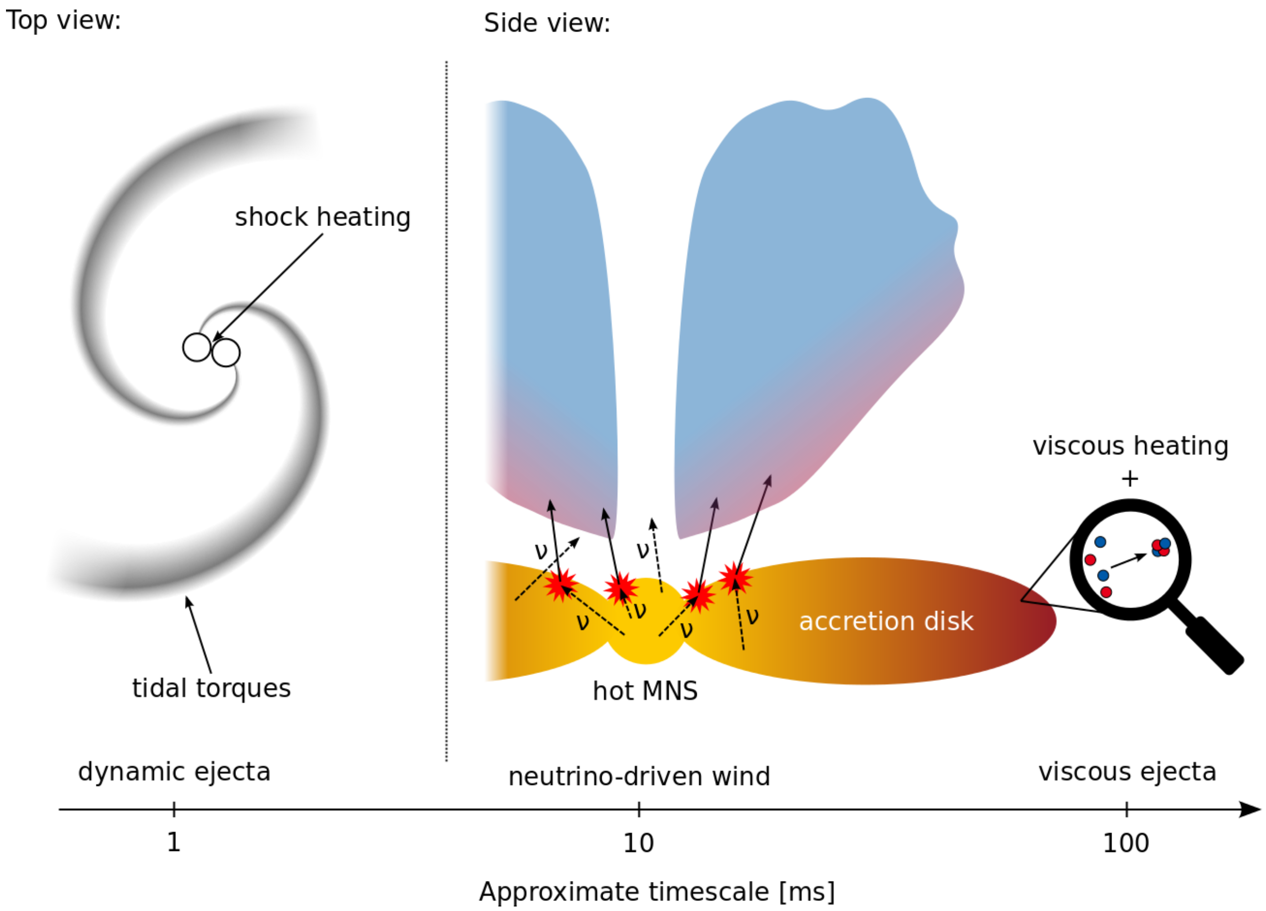

Figure 2.9: Overview of the ejecta from a neutron star merger. The left hand side shows the system about 1 ms after the merger, when the dynamic ejecta get unbound. The right hand side summarizes the mechanisms and timescales of the late-time channels of matter ejection, i.e., the neutrino-driven wind, and the viscous ejecta. Note that in addition to the ejecta shown, the magnetic field of a strongly magnetized MNS can drive magnetically-induced outflows.

is mainly because the stars are for a given equation of state (EoS) more compact due to the stronger relativistic gravity and hence achieve larger velocities prior to contact. A softer EoS leads to more compact neutron stars and also to smaller sound speeds which, in turn, make the occurrence of shocks more likely. Therefore, the dynamic ejecta are dominated by the hotter “interaction component” while Newtonian ejecta are dominated by the colder, unshocked “tidal component” [13]. Hence, a GR calculation will plausibly cause a higher temperature environment which is expected to lead to larger electron fractions in the ejecta [145]. Due to shock-heating, it is also likelier that unbound material is ejected out-of-plane. Thus, already the dynamic ejecta can produce a very broad range of r-process abundances [18, 89, 145]. The detailed effects of the shock-heating are not understood well. We investigate dynamic ejecta from full GR simulations in Sects. 4.1 and 4.2.

In addition to the dynamic ejecta, the presence of further post-merger mass loss channels has been appreciated and begun to be explored in more detail. The first one is the neutrino-driven wind [17, 18, 146–148], which emerges on a timescale of tens of milliseconds. The neutrino-driven wind from a neutron star merger is similar to the one of a proto-neutron star, resulting from a core-collapse supernova. Here, the central remnant is a massive neutron star (MNS) which is surrounded by a thick accretion disk. Gravitational binding energy is released in form of both neutrinos and anti-neutrinos with substantial luminosities of about 10^{53} erg/s and energies of $\sim$ 10—15 MeV. Due to neutrino absorption, matter is driven away from the accretion disk [17, 18]. Based on the first 3D simulation of the neutrino-driven wind in Ref. [17], we carry out a comprehensive nucleosynthesis study that is presented in Sect. 4.3 (see also Ref. [149]).

On a timescale of hundreds of milliseconds to seconds, a late-time accretion disk disintegration sets in [15, 18, 150–152]. The late-time disintegration of the accretion disk, driven by viscous heating and recombination of free nucleons into alpha particles, is referred to as viscous ejecta in the following. If the massive neutron star has a strong magnetic field, magnetically-induced outflows are possible. General relativistic simulations of a differentially rotating, long-lived neutron star revealed that the magnetohydrodynamic turbulence alone can lead to massive winds [153]. This can give rise to long-lasting X-ray afterglows up to $10^2 - 10^4$ s after the merger [154, 155].

Every type of ejecta has different physical properties and thus a unique impact on the overall nucleosynthesis. Understanding the different mass loss channels, their nucleosynthesis and possible electromagnetic transients are of prime importance for cosmic nucleosynthesis and galactical chemical evolution, for gravitational wave detection strategies and actually also for the GRB launch mechanism, since already a tiny mass loading of a fireball can "choke" an emerging jet [156].

3 Nucleosynthesis foundations

Any nucleosynthesis process can be described by means of the reactions that the available nuclei undergo. To follow the change in composition, we need to assemble the reaction rates, at which all possible reactions take place. In the most general case, this leads to a huge set of coupled differential equations that is solved with the aid of numerical tools [157, 158].

In this chapter, we present the basic principles to obtain nuclear reaction rates from both experimentally measured and theoretically calculated nuclear properties. We explain the concepts of nuclear reaction networks, and discuss two different strategies to solve these systems of ordinary differential equations numerically. For extremely high temperatures, the nuclear statistical equilibrium is attained, facilitating the description of compositional changes. If strong and electromagnetic reactions are in nuclear statistical equilibrium, there can be an equilibrium of weak reactions at high densities, the so-called beta-equilibrium. Finally, we consider the situation, where weak reactions can still alter the composition dynamically, causing an evolution of the electron fraction with time.

3.1 Nuclear reaction rates

Here, we give the fundamental relations for reaction rates [29]. Using the compound nucleus description in the framework of the Hauser-Feshbach theory, we outline the computation of cross sections and rates with the help of statistical models. Furthermore, we introduce the detailed balance that serves as a useful tool to receive reaction rates from the corresponding inverse process. Afterwards, we summarize relations for the reaction rates mediated by the strong interaction (reactions involving nucleons and nuclei), the electromagnetic force (emission and absorption of photons), and the weak interaction (emission and absorption of leptons).

3.1.1 Velocity integrated cross section

For a nuclear reaction $i + j \to o + m$, commonly abbreviated to $i(j,o)m$, the most basic information is encoded in the corresponding reaction cross section. This quantitative measure of the probability for an incoming projectile nucleus j to react with a target nucleus i, creating the nuclei o and m, is defined as

$$\sigma = \frac{\text{\# reactions per target per second}}{\text{flux of incoming particles}} = \frac{r/n_i}{n_j v}\,, \tag{3.1}$$

where n_i and n_j are the number densities of target and projectile, i.e., the number of particles N_i and N_j per volume V, respectively. Furthermore, $v = |\mathbf{v}_i - \mathbf{v}_j|$ is the relative velocity between target and projectile. In Eq. (3.1), $r = \sigma v n_i n_j$ is the number of reactions per cm^3 and sec. Therefore, the cross section σ has the dimensions cm^2 and can be interpreted as an area perpendicular to the projectile trajectory. In this classical picture, all projectiles that pass through this area, react with the target. While Eq. (3.1) is only true for constant velocities, projectiles and targets naturally obey velocity distributions. Then, r is given by

$$r_{i,j} = \int \sigma\left(\left|\mathbf{v}_i - \mathbf{v}_j\right|\right) \cdot \left|\mathbf{v}_i - \mathbf{v}_j\right| \,\mathrm{d}n_i \mathrm{d}n_j\,. \tag{3.2}$$

To evaluate this integral, we express $\mathrm{d}n_i$ and $\mathrm{d}n_j$ in terms of the underlying velocity distribution. For nuclei in an astrophysical plasma, both projectiles and targets follow a thermal distribution ϕ, described by the Maxwell-Boltzmann statistics, and we have

$$\mathrm{d}n_x = n_x \left(\frac{m_x}{2\pi k_\mathrm{B} T}\right)^{3/2} \exp\left(-\frac{m_x v_x^2}{2 k_\mathrm{B} T}\right) \mathrm{d}^3 v_x \equiv n_x \phi(\mathbf{v}_x)\,\mathrm{d}^3 v_x\,, \tag{3.3}$$

with Boltzmann's constant k_B, temperature T, mass m_x, and velocity v_x of the particle $x = i, j$. Thus, we write

$$r_{i,j} = n_i n_j \int \sigma\left(\left|\mathbf{v}_i - \mathbf{v}_j\right|\right) \left|\mathbf{v}_i - \mathbf{v}_j\right| \phi(\mathbf{v}_i)\phi(\mathbf{v}_j)\,\mathrm{d}^3 v_i \mathrm{d}^3 v_j = n_i n_j \langle \sigma v\rangle_{i,j}\,, \tag{3.4}$$

where we introduce the velocity integrated cross section $\langle\sigma v\rangle_{i,j}$, which is also referred to as reactivity. In center of mass coordinates, the integral in Eq. (3.4) can be rewritten in terms of the reduced mass $\mu = m_i m_j/(m_i + m_j)$ and the relative velocity v. Assuming that the center of mass frame is at rest, this leads to

$$\langle\sigma v\rangle = \left(\frac{\mu}{2\pi k_\mathrm{B} T}\right)^{3/2} \int v\,\sigma(v) \exp\left(-\frac{\mu v^2}{2k_\mathrm{B} T}\right) \mathrm{d}^3 v \tag{3.5}$$

$$= \left(\frac{8}{\mu\pi(k_\mathrm{B} T)^3}\right)^{1/2} \int_0^\infty E\,\sigma(E) \exp\left(-\frac{E}{k_\mathrm{B} T}\right) \mathrm{d}^3 E\,. \tag{3.6}$$

Here, we use $\mathrm{d}^3 v = 4\pi v^2 \mathrm{d}v$ and substitute the integration variable for the energy $E = \mu v^2/2$. As the right hand side of Eq. (3.6) only depends on the temperature, we can fully determine the reactivity $\langle\sigma v\rangle$, if the cross section $\sigma(E)$ is known experimentally or predicted theoretically, and if the above assumptions hold.

Additionally, any reaction rate for a particle i, being destroyed by a particle j, can be related to a mean lifetime

$$\tau_j(i) = \frac{1}{\langle\sigma v\rangle_{i,j} n_j}\,. \tag{3.7}$$

3.1.2 Compound nucleus

In general, forces mediated by nucleons and nuclei are the gradients of potential fields. The target effectively acts as a potential barrier, which a projectile can either overcome to form a compound nucleus, or it is reflected. This behavior is captured by the solutions ψ of Schrödinger's equation that reads in one dimension

$$\left[-\frac{\hbar^2}{2m}\frac{\mathrm{d}^2}{\mathrm{d}x^2} + V\right]\psi = E\psi\,, \tag{3.8}$$

where V is the potential and m is the mass of the projectile. The probability for a nuclear reaction to occur is described by the transmission coefficient

$$T = \frac{k_\mathrm{f}|\psi_\mathrm{f}|^2}{k_\mathrm{i}|\psi_\mathrm{i}|^2}\,, \tag{3.9}$$

with ingoing (i) and outgoing (f) wave function ψ and wave number k. It can be shown [159] that the cross section for the production of a compound nucleus is related to the sum over the transmission coefficients T_l for all possible angular momenta l of the projectile:

$$\sigma = \frac{\pi}{k^2}\sum_{l=0}^{\infty}(2l+1)T_l\,. \tag{3.10}$$

Equation (3.10) holds for spinless particles, however both target and projectile typically carry the spins I_i and I_j, respectively. Consequently, the spin for the production channel $\mathbf{S} = \mathbf{I}_i + \mathbf{I}_j$ has values from $|I_i - I_j|$ to $I_i + I_j$. The sum of all allowed spin orientations is then given by the product of the constituent spin contributions:

$$\sum_{S=|I_i-I_j|}^{I_i+I_j}(2S+1) = \frac{(2I_i+1)\big(2I_j+1\big)}{1+\delta_{ij}}\,, \tag{3.11}$$

where we bear in mind that the degenerate case of identical particles solely leads to even spin channels, cutting in half the total number of states. The total spin $\mathbf{J}$ of the compound nucleus state is the sum of the channel spin $\mathbf{S}$ and the angular momentum $\mathbf{l}$. Thus, we express the sum in Eq. (3.10) in terms of a sum over spin J and parity π

$$\sigma_\text{compound} = \frac{\pi}{k^2}\frac{1+\delta_{ij}}{(2I_i+1)\big(2I_j+1\big)}\sum_{J,\pi}(2J+1)\,T_J(E,J,\pi)\,. \tag{3.12}$$

For the reaction $i(j,o)m$ to occur, the compound nucleus decays into the ejectile o and nucleus m with a certain probability. At sufficiently high excitation energies, the level density of the compound nucleus is so large that the reaction cross section is by good approximation a smooth function. Accordingly, the average cross section can be well assessed by means of statistical descriptions. One very successful approach is the Hauser-Feshbach theory [160], based on assumption the formation of the compound nucleus and its decay can be treated independently from each other [161]. Consequently, the probability to decay into the specific outgoing channel o is the ratio of its branching probability and the sum over all possible decay channels, $p_o = T_o / \sum_n T_n$. Combined with Eq. (3.12), we arrive at the so-called Hauser-Feshbach formula

$$\sigma_{\text{HF}} = p_o \sigma_{\text{compound}} = \frac{\pi}{k^2} \frac{1+\delta_{ij}}{(2I_i+1)\left(2I_j+1\right)} \sum_{J,\pi} (2J+1) \frac{T_J(E,J,\pi)\, T_o(E,J,\pi)}{T_{\text{tot}}(E,J,\pi)} . \tag{3.13}$$

At low energies, the level density is small and the energies of a few excited state in the compound nucleus become important for the reaction mechanism. Hence, individual resonances can dominate the total cross section. Every excited state is unstable against decay and the life time of a compound nucleus state τ is directly connected to the decay width $\Gamma = \hbar/\tau$ by Heisenberg's uncertainty principle. Since the compound nucleus can decay over various decay channels, the total decay width Γ_n is the sum over all partial decay widths. Considering resonances in the shape of a Lorentz function, the Breit-Wigner resonance formula describes the resonance cross section as

$$\sigma_{\text{BW}} = \frac{\pi}{k^2} \frac{1+\delta_{ij}}{(2I_i+1)\left(2I_j+1\right)} \sum_{n} (2J_n+1) \frac{\Gamma_{j,n}\, \Gamma_{o,n}}{(E-E_n)^2 + (\Gamma_n/2)^2} . \tag{3.14}$$

3.1.3 Detailed balance

The cross section of the reaction $i + j \rightarrow o + m$ is fundamentally related to the one of the reverse reaction $o + m \rightarrow i + j$. As the direction of time does not explicitly enter the equations, these processes are invariant under time reversal. For a given total energy, the corresponding cross sections can be expressed in terms of the phase space available in the exit channel. This phase space is equivalent to the number final states per unit energy, respectively. Furthermore, the number of states in the interval $[p, p + \mathrm{d}p]$ is proportional to p^2. Using the wave number $k = p/\hbar$ of a de Broglie wave and accounting for the spin states of the ground state, we obtain for the ratio of the cross sections [29]

$$\frac{\sigma_i(j,o)_J}{\sigma_m(o,j)_J} = \frac{1+\delta_{ij}}{1+\delta_{om}} \frac{(2J_o+1)(2J_m+1)}{(2J_i+1)\left(2J_j+1\right)} \frac{k_o^2}{k_j^2} , \tag{3.15}$$

where the factors $(1+\delta_{ij})$ and $(1+\delta_{om})$ account for cases with identical particles in the entrance and exit channel, respectively. Moreover, J is the spin of an individual state populated in the compound nucleus. The result in Eq. (3.15) is called the principle of detailed balance, and also referred to as reciprocity theorem. This relation is valid for all states in the compound nucleus. Then, we get for the total cross section at energies $E_{ij} = E_{om} + Q_{(o,j)}$, involving the Q-value $Q_{(o,j)}$ of the reaction $m(o,j)i$:

$$\frac{\sigma_i(j,o;E_{ij})}{\sigma_m(o,j;E_{om})} = \frac{1+\delta_{ij}}{1+\delta_{om}} \frac{g_o g_m}{g_i g_j} \frac{k_o^2}{k_j^2} , \tag{3.16}$$

with the degeneracy factors of the ground state $g = (2j+1)$. However, in an astrophysical plasma the excited states of a nucleus are thermally populated. Therefore, we introduce partition functions $G_x = \sum_n g_{x,n} \exp(-E_n/[k_{\text{B}}T])$ to correct for the contribution of these states. We finally combine Eqs. (3.6) and (3.16) to obtain a general formula that relates forward and inverse reactions:

$$\langle \sigma v \rangle_{i,j} = \frac{1+\delta_{ij}}{1+\delta_{om}} \frac{g_o G_m}{g_j G_i} \left(\frac{\mu_{om}}{\mu_{ij}} \right)^{3/2} \exp\left(-\frac{Q_{(o,j)}}{k_{\text{B}}T} \right) \langle \sigma v \rangle_{o,m} . \tag{3.17}$$

This equation is particularly useful to calculate unknown forward reaction rates from measured inverse reactions, or vice versa. In addition, it allows to consistently determine reverse reaction rates from theoretically calculated rates, while maintaining detailed balance.

3.1.4 Photodisintegrations, lepton captures, and decays

Some reaction types do not only involve nuclei, but also particles whose interaction is mediated by the electromagnetic force or the weak force. We can analogously derive rates for these kinds of reactions with the aid of Eq. (3.2).

In the case of photodisintegrations, the relative velocity is the speed of light c, and the underlying particle distribution is the Planck distribution for photons

$$\mathrm{d}n_\gamma = \frac{8\pi}{c^3}\frac{\nu}{\exp(h\nu/[k_\mathrm{B}T])-1}\,\mathrm{d}\nu = \frac{1}{\pi^2(c\hbar)^3}\frac{E_\gamma^2}{\exp\left(E_\gamma/[k_\mathrm{B}T]\right)-1}\,\mathrm{d}E_\gamma\,. \tag{3.18}$$

As the target nucleus i still obeys a Boltzmann distribution, and because the photodisintegration cross section only depends on the photon energy E_γ, the number of phostodisintegrations per cm^3 and sec is

$$r_{i,\gamma} = \frac{n_i}{\pi^2 c^2\hbar^3}\int_0^\infty \frac{\sigma_i(\gamma,o;E_\gamma)E_\gamma^2}{\exp\left(E_\gamma/[k_\mathrm{B}T]\right)-1}\,\mathrm{d}E_\gamma\,. \tag{3.19}$$

In contrast to reactions that exclusively involve nucleons or nuclei, Eq. (3.19) has a linear dependence on the number density and can be effectively regarded as temperature dependent decay term for nucleus i. Basically, one needs to know the photodisintegration cross section. However, the principle of detailed balance greatly facilitates the calculation of photodisintegration cross section $\sigma_{i(\gamma,o)m}$ from the corresponding quantity of the reverse reaction, i.e., the capture cross section $\sigma_{m(o,\gamma)i}$.

With increasing density, electrons are degenerate and the Fermi energy increases as $(\rho Y_\mathrm{e})^{2/3}$, overcoming the proton-neutron mass difference eventually. This gives rise to electron captures

$$\mathrm{e}^- + (Z,A) \rightarrow (Z-1,A) + \nu_\mathrm{e}\,, \tag{3.20}$$

are otherwise prohibited energetically due to a negative Q-value. As nuclei have a considerably higher mass than electrons, we assume that the nucleus is at rest and the relative velocity is equal to the electron velocity. The number of reactions per volume and time is then given by

$$r_{i,\mathrm{e}} = n_i \int \sigma_\mathrm{e}(\nu_\mathrm{e})\ \nu_\mathrm{e}\,\mathrm{d}n_\mathrm{e} = n_i\lambda_{i,e}(\rho Y_\mathrm{e},T)\,, \tag{3.21}$$

where $n_\mathrm{e} = \rho N_\mathrm{A} Y_\mathrm{e}$ is the electron density and Y_e is the electron fraction, denoting the number of electrons per baryon. Similar to Eq. (3.19), the expression in Eq. (3.21) is linear in n_i, but this time there is a temperature as well as density dependence. If the temperature is high enough $T \gtrsim 1.022$ MeV, photons create electron-positron pairs and positron captures become feasible:

$$\mathrm{e}^+ + (Z,A) \rightarrow (Z+1,A) + \bar{\nu}_\mathrm{e}. \tag{3.22}$$

At very high densities $\rho \gtrsim 10^{12}$ g/cm^3, the neutrino scattering cross sections are large enough for neutrinos to be also captured by nuclei. Under these conditions, neutrinos become thermalized and their distribution is coupled to the medium properties. Being the reverse reactions of electron and positron captures, we determine the electron neutrino and electron antineutrino capture rates via detailed balance.

Finally, a nucleus can undergo β- or α-decay to a state of a corresponding daughter nucleus, if the outgoing channel is energetically favored. This implies that the difference between the energies of the final and the initial states is positive, as is the Q-value. The half-life $\tau_{1/2,i}$ of the decaying nucleus i is inversely proportional to the decay constant $\lambda_i = \ln 2/\tau_{1/2,i}$, and

$$r_i = n_i\lambda_i\,. \tag{3.23}$$

Since decays typically start from the ground state of the decaying nucleus under laboratory conditions, the decay constant λ_i is truly constant. However, in an astrophysical plasma, high temperatures lead to the population of excited states n in the nucleus. Each of these excited states contributes to the total decay "constant"

$$\lambda_i(T) = \frac{\sum_n \lambda_{i,n}(2J_n+1)\exp(-E_n/[k_\mathrm{B}T])}{\sum_n(2J_n+1)\exp(-E_n/[k_\mathrm{B}T])} = \frac{\sum_n \lambda_{i,n}(2J_n+1)\exp(-E_n/[k_\mathrm{B}T])}{G_i(T)}\,, \tag{3.24}$$

making use of the partition functions $G_i(T)$, defined for Eq. (3.17). Especially after beta decays, the resulting daughter nucleus can be in a highly excited state above the neutron separation threshold. Then, the decay is followed by the immediate emission of one or more neutrons, such that the final daughter nucleus is no longer an isobar of the initially beta-decaying nucleus. This is the so-called beta-delayed neutron emission.

3.1.5 Fission reactions

The most heavy nuclei likely decay via fission into daughter nuclei and potentially neutrons. We take into account three distinct fission decay channels:

$$(Z,A) \to (Z_1,A_1) + (Z_2,A_2) + \mathcal{N}\mathrm{n}\,, \tag{3.25}$$

$$(Z,A) \to (Z+1,A) \to (Z_1,A_1) + (Z_2,A_2) + \mathcal{N}\mathrm{n}\,, \tag{3.26}$$

$$\mathrm{n} + (Z,A) \to (Z,A+1) \to (Z_1,A_1) + (Z_2,A_2) + \mathcal{N}\mathrm{n}\,. \tag{3.27}$$

Equations (3.25)—(3.27) describe the decay of a mother nucleus (Z,A) into daughter nuclei (Z_1,A_1) and (Z_2,A_2) via spontaneous fission, beta-delayed fission, and neutron-induced fission, respectively. In the fission process, $\mathcal{N}$ neutrons n are emitted. For spontaneous fission, the decay rate can be viewed as the one of a beta decay. However, for beta-delayed fission, the mother nucleus first decays to an intermediate nucleus that can also decay over several other channels competing with fission. Thus, the beta-delayed fission rates are implemented with branching ratios into the already present (neutron-delayed) beta-decay rates. Neutron-induced fission is effectively treated as a neutron capture reaction.

3.2 Nuclear physics input for the r-process

We consider over 5800 nuclei between the valley of stability and the neutron drip line, comprising isotopes from H to Rg. The nuclear properties (e.g., mass excess, ground state spin, and partition functions) [162, 163] and reaction rates are taken from the compilation of Ref. [162] for the Finite Range Droplet Model (FRDM, [164]). In particular, the reaction rates are tabulated as the coefficients of a fit function in the JINA REACLIB format [165]. It is important to note that the nuclear masses basically enter the theoretical model of any reaction. To maintain consistency, one must calculate technically all rates in the framework of the same mass model. For part of our studies, we tabulate neutron capture and photodissociation rates for mass models in Ref. [20] (see Sect. 5.2) calculated with the code TALYS [166]. We compute these rates for 30 points between 0.0001 GK and 10 GK on a logarithmically-spaced temperature grid. Theoretical weak interaction rates including neutrino absorption on nucleons are taken into account [167–171], and we utilize chemical potentials from the Helmholtz equation of state [172]. Furthermore, neutron capture for nuclei with $Z > 83$ and neutron-induced fission rates are given by Ref. [173] as well as beta-delayed fission probabilities from Ref. [35].

3.3 Nuclear reaction networks

Once we know the number of reactions per volume and time for all the reaction types, we can assemble them in an arbitrarily large set of coupled differential equations. The size of this system of equations strongly depends on the underlying physical scenario. The r-process nucleosynthesis involves thousands of nuclei, linked by up to a few 10^5 reactions. In this section, we introduce the basic concepts of nuclear reaction networks.

3.3.1 System of differential equations

Since we consider mixtures with different species of nuclei, instead of one single reaction, we introduce the correction term $(1+\delta_{ij})$ to divide by two if the particles i and j are identical. Doing so, we prevent the network from counting particles twice, when exchanging projectiles for targets. Then, we rewrite Eq. (3.4) as

$$r_{i,j} = \frac{1}{1+\delta_{ij}} n_i n_j \langle \sigma v \rangle_{i,j}\,. \tag{3.28}$$

In the same manner, three-body reactions are adjusted:

$$r_{i,j,k} = \frac{1}{1+\Delta_{ijk}} n_i n_j n_k \langle \sigma v \rangle_{i,j,k}\,, \tag{3.29}$$

with the correction term $\Delta_{ijk} \equiv \delta_{ij} + \delta_{jk} + \delta_{ik} + 2\delta_{ijk}$. As $r_{i,j}$ and $r_{i,j,k}$ are the number of reactions per time and volume, it is useful to express the reactions of nuclei in terms of the change in number densities of the affected nuclear species. For the reaction $i(j,o)m$, e.g., the changes in number densities are given by

$$\left(\frac{\partial n_i}{\partial t}\right)_\rho = \left(\frac{\partial n_j}{\partial t}\right)_\rho = -r_{i,j}\,, \tag{3.30}$$

$$\left(\frac{\partial n_o}{\partial t}\right)_\rho = \left(\frac{\partial n_m}{\partial t}\right)_\rho = +r_{i,j}\,, \tag{3.31}$$

where we require that the changes in composition leave the density ρ unchanged. Typically, a lot of reactions take place at the same time, and we have

$$\left(\frac{\partial n_i}{\partial t}\right)_\rho = \sum_j N^i_j r_j + \sum_{j,k} \frac{N^i_{j,k}}{1+\delta_{jk}} r_{j,k} + \sum_{j,k,l} \frac{N^i_{j,k,l}}{1+\Delta_{jkl}} r_{j,k,l}\,, \tag{3.32}$$

In Eq. (3.32), the coefficients N^i are integer constants that take into account how many nuclei of the species i are destroyed ($N^i < 0$) or produced ($N^i > 0$).

For most astrophysical environments, the density does not remain constant. Explosive scenarios, e.g., show density variations over several orders of magnitude. To incorporate changes in density, we write the number density $n_i = \rho N_\mathrm{A} Y_i$ as a product of density ρ, Avogadro's number N_A and the abundance Y_i. Then, the derivative $\dot{Y}_i$ reads

$$\dot{Y}_i = \frac{\dot{n}_i}{\rho N_\mathrm{A}} - \frac{n_i}{\rho N_\mathrm{A}} \frac{\dot{\rho}}{\rho}\,. \tag{3.33}$$

The definition of abundances originates from the mass fraction X_i, i.e., the percentage of mass m_i (or, equivalently, density ρ_i) that one species holds with respect to the total mass (density) of a system:

$$X_i = \frac{\rho_i}{\rho} = \frac{n_i}{\rho N_\mathrm{A}} m_i N_\mathrm{A} = Y_i A_i\,, \tag{3.34}$$

where $m_i N_\mathrm{A}$ is the total mass of a mole of particles i, defining the atomic weight A_i. By construction, all mass fractions must add up to $\sum_i X_i = 1$.

We restate Eq. (3.32) in terms of abundances to arrive at the system of differential equations that is commonly referred to as nuclear reaction network

$$\dot{Y}_i = \sum_j N^i_j \lambda_j Y_j + \sum_{j,k} \frac{N^i_{j,k}}{1+\delta_{jk}} \rho N_\mathrm{A} \langle \sigma v \rangle_{j,k} Y_j Y_k + \sum_{j,k,l} \frac{N^i_{j,k,l}}{1+\Delta_{jkl}} \rho^2 N_\mathrm{A}^2 \langle \sigma v \rangle_{j,k,l} Y_j Y_k Y_l\,. \tag{3.35}$$

For a given input, obtained in hydrodynamical simulations or parametric studies, the system of Eq. (3.35) poses an initial value problem with a coupled set of ordinary differential equations and coefficients that are a function of density and temperature.

3.3.2 Energy generation

Let us consider nuclei in a given volume V with fixed total mass $M = \sum_i n_i m_i V$. The conversion of nuclei due to nuclear reactions drives the energy generation by the change in total mass $\dot{E} = \dot{M} c^2$. Since more stable nuclei are created in the long run, the increasing binding energy reduces the total mass and releases energy

$$\dot{E} = -V \sum_i \left(\frac{\partial n_i}{\partial t}\right)_\rho m_i c^2 = -\rho N_\mathrm{A} V \sum_i \dot{Y}_i m_i c^2\,. \tag{3.36}$$

To obtain the energy generation per gram of matter and sec, we divide by the specific volume that encloses one gram of matter and we have

$$\dot{\epsilon} = -N_\mathrm{A} \sum_i \dot{Y}_i m_i c^2\,. \tag{3.37}$$

We can use the nuclear heating in Eq. (3.37) to translate the generated energy into a self-consistent temperature update [11, 174].

Moreover, the energy generation by the r-process is calculated and its impact on the entropy is included [11]. As is common practice, we neglect the feedback of nuclear heating on the density evolution. In the case of the dynamic ejecta from a neutron star mergers, it has been shown that this approximation is very good for nucleosynthesis calculations, although the long-term hydrodynamical evolution of the ejecta is heavily influenced. We expect that the impact on the nucleosynthesis in the late-time ejecta is also small, but since the expansion time scales here are different from the dynamic ejecta, this issue may need further scrutiny in the future [133]. The heating mainly originates from beta decays and we assume that the energy is roughly equally distributed between thermalizing electrons and photons, and escaping neutrinos and photons [9].

$$kT\frac{\mathrm{d}S}{\mathrm{d}t} = \epsilon_{\mathrm{th}}\dot{q}\,. \tag{3.38}$$

3.4 Solving the network equations

The system of ordinary differential equations described by Eq. (3.35) can be generalized to the form

$$\frac{\mathrm{d}\mathbf{y}}{\mathrm{d}t} = \mathbf{f}(t,\mathbf{y})\,, \tag{3.39}$$

which we will use in this section to describe strategies for its solution as an initial value problem. In the case of a nuclear reaction network, the function $\mathbf{f}(t,\mathbf{y})$ on the right hand side of Eq. (3.39) defines the change of abundances by nuclear reaction rates. The reaction rates typically differ by many orders of magnitude and can exhibit extremely nonlinear dependencies on temperature. In addition, the abundances $\mathbf{y}$ range over many orders of magnitude, too. Such a system of differential equations is called stiff, and its solution is rather limited by numerical stability than by accuracy. In the following, we introduce two numerical strategies to solve the network equations and we discuss, how making use of the sparse matrix format greatly reduces the computational costs.

3.4.1 Implicit Euler method

The simplest, yet stable, method to solve a stiff system of ordinary differential equations is the implicit (or backward) Euler method. In general, this scheme is first order accurate, i.e., $\mathcal{O}(h)$, and the error term is $\mathcal{O}(h^2)$. The implicit Euler method relies on evaluating the function $\mathbf{f}$ at the new time step $t_{n+1} = t_n + h$ with the future abundances $\mathbf{y}_{n+1}$

$$\mathbf{y}_{n+1} = \mathbf{y}_n + h\,\mathbf{f}(t_{n+1},\mathbf{y}_{n+1})\,, \tag{3.40}$$

where n tracks the number of iterations. The implicit differentiation in Eq. (3.40) cannot be directly solved for $\mathbf{y}_{n+1}$. Hence, we rearrange the equation and rephrase it as the problem to find the root of

$$\frac{\mathbf{y}_{n+1}-\mathbf{y}_n}{h} - \mathbf{f}(t_{n+1},\mathbf{y}_{n+1}) = 0\,. \tag{3.41}$$

This nonlinear set of equations can be solved with the aid of the Newton-Raphson method, resulting in

$$\mathbf{y}^{(m+1)}_{n+1} = \mathbf{y}^{(m)}_{n+1} - \mathbf{J}^{-1}\cdot\left(\frac{\mathbf{y}^{(m)}_{n+1}-\mathbf{y}_n}{h} - \dot{\mathbf{y}}^{(m)}_{n+1}\right), \tag{3.42}$$

which is iterated over m until reaching convergence. Equation (3.42) involves the Jacobian matrix, whose components are

$$J_{ij} = \frac{1}{h} - \frac{\partial \dot{y}^{(m)}_{i,n+1}}{\partial y^{(m)}_{j,n+1}}\,. \tag{3.43}$$

It has to be inverted at every iteration step, making the Newton-Raphson scheme the computationally most expensive part of solving the nuclear reaction network.

In total, the implicit Euler method has relatively low computational cost per time step. Different from (fixed) higher order methods, we only require to evaluate Eq. (3.42) once within an iteration. However, the simple Euler method does not provide an error estimate for the accuracy of a time step. To overcome this shortcoming, we check for mass conservation at every iteration:

$$\sum_{i=1}^{N} X_i = 1\,, \tag{3.44}$$

where X_i is the mass fraction of a nucleus. If Eq. (3.44) exceeds a certain tolerance limit ϵ_{NR}, up to three Newton-Raphson steps are performed. In the case that the solution is still not converged, we cut the time step by half and restart the integration routine.

To choose an efficient time step that leads to convergence, we use the adaptive step size formula

$$h = \eta \min\left\{\frac{y_i}{\mathrm{d}y_i/\mathrm{d}t}\right\}\,, \tag{3.45}$$

with the positive constant $\eta < 1$. In Eq. (3.45), we only take into account nuclei with abundances y_i larger than 10^{-10}. Moreover, the thermodynamic quantities add another constraint, since we require them to alter by less than 5% in a time step. Avoiding to overshoot the solution, we limit any time step to increase by a factor of 2 at maximum for consecutive steps.

3.4.2 Gear's backward differentiation method

As an alternative to the implicit Euler method, we employ the backward differentiation method of Gear [175] to integrate the network equations (3.35). While being mathematically more involved, this method bears the advantage of both step size and accuracy control by considering higher order terms. Its basic idea is to approximate the exact solution of the ODE system by calculating an interpolatory polynomial of order q or less ($1 \leq q \leq 5$) that captures the past behavior of the numerical solution. It is used to construct an updated polynomial, predicting the solution at future times. In an iterative procedure, this solution is then corrected, until it reaches a predefined precision.

Gear's method stores the past behavior of the solution in the so-called Nordsieck vector $\mathbf{z}_n$. It is updated at each time step and is given by

$$\mathbf{z}_n = \left[\mathbf{y}_n, h\dot{\mathbf{y}}_n, \frac{h^2\ddot{\mathbf{y}}_n}{2}, \ldots, \frac{h^q\mathbf{y}_n^{(q)}}{q!}\right]\,, \tag{3.46}$$

where $h = t_{n+1} - t_n$ is the current time step, $\mathbf{y}_n$ is the abundance vector and $\dot{\mathbf{y}}_n, \ldots, \mathbf{y}_n^{(q)}$ are its derivatives with respect to time. The procedure to evolve the system from time t_n to t_{n+1} and beyond is divided into three parts: 1) the predictor step, 2) the corrector step, and 3) error estimation, step size control and selection of order.

Predictor step

In the predictor step, the future solution is approximated by calculating

$$\mathbf{z}_{n+1}^{(0)} = \mathbf{z}_n \cdot \mathbf{A}(q)\,. \tag{3.47}$$

Here, $A(q)$ is the $(q+1) \times (q+1)$ Pascal triangle matrix defined as

$$A^{ij}(q) = \begin{Bmatrix} 0 & \text{if} \quad i < j \\ \begin{pmatrix} i \\ j \end{pmatrix} = \frac{i!}{j!(i-j)!} & \text{if} \quad i \geq j \end{Bmatrix}\,, \quad \text{with} \quad i, j = 0, 1, \ldots, q\,. \tag{3.48}$$

The product in Eq. (3.47) is basically the Taylor expansion of $\mathbf{y}_n$ and its derivatives $\dot{\mathbf{y}}_n$, ..., $\mathbf{y}_n^{(q)}$. For a given value of q, the Taylor series for $\mathbf{y}_n$ is truncated at the order q, and evaluating it at $t = t_{n+1}$ yields a prediction for the future state of the system.

Corrector step

To obtain the solution $\mathbf{y}_{n+1}$, the first approximation from the predictor step $\mathbf{z}_{n+1}^{(0)}$ gets adjusted by a correction term

$$\mathbf{z}_{n+1} = \mathbf{z}_{n+1}^{(0)} + \mathbf{e}_{n+1}\ell\,, \tag{3.49}$$

where $\mathbf{e}_{n+1}$ is a correction vector and ℓ is a $1\times(q+1)$-vector, implicitly given by

$$\sum_{j=0}^{q}\ell_j x^j=\prod_{i=1}^{q}\left(1+\frac{x}{\xi_i}\right), \tag{3.50}$$

with $x=(t-t_{n+1})/h$ and $\xi_i=(t_{n+1}-t_{n+1-i})/h$. Using the successive partial products in Eq. (3.50), the components of the vector $\ell=[\ell_0(q),\ldots,\ell_j(q),\ldots,\ell_q(q)]$ at order q are calculated as follows:

$$\ell_0(q)=1,\quad \ell_1(q)=\sum_{i=1}^{q}\xi_i^{-1},\quad \ell_j(q)=\ell_j(q-1)+\ell_{j-1}(q-1)/\xi_q,\quad \ell_q(q)=\left(\prod_{i=1}^{q}\xi_i\right)^{-1}. \tag{3.51}$$

The correction vector $\mathbf{e}_{n+1}$ is determined simultaneously with the solution $\mathbf{y}_{n+1}$, using a modified Newton-Raphson scheme

$$\left[\mathbf{1}-\frac{h}{\ell_1}\mathbf{J}\right]\Delta^{(m)}=-\left(\mathbf{y}^{(m)}_{n+1}-\mathbf{y}^{(0)}_{n+1}\right)+\frac{h}{\ell_1}\left(\dot{\mathbf{y}}^{(m)}_{n+1}-\dot{\mathbf{y}}^{(0)}_{n+1}\right), \tag{3.52}$$

$$\mathbf{y}^{(m+1)}_{n+1}=\mathbf{y}^{(m)}_{n+1}+\Delta^{(m)}, \tag{3.53}$$

where m is the number of iterations, $\Delta^{(m)}$ is the iterative correction and $\mathbf{J}$ is the Jacobian with components

$$J_{ij}=\frac{\partial\dot{y}^{(m)}_{i,n+1}}{\partial y^{(m)}_{j,n+1}}. \tag{3.54}$$

In Eq. (3.52), both the derivative vector $\dot{\mathbf{y}}^{(m)}_{n+1}$ and the matrix $\mathbf{J}$ are calculated at every iteration. The authors of Ref. [176] argue that it is only necessary to update $\mathbf{J}$ once per time step. However, strong self-consistent nuclear heating, such as during the main r-process, can lead to rapid changes in the reaction rates. This is particularly true for the photodissociation reactions, having a steep temperature dependence $\lambda_{(\gamma,x)}\propto\exp(-1/T)$.

After the Newton-Raphson scheme in Eq. (3.52) has converged, the correction vector is obtained from

$$\mathbf{e}_{n+1}=\mathbf{y}_{n+1}-\mathbf{y}^{(0)}_{n+1}. \tag{3.55}$$

It can be shown that the corrected Nordsieck vector $\mathbf{z}_{n+1}$ in Eq. (3.49) is accurate to order q, i.e., the errors relative to the exact solution are at most of order $(q+1)$.

Error estimation, step size control and selection of order

For automatic step size control, it is necessary to consider the error of the current step. Due the Taylor series representation, the error can be estimated from the corresponding truncation error

$$\mathbf{E}_{n+1}(q)=-\frac{1}{\ell_1}\left[1+\prod_{i=2}^{q}\left(\frac{t_{n+1}-t_{n+1-i}}{t_n-t_{n+1-i}}\right)\right]^{-1}\mathbf{e}_{n+1}. \tag{3.56}$$

Next, the step size is computed for the subsequent step. Prescribing an error tolerance ϵ per step, the new step size is

$$h'=h\cdot K\left(\frac{\epsilon}{\max\left(\bar{\mathbf{E}}_{n+1}(q)\right)}\right)^{1/(q+1)}. \tag{3.57}$$

To prevent large changes in step size, the new time step h' is multiplied by a conservative factor $K\in[0.1,0.4]$. Moreover, Eq. (3.57) involves relative errors

$$\bar{E}_{i,n+1}=\begin{Bmatrix}E_{i,n+1}/y_i & \text{if} & y_i>y_{\text{scale}}\\ E_{i,n+1}/y_{\text{scale}} & \text{if} & y_i\le y_{\text{scale}}\end{Bmatrix}, \tag{3.58}$$

which are normalized to the respective abundance y_i or a cutoff scale y_{scale}, in order to reduce the weight of nuclei with very small abundances. In Ref. [176], the authors recommend the values $\epsilon=10^{-3}$ and $y_{\text{scale}}=10^{-10}$ as robust choice for the integration parameters.

To make beneficial use of different orders, we also calculate the errors for orders other than q. Following Ref. [177], we only consider $q \pm 1$, since all relevant data have been already computed at the same order. After q iterations at the order q, trial error estimates are determined to progressively ascend or descend to the most efficient order:

$$\mathbf{E}_{n+1}(q-1) = -\left[\frac{\prod_{i=1}^{q-1}\xi_i}{l_1(q-1)}\right]\frac{h^q \mathbf{y}_{n+1}^{(q)}}{q!}\,, \tag{3.59}$$

$$\mathbf{E}_{n+1}(q+1) = -\frac{\xi_{q+1}\left(\mathbf{e}_{n+1} - Q_{n+1}\mathbf{e}_n\right)}{(q+2)l_1(q+1)\left[1+\prod_{i=2}^{q}\left(\frac{t_{n+1}-t_{n+1-i}}{t_n-t_{n+1-i}}\right)\right]}\,, \tag{3.60}$$

with

$$Q_{n+1} = \frac{C_{n+1}}{C_n}\left(\frac{h_{n+1}}{h_n}\right)^{q+1}\,, \tag{3.61}$$

$$C_{n+1} = \frac{\prod_{i=1}^{q}\xi_i}{(q+1)!}\left[1+\prod_{i=2}^{q}\left(\frac{t_{n+1}-t_{n+1-i}}{t_n-t_{n+1-i}}\right)\right]. \tag{3.62}$$

Combining these expressions with Eq. (3.57) results in the corresponding trial step sizes. Then, the largest step size, i.e., $h' = \max\left(h'(q-1), h'(q), h'(q+1)\right)$, is selected and the order is adjusted respectively.

Finally, the Nordsieck vector is scaled to the new order and step size. If the order increases or stays the same, the Nordsieck vector remains unchanged. Only if the order decreases, a correction $\widetilde{\Delta}_i$ must be subtracted from each column of $\mathbf{z}_{i,n+1}$ $(i = 2, 3, ..., q-1)$:

$$\widetilde{\Delta}_i = d_i \mathbf{z}_{q,n+1}\,, \tag{3.63}$$

where the d_i are implicitly defined by

$$\sum_{j=0}^{q} d_j x^j = x^2 \prod_{i=1}^{q-2}(x+\xi_i)\,, \tag{3.64}$$

and their values $d_j(q)$ can be obtained similar to Eq. (3.50):

$$d_2(q) = \prod_{i=1}^{q-2}\xi_i, \quad d_j(q) = \xi_{q-2}\, d_j(q-1) + d_{j-1}(q-1), \quad d_{q-1}(q) = \sum_{i=1}^{q-2}\xi_i, \quad d_q(q) = 1\,, \tag{3.65}$$

and $d_0(q) = d_1(q) = 0$. Independent from changing the order, the Nordsieck vector is rescaled to the new step size with $\eta = h'/h$:

$$\mathbf{z}_{n+1} \leftarrow \mathbf{z}_{n+1} \cdot \mathrm{diag}\left(1, \eta, \eta^2, ..., \eta^q\right)\,, \tag{3.66}$$

initiating the next time step.

By setting $q = 1$, the above algorithm automatically takes care of building up enough history to make use of higher orders q. While Gear's method is more technical than the implicit Euler scheme, it reduces the number of time steps due to utilizing the past behavior of the system efficiently. Nevertheless, Gear's method requires slightly more Newton-Raphson iterations (for the reference integration parameters), resulting in similar overall computational costs.

3.4.3 Sparse matrix format

In the key step of both integration routines, we effectively have to invert the Jacobian in Eq. (3.43) or Eq. (3.54), an $N \times N$-matrix with $N \approx 7000$. This is computationally challenging, since standard algorithms, e.g. the Gauß-Jordan elimination, scale as $\mathcal{O}(n^3)$. Even more sophisticated methods are at the order of $\mathcal{O}(n^k)$ with $k \sim 2.373$, yet still costly due to the vast size of the matrix. Furthermore, we cannot make use of simplifying properties such as positive definiteness or symmetry, since forward and backward reactions generally differ.

In principle, all nuclei can be connected to all other nuclei. However, a particular nucleus does not undergo nuclear reactions with all other nuclei. Instead, only a small subset of reaction channels is important, whereas the

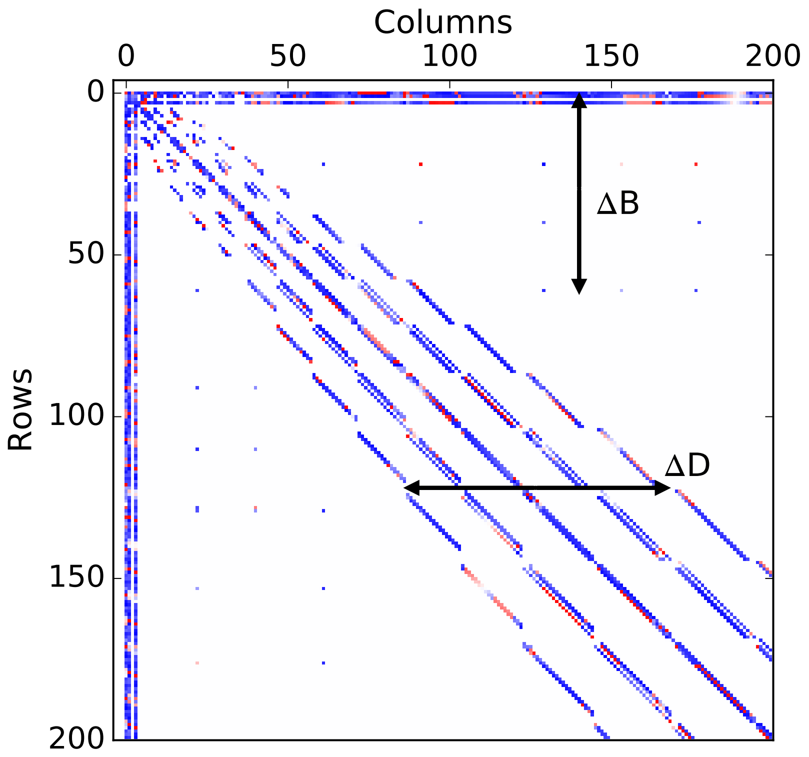

Figure 3.1: Example of a sparse matrix [50]. Negative and positive values are shown in blue and red, respectively. The width of the sideband ΔD is roughly 4 times the number of isotopes per element, and the width of the sideband ΔB is indicates the location of the heaviest fusion partners.

majority of theoretically possible reactions is physically not realized. Thus, the Jacobian contains mainly zeros as entries. Figure 3.1 shows the values for the Jacobian of Eq. (3.43) for an example reaction network with 789 nuclei [50]. White spaces mark zero entries. It can be seen that neutrons, protons and alpha particles are connected to almost all other nuclei. Additionally, every nucleus is linked to itself, resulting in finite values on the diagonal. As nuclei are ordered by elements and reactions with alpha particles can bridge isotopic chains, the width of the diagonal ΔD is approximately 4 times the mean number of isotopes per element. The width of the sideband ΔB is a measure for the location of the heaviest fusion partners in the network. For a sufficiently large number of nuclei ($N \gtrsim 100$), it is more efficient to carry along only the non-vanishing elements of the Jacobian. One such format is the so-called compressed sparse column format (CSCF). It stores the finite values of the matrix, and saves the information about the position of these values in two additional vectors: the first vector contains the row of the finite values and the second vector holds the index of the first finite value in every column.

To illustrate the storage of the CSCF, consider the simple example matrix

$$A = \begin{pmatrix} 1 & 0 & 5 & 0 \\ 0 & 2 & 6 & 0 \\ 7 & 0 & 3 & 0 \\ 0 & 8 & 0 & 4 \end{pmatrix}, \tag{3.67}$$

which we convert to

$$\begin{aligned} \mathrm{AA} &= [1,7,2,8,5,6,3,4], \\ \mathrm{JA} &= [1,3,2,4,1,2,3,4], \\ \mathrm{IA} &= [1,3,5,8,9]. \end{aligned}$$

Every finite entry of the matrix A is stored in the vector AA. The vector JA stores the position of the rows of AA and IA the position of the columns of the non-zero entries N_f. For a $N \times N$-matrix, the length of JA is equal to the length of AA, whereas IA has the length $N + 1$. From this construction, it follows that for an $N \times N$-matrix with $N^2 = N_\mathrm{f} + N_\mathrm{z}$, this format is advantageous, if the amount of zero entries N_z is larger than

$$N_\mathrm{z} \geq \frac{N^2 + N + 1}{2}. \tag{3.68}$$

From Eq. (3.68), it follows that more than

$$p \geq 50\left(1+\frac{1}{N}+\frac{1}{N^2}\right)\% \tag{3.69}$$

of the entries must be zero. Nevertheless, there is an overhead for calculating the position indices of the non-vanishing entries, raising the lower limit in Eq. (3.69) mildly. For the example of 789 nuclei shown in Fig. 3.1, the matrix has 13691 of 622521 non-zero entries. This means that ≈ 98% of the entries are zero. Due to the dependence on the inverse of N, the CSCF is more efficient for larger matrices.

In the network [81, 158], used and extended in the framework of this work, we employ Intel's PARDISO matrix solver [178] that brings along efficient algorithms to process data stored in the CSCF.

3.5 Nuclear statistical equilibrium

Nuclear statistical equilibrium (NSE) is reached, if the temperature is high enough ($T \gtrsim 5$ GK) for the photons to dissociate nuclei and if densities of $10^6\ \mathrm{g/cm^3} \lesssim \rho \lesssim 10^{13}\ \mathrm{g/cm^3}$ facilitate nuclear reactions to form nuclei rapidly. Then, strong and electromagnetic reactions are in an equilibrium such that the rates for production and destruction of nuclei are equal. In NSE, the chemical potentials for nucleons and nuclei satisfy the relation

$$\mu_{(Z,A)} = Z\mu_\mathrm{p} + N\mu_\mathrm{n}\,. \tag{3.70}$$

In Eq. (3.70), we use chemical potentials of the form

$$\mu_i = m_i c^2 + k_\mathrm{B} T \eta_i + \mu_\mathrm{C}\,, \tag{3.71}$$

with the degeneracy parameter η_i, and the term μ_C that absorbs the Coulomb contribution to the chemical potential [179].

Since nucleons are fermions, they obey the Fermi-Dirac statistics in general. The abundances of nucleons as well as those of electrons and positrons are directly related to the number densities $n_i = Y_i\ n = Y_i\ \rho/m_\mathrm{u}$ and we calculate them by finding the root of

$$Y_i = \frac{m_\mathrm{u}}{\rho}\frac{\sqrt{2}}{\pi^2(\hbar c)^3} m_i^3 c^6 \beta_i^{3/2}\left[\mathscr{F}_{1/2}(\eta_i,\beta_i) + \beta_i \mathscr{F}_{3/2}(\eta_i,\beta_i)\right]\,, \tag{3.72}$$

where $\beta_i = k_\mathrm{B}T/(m_i c^2)$ is the relativistic parameter and m_u is the atomic mass unit. Moreover, we use the integrals of Fermi functions

$$\mathscr{F}_k(\eta_i,\beta_i) = \int_0^\infty \frac{x^k(1+\frac{1}{2}\beta_i x)^{1/2}}{1+e^{x-\eta_i}}\,\mathrm{d}x\,. \tag{3.73}$$

The number density of an electron-positron gas is $n_\mathrm{e} = n_{\mathrm{e}^-} - n_{\mathrm{e}^+}$, for which we generally obtain $n_{\mathrm{e}^\pm}$ from Eq. (3.72). In a few limit cases ($\eta_\mathrm{e} \ll 0$: non-degenerate, $\eta_\mathrm{e} \gg 0$ extremely degenerate, $\beta_\mathrm{e} \ll 1$: non-relativistic, and $\beta_\mathrm{e} \gg 1$: extremely relativistic), the corresponding approximations greatly simplify the calculations [180]. Additionally, the chemical potentials of electrons and positrons are linked by $\mu_{\mathrm{e}^+} = -\mu_{\mathrm{e}^-}$, which translates to $\eta_{\mathrm{e}^+} = -\eta_{\mathrm{e}^-} - 2/\beta_\mathrm{e}$.

Heavier nuclei are assumed to follow Maxwell-Boltzmann statistics and therefore their abundance can be analytically obtained:

$$Y_i = \frac{m_\mathrm{u}}{\rho}\frac{G_i(T)e^{\eta_i}}{\Lambda_i^3}\,, \tag{3.74}$$

with the nuclear partition functions $G_i(T)$ (see Eq. (3.24)) and the thermal wavelength $\Lambda_i = \sqrt{2\pi(\hbar c)^2/(k_\mathrm{B}T m_i c^2)}$. Combining Eqs. (3.70) and (3.74), we get for nuclei with mass number $A_i > 1$

$$Y_i = \frac{G_i(T)}{\rho} m_\mathrm{u}\left(\frac{k_\mathrm{B} T A_i m_\mathrm{u} c^2}{2\pi(\hbar c)^2}\right)^{3/2} e^{N_i\eta_\mathrm{n} + Z_i\eta_\mathrm{p}} e^{B_i/(k_\mathrm{B}T)} e^{Z_i\mu_\mathrm{c,p} - \mu_{\mathrm{C},(Z_i,A_i)}}\,, \tag{3.75}$$

where $B_i = Z_i m_\mathrm{p} c^2 + N_i m_\mathrm{n} c^2 - m_{(Z_i,A_i)} c^2$ is the binding energy for a nucleus with mass $m_{(Z_i,A_i)} \approx A_i m_\mathrm{u}$, neglecting marginal contributions due to the mass excess.

For densities $\rho \lesssim 10^{11} - 10^{13}\ \mathrm{g/cm^3}$ (the exact transition depends on the temperature), nucleons are non-degenerate and approximated well by means of the Maxwell-Boltzmann statistics. Taking $m_\mathrm{p} \approx m_\mathrm{n} \approx m_\mathrm{u}$, the NSE abundances read

$$Y_i = G_i(T)\left(\frac{\rho}{m_\mathrm{u}}\right)^{A_i-1}\frac{A_i^{3/2}}{2^{A_i}}\left(\frac{2\pi(\hbar c)^2}{k_\mathrm{B} T m_\mathrm{u} c^2}\right)^{3(A_i-1)/2} Y_\mathrm{n}^{N_i} Y_\mathrm{p}^{Z_i} e^{B_i/(k_\mathrm{B}T)} e^{Z_i\mu_{\mathrm{c,p}}-\mu_{\mathrm{C},(Z_i,A_i)}}\,. \tag{3.76}$$

Finally, η_n and η_p are connected to Y_e and Y_i by charge neutrality and mass conservation, closing the system of equations:

$$\sum_i Z_i Y_i = Y_\mathrm{e}\,, \tag{3.77}$$

$$\sum_i A_i Y_i = 1\,. \tag{3.78}$$

Equations (3.76), (3.77) and (3.78) can be solved to determine the NSE composition for a given density, temperature and electron fraction. Instead of solving the full reaction network, the abundances can be calculated for all nuclei.

From Eq. (3.76), we can infer the qualitative behavior of the solution. For high temperatures, the term $(k_\mathrm{B}T)^{-3(A_i-1)/2}$ favors a composition made up of nucleons and small nuclei due to the photodisintegration of nuclei with higher masses. In contrast, the density factor ρ^{A_i-1} prefers nuclei with large mass numbers at high densities. Under moderate conditions, i.e., if neither of the latter two contributions dominates, the term $\exp(B_i/[k_\mathrm{B}T])$ takes over and yields the largest abundances for tightly bound nuclei. This leads to mostly iron group nuclei, since the binding energy is the highest for nuclei in this region. As an example for the latter case, the NSE composition is shown in Fig. 3.2 for $T = 8$ GK, $\rho = 10^{10}\ \mathrm{g/cm^3}$ and $Y_\mathrm{e} = 0.5$.

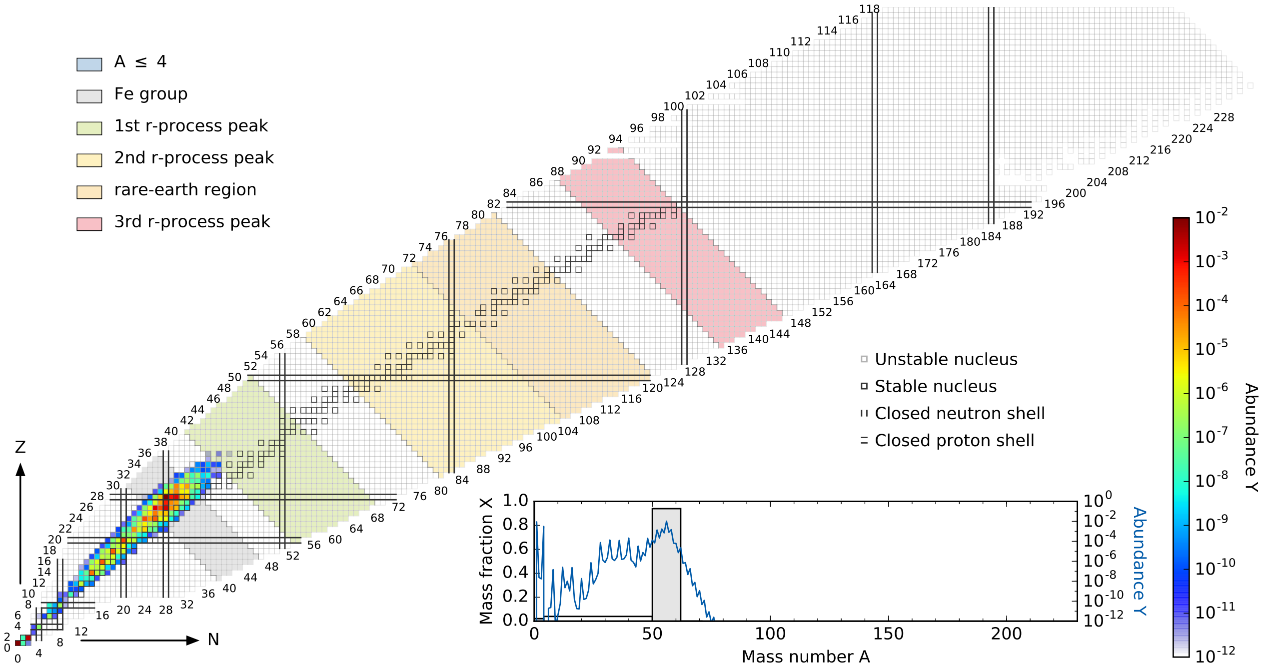

Figure 3.2: NSE composition for $T = 8$ GK, $\rho = 10^{10}\ \mathrm{g/cm^3}$ and $Y_\mathrm{e} = 0.5$. Due to the low temperature and the moderate density, the abundances are the highest for the tightly bound iron group nuclei. The design of the figure is inspired by Ref. [181].

3.6 Nuclear statistical equilibrium with beta-equilibrium

Weak reactions set the electron fractions of a system and typically take place on time scales that are much larger than the ones that are mediated by the strong or the electromagnetic interactions. If an environment stays in

NSE at a certain density and temperature long enough, the weak reactions can reach an equilibrium, too. Since the weak reactions involve neutrinos, the corresponding neutrino captures must contribute to maintain the equilibrium. Therefore, the densities must be high enough, to prevent neutrinos from escaping the system. We refer to the weak equilibrium that is achieved under these conditions as beta-equilibrium.

As soon as beta-equilibrium is reached, the chemical potentials of electrons, protons, neutrons and neutrinos fulfill the following condition:

$$\mu_{\mathrm{e}^-} + \mu_{\mathrm{p}} = \mu_{\mathrm{n}} + \mu_{\nu} \,. \tag{3.79}$$

Moreover, we assume $\mu_\nu = 0$, as the neutrino densities are negligible at low temperatures[1]. This assumption breaks down at high temperatures: for example at 100 GK and 10^{11} g/cm^3, the electron and neutrino densities are of comparable size. Then, a dynamical beta-equilibrium determines the electron fraction. Nevertheless, $\mu_\nu \approx 0$ provides a good approximation to the solution of the dynamical beta-equilibrium [182].

To solve the NSE equations with beta-equilibrium for an large set of nuclei, we extend the general system of NSE equations by two more equations for Y_e and the beta-equilibrium condition, Eq. (3.79). As for pure NSE, the abundance of any nucleus is given by Y_n and Y_p or likewise the corresponding degeneracies η_n and η_p. In total, the system of equations is given by

$$\begin{aligned}
0 &= \Delta - m_\mathrm{e}c^2 + k_\mathrm{B}T\left(\eta_\mathrm{n} - \eta_\mathrm{p} - \eta_\mathrm{e}\right) \,, \\
0 &= Y_\mathrm{e} - \mathscr{C}(\rho)\, m_\mathrm{e}^3 c^6 \beta_\mathrm{e}^{3/2} \left[\mathscr{F}_{1/2}(\eta_{\mathrm{e}^-},\beta_\mathrm{e}) + \beta_\mathrm{e}\mathscr{F}_{3/2}(\eta_{\mathrm{e}^-},\beta_\mathrm{e}) - \mathscr{F}_{1/2}(\eta_{\mathrm{e}^+},\beta_\mathrm{e}) - \beta_\mathrm{e}\mathscr{F}_{3/2}(\eta_{\mathrm{e}^+},\beta_\mathrm{e})\right] \,, \\
0 &= Y_\mathrm{n} - \mathscr{C}(\rho)\, m_\mathrm{n}^3 c^6 \beta_\mathrm{n}^{3/2} \left[\mathscr{F}_{1/2}(\eta_\mathrm{n},\beta_\mathrm{n}) + \beta_\mathrm{n}\mathscr{F}_{3/2}(\eta_\mathrm{n},\beta_\mathrm{n})\right] \,, \\
0 &= Y_\mathrm{p} - \mathscr{C}(\rho)\, m_\mathrm{p}^3 c^6 \beta_\mathrm{p}^{3/2} \left[\mathscr{F}_{1/2}(\eta_\mathrm{p},\beta_\mathrm{p}) + \beta_\mathrm{p}\mathscr{F}_{3/2}(\eta_\mathrm{p},\beta_\mathrm{p})\right] \,, \\
0 &= Y_\mathrm{e} - Y_\mathrm{p} - \sum_{i>1} Z_i Y_i \,, \\
0 &= 1 - Y_\mathrm{n} - Y_\mathrm{p} - \sum_{i>1} A_i Y_i \,,
\end{aligned} \tag{3.80}$$

and the coefficient $\mathscr{C}(\rho) = m_\mathrm{u}\sqrt{2}/[\rho\pi^2(\hbar c)^3]$ is defined for brevity. Next, $\mathbf{f}$ is defined as the column vector containing the right hand side of the system of Eqs. (3.80). We solve these equations by using a Newton-Raphson scheme. Hence, we define the solution vector $\mathbf{x} = \left(Y_\mathrm{e}, \eta_\mathrm{e}, \eta_\mathrm{n}, \eta_\mathrm{p}, Y_\mathrm{n}, Y_\mathrm{p}\right)^T$ and the Jacobian

$$\mathbf{J} = \begin{pmatrix}
0 & -k_\mathrm{B}T & k_\mathrm{B}T & -k_\mathrm{B}T & 0 & 0 \\
\rho/m_\mathrm{u} & \mathscr{D}_{\mathrm{e}^-} - \mathscr{D}_{\mathrm{e}^+} & 0 & 0 & 0 & 0 \\
0 & 0 & \mathscr{D}_\mathrm{n} & 0 & \rho/m_\mathrm{u} & 0 \\
0 & 0 & 0 & \mathscr{D}_\mathrm{p} & 0 & \rho/m_\mathrm{u} \\
1 & 0 & -\sum_{i>1} Z_i N_i Y_i & -\sum_{i>1} Z_i^2 Y_i & 0 & -1 \\
0 & 0 & -\sum_{i>1} A_i N_i Y_i & -\sum_{i>1} A_i Z_i Y_i & -1 & -1
\end{pmatrix}, \tag{3.81}$$

where the derivatives of the Fermi integrals yield the terms

$$\mathscr{D}_i = -\frac{\sqrt{2}}{\pi^2(\hbar c)^3} m_i^3 c^6 \beta_i^{3/2} \left[\frac{1}{2}\mathscr{F}_{-1/2}(\eta_i,\beta_i) + \frac{3}{2}\beta_i \mathscr{F}_{1/2}(\eta_i,\beta_i)\right]. \tag{3.82}$$

The solution is found iteratively by

$$\mathbf{x}_{n+1} = \mathbf{x}_n - \mathbf{J}^{-1} \cdot \mathbf{f}, \tag{3.83}$$

until convergence is reached. The results for densities in the range $10^6 - 10^{13}$ g/cm^3 and temperatures from $5 - 50$ GK are shown in Fig. 3.3. The contour plot in the left panel shows the electron fraction for NSE with beta-equilibrium. In the right panel, the colored regimes indicate the nuclear species that dominates, given NSE with beta-equilibrium for the respective conditions. Similar to the trend in pure NSE, heavy nuclei (X_heavy) and alpha particles (X_α) are most abundant for low temperatures and intermediate densities. At high temperatures $T \gtrsim 15$ GK, either neutrons or protons make up most of the material, defining the electron fraction. Dashed and dotted lines mark the densities, above which electrons and neutrons are degenerate, respectively. Neutrons are non-degenerate in almost the whole domain and it is appropriate to describe nucleons with Maxwell-Boltzmann statistics. This retrospectively justifies simplifications such as, e.g., from Eq. (3.75) to Eq. (3.76).

---

[1] Note that this implies the beta-equilibrium for positrons, neutrons, protons, and antineutrinos, i.e., $\mu_{\mathrm{e}^+} + \mu_\mathrm{n} = \mu_\mathrm{p} + \mu_{\bar{\nu}}$.

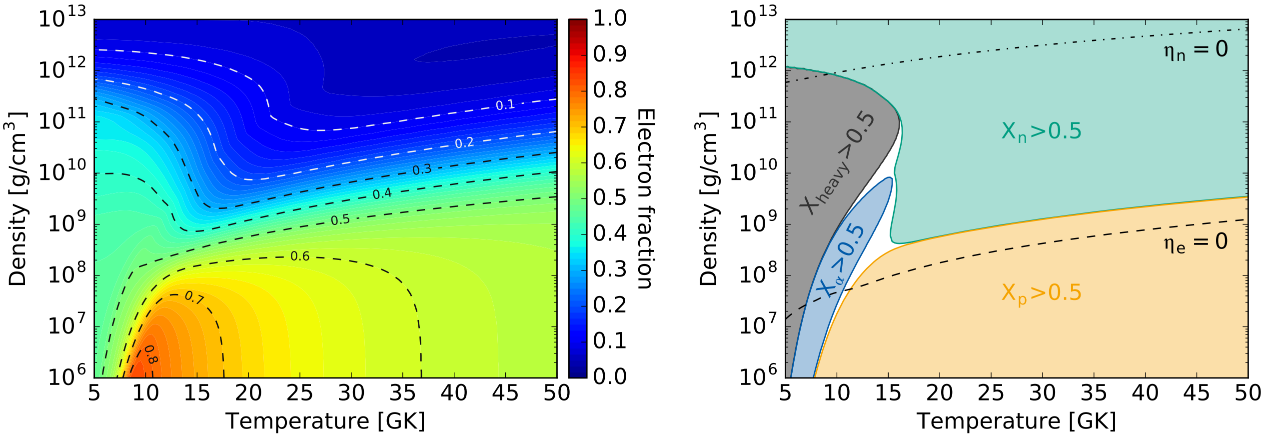

Figure 3.3: NSE with beta-equilibrium. The electron fraction is shown in the left panel, while the right panel illustrates the regimes for different nuclear species to dominated the abundances. A dashed line marks vanishing electron degeneracy and a dotted line denotes zero neutron degeneracy.

3.7 Electron fraction evolution

During an explosive scenario, the ejected material experiences different phases of nuclear evolution. We distinguish at least three different regimes [183], roughly separated by the density threshold $\rho_{\rm eq} \sim 10^{12}$ g/cm^3 and NSE temperature $T_{\rm NSE} \sim 10$ GK:

(I) The neutrino trapped regime; due to both high density $\rho \gtrsim \rho_{\rm eq}$ and temperature $T \gtrsim T_{\rm NSE}$, neutrinos diffuse on a longer time scale than the time it takes them to be captured by nucleons and nuclei. Thus, neutrinos are trapped and the electron fraction $Y_{\rm e}$ is part of the total lepton fraction $Y_{\rm l} = Y_{\rm e} + Y_{\nu_{\rm e}} - Y_{\bar{\nu}_{\rm e}}$.

(II) The neutrino free streaming regime; while the density has dropped below $\rho_{\rm eq}$, still high temperature $T \gtrsim T_{\rm NSE}$ prevails and the nuclei are in NSE. However, $Y_{\rm e}$ is set dynamically by the lepton captures, predominantly on nucleons

$$\mathrm{p} + \mathrm{e}^- \longleftrightarrow \mathrm{n} + \nu_{\rm e}, \tag{3.84a}$$

$$\mathrm{n} + \mathrm{e}^+ \longleftrightarrow \mathrm{p} + \bar{\nu}_{\rm e}. \tag{3.84b}$$

(III) The nucleosynthesis regime; once the temperature ultimately drops out of NSE conditions $T < T_{\rm NSE}$, the neutrinos are still free streaming and $Y_{\rm e}$ is determined from the solution of the full reaction network.

Between all these regimes, there are no sharp transitions. This is particularly true for the transition from phase (I) to (II), where neutrino become diffusive. Then, the electron fraction reaches an equilibrium value almost instantaneously, but neutrinos do not form a persistent gas any more. Both electron fraction and composition are given by the corresponding beta-equilibrium values.

In this section, we consider the evolution of the electron fraction in regime (II) [145, 183]. From Eqs. (3.84), we determine the change in electron fraction, using the reaction rates λ_x for captures on the species $x = \mathrm{e}^-, \mathrm{e}^+, \nu_{\rm e}, \bar{\nu}_{\rm e}$:

$$\frac{\mathrm{d}Y_{\rm e}}{\mathrm{d}t} = \left(\lambda_{\nu_{\rm e}} + \lambda_{\mathrm{e}^+}\right) Y_{\rm n} - \left(\lambda_{\bar{\nu}_{\rm e}} + \lambda_{\mathrm{e}^-}\right) Y_{\rm p} \equiv \lambda_+ Y_{\rm n} - \lambda_- Y_{\rm p}, \tag{3.85}$$

where $Y_{\rm n}$ and $Y_{\rm p}$ are the abundances of free nucleons. Additionally, we combine the reactions that increase $Y_{\rm e}$ to the rate λ_+, and those that decrease $Y_{\rm e}$ are subsumed in λ_-. In NSE, the nucleon fractions are related to the electron fraction according to charge and mass conservation:

$$Y_{\rm n} = 1 - Y_{\rm e} - \sum_{A \geq 2} N Y(Z,A), \tag{3.86}$$

$$Y_{\rm p} = Y_{\rm e} - \sum_{A \geq 2} Z Y(Z,A). \tag{3.87}$$

Thus, for a given NSE composition, we can write Eq. (3.85) as

$$\frac{\mathrm{d}Y_\mathrm{e}}{\mathrm{d}t} = -\lambda_\mathrm{tot} Y_\mathrm{e} + \left[\lambda_+\left(1-\sum_{A\geq 2} N Y(Z,A)\right) + \lambda_- \sum_{A\geq 2} Z Y(Z,A)\right] \equiv -\lambda_\mathrm{tot} Y_\mathrm{e} + \tilde{\lambda}\,, \tag{3.88}$$

where we introduce the total sum of the reaction rates $\lambda_\mathrm{tot} = \lambda_+ + \lambda_-$ and we define $\tilde{\lambda}$ by the term in square brackets. For environments consisting of nucleons only, we have $\tilde{\lambda} = \lambda_+$, while the production of nuclei heavier than nucleons drives $\tilde{\lambda}$ toward λ_-.

It is instructive to consider the limiting case with constant composition as well as constant rates λ_tot and $\tilde{\lambda}$ over a time interval Δt. Then, the integrated result for Eq. (3.88) is given by

$$Y_\mathrm{e}(t+\Delta t) \simeq Y_\mathrm{e}(t) e^{-\lambda_\mathrm{tot}\Delta t} + \frac{\tilde{\lambda}}{\lambda_\mathrm{tot}}\left(1-e^{-\lambda_\mathrm{tot}\Delta t}\right). \tag{3.89}$$

If the time Δt is substantially larger than the reaction time scales, i.e., $\Delta t \gg 1/\lambda_\mathrm{tot}$, the electron fraction attains the equilibrium value

$$Y_\mathrm{e}^\infty = \frac{\tilde{\lambda}}{\lambda_\mathrm{tot}} = \frac{\lambda_{\nu_\mathrm{e}} + \lambda_{\mathrm{e}^+}}{\lambda_{\nu_\mathrm{e}} + \lambda_{\mathrm{e}^+} + \lambda_{\bar{\nu}_\mathrm{e}} + \lambda_{e^-}}\,. \tag{3.90}$$

Generally, the (anti)neutrino capture rates are expressed in terms of the local densities $n_\nu = L_\nu/(4\pi r^2 c E_\nu)$ and capture cross sections σ_ν:

$$\lambda_{\nu_\mathrm{e}} = c n_{\nu_\mathrm{e}} \sigma_{\nu_\mathrm{e}}\,, \tag{3.91}$$

$$\lambda_{\bar{\nu}_\mathrm{e}} = c n_{\bar{\nu}_\mathrm{e}} \sigma_{\bar{\nu}_\mathrm{e}}\,. \tag{3.92}$$

In the free streaming regime, (anti)neutrinos propagate radially. Averaging the energies and cross sections, we express the capture rates in this simplified case as

$$\lambda_{\nu_\mathrm{e}} = \frac{L_{\nu_\mathrm{e}}}{4\pi r^2 \left\langle E_{\nu_\mathrm{e}}\right\rangle}\left\langle \sigma_{\nu_\mathrm{e}}\right\rangle, \tag{3.93}$$

$$\lambda_{\bar{\nu}_\mathrm{e}} = \frac{L_{\bar{\nu}_\mathrm{e}}}{4\pi r^2 \left\langle E_{\bar{\nu}_\mathrm{e}}\right\rangle}\left\langle \sigma_{\bar{\nu}_\mathrm{e}}\right\rangle, \tag{3.94}$$

where L_{ν_e} and $L_{\bar{\nu}_\mathrm{e}}$ are the luminosities, and $\langle E_{\nu_\mathrm{e}}\rangle$ and $\langle E_{\bar{\nu}_\mathrm{e}}\rangle$ are the mean spectral energies of ν_e and $\bar{\nu}_\mathrm{e}$, respectively. Generally, (anti)neutrino luminosities depend on time and the energies obey a spectral distribution that vary over time, too. We calculate the averaged (anti)neutrino capture cross sections in Eqs. (3.91) and (3.92) as [184]

$$\left\langle \sigma_{\nu_\mathrm{e}}\right\rangle = k\left\langle E_{\nu_\mathrm{e}}\right\rangle \varepsilon_{\nu_\mathrm{e}}\left[1+2\frac{\Delta}{\varepsilon_{\nu_\mathrm{e}}} + a_{\nu_\mathrm{e}}\left(\frac{\Delta}{\varepsilon_{\nu_\mathrm{e}}}\right)^2\right] W_{\nu_\mathrm{e}}\,, \tag{3.95}$$

$$\left\langle \sigma_{\bar{\nu}_\mathrm{e}}\right\rangle = k\left\langle E_{\bar{\nu}_\mathrm{e}}\right\rangle \varepsilon_{\bar{\nu}_\mathrm{e}}\left[1-2\frac{\Delta}{\varepsilon_{\bar{\nu}_\mathrm{e}}} + a_{\bar{\nu}_\mathrm{e}}\left(\frac{\Delta}{\varepsilon_{\bar{\nu}_\mathrm{e}}}\right)^2\right] W_{\bar{\nu}_\mathrm{e}}\,, \tag{3.96}$$

with the constant $k \simeq 9.3\cdot 10^{-44}\,\mathrm{cm}^2/\mathrm{MeV}^2$ and the nucleon mass difference $\Delta = m_\mathrm{n} - m_\mathrm{p}$. Moreover, Eqs. (3.95) and (3.96) involve the energy moment ratios $\varepsilon = \langle E_\nu^2\rangle/\langle E_\nu\rangle$, $a_\nu = \langle E_\nu^2\rangle/\langle E_\nu\rangle^2$ as well as the weak magnetism plus recoil corrections $W_{\nu_\mathrm{e}} = \left[1+1.02 b_{\nu_\mathrm{e}}\varepsilon_{\nu_\mathrm{e}}/m_\mathrm{nuc}\right]$ and $W_{\bar{\nu}_\mathrm{e}} = \left[1-7.22 b_{\bar{\nu}_\mathrm{e}}\varepsilon_{\bar{\nu}_\mathrm{e}}/m_\mathrm{nuc}\right]$, with $b_\nu = \langle E_\nu^3\rangle\langle E_\nu\rangle/\langle E_\nu^2\rangle^2$ and the nucleon mass $m_\mathrm{nuc} = (m_\mathrm{n}+m_\mathrm{p})/2$. For given $\langle E_\nu\rangle$, we obtain the other (anti)neutrino energy moments via

$$\left\langle E_\nu^n\right\rangle = (k_\mathrm{B} T_\nu)^n\,\frac{F_{n+2}(0)}{F_2(0)}\,, \tag{3.97}$$

where $F_k(\eta) = \mathscr{F}_k(\eta,0)$ is the Fermi integral from Eq. (3.73), setting $\beta = 0$. Similarly, we determine electron and positron reaction rates

$$\lambda_{\mathrm{e}^-} = c\tilde{n}_{\mathrm{e}^-}\left\langle \sigma_{\mathrm{e}^-}\right\rangle, \tag{3.98}$$

$$\lambda_{\mathrm{e}^+} = c n_{\mathrm{e}^+}\left\langle \sigma_{\mathrm{e}^+}\right\rangle, \tag{3.99}$$

where $\tilde{n}_{\mathrm{e}^-}$ and n_{e^+} are the electron and positron number densities, respectively, Here, the electron number density is slightly modified due to the proton-neutron mass difference Δ. For the number densities, we use

$$\tilde{n}_{\mathrm{e}^-} = \frac{8\pi}{(2\pi\hbar c)^3} \int_0^\infty \frac{\epsilon^2}{1+\exp\left(\frac{\epsilon-\tilde{\mu}_\mathrm{e}}{k_\mathrm{B}T}\right)} \mathrm{d}\epsilon\,, \tag{3.100}$$

$$n_{\mathrm{e}^+} = \frac{8\pi}{(2\pi\hbar c)^3} \int_0^\infty \frac{\epsilon^2}{1+\exp\left(\frac{\epsilon+\mu_\mathrm{e}}{k_\mathrm{B}T}\right)} \mathrm{d}\epsilon\,, \tag{3.101}$$

with $\tilde{\mu}_\mathrm{e} = \mu_\mathrm{e} - \Delta$ and the electron chemical potential $\mu_\mathrm{e} = m_\mathrm{e}c^2 + k_\mathrm{B}T\eta_{\mathrm{e}^-}$. In Eqs. (3.98) and (3.99), the average capture cross sections for electrons and positrons are

$$\langle\sigma_{\mathrm{e}^-}\rangle = \frac{1}{2}k\,\langle E_{\mathrm{e}^-}\rangle\,\varepsilon_{\mathrm{e}^-}\left[1+2\frac{\Delta}{\varepsilon_{\mathrm{e}^-}} + a_{\mathrm{e}^-}\left(\frac{\Delta}{\varepsilon_{\mathrm{e}^-}}\right)^2\right]\widetilde{W}_{\nu_\mathrm{e}}\,, \tag{3.102}$$

$$\langle\sigma_{\mathrm{e}^+}\rangle = \frac{1}{2}k\,\langle E_{\mathrm{e}^+}\rangle\,\varepsilon_{\mathrm{e}^+}\left[1+2\frac{\Delta}{\varepsilon_{\mathrm{e}^+}} + a_{\mathrm{e}^+}\left(\frac{\Delta}{\varepsilon_{\mathrm{e}^+}}\right)^2\right]\widetilde{W}_{\bar{\nu}_\mathrm{e}}\,. \tag{3.103}$$

Since the electron and positron chemical potentials are finite, we compute their energy moments analogously to Eq. (3.97), but using Fermi integrals with non-vanishing argument:

$$\left\langle E^n_{\mathrm{e}^-}\right\rangle = (k_\mathrm{B}T)^n\,\frac{F_{n+2}(\tilde{\mu}_\mathrm{e}/[k_\mathrm{B}T])}{F_2(\tilde{\mu}_\mathrm{e}/[k_\mathrm{B}T])}\,, \tag{3.104}$$

$$\left\langle E^n_{\mathrm{e}^+}\right\rangle = (k_\mathrm{B}T)^n\,\frac{F_{n+2}(-\mu_\mathrm{e}/[k_\mathrm{B}T])}{F_2(-\mu_\mathrm{e}/[k_\mathrm{B}T])}\,. \tag{3.105}$$

Furthermore, we employ approximate expressions [184] for the weak magnetism and recoil corrections $\widetilde{W}_{\nu_\mathrm{e}}$ and $\widetilde{W}_{\bar{\nu}_\mathrm{e}}$. In contrast to the corresponding terms for the (anti)neutrino captures, which are due to the free streaming (anti)neutrinos, the emitted (anti)neutrinos are assumed to be in thermal equilibrium with matter. Therefore, their properties depend on the local matter properties [185], and we use

$$\left\langle E^n_{\nu_\mathrm{e}}\right\rangle = (k_\mathrm{B}T)^n\,\frac{F_{n+4}(\tilde{\mu}_\mathrm{e}/[k_\mathrm{B}T])}{F_4(\tilde{\mu}_\mathrm{e}/[k_\mathrm{B}T])}\,, \tag{3.106}$$

$$\left\langle E^n_{\bar{\nu}_\mathrm{e}}\right\rangle = (k_\mathrm{B}T)^n\,\frac{F_{n+4}(-\mu_\mathrm{e}/[k_\mathrm{B}T])}{F_4(-\mu_\mathrm{e}/[k_\mathrm{B}T])}\,, \tag{3.107}$$

instead of the values from Eq. (3.97), to correct the electron and positron capture rates.

The weak reactions in Eqs. (3.84) do not only change the electron fraction, but they can also have an impact on the temperature evolution. We track heating and cooling contributions due to the weak reactions by evolving the internal energy $\mathrm{d}e_\mathrm{int}/\mathrm{d}t$: (anti)neutrino captures add internal energy ("heating"), whereas electron/positron captures remove internal energy ("cooling"). The total differential of the internal energy reads

$$\mathrm{d}e_\mathrm{int} = \left(\frac{\partial e_\mathrm{int}}{\partial T}\right)_{Y_\mathrm{e}}\mathrm{d}T + \left(\frac{\partial e_\mathrm{int}}{\partial Y_\mathrm{e}}\right)_T \mathrm{d}Y_\mathrm{e}\,. \tag{3.108}$$

Rearranging Eq. (3.108), we receive an expression for the temperature evolution due to weak reactions:

$$\left(\frac{\mathrm{d}T}{\mathrm{d}t}\right)_\mathrm{weak} = \left(\frac{\partial T}{\partial e_\mathrm{int}}\right)_{Y_\mathrm{e}}\frac{\mathrm{d}e_\mathrm{int}}{\mathrm{d}t} - \left(\frac{\partial e_\mathrm{int}}{\partial Y_\mathrm{e}}\right)_T\left(\frac{\partial T}{\partial e_\mathrm{int}}\right)_{Y_\mathrm{e}}\frac{\mathrm{d}Y_\mathrm{e}}{\mathrm{d}t}\,, \tag{3.109}$$

where we make use of the identity $\partial T/\partial e_\mathrm{int} = (\partial e_\mathrm{int}/\partial T)^{-1}$ and $\mathrm{d}Y_\mathrm{e}/\mathrm{d}t$ is given by the right-hand side of Eq. (3.88).

In summary, Eqs. (3.88) and (3.109) yield a description for the combined effects of weak reactions on the electron fraction and the temperature. To obtain the complete temperature evolution, we add these contributions to the hydrodynamic temperature profile

$$\frac{\mathrm{d}T}{\mathrm{d}t} = \left(\frac{\mathrm{d}T}{\mathrm{d}t}\right)_\mathrm{hydro} + \left(\frac{\mathrm{d}T}{\mathrm{d}t}\right)_\mathrm{weak}\,. \tag{3.110}$$

This system of differential equations (Eqs. (3.88) and (3.110)) is solved, until the temperature decreases to T_NSE. The outcome can serve as an input for the full reaction network, to proceed with the nucleosynthesis in regime (III).

4 r-process nucleosynthesis in the ejecta of neutron star mergers

Neutron star mergers are the most prominent candidate as a host for the r-process, and thus pose the central astrophysical scenario of this work. The various channels of matter ejection from the merger of two neutron stars are driven by different mechanisms, involving all four fundamental forces in physics. This renders the detailed simulation including all kinds of ejected material at once computationally challenging. However, the characteristic timescales of distinct ejecta are separated by up to one order of magnitude. The separation in time allows us to study each of the ejecta individually.

In this chapter, we present results on the r-process nucleosynthesis for the dynamic ejecta and the neutrino-driven wind in the aftermath of a neutron star merger. We use hydrodynamical data from state-of-the-art simulations in 3D to investigate time and direction effects of the final abundances. For both ejection channels, we explore the impact of the neutrino irradiation from the hot remnant system, consisting of a massive neutron star and an accretion disk. Toward this end, we consider the morphology of the combined ejecta to predict the expected electromagnetic signal.

4.1 Dynamic ejecta

As the first ejection channel after the coalescence of two neutron stars, the dynamic ejecta get unbound within milliseconds. Here, we introduce the aspects of neutron-richness in this particular channel of matter ejection, and define a reference case for the main r-process, i.e., the abundance pattern of nuclei with $A \gtrsim 130$. Then, we present results from the mass-integrated nucleosynthesis with trajectories from a recent simulation in full general relativity (GR). Finally, we explore the possible impact of weak reactions in another fully GR simulation in several post-processing steps.

4.1.1 Neutron-rich component

The dynamic ejecta from a binary neutron star merger (and, similarly, the merger of a neutron star with a black hole) are very neutron-rich or, equivalently, carry low electron fractions. In fact, this is a direct consequence of their origin from the outermost layer of the two neutron stars. Therefore, the decompression of cold, neutron-rich material from merging neutron stars had been considered a likely source of the strong r-process, even before detailed hydrodynamic simulations became available [11, 90, 91].

Newtonian simulations with detailed microphysics (i.e., an advanced equation of state and neutrino treatment) find such a neutron-rich component to emerge from mostly prompt, tidal ejecta [113, 185–187]. Figure 4.1 shows the nucleosynthesis for 30 trajectories of the simulations presented in Ref. [113]. Although the hydrodynamical conditions (i.e., temperature and density) can vary by an order of magnitude among the trajectories, the final abundance patterns differ only marginally. Due to the occurrence of several fission cycles, the r-process nucleosynthesis leads to robust yields [13, 137]. Even though this robustness is found to be partially broken in recent simulations with a full GR treatment [144, 188], all simulations still find a non-negligible fraction of the ejecta with sufficiently low electron fraction. For this reason, we use the yields shown in Fig. 4.1 as a proxy for the strong r-process.

4.1.2 Dynamic ejecta in a recent GR simulation

In collaboration with Luke Bovard, Filippo Galeazzi, Almudena Arcones, and Luciano Rezzolla, we have evaluated the r-process nucleosynthesis for full GR simulations. The simulations are carried out by Luke Bovard with a code that evolves spacetime with the BSSNOK formulation of the Einstein equations [189–191], using the Mclachlan code [192], which is part of the Einstein Toolkit [193]. The equations of GR hydrodynamics [194] are solved with the `WhiskyTHC` code [195, 196], making use of adaptive mesh refinement [197]. We study a binary merger of two neutron stars, having 1.35 $M_\odot$ each. To capture shocks, the temperature-dependent equation of state LS220 [198] is

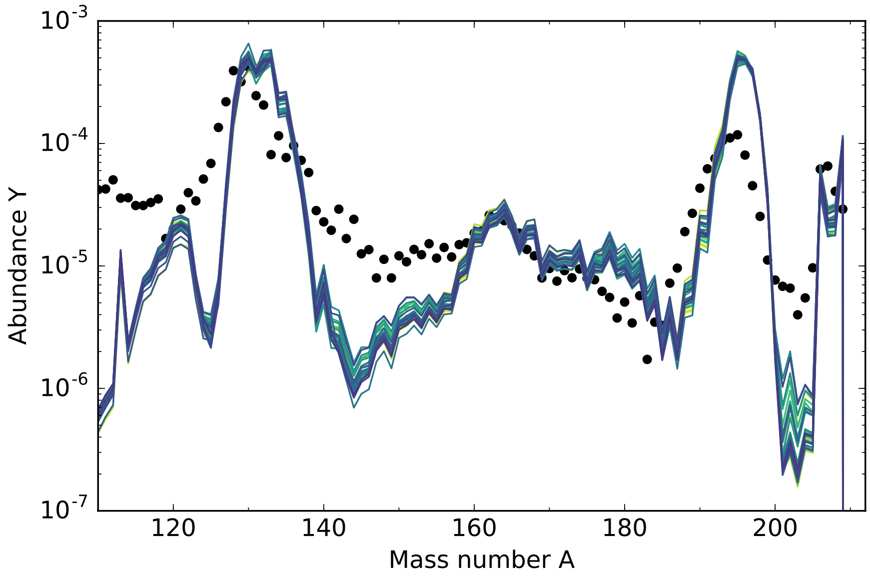

Figure 4.1: Final r-process abundances for very neutron-rich ejecta. Here, we show the results for 30 trajectories from a Newtonian simulation [113]. The nucleosynthesis is analyzed in more detail in Ref. [13].

employed. Moreover, the simulations involve a neutrino leakage scheme [199] that also accounts for emission and absorption of (anti)neutrinos, thus giving an approximate prescription for the evolution of the electron fractions. To follow the flow of ejected material, we place tracer particles [200, 201] that are passively advected with the fluid. For this first study, a total of $2 \cdot 10^5$ tracers are placed in the density region of $10^7\,\mathrm{g/cm^3} \lesssim \rho \lesssim 10^{15}\,\mathrm{g/cm^3}$. During the simulation, we use the assumption of geodesic motion as a predictor for unbound matter [202]. Figure 4.2 shows the density profile at three different times. After the neutron stars have merged, a rotating massive remnant forms that is surrounded by an accretion disk. Furthermore, matter gets ejected subsequently.

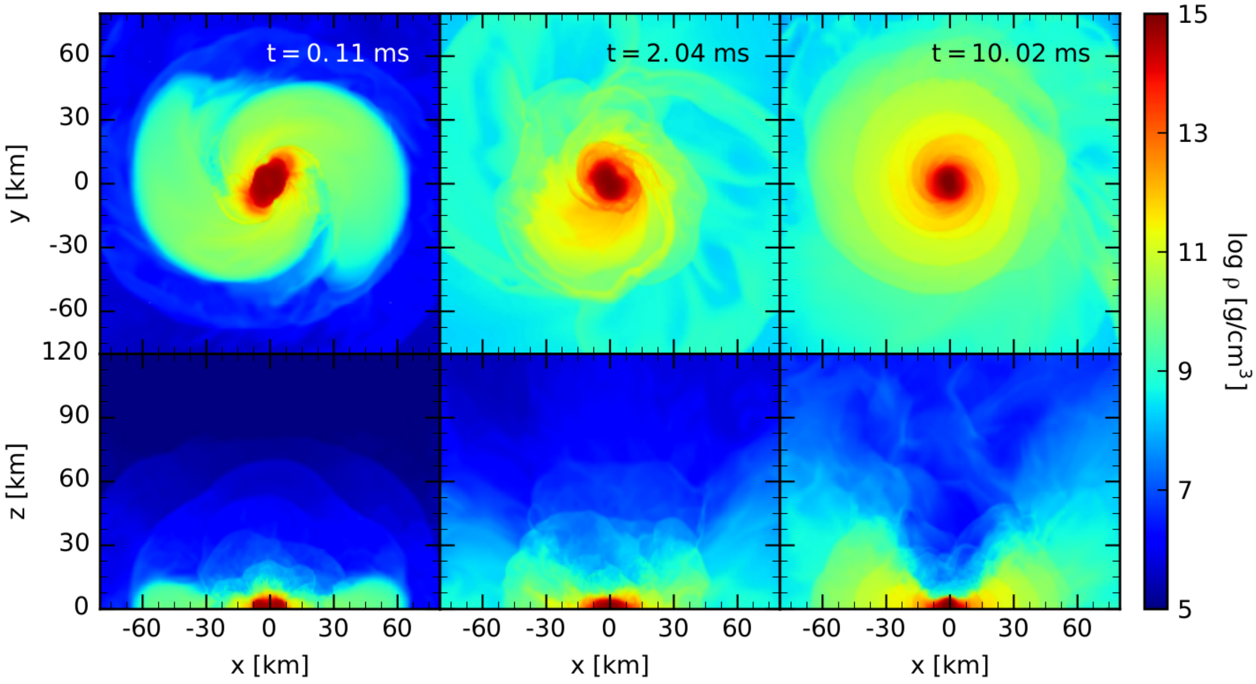

Figure 4.2: Density profile after the merger. Top: density in the $x - y$ plane at 0.11 ms, 2.04 ms, 10.02 ms, respectively. Bottom: aftermath of the merger in the $x - y$ plane at the same times. The rotating massive remnant is surrounded by an accretion disk. Material is ejected not only in the orbital plane, but also out-of-plane, to higher latitudes. Courtesy of Luke Bovard.

Overall, we find that $1.22 \cdot 10^{-3} M_\odot$ of material become unbound. Most of the ejecta are shock-heated and are therefore not confined to the $x - y$ plane, but reach high latitudes, too. Furthermore, the ejected mass features broad distributions in both the entropy and the electron fraction. With an average entropy of $\sim 20\,k_\mathrm{B}$/baryon, about 90 % of the ejecta have relatively low entropies $s \lesssim 50\,k_\mathrm{B}$/baryon, as shown in Fig. 4.3(a). Similarly, the electron fraction peaks at $Y_\mathrm{e} \sim 0.05$. However, the ejecta exhibit a varying degree of neutron-richness in Fig. 4.3(a). Although the electron fraction distribution has a long, flat tail to high values of $Y_\mathrm{e} \sim 0.3$, it shows no bimodal distribution with another peak as in Ref. [203] (see their quasi-circular merger case with leakage scheme). The average electron fraction $\langle Y_\mathrm{e} \rangle \approx 0.107$ is lower than the ones found in former studies with full GR [89, 144, 203]. In total, we post-process almost 40 000 unbound tracers for their nucleosynthesis yields.

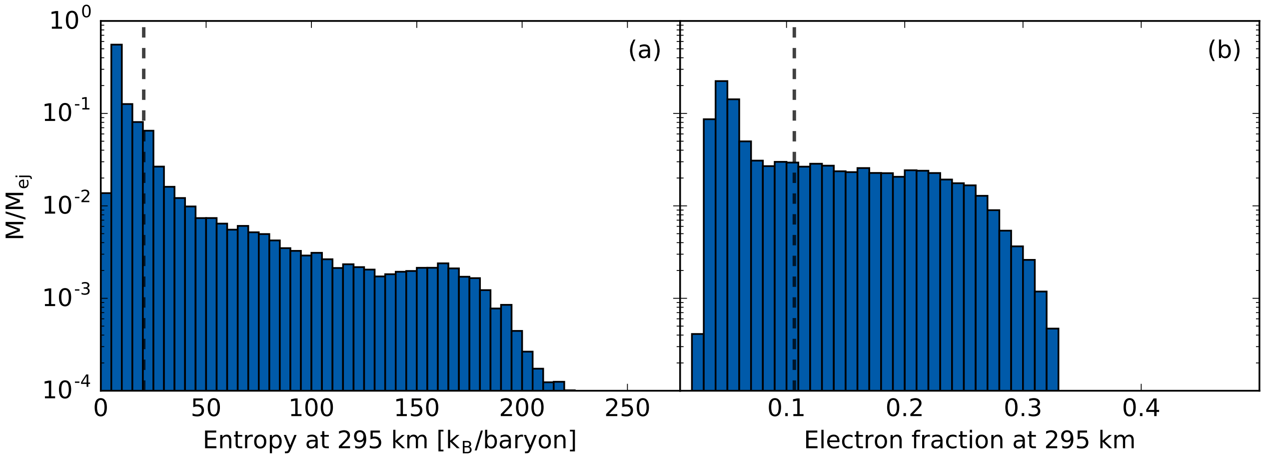

Figure 4.3: Entropy and electron fraction of the ejected tracers. Left: at a radius of 295 km, the bulk of the ejecta has an entropy lower than $50\,k_\mathrm{B}$/baryon, and a small part of the ejecta reaches entropies up to $200\,k_\mathrm{B}$/baryon. Right: the electron fraction of the ejecta features a dominant neutron-rich component with $Y_\mathrm{e} \lesssim 0.1$, while there is a non-negligible amount of tracers that attains electron fractions of up to 0.3.

Our nucleosynthesis calculations start when the temperature drops below $T = 10$ GK. Then, the initial composition is determined by nuclear statistical equilibrium (NSE) and is dominated by alpha particles, neutrons, and protons. NSE is assumed to hold for $T \gtrsim 8$ GK. Between $10 \text{ GK} > T > 8$ GK, the network evolves the weak reactions, since they are not in equilibrium and change the Y_e accordingly. As soon as the temperature undershoots the NSE threshold, the full network provides the abundances. The longest trajectories were simulated until $t_\mathrm{sim} \sim 10$ ms after the merger, therefore we extrapolate them following the prescription outlined in Ref. [13]:

$$r(t) = r_0 + vt\,, \tag{4.1}$$

$$\rho(t) = \rho_0 \left(\frac{t}{t_0}\right)^{-3}, \tag{4.2}$$

$$T(t) = T\,[S, \rho(t), Y_\mathrm{e}(t)]\,. \tag{4.3}$$

Moreover, we update the temperature due to the energy generation by nuclear heating as described in Sect. 3.39.

Figure 4.4 illustrates the nucleosynthesis results for the tracers. We plot individual tracers with $S < 70\,k_\mathrm{B}$/baryon (gray) or $S \geq 70\,k_\mathrm{B}$/baryon (orange), alongside with the mass-integrated abundances (blue line). As a consequence of the relatively low electron fractions (see Fig. 4.3(b)), we obtain the strong r-process component from the second to the third r-process peak. Nevertheless, we find that the entropy distribution of the ejecta gives rise to peculiar features in the abundances pattern. The low-entropy component ($S < 70\,k_\mathrm{B}$/baryon) leads to exactly the pattern that is observed in the neutron-rich of Newtonian simulations. On the contrary, the high-entropy ($S \geq 70\,k_\mathrm{B}$/baryon) part of the ejecta carries only roughly 6 % of the total ejected mass has a nucleosynthesis pattern with a shifted second and third peak. Additionally, it has diminished abundances in the rare-earth region, and effectively fills the gap between third r-process peak and elements in the lead region. We note that the abundance pattern of these tracers is very similar to the "fast" ejecta found by Ref. [140]. While we do not find them to expand faster in the beginning, their unusual abundance distribution can be traced back to an extremely high initial neutron-to-seed ratio $Y_\mathrm{n}/Y_\mathrm{seed} \gtrsim 1000$ and comparably low initial densities $\rho \lesssim 10^9\,\mathrm{g/cm}^3$. Due to the enormous amount of neutrons at low densities, the seed nuclei require substantially more time to incorporate the neutrons, delaying the freeze-out time (i.e., the time when $Y_n/Y_{\mathrm{seed}} = 1$). Additionally, the r-process runs along a path much closer to stability for these tracers, such that the magic neutron numbers are reached at higher mass numbers, and the abundances settle down for a pattern in between s-process and r-process.

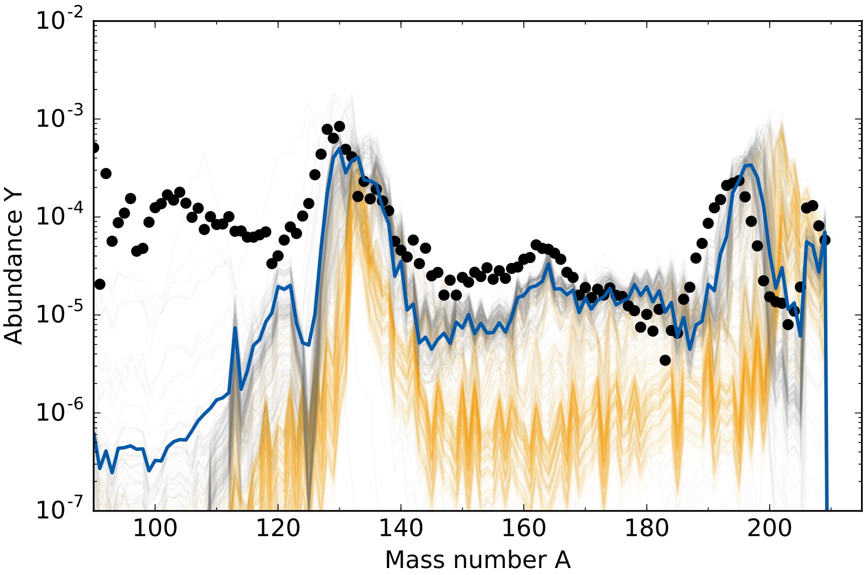

Figure 4.4: Final abundances for the dynamic ejecta of a simulation in full GR. Gray lines are the yields for individual tracers with low entropies $S < 70\,k_{\mathrm{B}}/\mathrm{baryon}$, and orange lines mark single tracers with high entropies $S \geq 70\,k_{\mathrm{B}}/\mathrm{baryon}$. The mass-integrated nucleosynthesis yields are shown with a blue line.

4.2 The impact of weak reactions on the dynamic ejecta

As pointed out in Sect. 2.3.3, recent general relativity simulations of the dynamic ejecta from compact object mergers including neutrino transport [144, 204] show that shocks in the interaction component significantly increase the temperature. The hotter environment enhances the weak reaction rates. In particular, the larger positron capture and electron neutrino absorption rates on neutrons increase the electron fraction, potentially up to values of $Y_e \approx 0.4$ [89]. This is critical, because parametric studies find a threshold of $Y_e \lesssim 0.25$ [66, 181], above which the production of heavy nuclei beyond the second r-process peak is strongly inhibited. Below this limit, there is a successful ("strong") r-process. Such a limit for the electron fraction is also observed for insignificant amounts of ejecta in Ref. [13]. Here, the electron fraction acts similar to an order parameter. The combination of ejecta from both regimes can likely explain the formation of all r-process nuclei from the first peak ($A = 80$) to the third one ($A = 195$). This holds true not solely in the dynamic ejecta, but also in the subsequent disk ejecta [16, 18]. In contrast, Newtonian simulations of the dynamic ejecta [13, 113] or approximate GR simulations without weak reactions [12, 14] only produce the heavy r-process elements ($A \geq 130$).

However, the influence of weak reactions on all kinds of ejecta has not been explored comprehensively yet. The main reason for this shortcoming is that a consistent treatment requires simulations with full neutrino transport, which is computationally expensive. Consequently, one resorts to approximations such as leakage schemes (e.g., Refs. [51, 185, 205]), lightbulb schemes (e.g., Ref. [15]), or moment schemes with analytic closure relations (e.g., Refs. [204, 206, 207]).

Here, we explore the effects of weak reactions on the nucleosynthesis in the dynamic ejecta. This project is carried out together with Albino Perego, Almudena Arcones, and Wolfgang Kastaun.

4.2.1 Hydrodynamical simulation and remnant neutrino luminosities

The hydrodynamical profiles are adopted from a simulation of Wolfang Kastaun and coworkers, reported on in Refs. [200, 208]. They solve the equations of GR hydrodynamics (see, e.g., Ref. [194]) with the aid of the code `WhiskyThermal` [199, 209]. The spacetime is evolved by the same means as in Sect. 4.1.2. To obtain a stable remnant, the equation of state SHT [210, 211] is utilized. It features an unusually large maximum baryonic (gravitational) mass of 3.38 $M_\odot$ (2.77 $M_\odot$) for non-rotating neutron stars. Since each of the neutron stars in the considered binary system carries a mass of 1.4 $M_\odot$, the sum of their masses is well below this limit, avoiding its collapse to a black hole. Hence, a stable massive neutron star forms as a remnant.

To follow the evolution of ejected material during and after merger, we study the trajectories of fluid elements. The typical approach to keep track of fluid trajectories is to passively advect tracer particles throughout the simulation (see Sects. 4.1.2 and 4.3.2). While tracer particles are relatively straightforward to implement, this method bears the difficulty to track the relevant outflow at all times with as few tracers as possible. This means that one needs to find the appropriate starting positions for the tracers, in order to cover the unbound fluid sufficiently at later times. As the material in the disk surrounding the remnant originates from an expanding fluid flow, the tracer density is expected to be smaller than when they are placed. However, simply increasing the number of tracers becomes computationally expensive. Therefore, we employ another approach here. In a first post-processing step, we integrate the fluid trajectories backward in time. This routine starts at the positions on the grid close to the end of the simulation when we require a homogeneous coverage of the unbound material. One shortcoming of this procedure is that the data need to be stored with sufficiently high resolution in both space and time to maintain accuracy in the backward integration. We consider matter to be ejected if the corresponding geodesic can be extended to infinity.

We find that practically all ejecta become unbound in a single wave, i.e., material is liberated by the shock at almost the same time and forms the shape of two concentric rings above and below the orbital plane. However, the ejecta cannot be categorized as being shock-heated in the interaction region of the merging neutron stars. In contrast, the fluid elements that are ejected later on orbit the remnant after the merger. Only when the breakout shock from the remnant passes the orbiting fluid, material gets kicked out from the edge of the disk. Since the matter is bound until the shock hits it, the material is also not tidally ejected. It is important to mention that material is classified as unbound when the temperature has already dropped below NSE conditions by adiabatic expansion. Since the temperature enters into the initial conditions for nucleosynthesis calculations, it is necessary to track ejected material back in time to get its full thermal history. The origin of the shock wave is the remnant. However, the exact nature is under investigation. Moreover, we find that the average ejecta temperature (entropy) is increased from about 10 GK to about 30 GK (from a few to $\sim 7\,k_\mathrm{B}$/baryon) when hit and liberated by the shock wave. As the ejecta expand, they cool down adiabatically. In this phase, we noticed that, in addition to gravitational attraction, the ejecta are slowed down by the artificial atmosphere close to the boundary of the numerical grid. The drag is so strong that matter is bound again. To correct for this, the trajectories are modified by assuming Keplerian hyperbolic orbits after a given time. Under the further assumption that density and temperature are functions of radius, they are remapped to their new positions on the Keplerian orbit. Overall, we consider all trajectories from $\sim$1000 ejected tracers in the following.

The hydrodynamical simulation does not incorporate effects due to weak reactions. These are mainly, e.g., electron, positron, electron neutrino, and electron antineutrino captures on predominantly nucleons. As a consequence, the electron fraction remains constant over time throughout the simulation. In the next step, we determine an estimate for the (anti)neutrino properties for the remnant system. We map the hydrodynamical profile of baryon density, matter temperature, and electron fraction at 17.5 ms after the merger [208] to the equidistant Cartesian grid of the Newtonian code `FISH` [212]. At this time, the system is already in an axially symmetric configuration. The remapping procedure is done by Albino Perego. For consistency with the GR simulation, we use the equation of state NL3 [213, 214] that is similar to the equation of state SHT [210, 211]. We distinguish between three different regimes by employing the following treatment:

(1) For densities $\rho \gtrsim 10^{12}\,\mathrm{g/cm^3}$, neutrinos are trapped and the electron fraction Y_e achieves an equilibrium and is determined via the lepton fraction $Y_\mathrm{l} = Y_\mathrm{e} + Y_{\nu_\mathrm{e}} - Y_{\bar{\nu}_\mathrm{e}}$. Hence, we set the lepton fraction equal to the electron fraction found in the simulation, $Y_\mathrm{l} = Y_\mathrm{e,\,sim}$, and compute the fractions of the individual leptons in equilibrium.

(2) In the regime where $8 \cdot 10^{11}\,\mathrm{g/cm^3} \lesssim \rho \lesssim 10^{12}\,\mathrm{g/cm^3}$, neutrinos are assumed to be diffusive. However, the temperatures are still high enough that the electron fraction is exchanged for the corresponding value from beta-equilibrium.

(3) Below densities of $8 \cdot 10^{11}\,\mathrm{g/cm^3}$, we assume free-streaming neutrinos, such that the electron fraction is evolved dynamically. Then, we evolve temperature and electron fraction of the system with a spectral neu-

trino leakage scheme [51], while keeping the velocity distribution and density profile of baryonic matter at their initial values.

In the beginning, the luminosities are very high, since the low electron fraction from the GR simulation is far from equilibrium in the free-streaming regime. Nevertheless, the strong neutrino-emission in this low-density area adjusts the electron fraction quickly. Due to the combined effects of adjusted electron fraction and decreasing temperature, decrease the luminosities on a long timescale. Maintaining a constant densities and velocities, the neutrino emission effectively cools the system, as the energy removal is not replenished by accretion. The neutrino luminosities start with high values, decreasing rapidly. After an initial transient phase of $\sim 1\,\text{ms}$, the electron fraction in the disk adjusts to its new equilibrium value. From then on, the neutrino luminosities decrease smoothly due to neutrino cooling of the disk. We consider the late-time luminosities to be slightly underestimated, whereas the initial luminosities are overestimated. We select four significant time steps in between. Figure 4.5 shows the time steps and luminosities that we select as representative cases. Particularly, the luminosity case "medium" marks an intermediate case. This profile is extracted by using the luminosities as soon as the electron fraction does not change significantly any more.

To check the (in)sensitivity of these values on the density limits, we vary the thresholds between the three regimes by a factor of 2, respectively, and find the (anti)neutrino luminosities to change by less than 10 %. Thus, we incorporate these variations into our final estimates.

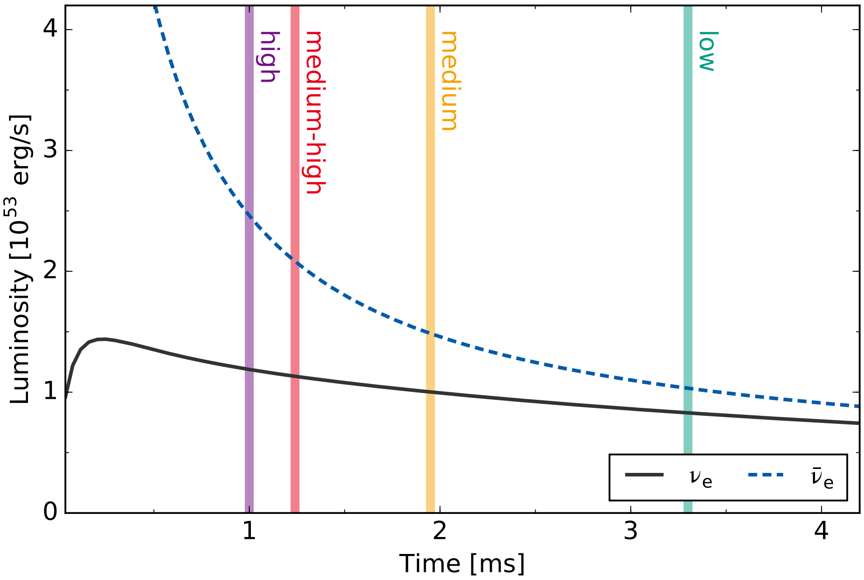

Figure 4.5: Analysis of the luminosities of electron neutrinos and electron antineutrinos. After an initial transient phase of $\sim 1\,\text{ms}$, the electron fraction in the disk adjusts to its new equilibrium value. We select the values at four significant time steps thereafter to parameterize the energy and luminosity profiles.

For the merger simulation, we prescribe the following profile for electron (anti)neutrino energies ($\mathscr{X} = E$) and luminosities ($\mathscr{X} = L$):

$$\mathscr{X}_\nu = \left\{ \begin{array}{lll} \mathscr{X}_{\nu,\text{min}} & \text{if} & t \leq t_0 \\ \mathscr{X}_{\nu,\text{min}} + \left(\mathscr{X}_{\nu,\text{max}} - \mathscr{X}_{\nu,\text{min}}\right) \frac{t-t_0}{t_\text{max}-t_0} & \text{if} & t_0 < t \leq t_\text{max} \\ \mathscr{X}_{\nu,\text{max}} \exp\left(\frac{t_{\nu,\text{max}}-t}{\tau}\right) & \text{if} & t > t_\text{max} \end{array} \right\}, \tag{4.4}$$

where $t_0 = 12.5\,\text{ms}$, $t_\text{max} = 17.5\,\text{ms}$, and $\tau = 0.5\,\text{s}$. The time t_0 is the time at which the merger occurs and t_max marks the time at which the (anti)neutrino luminosities reach their maximum values. The timescale τ accounts for the exponential decay of the luminosities that is found in simulations with neutrino treatment. Initially, we assume negligible luminosities $L_{\nu_e,\text{min}} = L_{\bar{\nu}_e,\text{min}} = 0$ and keep the the energies constant at $E_{\nu_e,\text{min}} = E_{\bar{\nu}_e,\text{min}} = 8\,\text{MeV}$. For the maxima $L_{\nu_e,\text{max}}$, $L_{\bar{\nu}_e,\text{max}}$, $E_{\nu_e,\text{max}}$, and $E_{\bar{\nu}_e,\text{max}}$, we consider the values extracted with the above procedure.

In total, we use five different scenarios. The first case takes into account only electron and positron captures, while the other four cases also include electron (anti)neutrino captures for different (anti)neutrino properties. The maximum energies and luminosities are listed for each case in Tab. 4.1. Furthermore, we show the time dependence of both energies and luminosities for electron (anti)neutrinos in Fig. 4.6.

Table 4.1: Parameters for the maximum neutrino and antineutrino luminosities and energies. In the beginning, we assume vanishing luminosities $L_{\nu_e,\min} = L_{\bar{\nu}_e,\min} = 0$ and constant energies $E_{\nu_e,\min} = E_{\bar{\nu}_e,\min} = 8\,\mathrm{MeV}$.

Name	$L_{\nu_e,\max}$ $[10^{53}$ erg/s]	$L_{\bar{\nu}_e,\max}$ $[10^{53}$ erg/s]	$E_{\nu_e,\max}$ [MeV]	$E_{\bar{\nu}_e,\max}$ [MeV]
capture	0.0	0.0	0.0	0.0
low	0.86	1.0	11.5	16.2
medium	1.0	1.5	12.0	16.3
medium-high	1.13	2.0	12.7	16.6
high	1.2	2.4	13.0	16.7

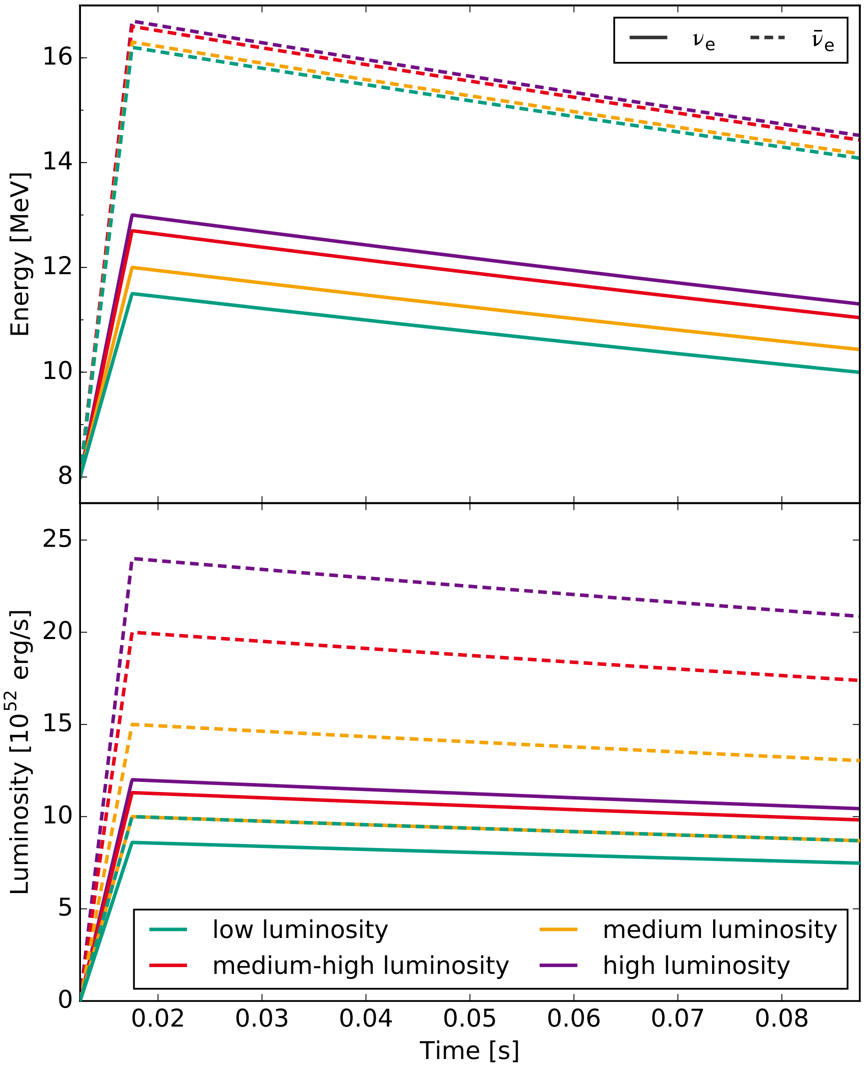

Figure 4.6: Profiles of the electron neutrino and antineutrino energies and luminosities. At the onset of the merger, both quantities are approximately increasing linearly. After reaching a peak value, the profiles decay exponentially with a long timescale.

Moreover, we consider two possible geometries for the (anti)neutrino emission and propagation:

(a) The first approach assumes spherical symmetry and is given by Eq. (4.4).

(b) In simulations, the luminosities usually feature an angular dependence due to a non-spherically symmetric structure of the system in the aftermath of a neutron star merger. More likely is a rather axially symmetric configuration comprising a central remnant that is surrounded by an accretion disk in the $x-y$ plane. Therefore, we modulate the (anti)neutrino luminosities as

$$L_\nu(\theta) = L_{\nu,0} \cdot \frac{3}{3+\alpha}\left(1+\alpha\cos^2\theta\right), \tag{4.5}$$

where $L_{\nu,0}$ is the isotropic luminosity, and the parameter α reduces the luminosity toward the equator. The profile of the resulting luminosities from Eq. (4.5) is shown in Fig. 4.7 for two examples with $L_{\nu,0} = 10^{52}$ erg/s as well as $\alpha = 0$ and $\alpha = 2$, respectively. The angular variation of the luminosities leads to a rise in the values close to the poles, while the region near the equator experiences an effective decrease in radiated (anti)neutrinos.

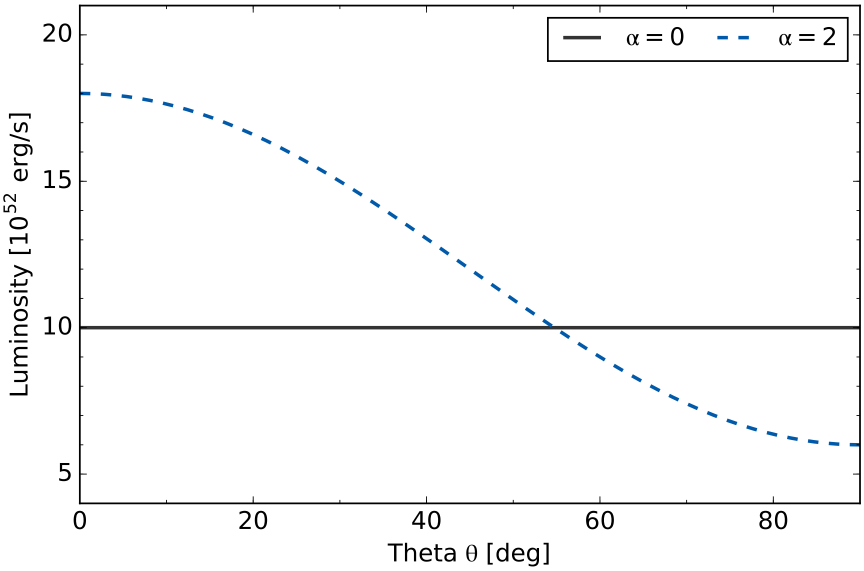

Figure 4.7: Angular dependence of the neutrino luminosities. The curves show plots of Eq. (4.5) for the parameters $L_{\nu,0} = 10^{52}$ erg/s as well as $\alpha = 0$ and $\alpha = 2$, respectively. In total, the angle dependence tends to decrease the local luminosities in close to the equator, but gives rise to higher values near the poles.

As the simulation ends for $t \sim 20$ ms, the expanding ejecta reach large radii rather fast. Accordingly, the neutrino reactions are not so much ruled by the long-term exponential decay, but by the r^{-2} dependence of the (anti)neutrino reaction cross sections.

4.2.2 Evolution of the electron fraction

We investigate the effect of weak reactions in two post-processing steps. The first step employs the matter properties recored by the tracers and the neutrino properties from the previous section to determine the electron fraction evolution in the ejecta. In a second post-processing step we calculate the resulting impact on the r-process nucleosynthesis, using the nuclear reaction network.

We evolve the electron fraction Y_e via Eq. (3.85) and the temperature via Eq. (3.110). Furthermore, we approximately take into account two general relativistic effects. Since neutrinos escape from regions deeper in the gravitational well, they are redshifted by the redshift factor

$$\Phi(r) = \sqrt{\frac{1-R_s/R_\nu}{1-R_s/r}}, \tag{4.6}$$

with the Schwarzschild radius $R_s = 2GM_{\mathrm{MNS}}/c^2$, and the mass of the massive neutron star $M_{\mathrm{MNS}} = 2.79\,M_\odot$. Here, $R_\nu = 33$ km is the radius of the (anti)neutrino sphere. Additionally, we include a geometrical factor for the bending of the neutrino trajectory with

$$1-g(r) = 1-\sqrt{1-\left(\frac{R_\nu}{r}\right)^2\frac{1}{\Phi^2}}. \tag{4.7}$$

For all trajectories, we assume beta-equilibrium down to very high densities ($\rho > 8 \cdot 10^{11}\,\mathrm{g/cm^3}$), consistent with the neutrino treatment in Sect. 4.2.1. This is important, because the freeze-out value of the electron fraction becomes the initial condition for our subsequent evolution. If the conditions for beta-equilibrium are not met, we resort to assigning an electron fraction of $Y_\mathrm{e} = 0.044$ to this tracer. This value is the average electron fraction of the grid from the hydrodynamical simulation. Figure 4.8 shows the cumulative distribution of the electron fractions for all tracers. The mass-weighted average Y_e when leaving beta-equilibrium is already higher than the frozen electron fraction of $Y_\mathrm{e} = 0.044$ from the hydrodynamical simulation that does not consider weak reactions and expansion.

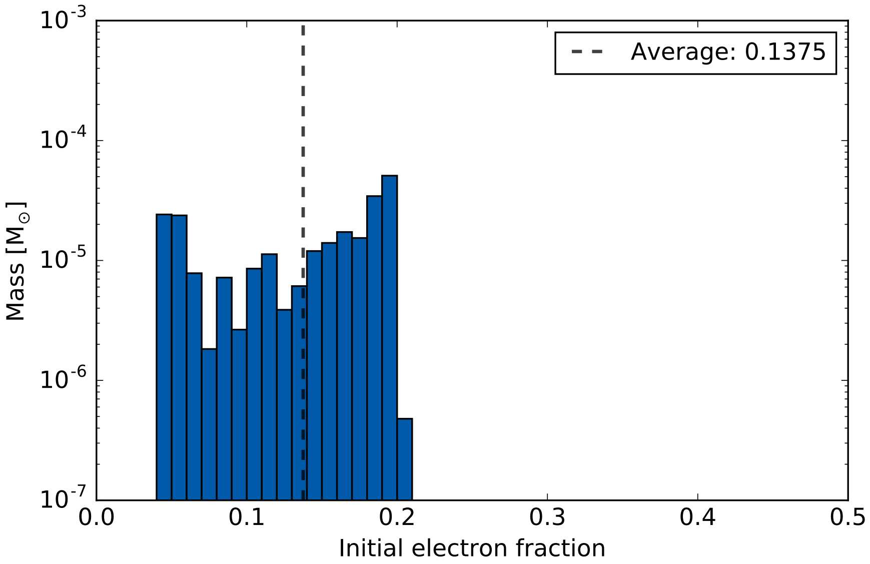

Figure 4.8: Beta-equilibrium electron fraction of the ejecta. either electron fraction under the assumption of beta-equilibrium at a density of $\rho = 8 \cdot 10^{11}\,\mathrm{g/cm^3}$, or set to the average value of $\langle Y_\mathrm{e} \rangle = 0.044$ from the simulation.

Descending from this initial value, we determine the changes in both temperature and electron fraction due to weak reactions. A characteristic trend for the evolution that we find is presented in Fig. 4.9. The top panel shows the hydrodynamical properties of the tracer, featuring a pronounced temperature and density peak when the shock passes the tracer at $t \approx 16.4\,\mathrm{ms}$. In the bottom panel, we plot the time dependence of the individual lepton capture rates as well as the resulting electron fraction. Rates that decrease the electron fraction are presented with solid lines, while dashed lines mark rates increasing the electron fraction. Due to the low initial temperature and electron fraction, the increasing electron fraction results from electron neutrino captures. As soon as the shock kicks in, high temperatures favor electron captures, leading to a sharp decrease of the electron fraction. We explore the details of this distinct feature in Sect. 4.2.3. Afterwards, the traced environment cools, such that the late-time increase of the electron fraction is solely driven by electron neutrino captures again. Since the ejecta expand fast to large radii, neutrino captures become less efficient because of the flux dilution, and the electron fraction saturates eventually. The inclusion of neutrino absorption enhances the temperature of the original trajectory to high temperatures above 10 GK, even at the final time step of the simulation. Thus, we extrapolate the tracers with an adiabatic homologous expansion (see Sect. 4.1.2). Since the neutrinos are still affecting the electron fraction at the end of the (simulated) trajectory, we include the evolution of Y_e and temperature due to neutrino processes also during the extrapolation. In this way, we follow the evolution down to temperatures of $T \sim 3\,\mathrm{GK}$, before calculating the nucleosynthesis with the nuclear reaction network in a second post-processing step.

4.2.3 Effects of the shock

The shock has the strongest effect on the electron fraction evolution. As discussed in the previous section, the sudden temperature increase triggers electron captures and, to smaller extent, positron captures. Thus, we examine how the shock leads to decreasing electron fraction in detail. Since (anti)neutrino captures remain basically unchanged, we assume the electron captures and positron captures to dominate in the following. Using the rates of Eqs. (3.98) and (3.99), we compute their values for a given density and temperature. To obtain their direct impact on the electron fraction, we consider the product of the rates and the corresponding target fraction. The nucleon

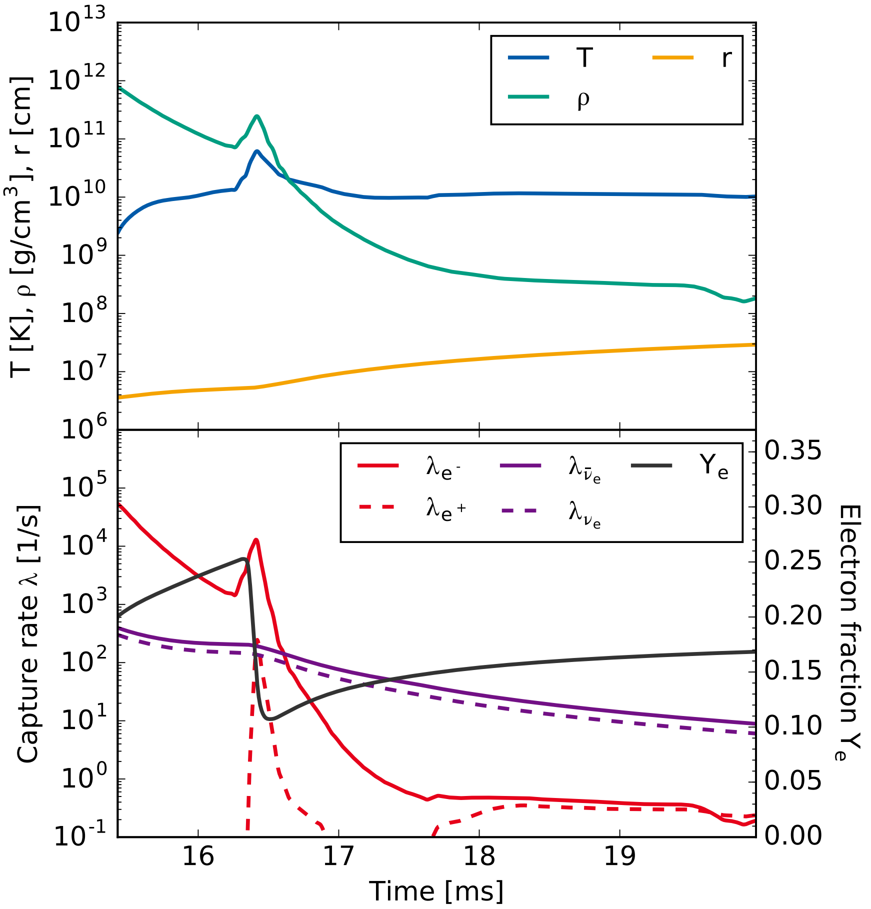

Figure 4.9: Temporal evolution of hydrodynamical quantities, capture rates, and electron fraction. Top panel: hydrodynamic evolution of the tracer with a pronounced peak when the shock passes. Bottom panel: Capture rates for the various kind of included weak reactions, as well as the electron fraction evolution. Solid lines mark rates that decrease Y_e, whereas dashed lines tag rates increasing Y_e.

fractions are calculated for NSE conditions with the help of the equation of state. Figure 4.10 shows the ratios of the resulting products $\lambda_{\mathrm{e}^-}Y_\mathrm{p}/(\lambda_{\mathrm{e}^+}Y_\mathrm{n})$ with contour surfaces as a function of density and temperature. We plot the hydrodynamical properties of the tracer from Fig. 4.9 with a dashed blue line. The threshold at which electron captures and positron captures cancel each other is reached if their ratio is equal to one. Applying the formulas from Sect. 3.7, we can approximate this limit by setting

$$1 \equiv \frac{\lambda_{\mathrm{e}^-}\,Y_\mathrm{p}}{\lambda_{\mathrm{e}^+}\,Y_\mathrm{n}} = \frac{c\tilde{n}_{\mathrm{e}^-}\,\langle\sigma_{\mathrm{e}^-}\rangle\,Y_\mathrm{p}}{c\tilde{n}_{\mathrm{e}^+}\,\langle\sigma_{\mathrm{e}^+}\rangle\,Y_\mathrm{n}} \approx \frac{F_2\left(\frac{\mu_\mathrm{e}-\Delta}{k_\mathrm{B}T}\right)\left\langle\tilde{E}^2_{\mathrm{e}^-}\right\rangle\,Y_\mathrm{p}}{F_2\left(-\frac{\mu_\mathrm{e}}{k_\mathrm{B}T}\right)\left\langle E^2_{\mathrm{e}^+}\right\rangle\,Y_\mathrm{n}} = \frac{F_4\left(\frac{\mu_\mathrm{e}-\Delta}{k_\mathrm{B}T}\right)\,Y_\mathrm{p}}{F_4\left(-\frac{\mu_\mathrm{e}}{k_\mathrm{B}T}\right)\,Y_\mathrm{n}} = \frac{F_4\left(\eta_{\mathrm{e}^-}+\frac{m_\mathrm{e}c^2}{k_\mathrm{B}T}-\frac{\Delta}{k_\mathrm{B}T}\right)\,Y_\mathrm{p}}{F_4\left(-\eta_{\mathrm{e}^-}-\frac{m_\mathrm{e}c^2}{k_\mathrm{B}T}\right)\,Y_\mathrm{n}}\,, \tag{4.8}$$

where we assume that both electrons and positrons obey Fermi-Dirac distributions. In general, Eq. (4.8) needs to be solved for the electron degeneracy η_{e^-}. Although the temperatures during the shock are relatively high, the electron degeneracy is of intermediate degree, i.e., neither vanishing nor very large. Hence, we solve Eq. (4.8) numerically. For a given temperature and electron fraction, the density at which electron and positron captures cancel is then

$$\begin{aligned}\rho\left(T,Y_\mathrm{e}\right) = \frac{m_\mathrm{u}}{Y_\mathrm{e}}\frac{\sqrt{2}}{\pi^2(\hbar c)^3}m_\mathrm{e}^3c^6\beta_\mathrm{e}^{3/2}\big[&\mathscr{F}_{1/2}\left(\eta_{\mathrm{e}^-},\beta_e\right)+\beta_\mathrm{e}\mathscr{F}_{3/2}\left(\eta_{\mathrm{e}^-},\beta_e\right)\\ &-\mathscr{F}_{1/2}\left(-\eta_{\mathrm{e}^-}-2/\beta_\mathrm{e},\beta_e\right)-\beta_\mathrm{e}\mathscr{F}_{3/2}\left(-\eta_{\mathrm{e}^-}-2/\beta_\mathrm{e},\beta_e\right)\big]\,.\end{aligned} \tag{4.9}$$

Here, we use again the relativistic parameter $\beta_\mathrm{e} = k_\mathrm{B}T/(m_\mathrm{e}c^2)$ for conciseness. Since nucleons dominate the composition at high temperatures $T \gtrsim 20\,\mathrm{GK}$, we use the approximations $Y_\mathrm{p} = Y_\mathrm{e}$ and $Y_\mathrm{n} = 1 - Y_\mathrm{e}$. Combining Eqs. (4.8) and (4.9), we arrive at the density profile that is plotted with a dotted-dashed black line in Fig. 4.10.

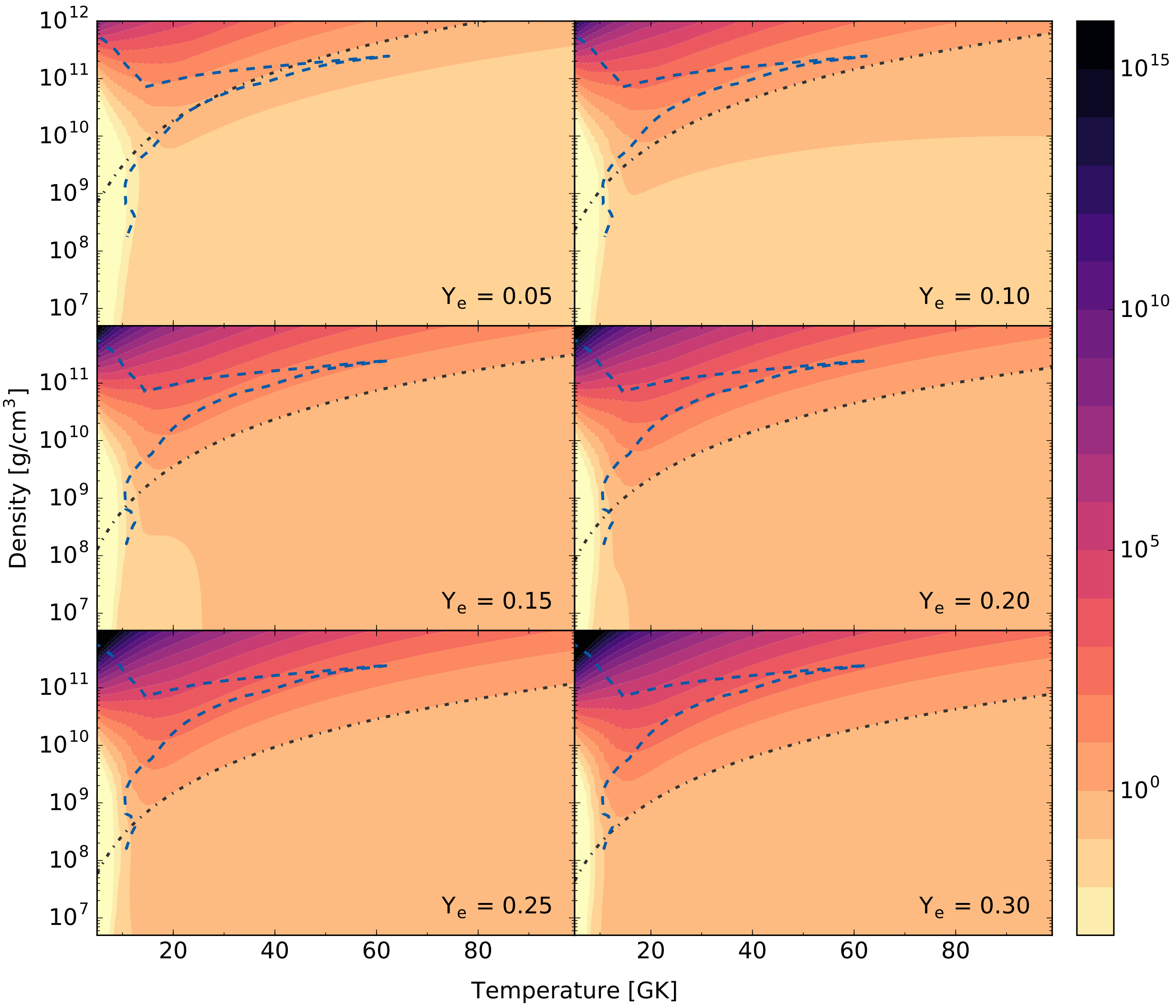

Figure 4.10: Ratio of the electron and positron capture rates. The contours shows the values of $\lambda_{e^-} Y_p/(\lambda_{e^+} Y_n)$ in the density-temperature plane for varying electron fractions. We plot the trajectory from Fig. 4.9 with a dashed blue line. The dotted-dashed black line marks the solution of Eqs. (4.8) and (4.9) for a composition made up of only nucleons.

We find that our approximation yields a reasonable description for the region of canceling rates in the considered temperature range.

It is instructive to discuss the effects of the shock with the help of the different conditions in Fig. 4.10. When the ejecta are hit by the shock, the electron fraction of the trajectory is $Y_e \approx 0.25$. For the high density and temperature conditions during the shock heating, electron captures are favored by a factor of ~ 100 over positron captures. As the temperature increases toward the peak value, this factor is reduced slightly. Nevertheless, the timescale at which the shock occurs is too short for boosting positron captures to become the dominant reaction. Instead, the ongoing electron captures rapidly decrease the electron fraction, shifting the line of $\lambda_{e^-} Y_p/(\lambda_{e^+} Y_n) = 1$ into the direction of the conditions found for the trajectory. This effectively flattens the evolution of the electron fraction, as it tends to balance the capture rates. When the electron fraction has dropped to $Y_e \approx 0.1$, the ratio of electron and positron capture rates is close to unity. However, the temperature is already low at this point, shutting off both kinds of captures. If these reaction types were the only ones involved in the electron fraction evolution, then its profile would be constant at later times.

Our discussion is not necessarily restricted to shocks happening with a delay after the merger. In fact, the same argumentation holds true when descending from high temperatures initially, although positron captures can play a more prominent role in this case. This can be seen in the panel with $Y_e = 0.05$ (see Fig. 4.10), where positron captures rule the evolution of the electron fraction during a shock.

Using the whole ensemble of ejected tracers from the simulation, we obtain distributions of the late-time electron fraction for different treatments of weak reactions. At first, we consider a case with electron and positron captures only. Thereafter, we take into account isotropic (anti)neutrino luminosities with three distinct sets of (anti)neutrino properties.

If we only include electron and positron captures into our calculations to evolve the electron fraction, we find that the final electron fractions are reduced below the beta-equilibrium values (cf., Fig. 4.8). In the absence of neutrino captures, the electron fraction stays at a low level after being processed by the shock wave. We show the electron fraction distribution in the upper left panel of Fig. 4.11. The values are taken at a temperature of 8 GK, well after the shock has passed. The resulting electron fraction exhibits a distribution with values up to $Y_\mathrm{e} \sim 0.2$. However, the mass-weighted average is pushed down below $Y_\mathrm{e} = 0.1$.

The other panels of Fig. 4.11 show three of the cases with including (anti)neutrino reactions (see Tab. 4.1). For all considered combinations, the late-time electron fraction is generally shifted to higher values, compared to the beta-equilibrium one. This is because the initial and late-time neutrino captures make the ejecta more proton-rich. The mass-weighted average is situated in the range of $Y_\mathrm{e} \sim 0.2-0.25$, and the distributions have long tails toward low electron fractions $Y_\mathrm{e} \sim 0.1$ as well as high electron fractions up to $Y_\mathrm{e} \sim 0.5$.

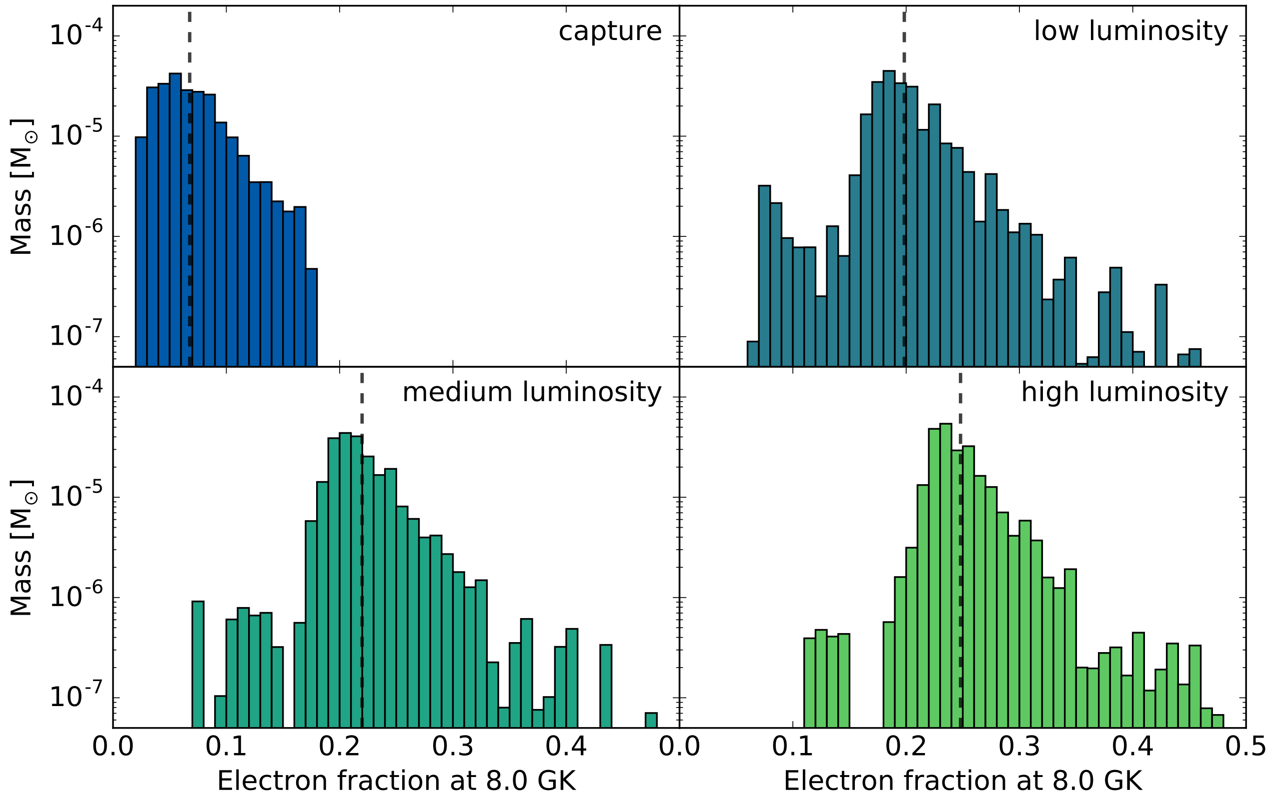

Figure 4.11: Y_e distributions due to weak reactions. We switch on first electron and positron captures and then different degrees of (anti)neutrino captures. In all cases we see a rather broad distribution of the electron fraction, with generally more proton-rich values, as we assume higher (anti)neutrino luminosities.

Having post-processed the ejected tracers once for obtaining an updated electron fraction evolution, we use the outcome as an input for subsequent nucleosynthesis calculations. To obtain a smooth transition between the two different post-processing steps, we initialize the reaction network with the values of the previous results that are still determined under NSE conditions. From then on, we let the network descend to lower temperatures (and densities) to consistently compute the final abundances at 10^9 years. The corresponding nucleosynthesis yields are shown in Fig. 4.12. For a straightforward comparison, we apply the same colors as for the electron fraction distributions in Fig. 4.11. Gray lines represent the abundance patterns of individual tracers. In the reference case with only electron and positron captures, we find a robust r-process nucleosynthesis from second to third peak due to the extremely neutron-rich conditions. The results for individual tracers resemble the pattern presented for the dynamic ejecta from the Newtonian simulation in Fig. 4.1. In contrast, the three remaining cases with neutrino captures show a rather strong dependence on the neutrino flux. This leads to a component with relatively high electron fraction, forming r-process nuclei up to the second peak. As these ejecta are complemented by a neutron-rich component, the mass-integrated nucleosynthesis almost ranges from the first to the third r-process peak. Still, the first peak is somewhat underproduced in our case with low luminosities. Increasing the (anti)neutrino luminosities has two effects. First, the abundances of nuclei up to the second r-process peak are enhanced. Second, the abundances of heavy nuclei with $A \gtrsim 130$ decrease by up to more than an order of magnitude with respect to the solar abundances.

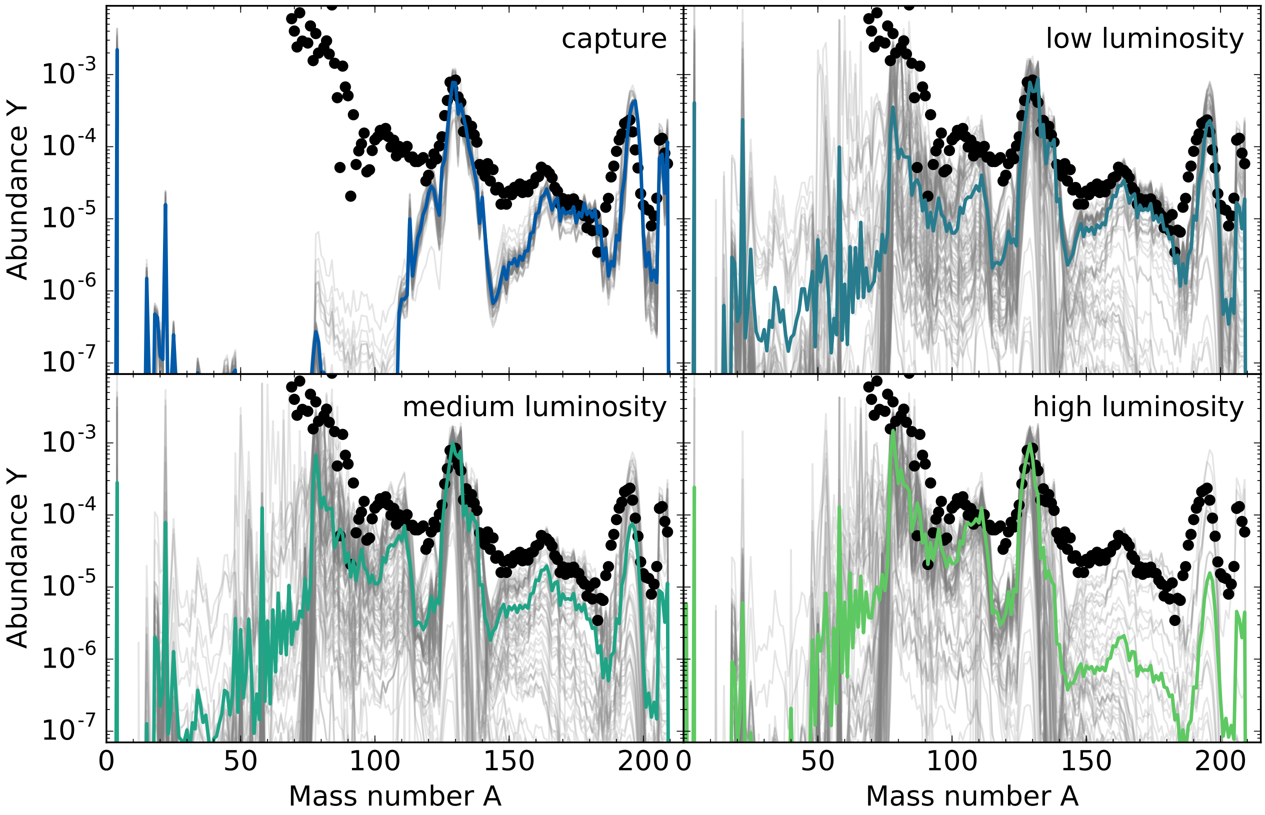

Figure 4.12: Nucleosynthesis yields when including weak reactions. We find a robust r-process for the case including only electron and positron captures. However, the abundances for heavy nuclei with ($A \gtrsim 130$) decreases and the ones for lower mass nuclei ($A \lesssim 130$) increases if higher (anti)neutrino luminosities are assumed. Color scheme and luminosity cases are the same as in Fig. 4.11. Gray lines show the abundance pattern of individual tracers.

From the considered cases, we can draw already two conclusions. The assumption of beta-equilibrium as well as the inclusion electron and positron captures is important. Although the resulting electron fraction distributions are still very neutron-rich, they are somewhat different from the frozen value $Y_e = 0.044$ assumed during the simulation. Moreover, high neutrino luminosities can inhibit the strong r-process component and enhance the weak r-process component.

4.2.5 Ejecta ensembles for angle dependent luminosities

We analyze how the modulation affects the electron fraction of the ejecta. Therefore, we plot again the reference case of electron and positron captures only together with three distinct cases for (anti)neutrino properties in Fig. 4.13. As the bulk of the ejecta starts orbiting the central remnant very close to the $x-y$ plane, the initial luminosities are strongly decreased by our prescription. Even when the shock liberates material later on, the ejecta are driven to marginally higher latitudes ($\theta \approx 60° - 70°$). Due to the alleviated effects, we concentrate on the cases with the highest luminosities from Tab. 4.1, exchanging the low luminosity case for the medium-high luminosity case. Again, the (anti)neutrino irradiation cases broad electron fraction distributions, centered around $Y_e \sim 0.2$. In contrast to the isotropic cases, all the distributions here are only mildly shifted if luminosities increase.

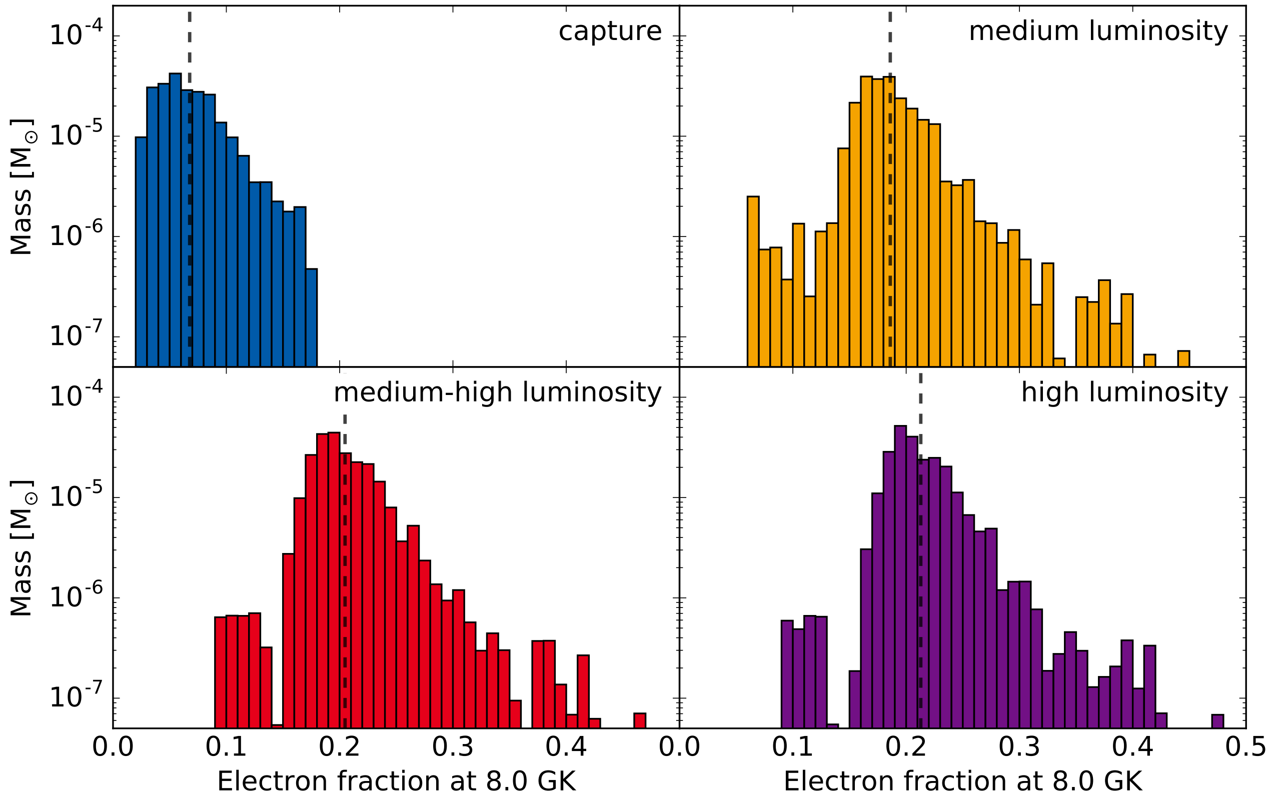

Figure 4.13: Y_e distributions due to weak reactions and angle dependent luminosities. Note that the case with low luminosity is exchanged for the case with medium-high luminosity, compared to Fig. 4.11.

The angular dependence also affects the r-process nucleosynthesis in the dynamic ejecta. We present the final abundance yields in Fig. 4.14. Similar to the cases in Sect. 4.2.4, a weak component is coproduced that comprises nuclei with $A \lesssim 130$. As a consequence, this reduces the abundances in the region beyond the second r-process peak, but not as much as in the cases exhibiting isotropic luminosity. On the contrary, we find a rather robust r-process pattern, which underproduces the rare-earth peak and the third peak by up to a factor of ~ 2 for the highest assumed (anti)neutrino luminosities. All yields are complemented by lighter heavy elements between the first and the second peak.

All in all, we conclude that while the luminosity is a global quantity, the local (anti)neutrino flux is crucial for the final nucleosynthesis pattern. As observed in parametric studies [145, 215], we find that weak ($A \lesssim 130$) and strong ($A \gtrsim 130$) r-process features are not produced simultaneously. Under the assumptions made here, there are always admixtures of these two distinct components and there is a trade-off to produce either of the two. Therefore, we need at least a second kind of ejecta to explain the full r-process pattern from the first to the third r-process peak.

4.3 Neutrino-driven winds from neutron star mergers

In this section, we focus on the neutrino-driven wind from a post-merger remnant that consists of a central massive neutron star (MNS) surrounded by an accretion disk and present a comprehensive nucleosynthesis study based on the first three dimensional simulation recently performed by Ref. [17]. In the latter work, preliminary nucleosynthesis results based on ten representative trajectories were presented. Here, we follow the nucleosynthesis evolution based on 17 000 trajectories and we discuss the implications for radioactively powered electromagnetic transients. This project was carried out together with Albino Perego, Almudena Arcones, Friedrich-Karl Thielemann, Oleg Korobkin, and Stephan Rosswog. Part of the content of this section is published in Martin et al. (2015) [149].

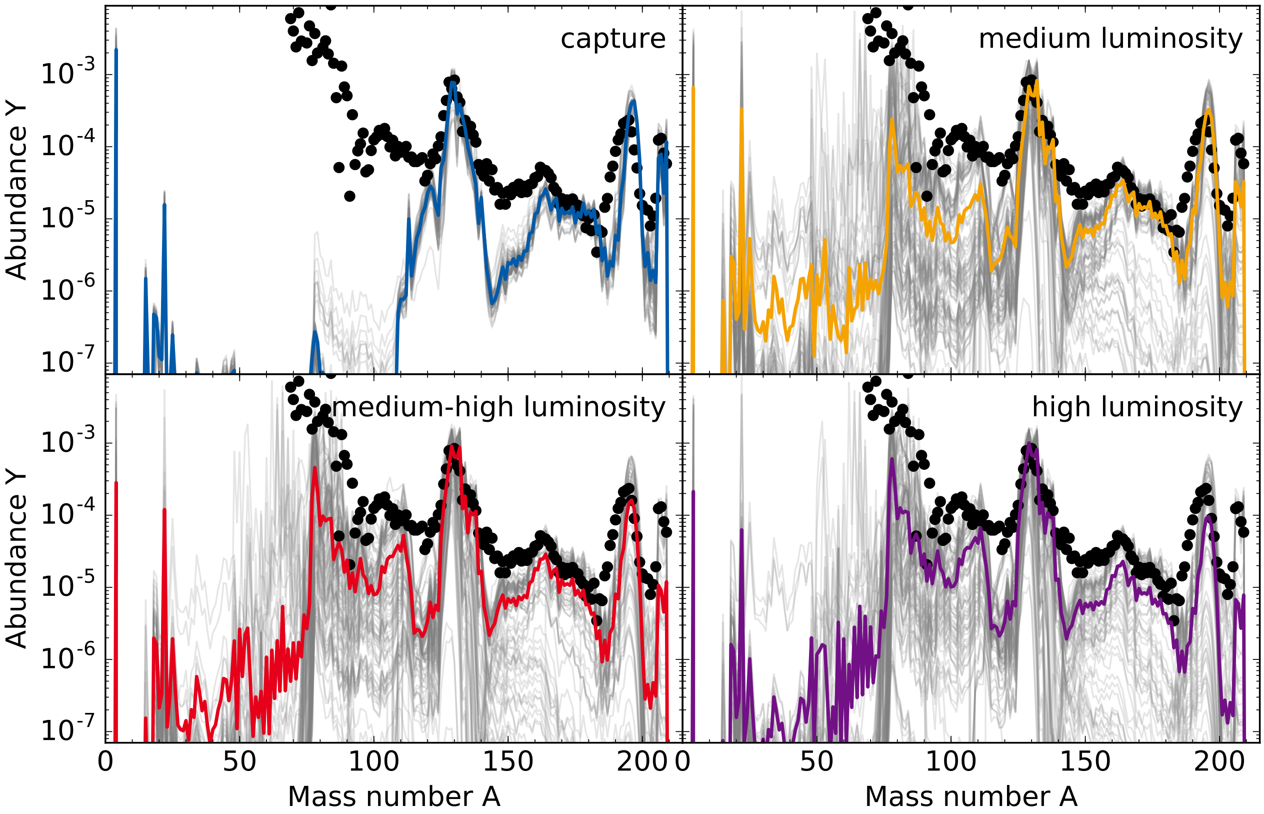

Figure 4.14: Nucleosynthesis yields when including weak reactions and angle dependent luminosities. Color scheme and luminosity cases are the same as in Fig. 4.13.

4.3.1 Hydrodynamical simulations

Our nucleosynthesis study is based on the first three dimensional, Newtonian simulation of the neutrino-driven wind that emerges during the aftermath of a binary neutron star merger [17]. The merger remnant is characterized by a long-lived massive neutron star, surrounded by a quasi-Keplerian accretion disk with an inital mass of $M_{\rm disk} \simeq 0.19\,M_{\odot}$. For the present analysis, the previous simulation are repeated and extended by Albino Perego to longer times, and we follow a substantially larger number of particles.

The parallel grid code `FISH` [212] solves the hydrodynamical equations on a uniform Cartesian grid. Nuclear matter description is provided by the TM1 nuclear equation of state, supplemented with electron-positron and photon contributions [172, 216]. As initial condition we use a late matter configuration from a three dimensional high resolution simulation of two non-spinning 1.4 $\mathrm{M}_{\odot}$ neutron stars (e.g., Ref. [217]). Neutrino-matter interactions are taken into account using the multiflavor Advanced Spectral Leakage (ASL) scheme, see Ref. [51]. It models the neutrino emission effectively by smoothly interpolating between diffusive and free-streaming rates, separately for different neutrino energies, and it has been carefully gauged at full transport calculations. Neutrino absorption is also included in optically thin conditions, based on the calculation of the neutrino densities outside the neutrino last scattering surfaces. The list of the neutrino reactions implemented inside the ASL scheme can be found in Tab. 1 of Ref. [17]. The present simulation corresponds to an extension of the ones presented in Refs. [17, 218]. The simulations starts at 25 ms after the beginning of the merger, including 10 ms of relaxation of the SPH final conditions on the grid, and follows the post merger evolution for 190 ms. The temporal evolution of the neutrino luminosities and mean energies during the whole simulation follows the same trends reported in Fig. 10 of Ref. [17] for the first 90 ms. The relevant mean energies stay approximately constant: $\sim$11 MeV for the electron neutrinos and $\sim$15.5 MeV for the electron antineutrinos. The total neutrino luminosities, integrated over the whole solid angle, decrease slowly with time. At the end of the simulation ($t_{\rm sim} \approx 190$ ms) the electron (anti)neutrino luminosity due to cooling processes only is equal to $\sim 2.2 \cdot 10^{52}$ erg/s ($\sim 2.9 \cdot 10^{52}$ erg/s), while the inclusion of the neutrino absorption in optically thin conditions decreases it to $\sim 1.5 \cdot 10^{52}$ erg/s ($\sim 2.4 \cdot 10^{52}$ erg/s). Due to the larger optical depth along the equatorial plane, the neutrino fluxes measured far from the MNS along the polar direction are roughly three times larger than the ones in the equatorial plane (cf., Fig. 12 of Ref. [17]).

The inclusion of the energy deposition provided by the neutrino absorption on nucleons inside the disk drives a baryonic wind on a time scale of tens of milliseconds, see Fig. 4.15. Matter expanding inside the wind becomes unbound at a distance $\lesssim 600\,\mathrm{km}$ from the center. The resulting ejecta are confined within a polar angle of 60°, measured from the rotational axis of the disk. Due to the strong neutrino irradiation, the initially highly neutron-rich matter inside the disk changes its electron fraction in the wind. The dominant ν_e-absorption of neutrons raises Y_e toward equilibrium values (see, e.g., Ref. [68]). The evolution towards this equilibrium value may be affected by general relativistic treatment of the merger phase. GR simulations of a binary neutron star merger including neutrinos [219] and following the onset of the neutrino-driven wind [144] indicate that the luminosities can be larger than in Newtonian simulations, due to the higher temperature inside the massive neutron star and the disk. However, the ratio between the electron neutrino and antineutrino luminosities is similar in both cases, as well as the values of the mean energies. Therefore, the equilibrium electron fraction is expected to be almost the same, while the evolution towards this Y_e should be faster in the GR simulations. This difference does not come directly from the Newtonian treatment of the disk and of the wind, but from the initial profiles resulting from the merger process.

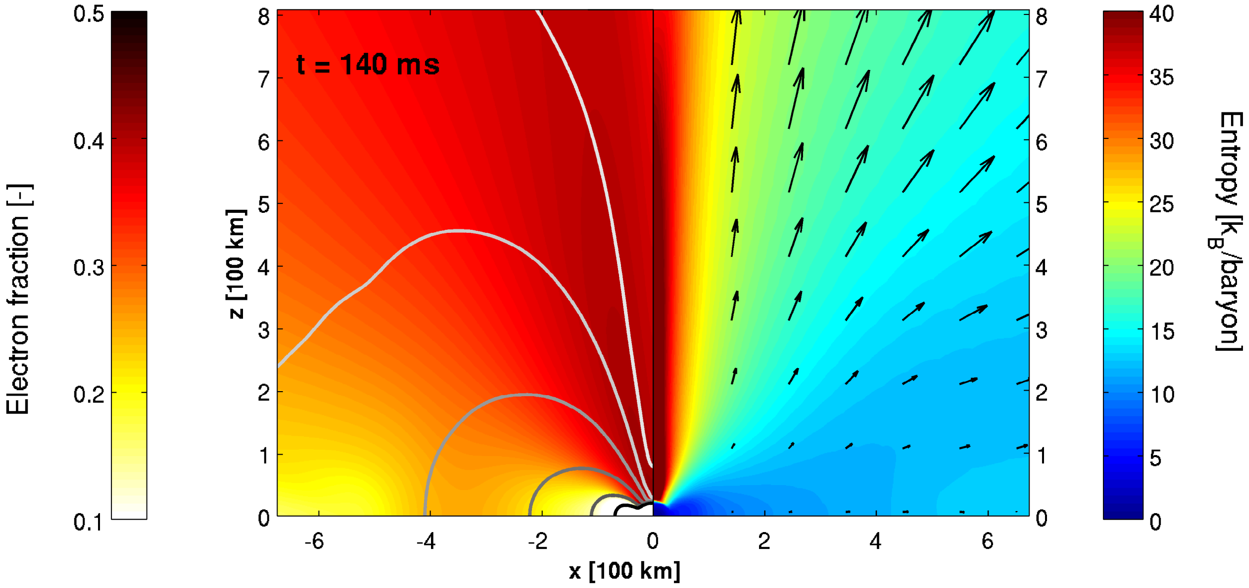

Figure 4.15: $x-z$ plane at 140 ms after the beginning of the simulation. The left panel shows the electron fraction with a superimposed contour plot of the density. A color gradient from white to black indicates the regions with densities of $\rho = 10^6\ \mathrm{g/cm^3}$ to $\rho = 10^{11}\ \mathrm{g/cm^3}$. Entropy profile and the projected velocity are presented in the right panel. The length of the arrows characterizes the magnitude of the velocity.

4.3.2 Tracer particles

At the beginning of our simulation we place 10^5 tracers inside our computational domain. The wind tracers are ejected from a region with initial density of $\rho \lesssim 10^{10}\,\mathrm{g/cm^3}$, as found in backtracking procedures of preliminary tests following [17]. Thus, we locate our tracers initially inside the thick accretion disk where the density is between $2 \cdot 10^6\,\mathrm{g/cm^3}$ and $2 \cdot 10^{10}\,\mathrm{g/cm^3}$ (see Fig. 4.16). The number of tracers assigned to each grid cell is proportional to its mass content and the actual location of each particle within a cell is randomly assigned. Hence, the resulting tracer distribution tracks the matter density distribution inside the disk. The mass of the region of the disk where the tracers are placed is 0.0542 $M_\odot$. Therefore, we assign to each of them an inherent mass of $m_i = m = 5.420 \cdot 10^{-7} M_\odot$. Every tracer records the local properties of matter (density, internal energy, electron fraction and velocity components) at its present location by linearly interpolating the corresponding values on the computational grid. The total specific energy, e_{tot}, is computed as the algebraic sum of the kinetic, thermal and gravitational specific energy. We recall here that the thermal energy is obtained from the relativistic internal energy, reduced by the rest mass energy (both obtained from the nuclear equation of state). All tracers are passively advected by the fluid and their location is evolved in time inside the grid by solving the equation $\mathrm{d}\mathbf{x}/\mathrm{d}t = \mathbf{v}$ with a second order accurate Euler integration scheme. A tracer particle is considered unbound if $e_{\mathrm{tot}} > 0$ and if its radial component of the velocity is positive, steadily from a certain time until the end of the simulation. For each ejected tracer, neutrino fluxes and mean energies as a function of time come from the axisymmetric output provided by the hydrodynamic simulations, see Sect. 4.3.1 and Ref. [17]. We perform nucleosynthesis calculations for over 17 000 ejected tracers from the hydrodynamical simulation.

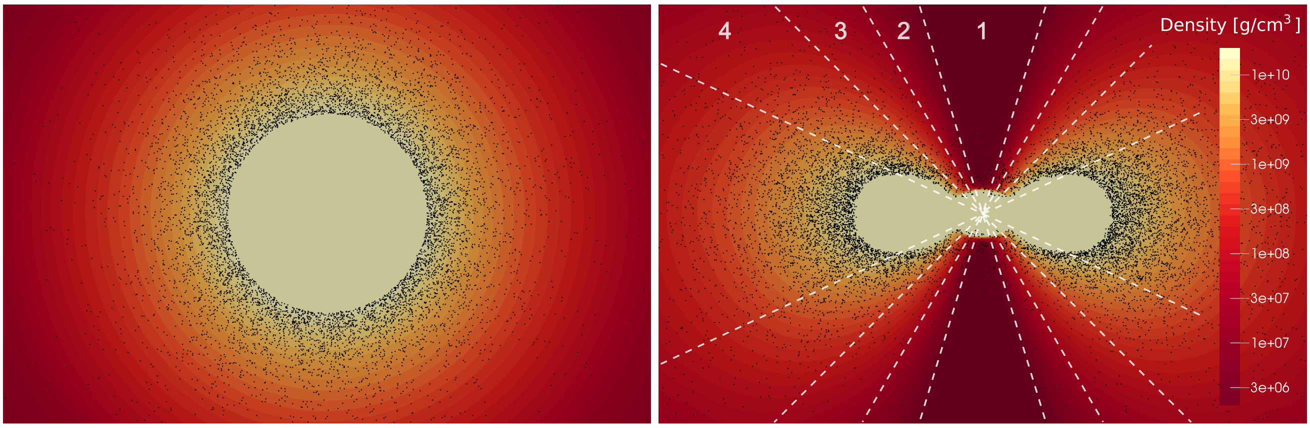

Figure 4.16: Distribution of the tracers at the beginning of the simulation. The density profile is shown for $2 \cdot 10^6\,\mathrm{g/cm^3} \leq \rho \leq 2 \cdot 10^{10}\,\mathrm{g/cm^3}$. Tracers are marked by black dots. Left: tracers in the $x - y$ plane as seen when looking at the configuration of MNS and disk from above. Right: side view of the tracers in the $x - z$ plane. White dashed lines and numbers label the four angular regions of interest, which are referred to as (angular) bins $1 - 4$ in the following.

4.3.3 Time and angle dependency

The composition and amount of matter ejected in the neutrino-driven wind depends on the temporal evolution of the disk and the fate of the compact central object. Here we consider a long-lived MNS. In the following, we present abundances at various times after the merger and for different latitudes to understand the angular distribution and temporal evolution of ejected matter. The potential consequences for the mixing with the dynamic ejecta and thus for the light curve are discussed in Sects. 4.4 and 4.5, respectively. In the following, t_{sim} refers to the time since merger. When abundances are shown at t_{sim}, we consider all tracers having become unbound until this time. Therefore, at later times early ejecta are also included.

An idea of the amount of matter ejected and its potential composition can be gained by exploring the dependence of the ejected mass on the electron fraction and time. This evolution is shown in Fig. 4.17. Within the first 50 ms only a marginal amount of mass with electron fraction $Y_{\mathrm{e}} \lesssim 0.3$ gets unbound. Until $t_{\mathrm{sim}} = 100$ ms approximately $2 \cdot 10^{-3} M_{\odot}$ are ejected with a central value of $Y_{\mathrm{e}} \approx 0.3$. After almost twice that time, i.e., $t_{\mathrm{sim}} = 190$ ms, the mass of unbound material reaches $9 \cdot 10^{-3}\,M_{\odot}$. These late-time ejecta has relatively high electron fractions (with a mean value between 0.3 and 0.35) since neutrinos have more time to interact with nucleons. Furthermore, the growth rate of unbound mass by the late ejection of tracers remains approximately constant from 110 ms on. The substantial mass accretion rate inside the accretion disk, amounting to a few tenths of solar masses per second, provides quasi steady-state conditions with neutrinos as primary cooling agent. As a consequence, the neutrino luminosities decrease only slowly over the expansion time scale (cf., Fig. 10 in Ref. [17]) and the interaction rates get close to equilibrium.

In the following, abundances are shown using either of these two normalizations for a given nuclear mass A:

- Total mass:

$$X_{\mathrm{tot}}(A) = \sum_{i=1}^{N} X_i(A) \cdot m_i, \tag{4.10}$$

  with N, X_i and m_i being the number of tracers considered, the mass fractions and the mass of one tracer i, respectively. This quantity has mass units and thus allows to compare different ejection channels to each other, as we will discuss in Sect. 4.4.

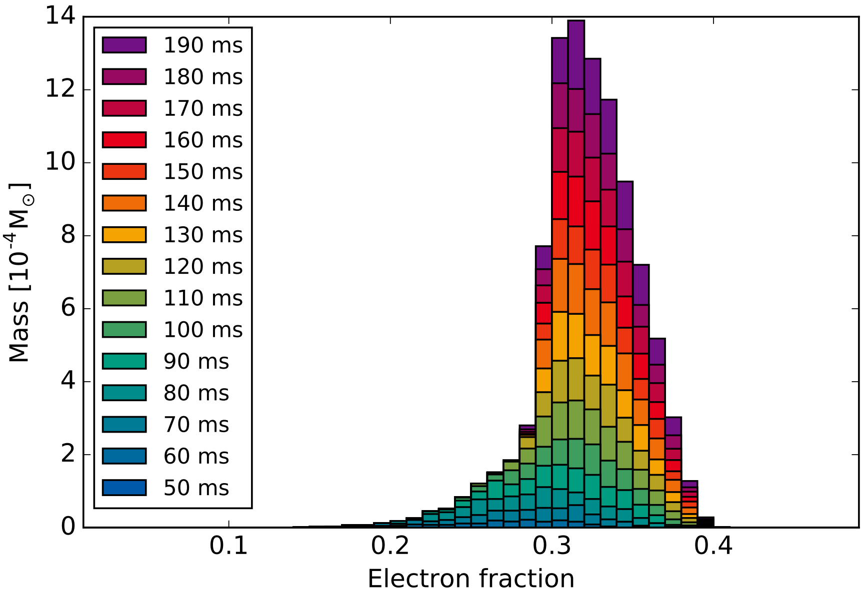

Figure 4.17: Evolution of the electron fraction for ejected tracers. The Y_e distributions at various simulation times are represented by superposing bars with different colors.

- Integrated abundances:

$$Y_\mathrm{int}(A) = \frac{\sum_{i=1}^{N} Y_i(A) \cdot m_i}{\sum_{i=1}^{N} m_i}. \tag{4.11}$$

Normalizing the abundances via Eq. (4.11) allows to explore the average nucleosynthesis yields of a certain subclass of tracers, for instance tracers ejected into a particular solid angle. Additionally, the impact of single trajectories on the overall nucleosynthesis is directly evident from the comparison with the average abundance curve.

Figure 4.18 shows total ejected masses for simulation times t_sim = 90 ms, 140 ms and 190 ms. The heavy nuclei beyond the second r-process peak ($A \sim 130$) are produced by early, very neutron-rich ejecta, as indicated by the overlap of the three curves at different simulation times. Later on, no heavy r-process elements ($A \gtrsim 130$) are produced any more. There is a threshold $Y_\mathrm{e} \sim 0.25$ below which heavy r-process elements (i.e., beyond the second peak at $A = 130$) can be synthesized (see also Ref. [220]). As time passes, a substantial amount of tracers contributing to nuclei with $A \lesssim 120$ becomes unbound. This evolution is in fact a direct consequence of the trend of Y_e presented in Fig. 4.17.

In addition, the nucleosynthesis has an angular dependency. We divide the neutrino-driven wind into four regions above and below the disk by setting cuts on the polar angle and investigate the angular dependence of the ejecta. Each of the cuts has a width of $\Delta\theta = 15°$, hence the whole neutrino-driven wind is captured within $0° \leq \theta \leq 60°$ (as a convention we define $\theta = 0°$ at the poles). These four regions or bins are indicated with white dashed lines in the right panel of Fig. 4.16 and are labeled with the number of the bin. The properties of the tracers ejected until $t_\mathrm{sim} = 190$ ms in each of the angular bins are shown in Fig. 4.19, when passing a sphere with a radius of 750 km. We select the nucleosynthesis-relevant quantities: electron fraction Y_e, entropy per baryon s and radial velocity v_r. The major part of the cumulative mass is approximately equally distributed to the two angular bins close to the accretion disk. On the contrary, the two bins in the polar region contain 15% — 20% of the total cumulative mass. While the entropy of the unbound tracers ranges from 10 k_B/baryon to 30 k_B/baryon (left panel of Fig. 4.19), it is still very low and has therefore little impact on the nucleosynthesis. The radial velocity provides a measure for the dynamical time-scale and is constrained to $0.04c - 0.08c$ (right panel of Fig. 4.19). In the neutrino-driven wind the nucleosynthesis is most sensitive to the electron fraction distribution which varies for every angular region. As a general trend, the average electron fraction decreases as a function of the angle and reaches values down to 0.3 for the two zones closest to the disk. Both of these bins also contain extreme cases with very neutron-rich conditions of $Y_\mathrm{e} < 0.2$.

Figure 4.20 shows the resulting integrated abundances for tracers ejected at t_sim = 140 ms. All yields are presented in comparison to the solar abundances (black dots, taken from Ref. [23]) for one angular bin in every

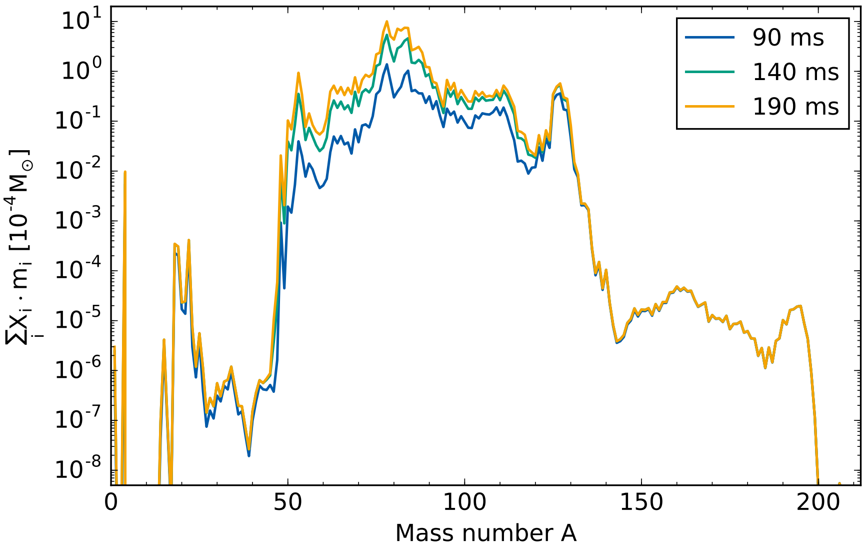

Figure 4.18: Total final mass fractions times the mass of the ejecta until $t_{\rm sim} = 90$ ms, 140 ms, and 190 ms. Early neutron-rich ejecta produce heavy r-nuclei with $A \gtrsim 130$, leading to overlapping abundances in this region. Later ejecta contribute strongly to the lighter heavy elements (note the logarithmic ordinate).

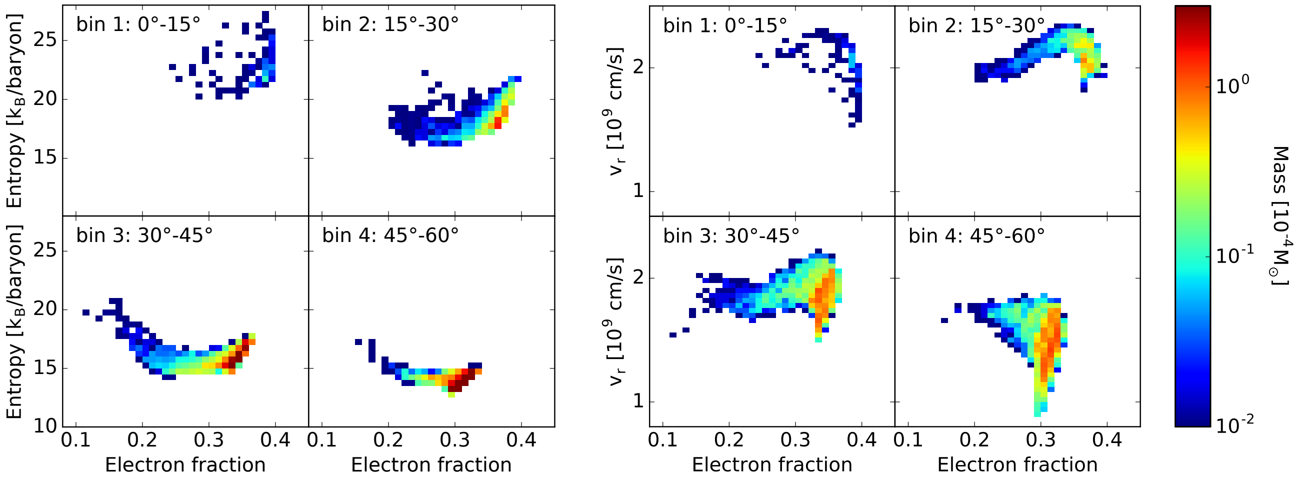

Figure 4.19: Left: distribution of the unbound tracers in the $Y_e - s$ plane at a sphere with a radius of 750 km. Right: distribution of the unbound tracers in the $Y_e - v_r$ plane at the same radius. We present the logarithmic scale of the total mass for all tracers in a certain angular bin of the respective plane with a color code. The panels correspond to the angle intervals defined in Fig. 4.16.

panel. The thin gray lines represent individual tracers, while averages are indicated by a solid thick line in every panel. The patterns in Fig. 4.20 reveal significant differences in abundances for distinct latitudes. We find that the first r-process peak ($A \sim 80$) forms for each angular region, whereas the second abundance peak ($A \sim 130$) is only reached in bin 3 and bin 4. In particular, the angular zone closest to the disk, i.e., bin 4, successfully attains elemental abundances close to the solar system values up to the second abundance peak. When moving to lower polar angles (bin 1), less heavy elements are synthesized.

To gain further insights into the dependence on time, it is instructive to compare the trends of the angular bins at various times. Total masses as a function of mass number A (see Eq. (4.10)) for unbound tracers at $t_{\rm sim} = 90$ ms, 140 ms and 190 ms are presented in Fig. 4.21. At early times $t_{\rm sim} \lesssim 90$ ms, elements up to $A \sim 120$ are produced predominantly by the ejecta in bin 3, while only bin 4 synthesizes nuclei within the vicinity of the third abundance peak ($A \sim 195$). The yields resulting from both bin 3 and bin 4 clearly dominate the abundances, as is expected from the distribution of the mass and the electron fraction for the tracers among the four bins (cf., Fig. 4.19). In contrast, bin 1 and bin 2 give marginal contributions. With time, increasing yields for lighter heavy nuclei ($A \lesssim 120$) (cf., Fig. 4.18) are present in all considered angular regions.

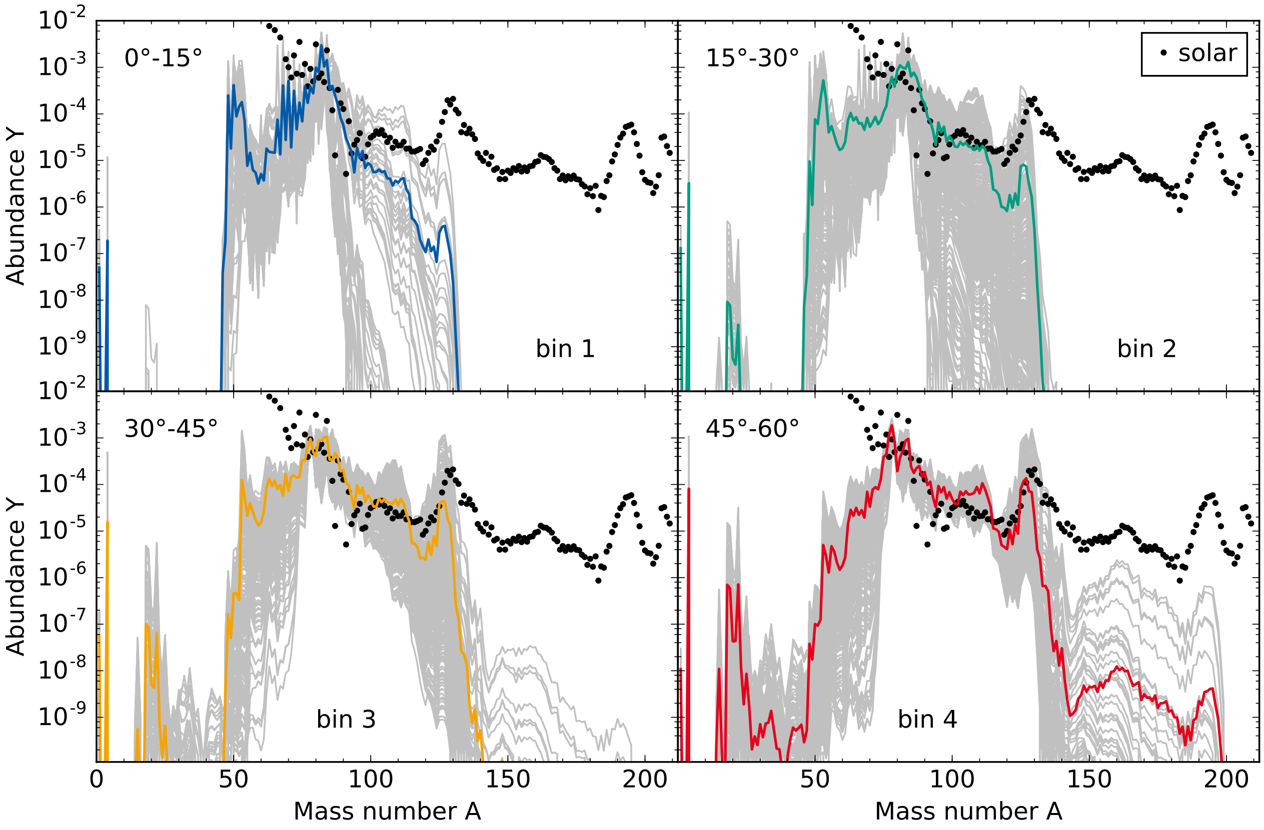

Figure 4.20: Individual abundances and integrated final abundances for ejecta until $t_{\text{sim}} = 140$ ms in each of the four considered angular bins. Thick colored lines mark the average yields for each angular region. Note that we apply the same color code consistently in all following figures. Moreover, thin gray lines denote abundances from individual trajectories to hint the variety of the nucleosynthesis. Solar abundances are shown with dots for comparison.

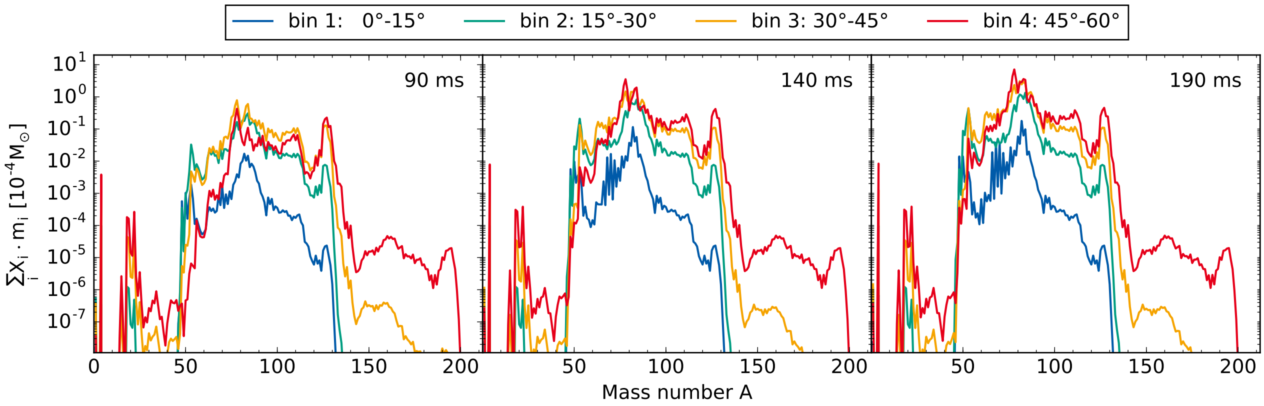

Figure 4.21: Total final masses. The panels show the yields for tracers ejected until $t_{\text{sim}} = 90$ ms, 140 ms, and 190 ms from top to bottom. We use the same color scheme as in Fig. 4.20 to identify the different angular bins.

Let us take a closer look at the relevant physical quantities characterizing the nucleosynthesis. Figure 4.22 shows the evolution of individual electron fractions for tracers unbound at 140 ms (gray, thin lines), along with the corresponding average curves (colored, thick lines). Note that the elapsed time of a tracer is defined with respect to the moment when it gets out of NSE in the network calculations. The individual tracers provide information about the spread in the initial Y_e (i.e., at $T = 10$ GK), also visible in the panels of Fig. 4.19. The slight increase of the electron fraction shortly after the beginning of the calculations is due to neutrino absorption on nucleons, whereas the steep rise at around $t \simeq 10^{-1}$ s is caused by beta decays.

The electron fraction in the neutrino-driven wind depends on the competition between the expansion and the weak equilibrium time scales, on the ratio between the ν_e and $\bar{\nu}_e$ luminosities, as well as on the neutrino mean energies (e.g., Ref. [68]). As we mentioned in Sect. 4.3.1, the larger luminosities predicted by GR simulations can lead to a faster evolution towards the equilibrium Y_e. Therefore, the very small amount of heavy elements ($A > 130$) that are produced in the initial phase of our Newtonian simulation may not be present in a GR simulation. In addition to the GR effects, an accurate calculation of Y_e would require the usage of a detailed neutrino transport scheme, which is presently computationally prohibitive in long-time three dimensional simulations, without global symmetries. Assuming uncertainties of the order of 20% for the neutrino luminosities and of 10% for the mean energies[1], we estimate a potential uncertainty of $\sim$ 15% on the values of the equilibrium electron fraction. Given the broad range of Y_e obtained in the ejecta (Figs. 4.19 and 4.22), we consider this uncertainty as being important to be mentioned, but not crucial for our analysis.

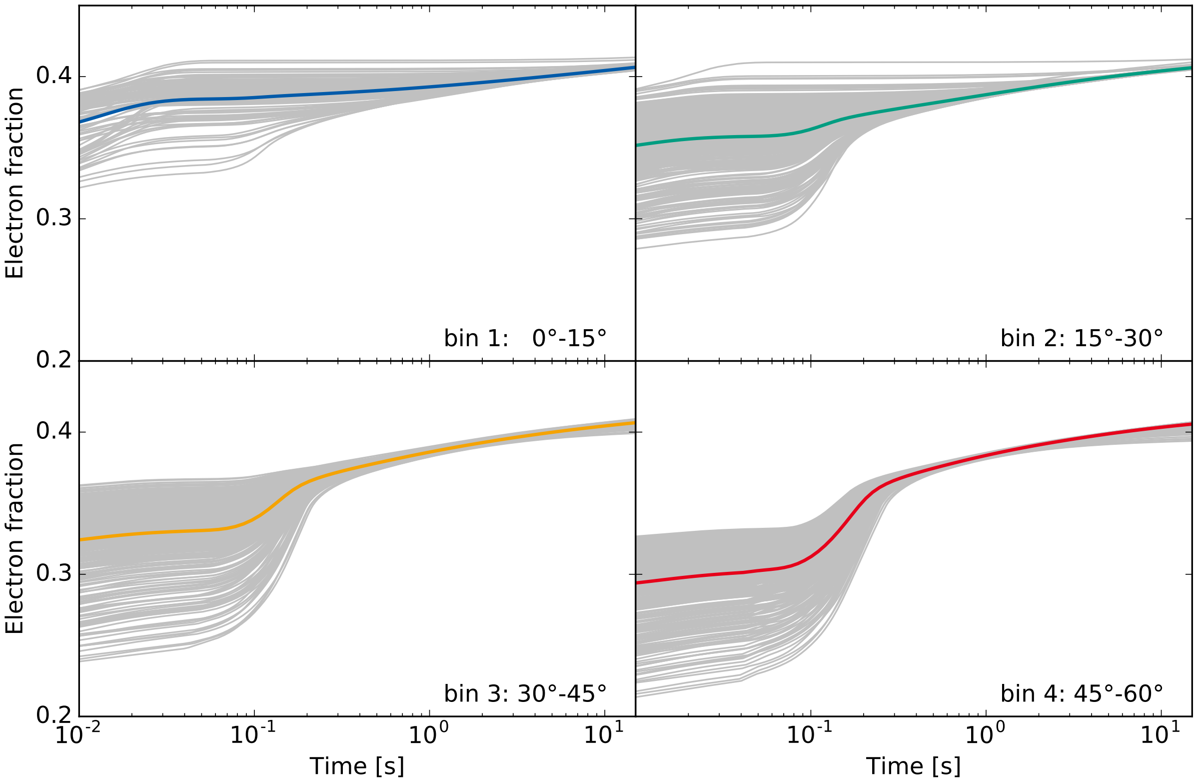

Figure 4.22: Temporal evolution of the electron fraction for tracers that become unbound until $t_{\mathrm{sim}} = 140$ ms. The solid thick lines are averages $\langle Y_e \rangle$ for every angular bin as introduced in Fig. 4.20. Thin gray lines represent individual tracers.

In order to examine the production of heavy elements, we present the evolution of neutron density n_n, the average mass number $\langle A \rangle$ and the average proton number $\langle Z \rangle$ in Fig. 4.23 for different angular regions. At the beginning, the neutron density is larger than 10^{30} cm^{-3} and the composition is dominated by alpha particles and neutrons. The onset of the r-process nucleosynthesis is triggered when the temperature decreases to $\sim$ 3 GK (marked by triangles in the top panel of Fig. 4.23; see, e.g., the dependence of r-process efficiency as a function of entropy, electron fraction and expansion time scale in Refs. [221, 222]. For $t \simeq (1.5 - 3.0) \cdot 10^{-1}$ s, most of the neutrons are consumed as indicated by the rapid neutron density drop. After this, matter beta-decays to stability and this leads to an increase of Y_e (see Fig. 4.22). Then, the mass number stagnates, since no more heavy elements are formed (see middle panel of Fig. 4.23). No fission takes place, resulting in the monotonic evolution of mass and proton number. The higher neutron density in bin 4 favors the build-up of heavier nuclei compared to the other regions. With decreasing polar angle the neutrons are consumed earlier, as their initial density is smaller and the expansion velocity of the corresponding tracers is larger.

---

[1] This estimate is consistent with the quantitative differences spotted between our ASL scheme results and the ones obtained using a multigroup flux limited diffusion transport in axisymmetric simulations [148].

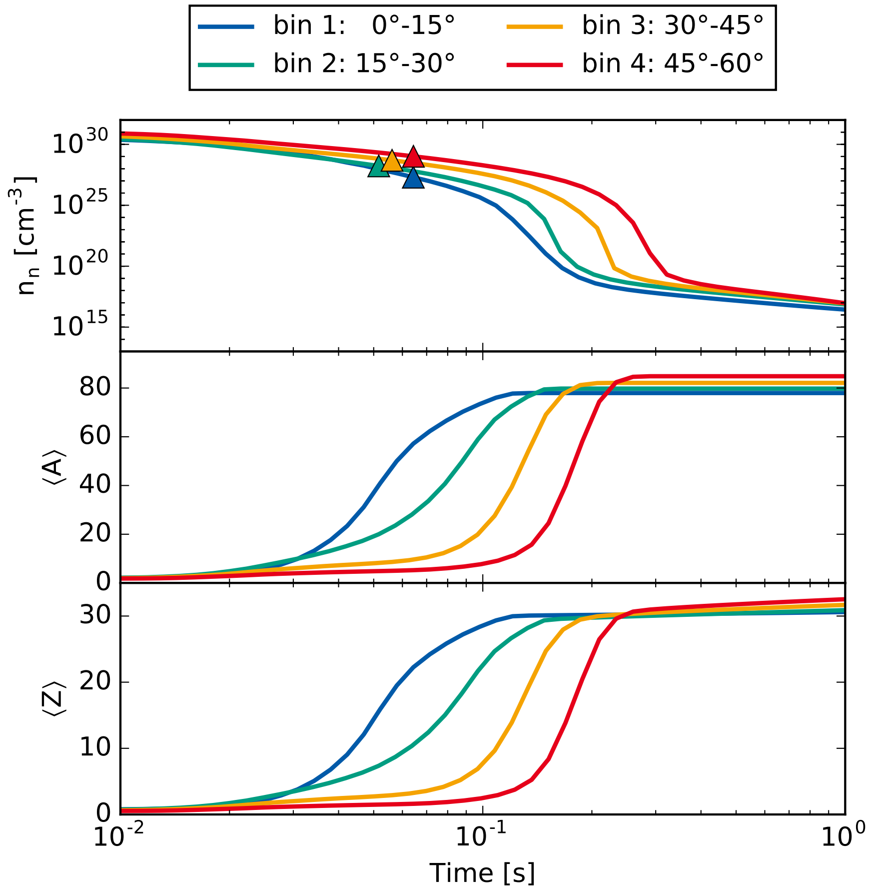

Figure 4.23: Evolution of the neutron density n_n (top), average mass number $\langle A\rangle$ (middle) and average proton number $\langle Z\rangle$ (bottom). The solid lines follow the mean values of the four angular bins (see also Fig. 4.22). Triangles indicate times, when the temperature reaches $T = 3$ GK, i.e., the onset of the r-process.

4.4 Combined ejecta

The neutrino-driven wind is only one of three nucleosynthesis-relevant ejecta in neutron star mergers. In order to have the complete nucleosynthesis picture, one would need to follow the evolution of the dynamic and disk (neutrino- and viscous-driven) ejecta, and investigate how they mix. However, this is currently too complicated to be studied in a single simulation due to the different time-scales and physics involved. The dynamic ejecta expand very fast from the beginning. While neutrinos may be initially important for the Y_e their impact is insignificant when the disk becomes transparent [15, 18, 223]. Nevertheless, mixing of the different types of ejecta can occur once the unbound matter becomes considerably decelerated by the ambient medium. Where this happens depends on the merger location with respect to the galaxy. Simple estimates indicate that the time scale for being noticeably decelerated is by far greater than years, see, for example, the discussion in Sect. 2.1 of Ref. [133]).

In the first study of the mixing between the disk and dynamic ejecta, [224] showed that there is no significant mixing between these ejecta. This study focuses on neutron star black hole mergers, where neutrino-driven ejecta are less important as it was discussed also by [15] compared to [223]. However, their conclusion may also apply to our results that are based on a long-lived MNS. From the nucleosynthesis perspective, [18] have also investigated the mixing of disk and dynamic ejecta. They have modeled the long-time evolution of a black hole surrounded by a disk where matter is neutrino- and viscous-driven ejected. In a post-processing step, the nucleosynthesis of such simulations was added to the dynamic ejecta from a merger simulation [14].

We combine the nucleosynthesis of the neutrino-driven wind presented in Sect. 4.3.3 with the dynamic ejecta computed by Ref. [13]. Although the ejecta masses show a substantial spread depending on the parameters of the merging binary system [132], the resulting abundance patterns have been found to be practically identical [13]. In contrast to previous studies (i.e., Refs. [15, 18]) with a black hole as central object, we assume a long-lived MNS. This has strong consequences on the amount and properties (i.e., Y_e) of the matter ejected by neutrinos as discussed by Refs. [17, 220, 223].

The comparison between dynamic and wind ejecta is given in Fig. 4.24 showing the total ejected masses (calculated with Eq. (4.10)) as a function of A for both contributions. Note that the approach here differs from the one in the previous sections, in which we treated the different times t_{sim} to be merely snapshots of the neutrino-driven wind. Now, we assume that the MNS collapses after t_{sim}, terminating the ejection of further material in the wind. Three different simulations times are considered, $t_{\mathrm{sim}} = 90$ ms, 140 ms, and 190 ms. This comparison indicates that the wind ejecta complement the dynamic ejecta by producing elements below the second peak. We note that if the dynamic ejecta could produce the full r-process, as suggested by recent GR simulations [89, 144] and by parametric studies [145], the combination of the dynamic and wind nucleosynthesis would again allow the production of lighter heavy elements ($A < 130$) in addition to the heavy r-process. In the latter case, the wind ejecta would increase only the relative contribution of the lighter heavy elements. Moreover, the amount of wind ejecta becomes comparable to the dynamic ejecta if the MNS survives long enough ($t_{\mathrm{sim}} \gtrsim 140$ ms in our model). These ejecta amounts will be further enhanced by viscous ejecta that can produce r-process elements from the first to the third peak [18]. If the three ejecta completely mix, the wind contribution may still lead to variations in the abundances below $A = 130$ (i.e., $Z < 50$). Such variations are also expected from observations of the oldest stars (see Ref. [37] for a review). The size of the observed variations could help to constrain different contributions of the three ejecta types to the r-process abundances.

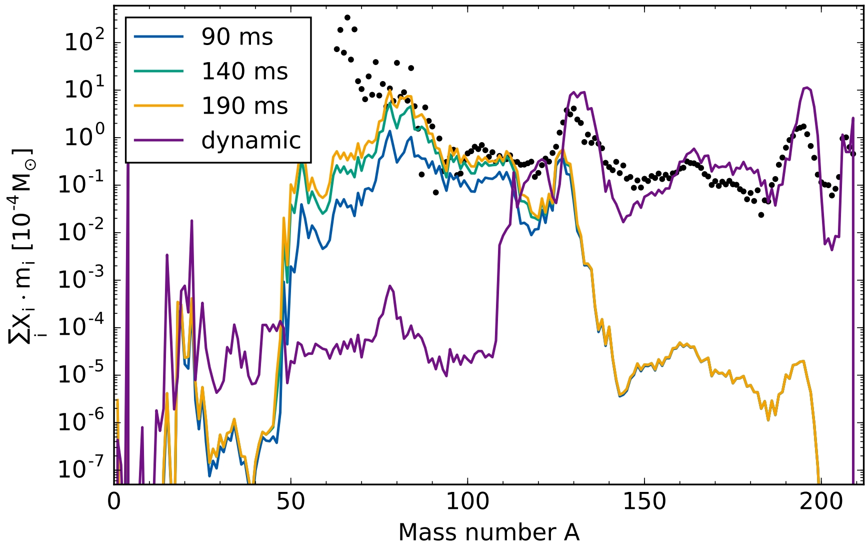

Figure 4.24: Comparison of the nucleosynthesis yields for neutrino-driven wind (cf. Fig. 4.18) and dynamic ejecta (labeled with dynamic). While the dynamic ejecta produce very heavy nuclei, the neutrino-driven wind complements its abundances by producing the lighter heavy elements from the first to the second r-process peak.

The oldest observed stars were formed in an interstellar medium polluted by only one or few nucleosynthesis events. Therefore, their atmospheres present a unique fingerprint for the r-process. Observations indicate that there are at least two types of abundance patterns among the oldest r-process stars (see, e.g., Refs. [37, 225]):

(1) stars with high enhancement of heavy elements ($Z > 50$) present a robust pattern for those and some variations for the lighter heavy elements ($Z < 50$);

(2) stars with low enhancement of heavy r-process.

Two stars are typically identified with these trends: (1) CS 22829-052 [226] and (2) HD 122563 [38, 227, 228]. Recently, the authors of Ref. [39] have shown that this second kind of pattern can be explained by the superposition of two components: an H-component producing the heavy r-process elements (and maybe also lighter ones) and an L-component contributing only below $Z = 50$. In neutron star mergers, the dynamic and viscous ejecta can account for the H-component while the wind ejecta would be the L-component. Matter with a perfect mixing of the three ejecta will lead to a pattern like in CS 22829-052. This is shown in the left panel of Fig. 4.25, where the combination of wind (L-component) and dynamic (H-component) ejecta reproduce the observed abundances. The differences around the third peak are due to nuclear physics input as shown, e.g., in Ref. [137]. If the mixing is not perfect and the wind ejecta combines only with a small amount of dynamic and/or viscous ejecta, then one can explain the trend observed in HD 122563 (see also Ref. [18]). This is shown in the right panel of Fig. 4.25 where the dynamic ejecta has been reduced by a factor of 50. In this case, one would expect to have more variability in the observations depending on the amount of the H-component that is mixed. Indeed observations show variability for $Z > 50$ in these kind of stars [39, 229].

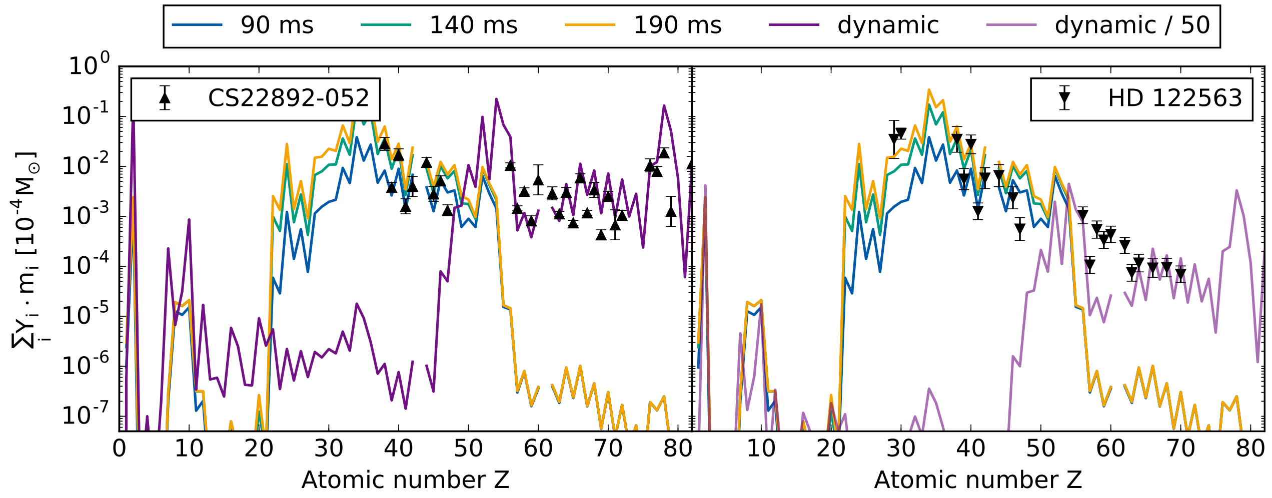

Figure 4.25: Left: combined elemental abundances of neutrino-driven wind and dynamic ejecta in comparison to the yields of the metal-poor star CS22892-052 [226]. Abundances are weighted with the ejecta mass to consistently add the two contributions. Right: comparison of the combined yields with the ones of the HD stars [38, 227, 228]. Note that the dynamic ejecta are scaled down by a factor of 50.

On the time scale of star formation, it is likely that all the ejecta have efficiently mixed, even if the wind expands perpendicular to the disk and the other two are more homogeneously distributed or stay in the disk plane. Do we expect stars to be polluted by a neutron star merger preferentially only receiving axial ejecta rather than disk ejecta? Or do Honda-like abundances (L-component) come from different sources (e.g., core-collapse supernovae with slightly neutron-rich conditions)? More investigation of the long-term mixing is necessary to understand the contribution of neutron star mergers to the different patterns found in the oldest observed stars.

However, the dynamic and wind ejecta will not mix before they are substantially decelerated by the dilute ambient medium [230]. A merger is engulfed by a dilute medium of a density $\rho_{\rm amb} = m_{\rm amb} n_{\rm amb}$ that depends on the actual merger location with respect to its host galaxy. If the merger occurs early after the neutron star binary has formed, it takes place close to the mid plane of their host galaxies. Here, the particle density may be $n_{\rm amb} \sim 1$ cm^{-3}. On the other hand, binary systems that had time to travel a few kpc out of the mid plane can be embedded into a much lower density surrounding. The initial expansion stage is unaffected by the ambient medium, but once the matter swept up is comparable to the ejected mass ($m_{\rm su} \approx m_{\rm ej}$), the ejecta start to slow down. This transition defines the deceleration radius of

$$R_{\rm dec} \simeq 0.5\,{\rm pc} \left(\frac{m_{\rm ej}}{10^{-2}\,M_\odot} \right)^{1/3} \left(\frac{n_{\rm amb}}{1\,{\rm cm}^{-3}} \right)^{-1/3} , \tag{4.12}$$

which is reached after the deceleration time

$$\tau_{\rm dec} \simeq 15\,{\rm yr} \left(\frac{m_{\rm ej}}{10^{-2}\,M_\odot} \right)^{1/3} \left(\frac{n_{\rm amb}}{1\,{\rm cm}^{-3}} \right)^{-1/3} \left(\frac{v_{\rm ej}}{0.1c} \right)^{-1} . \tag{4.13}$$

The dynamic ejecta expand earlier and with high initial velocities of $\sim 0.1c$. Our estimates are rather insensitive to the poorly known ambient matter density. Therefore, ambient matter effects start to become noticeable after a deceleration time of 15 (150) years in an environment of $n_{\rm amb} = 1$ (10^{-3}) cm^{-3}. The neutrino-driven wind, in contrast, gets unbound after neutrinos have deposited enough energy. Therefore, the wind matter is ejected later and eventually reaches asymptotic velocities of up to $\sim 0.08c$. The different ejection times and velocities make it possible to observe a kilonova signal from different parts of the ejecta with different composition, as we discuss in the next section.

4.5 The electromagnetic signal: a semi-analytical model

The nucleosynthesis network allows us to compute radioactive heating rates for the wind outflow. Figure 4.26 shows the heating rates for different bins, normalized to $\dot{\epsilon}_0(t) = 10^{10} t_\mathrm{d}^{-1.3}$ erg $\mathrm{g}^{-1}\mathrm{s}^{-1}$ with time t_d in units of days [9, 13]. It is interesting to point out that all the normalized heating rates show considerable excess at $t \sim 4$ h. This excess is caused by decay of radioactive nuclei in the vicinity of the first r-process abundance peak ($A \sim 80$), as those possess the highest mass fractions. The properties of the isotopes which contribute most to the heating rates in the neutrino-driven wind are listed in Tab. 4.2. On average, about 40% of the decay energy is carried away only by neutrinos. An additional fraction of energy is radiated away by escaping photons, while both the electrons and the remaining part of the photons thermalize. Therefore our hypothesis of an effective beta-decay thermalization fraction of 50% is reasonable.

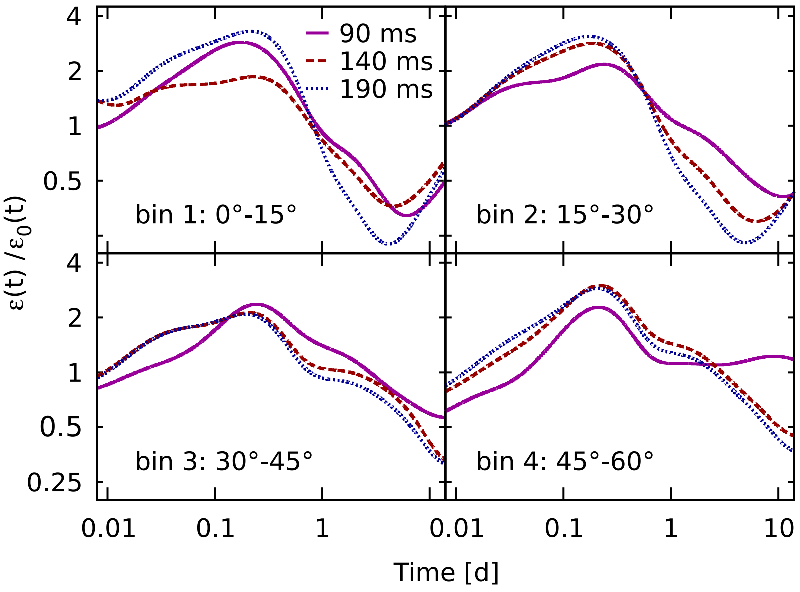

Figure 4.26: Radioactive heating rate, calculated with the nucleosynthesis network for a representative tracer of the neutrino-driven wind in each angular bin, normalized to the fitted expression $\dot{\epsilon}_0(t) = 10^{10} t_\mathrm{d}^{-1.3}$ erg $\mathrm{g}^{-1}\mathrm{s}^{-1}$ (see, e.g., Refs. [9, 13]). In all cases the heating rate exhibits an excess by a factor of ~ 2.5 at $t \sim 4$ h.

Table 4.2: Properties of the dominant beta decay nuclei at $t \sim 1$ day; based on the data from NuDat 2.6 database (http://www.nndc.bnl.gov/nudat2/)

Isotope	$t_{1/2}$ [h]	Q$^{(a)}$ [MeV]	$\epsilon_e^{(b)}$	$\epsilon_\nu^{(c)}$	$\epsilon_\gamma^{(d)}$	$E_\gamma^{\mathrm{avg}\,(e)}$ [MeV]
^{88}Kr	2.83	2.92	0.12	0.21	0.67	1.34
^{88}Rb	0.30	5.31	0.39	0.49	0.13	1.59
^{87}Kr	1.27	3.89	0.34	0.46	0.20	0.95
^{83}Br	2.37	0.98	0.33	0.66	0.007	0.46
^{81}Sr	0.37	3.93	0.28	0.37	0.35	0.42
^{78}Ge	1.47	0.96	0.24	0.47	0.29	0.28
^{78}As	1.51	4.21	0.30	0.39	0.31	0.94
^{77}Ge	11.2	2.70	0.23	0.36	0.41	0.47

(a) Total energy released in the decay; (b),(c),(d) Fraction of the decay energy released in electrons, neutrinos, and γ-rays; (e) Average photon energy produced in the decay.

Here we extend the semi-analytical model of Refs. [112] and [17] to compute light curves. The light curve modeling was provided by Oleg Korobkin. We assume that the wind shuts off immediately after the collapse of the

MNS and we explore collapse times of 90 ms, 140 ms and 190 ms after merger. The masses as well as average properties of the ejecta in the four bins for each of the cases are given in Tab. 4.3. The higher value of $\kappa = 10\ \mathrm{cm^2/g}$ for the opacity in the last angular bin is justified by inspecting the distribution of mass fractions for heavy elements X_{heavy} (for mass numbers $A > 130$) in the neutrino-driven wind. This distribution is portrayed for extrapolated positions of the unbound tracers in Fig. 4.27 at $t = 50$ s after the merger. Mass fractions of heavy elements are marginal in the bins 1—3, but heap up in the area of bin 4. Reflecting that sizeable fractions of heavy elements are present, we adopt an opacity similar to the one of lanthanides or actinides [110] for the last bin.

Table 4.3: Parameters used for computing luminosities of individual bins: spanned solid angle, mass of the bin, average asymptotic velocity of the ejecta in the bin, and the adopted value of the gray opacity.

t_{sim}	bin	$\Delta\Omega$	$\Delta m_{\mathrm{ej}}/\left(10^{-3}M_{\odot}\right)$	v_{ej}/c	$\kappa\ [\mathrm{cm^2/g}]$
90 ms	1	0.21409	0.013	0.05055	1
	2	0.62769	0.30	0.07974	1
	3	0.99851	0.77	0.07287	1
	4	1.30129	0.34	0.06808	10
140 ms	1	0.21409	0.05	0.04655	1
	2	0.62769	0.75	0.07483	1
	3	0.99851	1.99	0.07626	1
	4	1.30129	2.43	0.06694	10
190 ms	1	0.21409	0.07	0.04694	1
	2	0.62769	1.18	0.07325	1
	3	0.99851	3.39	0.07500	1
	4	1.30129	4.80	0.06466	10

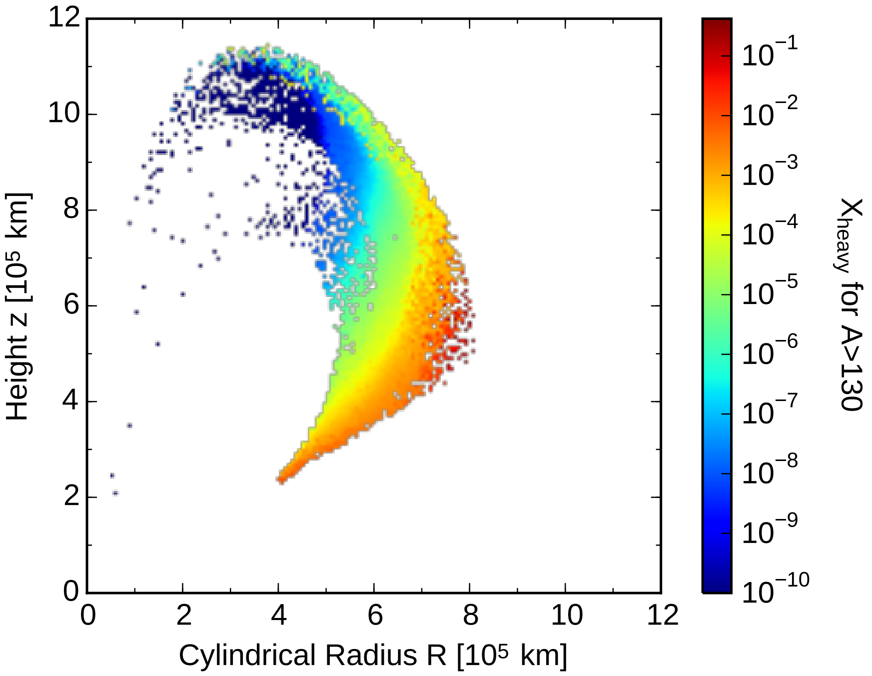

Figure 4.27: Distribution of summed up mass fractions for nuclei with mass number $A > 130$ in the neutrino-driven wind. The upper half space is shown in cylindrical coordinates for a time of 50 s after the merger. Tracers with vanishing total mass fractions $X_{\mathrm{heavy}} < 10^{-10}$ are set to 10^{-10}.

Figure 4.28 illustrates our semi-analytical model for light curve calculations, combining the results of this work and of Ref. [133]. The neutrino-driven wind is schematically shown in blue, while the gray-shaded areas tag the density of the dynamic ejecta in steps of 0.5 dex. We subdivide the wind outflow into the same four bins as in Sect. 4.3.2. Each bin is then approximated by a conical slice of a spherically-symmetric outflow with radial density distribution averaged over the bin and expanding with averaged velocity (a similar approach is employed in Ref. [231] in a context of radio flares). All radiation is assumed to escape from the photosphere for each bin. Vector $\mathbf{n}$ is the unit normal to the photosphere, and an observer is pointed to by a unit vector $\mathbf{q}$. The sketch also illustrates possible obscuration effects from the dynamic, very opaque ejecta, which are concentrated in a puffed up toroid around the equatorial plane. It is apparent that when viewed from the equatorial plane, the wind emission is completely obscured, while from the pole it is possible to observe at least the first three bins.

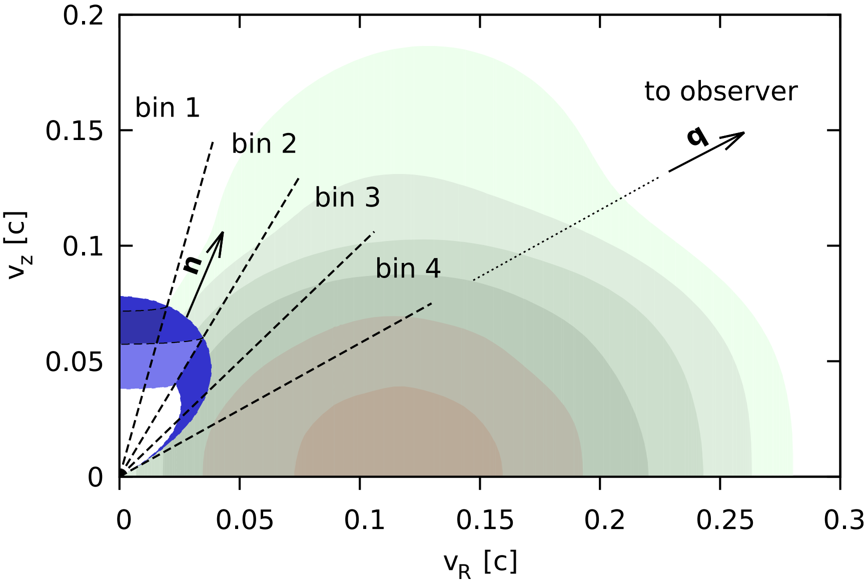

Figure 4.28: Morphology of the neutrino-driven wind (blue, this work) and dynamic ejecta (gray, cf. Ref. [133]) in asymptotic velocity space, represented by a polar cut through the outflows. Shaded areas represent the density of dynamic ejecta, spaced by 0.5 dex from the maximum density at about $v_R \sim 0.115\,c$. Each angular bin is approximated by a conical slab with unit vector $\mathbf{n}$ normal to the photosphere. An observer is pointed to by a unit vector $\mathbf{q}$.

For a bin k with mass Δm_k which spans a solid angle $2\Delta\Omega_k$ (a factor of 2 takes into account upper and lower lobes), we take a spherically-symmetric outflow with mass $4\pi\Delta m_k/2\Delta\Omega_k$ and compute its isotropic bolometric luminosity $L_{k,\mathrm{iso}}$ as described in Sect. 4.1 of Ref. [112].

The luminosity is generated by radioactive heating in the bulk of the outflow and the resulting photons escape from a photosphere. Spanning the same solid angle $2\Delta\Omega_k$ for each bin, the luminosity for bin k is a proportional fraction of isotropic luminosity of the spherical model:

$$L_k = \frac{\Delta\Omega_k}{2\pi} L_{k,\mathrm{iso}}.$$

We then compute the total luminosity of the wind outflow by summing up individual bin contributions, ignoring possible radiative flux between the bins. Individual bin contributions for the combined bolometric luminosity of the neutrino-driven wind and dynamic ejecta for three cases of the MNS collapse time delay are displayed in Fig. 4.29. For the dynamic ejecta, we used an average case (model A from Ref. [112]) with mass $1.3 \cdot 10^{-2}\, M_\odot$. Notice that the luminosity of bin 1 is dimmer than for the bins 2 and 3, because it spans a smaller solid angle. The contribution from bin 4 is not only smaller, but also peaks much later $(3-4$ days) due to the high opacity caused by the very heavy nuclear content [110], such that the medium becomes delayed transparent when the temperature has decreased.

Combined bolometric luminosities of the neutrino-driven wind and dynamic ejecta are shown in Fig. 4.30. A first peak of $L_\mathrm{peak} \sim 4 \cdot 10^{40}$ erg/s is reached at about 4 h after the merger. This luminosity stays roughly constant for several days while rapidly shifting into the infrared band, as shown below. For higher MNS collapse times, the light curve exhibits a double peak structure, but overall the bolometric light curves on the plots exhibit no appreciable difference between different MNS collapse times.

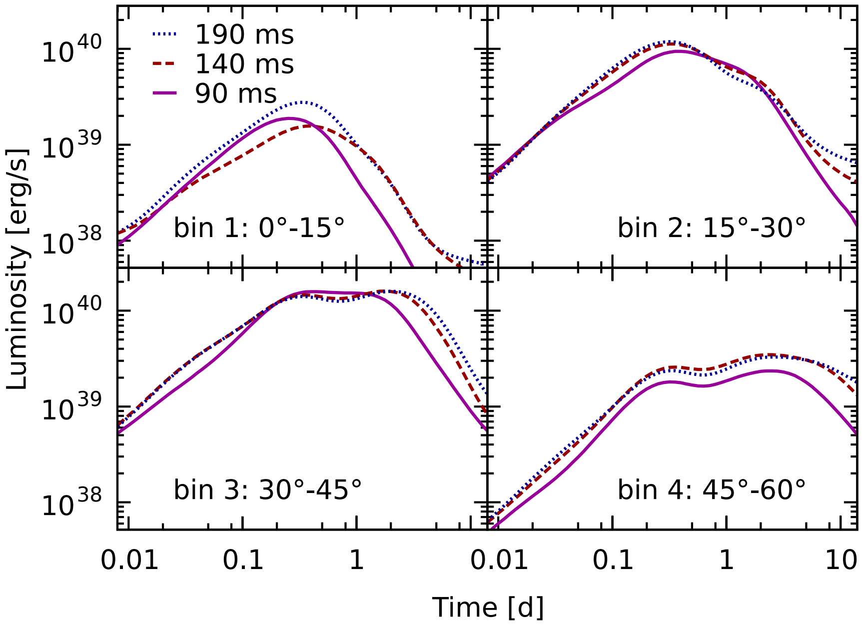

Figure 4.29: Individual contributions of the combined ejecta to the luminosity in the angular bins for three different MNS collapse times: 90 ms (solid), 140 ms (dashed), and 190 ms (dotted line).

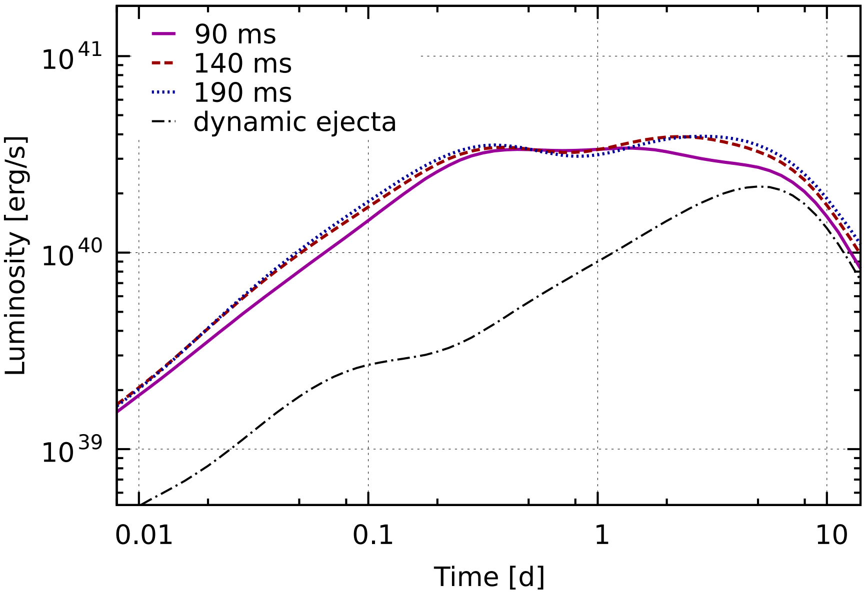

Figure 4.30: Bolometric luminosities for three cases of MNS collapse times: 90 ms (solid), 140 ms (dashed), and 190 ms (dotted line), computed by summing up contributions from individual bins and adding the contribution from dynamic ejecta. Contribution from the latter is also plotted separately (dash-dotted line).

Our simple model also allows to calculate approximate light curves in different bands for different orientations of the system with respect to an observer. At any given moment t we can compute an effective temperature $T_{k,\mathrm{eff}}$ for a bin k using the formula:

$$L_{k,\mathrm{iso}}(t) = 4\pi r_{k,\mathrm{ph}}^2 \cdot (\sigma_{\mathrm{SB}} T_{k,\mathrm{eff}}^4)\,, \tag{4.14}$$

where $r_{k,\mathrm{ph}}(t)$ is the photosphere radius for the spherical model of bin k, and σ_{SB} is the Stefan-Boltzmann constant. We make an assumption that all the flux is emitted from the photosphere with blackbody spectrum $B_\nu(T_{k,\mathrm{eff}})$ and isotropic intensity (following Lambert's law). Then, the spectral flux in the direction $\mathbf{q}$ is given by:

$$\mathcal{F}_\nu(\mathbf{q}, t) = \sum_k B_\nu(T_{k,\mathrm{eff}}(t)) \iint_{(\mathbf{n}_k \cdot \mathbf{q})>0} (\mathbf{q} \cdot \mathrm{d}\mathbf{\Omega}), \tag{4.15}$$

where $\mathbf{n}_k$ is unit normal to the photosphere of bin k, and integration for each bin spans the part of the surface facing the observer (stated by the condition $(\mathbf{n}_k \cdot \mathbf{q}) > 0$). This is also illustrated in Fig. 4.28. Essentially, the integrals in this formula are simply time-independent geometric projections of the photosphere for each bin onto the viewing plane. They can be computed beforehand and used as weighting factors $p_k(\mathbf{q})$ for calculating the combined light curve:

$$\mathcal{F}_\nu(\mathbf{q}, t) = \sum_k p_k(\mathbf{q}) B_\nu(T_{k,\mathrm{eff}}(t)). \tag{4.16}$$

After integrating $\mathcal{F}_\nu(\mathbf{q}, t)$ over certain frequency ranges, we obtain broadband light curves, shown in Fig. 4.31. The left-hand panel shows synthetic light curves for wind outflow only, while the right-hand panel displays the combined contribution from both wind and dynamic ejecta.

Orientation effects are displayed as a range of values for each band, with the maximum magnitude achieved when the system is viewed "face-on", i.e., from the pole. As pointed out by Ref. [220], even a small amount of dynamic ejecta can completely obscure the optical emission from the winds. Therefore, when adding up contributions from different bins and dynamic ejecta, we emulate this obscuration by excluding certain bins, depending on the inclination angle θ with respect to the observer. Our choice of which bins to exclude is motivated by the geometry of the ejecta (depicted schematically in Fig. 4.28). Specifically, we assume that bin 4 is completely obscured for all observing angles; bins 2 and 3 are obscured when $\theta \geq 60°$, and for the edge-on view with $\theta = 90°$ the wind outflow emission is obscured completely. For this reason, depending on system orientation, the luminosity in different bands can vary by up to an order of magnitude, from bright blue when observed from the pole, to dim infrared when observed from the side.

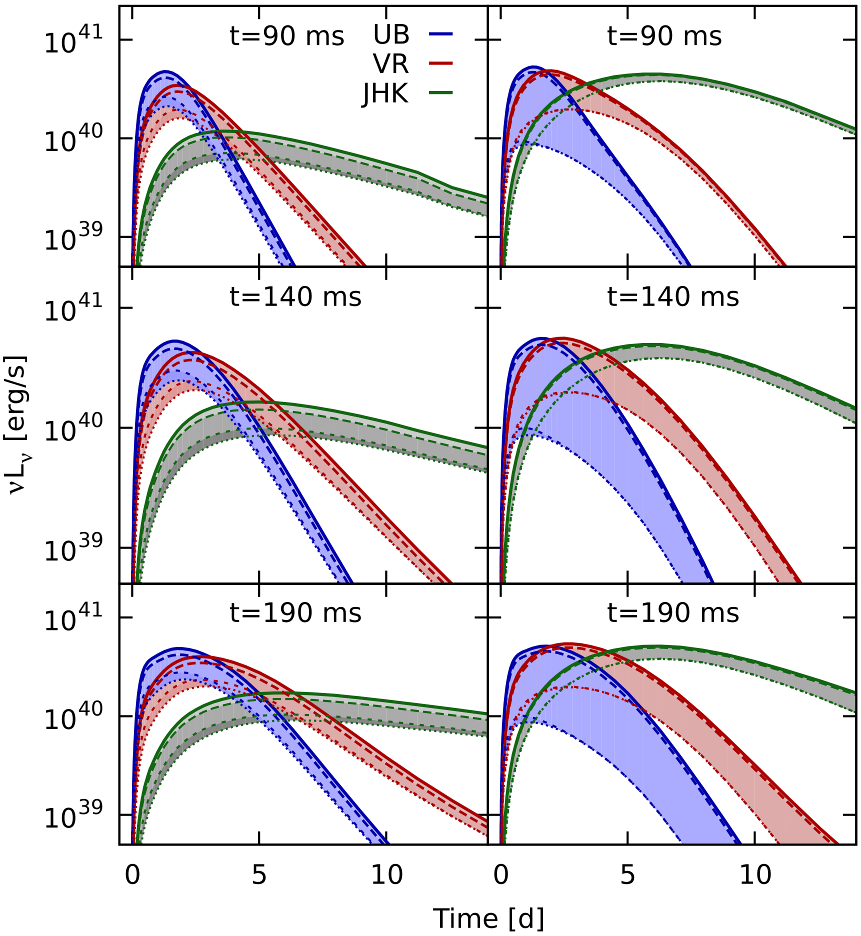

Figure 4.31: Broadband light curves of the wind outflow (left panel) and wind+dynamic ejecta (right panel), showing the combined blue (U+V bands), red (V+R) and infrared (J+H+K) contributions. The top, middle and bottom rows show the three cases of MNS collapse times: 90 ms, 140 ms, and 190 ms, respectively. The range for each light curve spans possible inclination angles of the system axis with respect to the observer: $0°$ (solid) – view from the top, $30°$ (dashed), $60°$ (short dashes) and $90°$ (dotted) – view "edge-on".

5 Nuclear physics uncertainties

When it comes to the nuclear physics input for the r-process, one relies on global predictions of nuclear properties [36, 138, 140, 232]. Among all nuclear physics quantities, the contribution of nuclear masses is crucial, since they enter into the calculations of a variety of relevant nuclear physics quantities, e.g., half-lives [233], gamma strength functions [234], and delayed neutron emission probabilities [171]. Hence, nuclear masses and the mass differences ultimately determine the nuclear reaction rates. Together with the astrophysical conditions, they shape the final observables, such as the elemental abundances.

In this chapter, we first summarize established procedures to give an overview of what has been done so far. Then, we explain our methodology, sketch the schematic characteristics of the mass models, and finally discuss our implications for the r-process nucleosynthesis. Part of the content of this chapter is published in Martin et al. (2016) [142] as a result of the project worked out together with Almudena Arcones, Witold Nazarewicz, and Erik Olsen.

5.1 From nuclear masses to astrophysical uncertainties

To disentangle the imprints of the astrophysical scenario and the fundamental nuclear properties, a common strategy is to consider a specific astrophysical environment and vary the nuclear physics input. This can be done in various ways, differing in their justifications, advantages, and shortcomings. All methods have in common that the uncertainties of the nuclear physics are translated into the uncertainties of an astrophysical observable.

The impact of the nuclear physics input on the heaviest elements has already been investigated in classical r-process studies [28] as well as with parametric dynamical calculations [235, 236]. While many works focused on reproducing the solar abundance pattern [24], some of them began to examine specific aspects, for example the imprint of different mass models [237, 238], the importance of beta decays [239], or effects of neutron captures during the decays to stability [33, 240]. Comprehensive dynamical r-process calculations confirm that the r-process abundances are sensitive to nuclear masses in particular (e.g., Refs. [138, 140, 232]).

One approach is to calculate the reaction rates for whole mass models. Figure 5.1 compares the predicted masses from several distinct models [241–245] to the measured ones [246, 247] for the example of the tin isotopes chain ($Z = 50$). We normalize all masses to the corresponding prediction of the model FRDM1995 [164]. Close to the valley of stability, where the masses of isotopes are well-known, all theoretical models deviate from the experimental masses less than about 1 MeV. However, as the isotopes get more neutron-rich, the predicted theoretical masses tend to differ tremendously. Note that the mass models do not necessarily diverge. In fact, the uncertainties for the extrapolation of masses to very neutron-rich nuclei are without doubt extremely large. Therefore, the (undetermined) error bands for the various mass models can overlap, even though the average trends exhibit a different qualitative behavior. We can take the above mass models, compute the corresponding reaction rates for neutron captures and photodissociation, and thus study the impact of nuclear masses by comparing the results due to the different mass models. In contrast to the MC approach, the uncertainties in the final abundances are consistently determined with respect to the properties of one mass model. This allows to relate features of the abundance pattern to the shape of the respective mass surface [138, 139]. Nevertheless, it is difficult to quantify uncertainties, since the predicted masses from different mass models do not obey the same systematics.

As an example, we show the resulting r-process abundances for a typical trajectory from a Newtonian simulation of the dynamic ejecta during a neutron star merger event (see Sect. 4.1), when employing the mass models of Fig. 5.1. As these neutron-rich ejecta are known to robustly produce the r-process [13], we expect variations among the final abundances to only originate from the distinct mass models. This is similar to the work of Ref. [140], although we use a simpler fission treatment. The results are shown in Fig. 5.2. Due to effective fission cycling, the abundances around the second r-process peak are produced in basically the same amounts in all cases. Details of the nuclear mass surface play a critical role around the third r-process peak.

Another approach to propagate uncertainties from the nuclear input to the final abundances is Monte Carlo (MC) variations (see Ref. [232] for a more detailed review). Starting from one particular mass model, the rates for beta decays, neutron captures, and thus photodissociations can be calculated, utilizing probability distributions that are derived from theoretical uncertainties. This strategy also allows to perform sensitivity studies, identifying

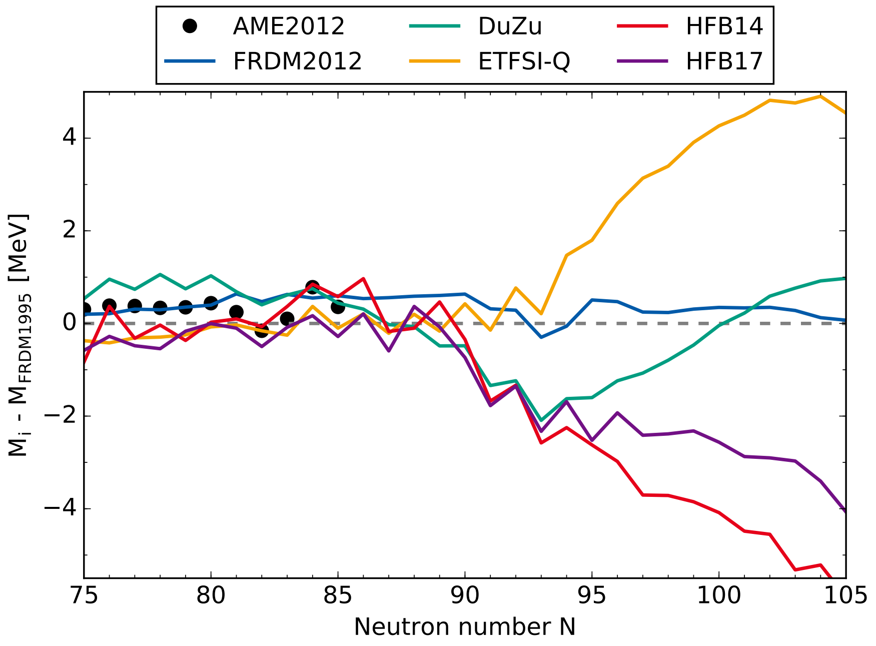

Figure 5.1: Comparison of measured and predicted masses for the tin isotope chain ($Z = 50$). The masses of the atomic mass evaluation (AME2012) [246, 247] are shown together with the values for the theoretical mass models FRDM2012 [241], Duflo-Zuker [242], ETFSI-Q [243], HFB14 [244], and HFB17 [245]. All masses are normalized to the ones of FRDM1995 [164].

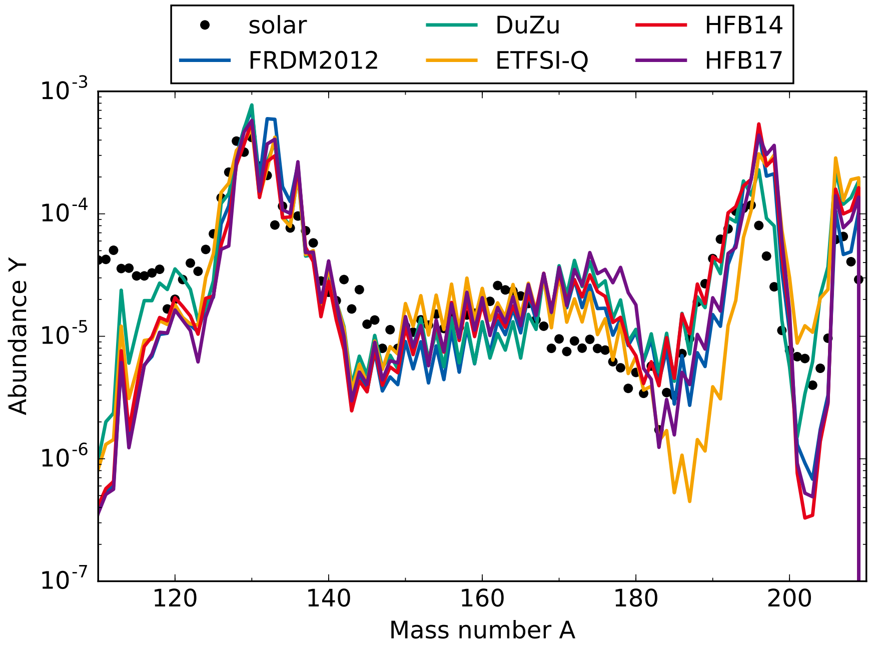

Figure 5.2: Final abundances for calculations with different mass models. For every model, we recalculate the neutron capture and photodissociation rates. The mass models are the same as in Fig. 5.1.

key reactions or key nuclei to be measured experimentally [248]. We note that MC studies bear the possibility for an inverse treatment of the r-process. If the nuclear masses are varied with the aim of reproducing the r-process abundance pattern, then it is (in theory) feasible to infer the necessary nuclear properties. However, the authors of Ref. [31] show that there is no unambiguous solution already for the rare earth peak, if both the measured masses and the abundances in the rare earth region are used as constraints.

5.2 Rates based on masses from DFT models

This section deals with our new approach to determine uncertainties for the r-process abundances from different parameterizations of one mass model. Therefore, we briefly introduce the results of Ref. [20], on which our method is based. Afterwards, we elaborate on our procedure to compute reaction rates and argue how beta decays and fission affect our results.

5.2.1 The nuclear landscape

There are only about 300 nuclei in the nuclear chart that are stable or have at least half-lives exceeding the expected life time of the solar system. This set of nuclei shapes the already mentioned valley of stability in the nuclear landscape. As one adds nucleons to move away from this valley, any resulting nucleus eventually decays by predominantly beta decay, alpha decay, or fission. A nucleus is considered bound if its binding energy is positive. Thus, the boundaries of the nuclear landscape are defined by the drip lines, where the vanishing nuclear binding energy forbids the existence of nuclei beyond this limit. In total, roughly 3200 nuclei are known [19], but new ones are discovered every year. Experimentally, there has been impressive progress in approaching r-process nuclei (see Refs. [249–255], and references therein). New-generation radioactive ion beam facilities [256–258] will be able to reach a range of nuclei never possible before, including the neutron-rich frontier of the nuclear landscape. Nevertheless, a large portion of the nuclear chart is not accessible by experiments yet.

Theoretically, there have been major advances in nuclear modeling, greatly facilitated by high-performance computing [259–264]. A microscopic tool that is well suited to provide quantified microphysics anywhere on the nuclear chart is the nuclear density functional theory (DFT) [265] based on an energy density functional (EDF) representing the density-dependent effective nuclear interaction. This approach is capable of predicting a variety of observables needed and is able to assess the uncertainties on those observables, both statistical and systematic [266, 267]. Such a capability is essential in the context of making extrapolations into the regions where experiments are impossible [20, 267–269].

Utilizing DFT, the authors of Ref. [20] virtually paved the way to explore the limits of stability. As the coupling constants for nuclear EDFs cannot be derived from first principles, they are typically adjusted to selected sets of experimental data. In Ref. [20], a quasi-local Skyrme EDF with 14 coupling constants is used, which is optimized according to six distinct protocols. The functional SKM* has a focus on surface energy of the liquid drop model and fission barriers [270]. Another variation, the SKP, aims at the simultaneous description of the mean field and pairing effects at the same time [271]. SLy4 exhibits a bias on neutron-rich nuclei and properties of neutron matter [272]. In contrast, SV-min is adjusted to a variety of data on spherical nuclei, including diffraction radii and surface thickness [273]. The functional UNEDF0 considers data on spherical and deformed nuclei [274]. Being closely related to UNEDF0, the functional UNEDF1 also takes into account excitation energies of fission isomers [275]. Combining the predictions from these very different optimization emphases allows to determine systematic uncertainties. The masses of even-even nuclei were computed for all six different EDFs, in order to carry out extrapolations toward the two-neutron drip line. As shown in Fig. 5.3, the agreement of the predicted two-neutron separation energies is good close to stability. However, the discrepancy grows as nuclei get more neutron-rich. In the illustrated case of the erbium isotopes ($Z = 68$), the two-neutron drip line is predicted with a systematical uncertainty of $\Delta N = 8$. For comparison, the statistical errors (represented by the uncertainties for the coupling constants of SV-min), lie well within the band spanned by the systematic uncertainties. This technique can be extended over all isotope chains to give an estimate for the number and properties of bound nuclei. Overall, 7000 nuclei are predicted to exist within the range set by proton drip line and neutron drip line.

5.2.2 Statistical calculations

We use the masses obtained from the six sets of EDF parameterizations to determine the reaction rates for neutron captures and photodissociations (for the corresponding mass tables, see Ref. [276]). But before actually computing the reaction rates, it is important to note that theoretical predictions for the mass surface usually yield the masses of even-even nuclei only. Consequently, the theoretically predicted masses need to be extended to the nuclei whose masses were not calculated. The masses of odd-A and odd-odd nuclides were interpolated by adding average pairing gaps to the binding energy of the corresponding zero-quasiparticle vacuum obtained by averaging binding energies of even-even neighbors (cf., supplemental material of Ref. [20]). Figure 5.4 shows the idea of this

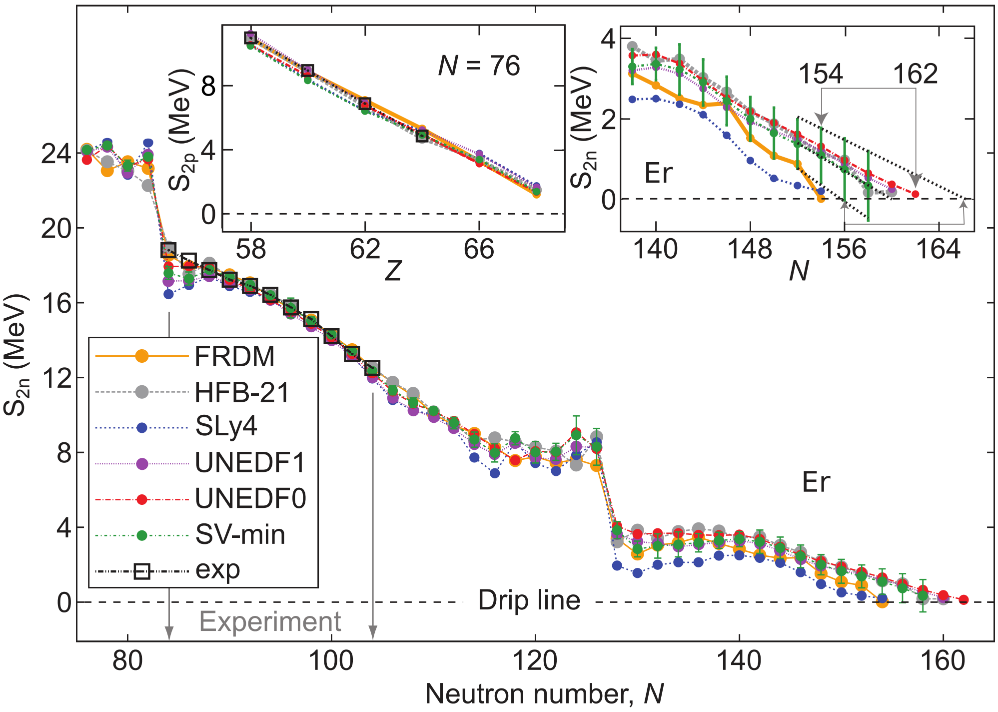

Figure 5.3: Two-neutron separation energies of the erbium isotopes ($Z = 68$). The position and uncertainty (two-)neutron drip line are estimated by utilizing the predictions of the Skyrme EDFs. For comparison, the values determined with two different models, FRDM and HFB-21, are shown. Taken from Ref. [20].

interpolation routine. Black boxes mark the already known even-even nuclei. The remaining colored rectangles indicate the nuclear properties that we use for calculating their masses, listed in the following equations:

$$\mathrm{BE}(Z,N-1) = \frac{1}{2}\left[\mathrm{BE}(Z,N)+\mathrm{BE}(Z,N-2)\right]+\frac{1}{2}\left[\Delta_{\mathrm{n}}(Z,N)+\Delta_{\mathrm{n}}(Z,N-2)\right], \tag{5.1}$$

$$\mathrm{BE}(Z-1,N) = \frac{1}{2}\left[\mathrm{BE}(Z,N)+\mathrm{BE}(Z-2,N)\right]+\frac{1}{2}\left[\Delta_{\mathrm{p}}(Z,N)+\Delta_{\mathrm{p}}(Z-2,N)\right], \tag{5.2}$$

$$\begin{aligned}\mathrm{BE}(Z-1,N-1) &= \frac{1}{2}\left[\mathrm{BE}(Z,N-1)+\mathrm{BE}(Z-2,N-1)+\Delta_{\mathrm{p}}(Z,N-1)+\Delta_{\mathrm{p}}(Z-2,N-1)\right]\\ &= \frac{1}{2}\left[\mathrm{BE}(Z-1,N)+\mathrm{BE}(Z-1,N-2)+\Delta_{\mathrm{n}}(Z-1,N)+\Delta_{\mathrm{n}}(Z-1,N-2)\right]\\ &= \frac{1}{4}\left[\mathrm{BE}(Z,N)+\mathrm{BE}(Z,N-2)+\mathrm{BE}(Z-2,N)+\mathrm{BE}(Z-2,N-2)\right.\\ &\quad +\Delta_{\mathrm{n}}(Z,N)+\Delta_{\mathrm{n}}(Z,N-2)+\Delta_{\mathrm{n}}(Z-2,N)+\Delta_{\mathrm{n}}(Z-2,N-2)\\ &\quad \left.+\Delta_{\mathrm{p}}(Z,N)+\Delta_{\mathrm{p}}(Z,N-2)+\Delta_{\mathrm{p}}(Z-2,N)+\Delta_{\mathrm{p}}(Z-2,N-2)\right],\end{aligned} \tag{5.3}$$

The binding energies of nuclei marked in blue are computed as the averaged binding energies and neutron pairing gaps of the adjacent isotopes. Analogously, we obtain the binding energies for nuclei in red via the averaged binding energies and proton pairing gaps of the neighboring isotones. The binding energies of odd-odd nuclei are derived from the respective average of all four even-even nuclides nearby. From the binding energy, we get the (atomic) mass of the nuclei in a straightforward way:

$$m(Z,N) = Zm_{\mathrm{p}}+Nm_{\mathrm{n}}+Zm_{\mathrm{e}}-\mathrm{BE}(Z,N). \tag{5.4}$$

Next, we determine astrophysical reaction cross section given by Eq. (3.6). For each EDF model, we compute Maxwellian-averaged (n,γ) cross sections in the framework of the statistical model [277] using the TALYS code [166] with standard input (apart from the masses, which have to be given in atomic mass units). This model relies on the assumption of a thermodynamic equilibrium in combination with compound nucleus reactions for excited

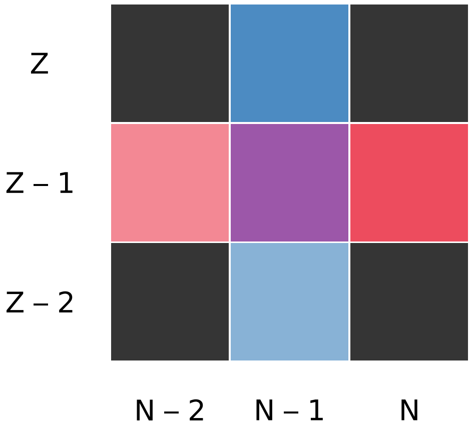

Figure 5.4: Interpolation scheme for the binding energies of odd-A and odd-odd isotopes. The binding energies of blue (red) odd-A nuclei are determined by adding the averages of the binding energies and neutron (proton) pairing gaps of the adjacent even-even isotopes (isotones). For odd-odd nuclei, the same method is used, but with all four neighboring even-even nuclei.

states. The respective neutron capture rates are $N_\mathrm{A}\,\langle\sigma v\rangle_{(\mathrm{n},\gamma)}$. Photodissociation rates are derived from detailed balance with partition functions that are consistently obtained from the statistical model:

$$\begin{aligned}\lambda_{(\gamma,\mathrm{n})}\Big|_{(Z,A+1)} = &\frac{2\left(2I_{(Z,A)}+1\right)}{\left(2I_{(Z,A+1)}+1\right)}\frac{G(Z,A)}{G(Z,A+1)}\left(\frac{A}{A+1}\right)^{3/2}\\ &\times\left(\frac{m_\mathrm{u}c^2k_\mathrm{B}T}{2\pi\hbar^2c^2}\right)^{3/2}\langle\sigma v\rangle_{(\mathrm{n},\gamma)}\Big|_{(Z,A)}\exp\left(-\frac{S_\mathrm{n}}{k_\mathrm{B}T}\right),\end{aligned} \tag{5.5}$$

where the atomic number Z and the mass number A on the complete right hand side are the ones for the isotope whose neutron capture rate is used.

5.2.3 Beta decays and fission

Apart from neutron captures and photodissociations, several other kinds of reactions take place during the r-process. The next order contributions stem from beta decays and fission. In principle, beta decay rates as well as various modes of fission rates (for spontaneous, neutron-induced, and beta-induced fission), need to be calculated consistently from the nuclear masses. Furthermore, the unknown fission fragment distribution adds another layer of complexity. Here, we argue that the influence of both these reaction classes are subdominant, although important to understand the detailed imprints of nuclear properties on the final r-process abundances.

The impact of beta decays on the abundances has been shown to be moderate [249, 250, 252, 278]. The beta decay rate depends on the nuclear mass model, as it is proportional to Q^5, where Q is the Q-value of the beta decay. However, beta decay rates are not expected to dramatically change when varying mass models as compared to photodissociation reaction rates, which involve an exponential dependence on the separation energy S_n (see Eq. (5.5)). As the neutron capture rates are (assumed to be) in detailed balance with the photodissociation rates, their values can also vary significantly. Additionally, different studies (see, e.g., Ref. [137]) found that increased beta decay rates affect the final abundances, but not as much as (n,γ) and (γ,n) reactions when considering different mass models. Nevertheless, beta decays and beta-delayed neutron emission are important at waiting point nuclei once the $(\mathrm{n},\gamma)-(\gamma,\mathrm{n})$ equilibrium has been established. Faster beta decays lead to to an accelerated evolution after freeze-out [137]. This can partly prevent the shift of the third r-process peak ($A\sim 195$) to higher mass numbers.

For fission, we use the same input as in Refs. [13, 149]. This prescription assumes the fission fragments to consist of two daughter nuclei and neutrons only, instead of a distribution [279]. Symmetric fission is assumed to occur for $255 < A < 265$ and an analytic formula is applied to determine asymmetric fission yields otherwise. The neutron capture and neutron-induced fission rates are taken from Ref. [173], while the beta-delayed fission of Ref. [35] is used. Therefore, fission barriers and yield distributions are not consistent with the underlying mass model. Note, however, that the majority of models of fission yields currently used in r-process simulations are based on a simplistic barrier penetration approach that employs a notion of the static fission barrier. As this approach ignores collective dynamics, current fission models are prone to errors that exceed uncertainties related to the assumed input (mass models); see the discussion in Ref. [280]. Fission has a significant influence on the r-process nucleosynthesis for very neutron-rich environments such as neutron star mergers. We illustrate this in Fig. 5.5 for different fission models. The model of Panov is the one that we use throughout this work, releasing neutrons if a daughter nucleus lies beyond the neutron drip line [279]. The Kodama-Takahashi model uses Gaussian distributions for the daughter nuclei, but does not release fission neutrons [281]. Finally, the model ABLA07 is the most sophisticated, but also the computationally most expensive fission scheme [282]. ABLA07 incorporates detailed microphysics and matches experimental results for the fragment distributions and the number of released neutrons very well. The fission barriers and yield distributions affect the abundances especially in the mass region around the second peak, especially in the mass region around the second peak [13, 36, 137, 283]. Consequently, in the results presented below, the impact of mass uncertainties on this region should be taken with caution, while for the third r-process peak our conclusions are robust.

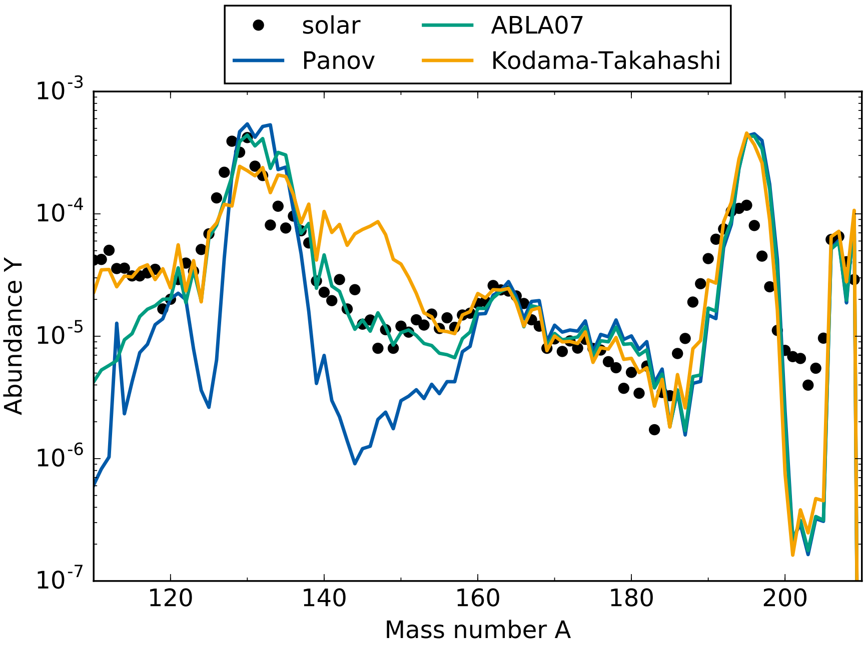

Figure 5.5: Final abundances according to different fission treatments. The individual fission models lead to considerably different abundance patterns around the second r-process peak, while having no major impact on the third peak.

5.3 Schematic r-process path

It is instructive to establish an overview of the qualitative characteristics to expect. The r-process runs along the nuclear chart on a path that is shaped mainly by a $(n,\gamma)-(\gamma,n)$ equilibrium. To show this fact, we compute the average timescales

$$\langle\tau_x\rangle = \frac{1}{\langle\lambda_x\rangle} = \frac{\sum_{(Z,A)} \lambda_x(Z,A)}{\sum_{(Z,A)} \lambda_x(Z,A)\,Y(Z,A)}, \tag{5.6}$$

where the sums over Z and A include all rates for reactions of the kind x. Figure 5.6 illustrates the timescales for neutron captures, photodissociations, and beta decays. Plotted are the temporal evolutions in nucleosynthesis calculations for neutron star mergers (right hand side) and jetlike supernovae (left hand side). Clearly, an $(n,\gamma)-(\gamma,n)$ equilibrium is achieved in both astrophysical scenarios considered here. The overlap of the corresponding curves demonstrates how this equilibrium is maintained until freeze-out. Close to the neutron drip line, beta decays are suppressed initially. Nevertheless, they are important for the abundances to proceed to higher atomic numbers. This is especially true at neutron shell closures, where a quasi-$(n,\gamma)-(\gamma,n)$ equilibrium is maintained, because the neutron separation energy vanishes quickly for the next isotope with a non-magic neutron number. When the temperature drops, photodissociation becomes negligible, suffering from the exponential dependence on the negative inverse of the temperature. Thus, there is a competition between beta decays and neutron captures after freeze-out (marked by the dashed red line in Fig. 5.6). We restrict the further discussion on the time of freeze-out, when the temperatures are just high enough to support an $(n,\gamma)-(\gamma,n)$ equilibrium.

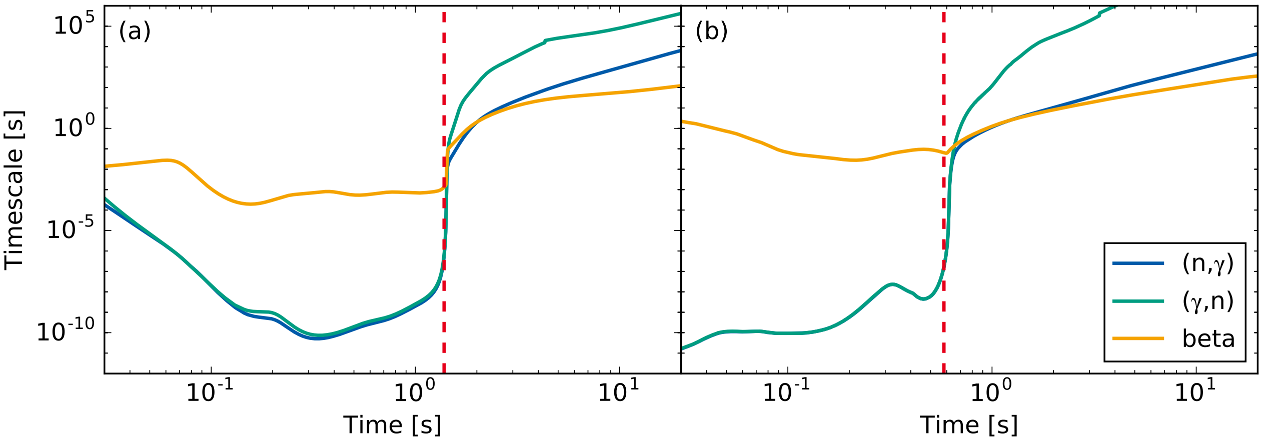

Figure 5.6: Average timescales of neutron captures, photodissociations and beta decays for neutron star mergers (left panel) and jet-like supernovae (right panel). (n,γ) and (γ,n) reactions are in equilibrium up to freeze-out (vertical dashed lines), as indicated by the overlap of the average timescales for these kinds of reactions.

During $(n,\gamma)-(\gamma,n)$ equilibrium, the flux of abundances is very sensitive on the properties of the involved nuclei. We consider two extreme cases of mass models to explain the formation of characteristic troughs in the abundance distribution. In order to illustrate the behavior of the freeze-out abundances before $N = 126$, the left panel of Fig. 5.7 shows half the (two-)neutron separation energy $S_{2n}/2$ for SLy4 and UNEDF0 in the region where the third r-process peak forms. Far from stability, the r-process path stays at an almost constant neutron separation energy during the (n,γ)—(γ,n) equilibrium. This value is marked in Figs. 5.7(a) and 5.7(b) by the dashed line at a representative value of $S_{2n}/2 = 1.5\,\mathrm{MeV}$. Note that the explanation here is valid for any (n,γ)—(γ,n) equilibrium in general, but inspired by the values found in our calculations (cf., Fig. 5.10 later on). When matter approaches this limit, it stays there until a beta decay occurs. Afterwards, more neutron captures are possible until the separation energy reaches this limit again. Figure 5.7(a) shows that for SLy4 the nonmonotonic behavior of S_{2n} leads to a long sequence of neutron captures at a fixed Z value, until reaching the magic neutron number $N = 126$. Hence, it results in a trough in the abundances versus mass number. In the case of UNEDF0, on the other hand, after a beta decay, the (n,γ)—(γ,n)-equilibrium value of S_{2n} is reached again after only a few neutron captures. The nonmonotonic behavior of neutron separation energies can be traced back to structural changes due to rapid shape transitions from prolate to spherical to oblate. While the global deformation patterns predicted by various EDFs are fairly similar [20], the subtle details of shape transitions are predicted differently. This is illustrated in Figs. 5.7(c) and 5.7(d) for SLy4 and UNEDF0, respectively.

5.4 The impact of nuclear masses

The neutron capture and photodissociation rates based on Skyrme DFT masses [20] have been used to calculate final abundances for the r-process nucleosynthesis. In the reaction network, all (γ,n) and (n,γ) rates are replaced by new ones based on individual EDF parameterizations. Here, we present the impact of systematic uncertainties on nuclear masses for the two most promising astrophysical r-process scenarios: neutron star mergers [13] and jetlike supernovae [81]. The systematic (model) uncertainties are estimated by considering all six EDFs. The corresponding systematic error thus represents the root-mean-squared spread of predictions of different EDF parameterizations obtained by means of diverse fitting protocols. In the absence of the exact reference model, such an intermodel deviation should be viewed as a rough approximation to the systematic error. A similar strategy was employed to estimate the position of neutron and proton drip lines [20, 284], to study the landscape of two-proton radioactivity [285, 286], and to assess neutron-skin uncertainties [269]. This approach is complementary to vary-

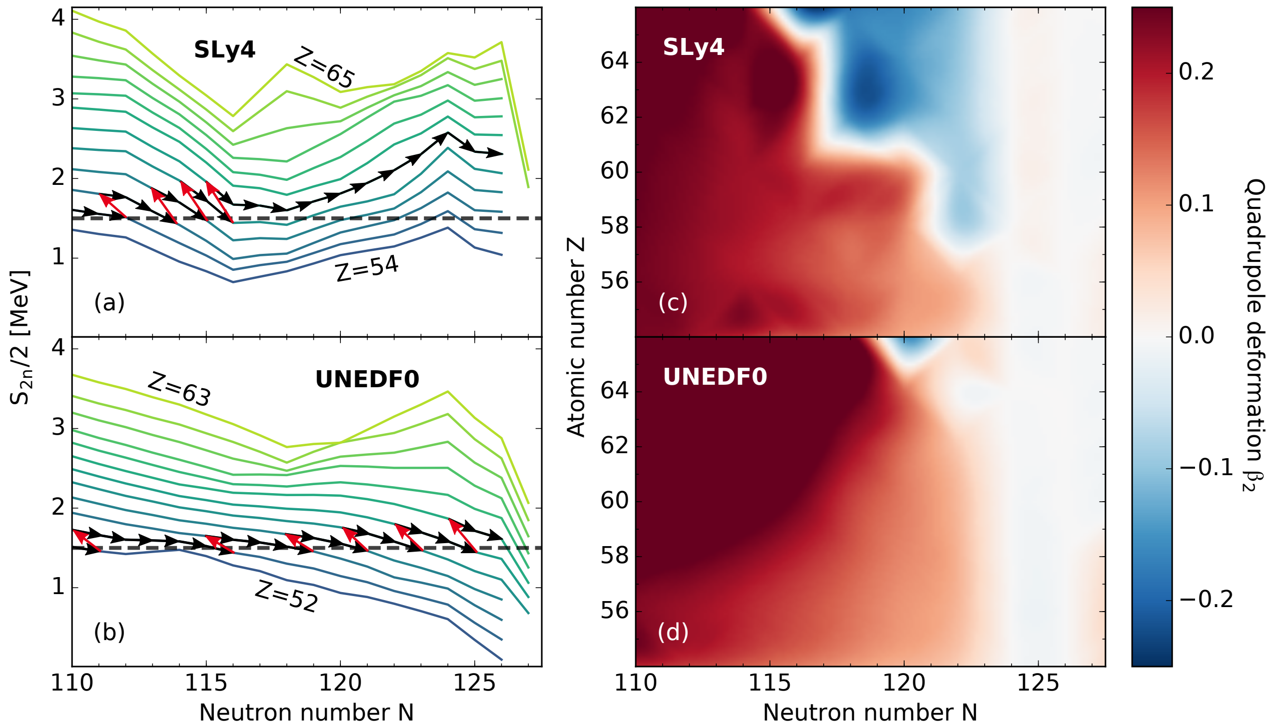

Figure 5.7: Left: Half the two-neutron separation energies predicted by the models SLy4 (a) and UNEDF0 (b) versus the neutron number in the region where the third r-process peak forms. The dashed line marks the approximate r-process path during (n,γ)—(γ,n) equilibrium ($S_{2n}/2 = 1.5$ MeV). Black arrows indicate neutron captures; red arrows mark beta decays along the path. Right: The corresponding quadrupole deformations β_2 for SLy4 (c) and UNEDF0 (d).

ing individual masses within some assumed error bars [141, 232] or considering mass models and mass formulas based on vastly different physical approaches [138, 140, 287].

The various EDFs lead to different abundances; this variation is expected given their different optimization schemes. Therefore, when the six mass sets are considered, we obtain a systematic uncertainty band for the r-process abundances as shown in Fig. 5.8. The solar system r-process abundances do not always lie within the uncertainty band. This indicates that improvements in nuclear physics and astrophysical inputs are still necessary. However, important hints for future developments are offered by inspecting our uncertainty estimates. For example, the uncertainty band is not uniform but strongly depends on the mass number. This is in contrast to the sensitivity studies summarized in Ref. [141]. Therein, they find a broad and homogeneous uncertainty band for all mass numbers as a consequence of randomly varying individual masses within the same range. In our work, mass variations are correlated through the microscopic framework employed. The mass dependence can be seen in the abundances for neutron star mergers in Fig. 5.8(a) where the uncertainty band is narrow for the second r-process peak ($A \sim 130$) and broadens up before the third peak ($A \sim 195$). The second peak gets its major contribution from fission [13, 137]. Since in this pilot study we are using the same fission barrier and yield distribution data for the six mass sets, only small variations are expected in this region. In contrast, the evolution of nuclear masses as a function of the neutron number critically impacts the abundances around shell closures when nuclei change character from deformed to spherical and back to deformed again. This occurs around neutron magic numbers where the abundance peaks form, thus leading to a broad uncertainty band. Since fission plays a minor role for jetlike supernovae in Fig. 5.8(b), the uncertainty band is broader than in the case of neutron star mergers before and after the second r-process peak.

Observations typically yield the abundances for individual elements only. We compare the elemental abundances found in our calculations with the abundances of the r-process enriched metal-poor star CS22892-052 [226] in Fig. 5.9. Since it is unknown, by which amounts of r-process material this star was enriched, we arbitrarily normalize the elemental abundances to europium ($Z = 63$). The abundances found for neutron star mergers agree quite well, but tend to overpredict the observed abundances. The pattern for jetlike supernovae describes the qualitative trend a bit better, particularly for $60 \lesssim Z \lesssim 70$. However, the values for elements with heavier atomic numbers are slightly underpredicted. As the observed abundances are in accordance with both predictions

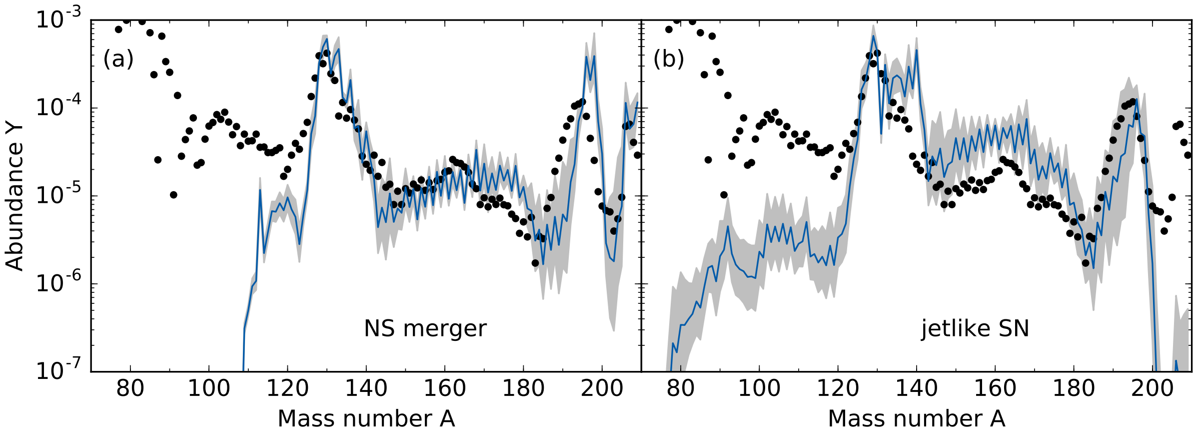

Figure 5.8: Predicted abundance distributions for neutron star mergers (a) and jetlike supernovae (b). Dots indicate the Solar System r-process abundances. The systematic uncertainties (gray bands) are due to variations of the masses predicted in the six Skyrme-DFT models of Ref. [20]. The mean predicted abundances are marked by the solid line.

when considering the uncertainty bands, the unambiguous identification of the main r-process site is difficult by this measure.

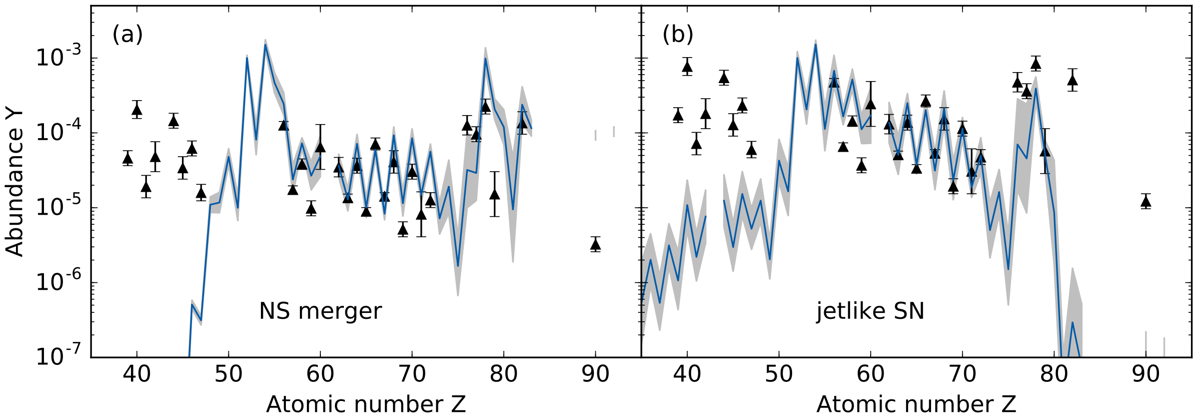

Figure 5.9: Final abundances vs. atomic number Z. This figure shows the same distribution as Fig. 5.8, however the elemental abundances are normalized to Eu ($Z = 63$) and compared to the r-process observed in the old, metal-poor star CS22892-052 [226]. The unambiguous identification of the main r-process site remains challenging.

5.4.1 Neutron star mergers

In order to better understand the impact of nuclear masses on the predicted abundances, in Fig. 5.10 (bottom panels) we analyze the trend of two-neutron separation energies S_{2n} for the models SkM*, SLy4, and UNEDF0 in the upper part, as well as for the models SkP, SV-min, and UNEDF1 in the lower part. The red dots indicate the r-process path at freeze-out, i.e., the mass number with the highest abundance for every isotopic chain. Due to fission, some of the freeze-out maxima lie below the imaginary horizontal line spanned by the maximum abundances between the second and third r-process peaks (cf., Fig. 5.7). At r-process freeze-out, most of the neutrons are consumed, and neutron-rich material starts to decay to stability. The abundances at freeze-out are marked by thin red lines in the upper panels, while the final abundances, following beta decays back to the valley of stability, are indicated by thick black lines. The most remarkable features are the rapid variations of separation energies of neutron-rich nuclei for $A \approx 120-140$ and $A \approx 180-200$, associated with the neutron magic numbers $N = 82$ and $N = 126$, respectively. Moreover, one can identify the formation of peaks shown in the freeze-out abundances with the regions where matter accumulates. The third r-process peak at freeze-out is located at smaller mass numbers

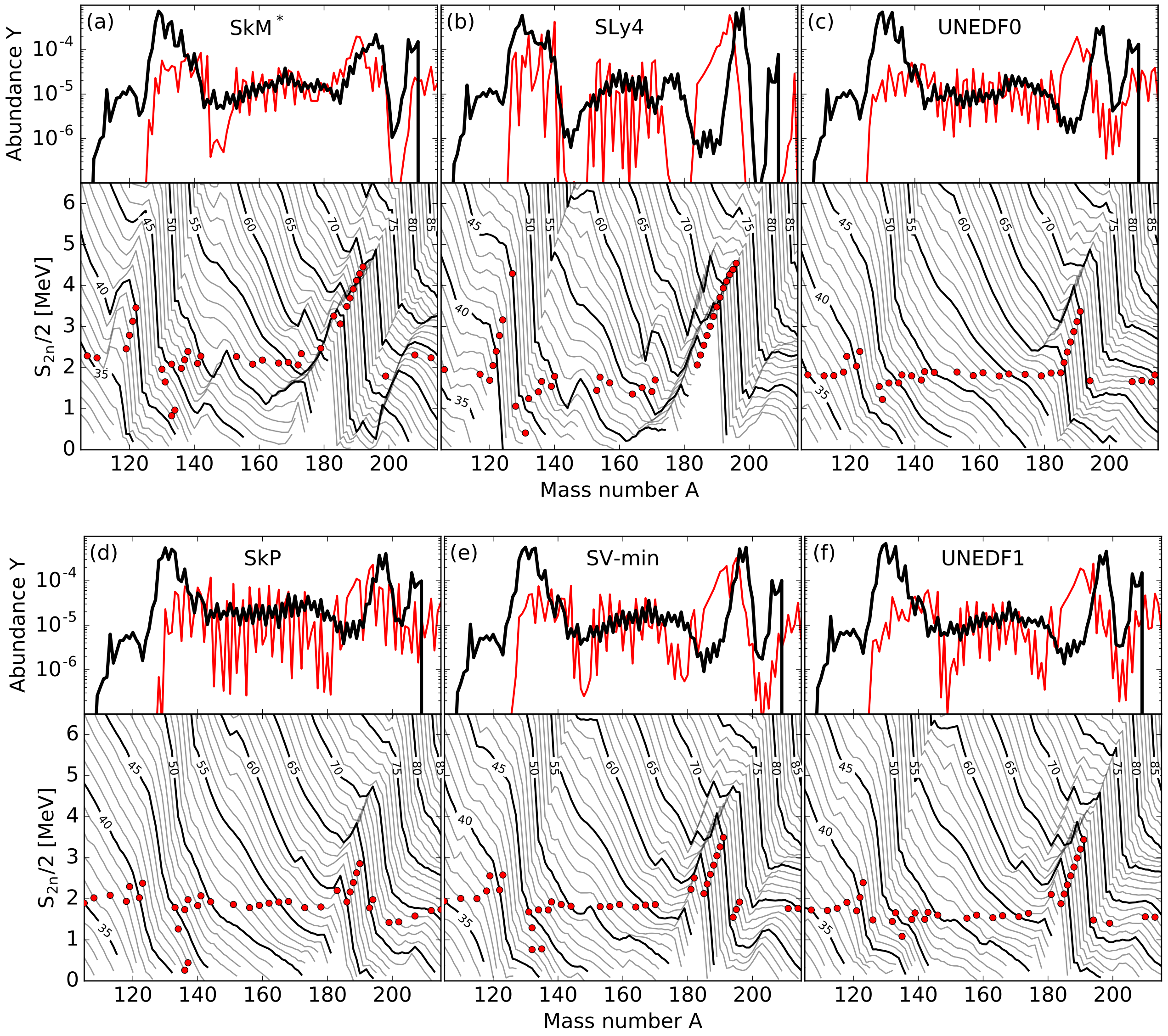

Figure 5.10: Nucleosynthesis predictions for the six EDF parametrizations in neutron star mergers. Top row: (a) SkM*, (b) SLy4, and (c) UNEDF0. Bottom row: (d) SkP, (e) SV-min, and (f) UNEDF1. Bottom panels: (Half the) two-neutron separation energies along different isotopic chains (gray lines); every fifth isotope chain is plotted with black lines. The red dots correspond to the freeze-out abundances, i.e., the r-process path before matter starts to decay to stability. A few dots around $A \sim 135$ lie below the separation energy that is expected from (n,γ)—(γ,n) equilibrium. Here, fission of nuclei with $A > 240$ populates regions beyond the r-process path. Top panels: The freeze-out (thin red lines) and final (thick black lines) abundances for a neutron star merger scenario.

than in the final abundances, pointing to some important reactions occurring during the decay to stability. Beta decays keep the mass number constant or reduce it in the case of beta-delayed neutron emission (which can be significant, as it increases the number of neutrons). This deviation indicates that the shift of the third peak is due to neutron captures [138, 240]. Neutrons are thus critical in understanding both the evolution toward stability and the final abundances. In addition to the few leftover neutrons after freeze-out, there are also contributions from beta-delayed neutron emission and fission. In the case of neutron star mergers [137], there are many neutrons produced in fission and this leads to a more pronounced shift of the third peak than in the jetlike supernovae (see Fig. 5.8).

The results shown in Fig. 5.10 were obtained using EDFs developed using different protocols. Hence, it is possible to relate their optimization focuses to the features found in the (two-)neutron separation energy. The functional SkM* [270] is the traditional Skyrme EDF fitted to binding energies and charge radii of selected spherical nuclei, spin-orbit splitting in ^{16}O, giant resonance energies in ^{208}Pb, and fission barriers. We find that the model SkM* leads to the smallest shift of the third peak from freeze-out to final abundances. The functional SLy4 [272] was optimized with a focus on neutron-rich nuclei and neutron matter. In addition to properties of spherical nuclei, this functional was also constrained to basic properties of symmetric nuclear matter and the equation of state for pure neutron matter. For SLy4, the third peak is strongly shifted compared to SkM* already during freeze-out, and there is a big trough in abundances before it. The trough corresponds to the region without dots in the lower panel of Fig. 5.10(b) ($A \sim 180$). The origin of this trough is the nonmonotonic behavior of the separation energy [138, 139] predicted in this model. The behavior of the freeze-out abundances before $N = 126$ is exactly due to the features explained in the left panel of Fig. 5.7. A more recent model UNEDF0 [274] was carefully optimized to a large database including masses of spherical and deformed nuclei, charge radii of spherical nuclei, odd-even mass differences, and selected nuclear matter properties. It features the smoothest trend in the (two-)neutron separation energy surface, when compared to any of the other five parameterizations. Therefore, the freeze-out abundances are on an almost featureless horizontal path (except for the region around the third r-process peak), as seen in the schematic description of Fig. 5.7. In fact, evolution of S_{2n} versus A is so much less steep for $N = 82$ that the shell closure is quenched for very neutron-rich nuclei with $Z \leq 40$; see Fig. 5.8(c). This results in the lack of the second peak in the freeze-out abundances. However, as discussed above, the second peak in the final abundances has its origin in fission. The functional SkP [271] incorporates a mean field description and pairing effects. While it shows a very pronounced odd-even effect for the freeze-out abundances as a function of mass number, the final abundances are remarkably flat between the second and the third r-process peak in particular. The remaining two functionals, SV-MIN [273] and UNEDF1 [275], are tweaked with respect to similar nuclear properties as the model UNEDF0. Thus, these models lead to practically the same freeze-out and final abundances.

All of these models have different performances when it comes to masses. For instance, the older models SkM* and SLy4 yield a large rms deviation from experiment, around and greater than 5 MeV. This can be attributed to an overemphasis on doubly magic nuclei during optimization as well as a fairly limited data set. As discussed in Ref. [274], the functional UNEDF0, with its rms deviation of 1.45 MeV, is probably within a few hundreds of keV of a globally optimal mass fit within the Skyrme EDF parameter space. To put things in perspective, we note that the best overall agreement with experimental masses, obtained with the Skyrme EDF, is around 600 keV [245]. However, this excellent result was obtained at a price of several phenomenological corrections on top of the original Skyrme DFT model.

5.4.2 Jetlike supernovae

The freeze-out abundances and the evolution toward stability to produce the final abundances depend on astrophysical conditions. Thus, we investigate, how the nucleosynthesis results change when turning to a different environment, namely a jetlike supernova for all six mass models. Figure 5.11 shows the same plots as Fig. 5.10 for the six EDF parameterizations, but with the abundances replaced by the ones from the jetlike supernova case. For the jetlike supernova trajectory the freeze-out path is closer to stability (i.e., at higher neutron separation energies). The minor influence of fission is reflected in the missing abundance maxima for rather low (two-)neutron separation energies around $A \sim 130$. Indeed, the freeze-out abundances behave much more like beads on a straight string, being almost perfectly on a line with constant S_{2n} (of course, except for mass numbers in the vicinity of neutron shell closures). The consequences of the reduced effects of fission are twofold. First, the abundances shape the second r-process peak already during the freeze-out, changing only very little until the end of the nucleosynthesis calculations. Second, there are less neutrons available during the decay because of the reduced effect of fission. Accordingly, the major neutron source after the freeze-out is beta-delayed neutron emission. Except for the calculations with one mass model (SLy4), we find that the late-time capture of these neutrons is mild enough to shift the third r-process peak to be still in accordance with the solar abundances. Similar to the neutron star merger case, the model SkM* also leads to the smallest shift of the third peak from freeze-out to final abundances. On the contrary, the nucleosynthesis results for the model SLy4 do not only show basically the same troughs, but the corresponding final abundances exhibit the largest displacement of the third r-process peak. Thus, the final abundances obtained with this model account for virtually the whole width of the uncertainty band in this region, as seen in Fig. 5.8. The abundance patterns are almost alike when using one of the other four models UNEDF0, SkP, SV-min, and UNEDF1. Small variations arise in the magnitude of the third peak and the troughs below the magic neutron numbers.

The features that we have explained before for the neutron star merger affect the abundances of jetlike supernovae differently. Therefore, reducing uncertainties in the nuclear physics input should enable us to use observations to constrain and understand the astrophysical conditions related to the r-process site.

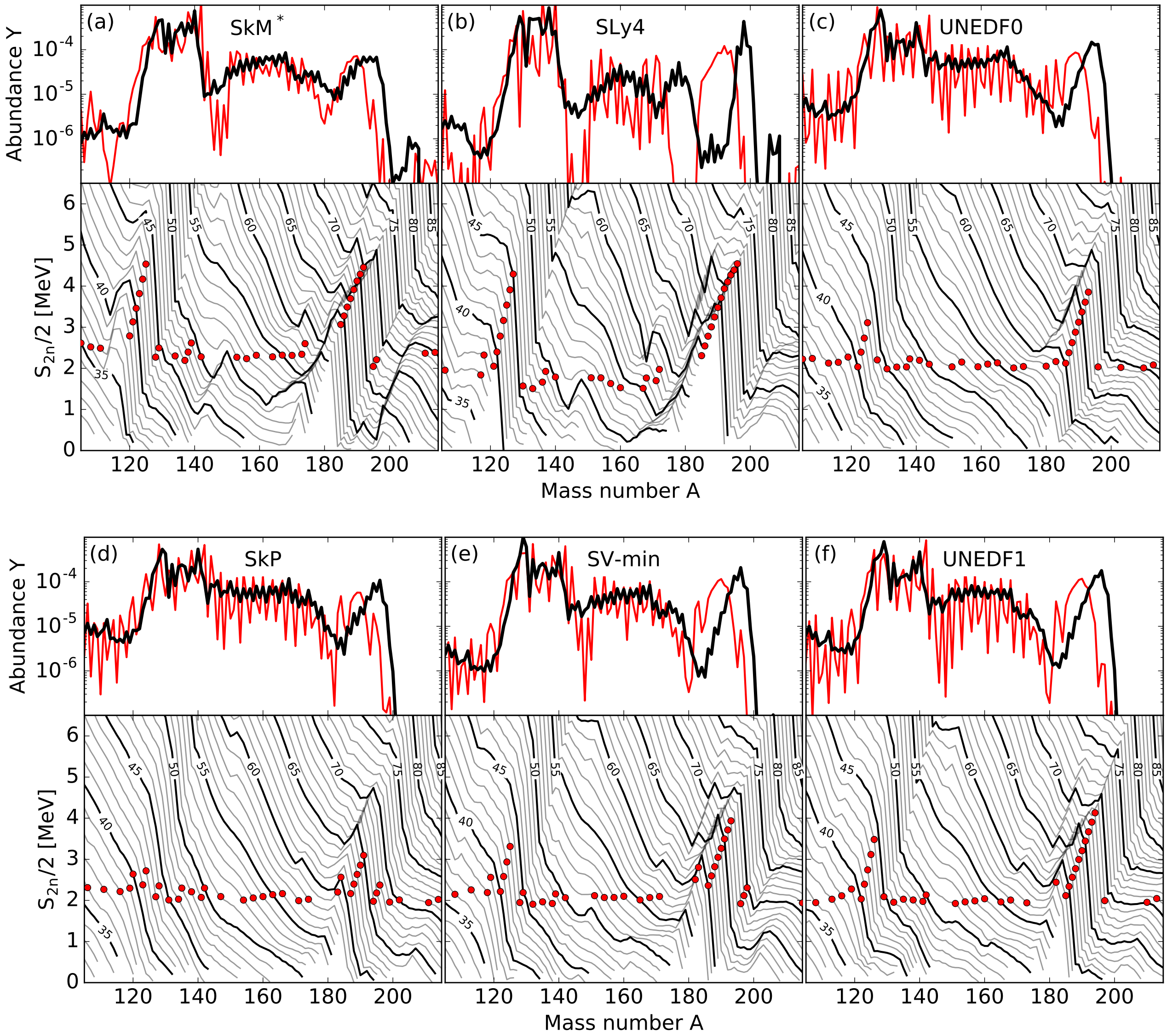

Figure 5.11: Nucleosynthesis predictions for the six EDF parameterizations. Same as Fig. 5.10, but for the jetlike supernova scenario.

5.4.3 On the importance of neutrons

The supply of neutrons is crucial over the whole course of r-process nucleosynthesis. With the exhaustion of most of the neutrons during the r-process freeze-out, the influence of neutron capture reactions does not die off. Quite the contrary is true [33, 34, 138, 232, 240]. In both r-process scenarios considered, the (n,γ) reactions play a significant role for the final abundances. To support this point, we carried out calculations having the (n,γ) reactions disabled after freeze-out. The results are representative for the nucleosynthesis in a jetlike supernova, but are valid likewise for the case of neutron star mergers. However, in the latter case one has to unravel the effects from fission, too. We show the final abundances of this (artificial) scenario in Fig. 5.12 with a blue line. Moreover, we plot the freeze-out abundances (red) and the former final abundances (black) considering the neutron captures during decay to stability. Without these neutron captures, the predominant reactions active are beta decays with and without neutron emission. This means that the abundance can only stay constant as in freeze-out or shift to lower mass number due to delayed neutron emission. This is clearly seen in the blue curve. In contrast, if neutron captures are considered, they shift the freeze-out abundances toward higher A as shown by the black curve. While a mild shift due to late-time neutron captures is inevitable, the incorporation of too many neutrons displaces the third r-process peak beyond its observed position in the solar abundance pattern.

In fact, this displacement is present in all nucleosynthesis calculations of neutron-rich ejecta from a neutron star merger. Surprisingly, it also arises in the r-process yields expected from a jetlike supernova when using the

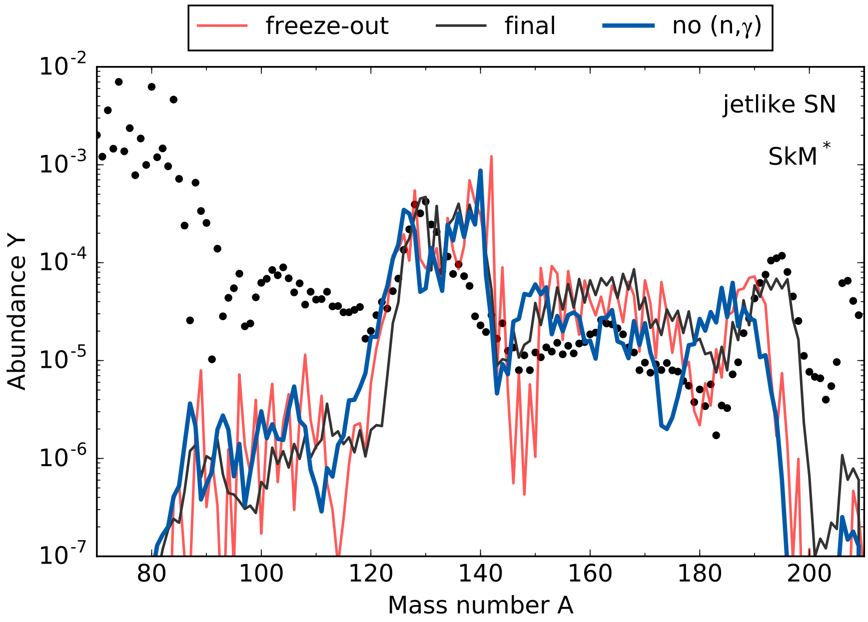

Figure 5.12: Importance of neutron captures after the freeze-out. The red line marks the freeze-out abundances and the gray line the actual final abundances if neutron captures are included at any time. The blue line represents the final abundances in the (artificial) scenario without neutron capture when matter decays to stability, i.e., after freeze-out. The lack of (n,γ) reactions particularly leads to a shift of the third peak due to beta-delayed neutron emission.

nuclear masses predicted by the EDF parameterization SLy4 (see Fig. 5.11). To shed a light on this unique feature, we explore the evolution of the neutron density n_n. Figure 5.13 illustrates the time dependence of the neutron density for all combinations of nuclear physics input and astrophysical scenarios used in our study. Initially, the neutron density starts at high values of $n_\mathrm{n} = (10^{29} - 10^{30})\,\mathrm{cm}^{-3}$, which are typical for r-process hosts. Then, n_n decreases monotonically, but slowly. As soon as the conditions for freeze-out are reached, vast amounts of neutrons are consumed, causing a steep drop over many orders of magnitude. Later on, the neutron density profile flattens out due to beta-delayed neutron emission. This produces new neutrons to be captured, giving rise to at least two effects. On one hand, the odd-even effects are smoothed out. On the other hand, subsequent neutron captures shift the third r-process peak to higher mass numbers. Furthermore, these neutron captures can contribute to the dynamic formation of the rare earth peak [33, 34].

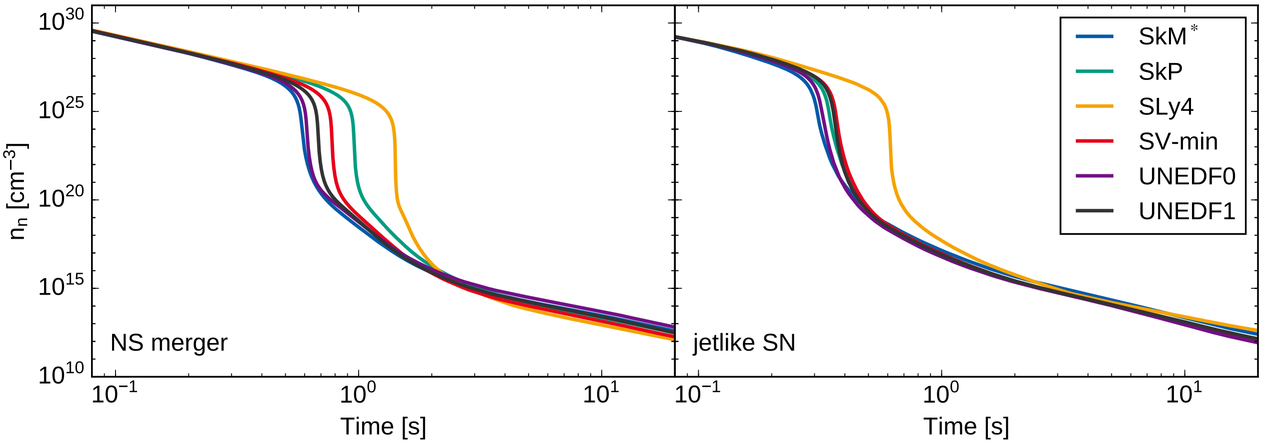

Figure 5.13: Evolution of the neutron density for different mass models and astrophysical sites. Left: time dependence of the neutron density for neutron star mergers in nucleosynthesis calculations based upon each of the six parameterizations of the DFT mass model. Right: neutron density evolutions in the case of the jetlike supernova.

It turns out to be utterly important, when exactly the freeze-out occurs. The earlier most of the neutrons are captured, the smaller the shift of the third peak, compared to the solar abundances. In general, the neutron star merger scenario supports high neutron densities for a longer time. However, we find the neutron densities to stay at a high level similarly long even in the jetlike supernova when performing a nucleosynthesis calculation with the model SLy4.

6 Summary and outlook

In this work, we studied the r-process nucleosynthesis along two lines. Using hydrodynamical conditions from recent astrophysical simulations of neutron star mergers in 3D, we computed for the first time the mass-integrated nucleosynthesis yields of the dynamic ejecta in full GR and of the neutrino-driven wind [149]. Toward the microphysics, we determined for the first time systematic uncertainty bands – related to nuclear mass modeling – for r-process abundances in realistic astrophysical scenarios [142].

We analyzed the results from a state-of-the-art simulation of the dynamic ejecta in full GR and with an approximate neutrino treatment. Our analysis of $\sim 40\,000$ tracers reveals that the bulk material in this ejection channel is sufficiently neutron-rich to support a strong r-process up to the heaviest elements. However, there is a high-entropy component that particularly fills the abundance gap between the third r-process peak and the lead region. The abundance pattern of these tracers is very similar to the ”fast“ ejecta found by Ref. [140].

In parallel, we investigated in detail the possible influence of weak reactions with the help of another full GR simulation that had no neutrino treatment. Via a post-processing step, we estimated a realistic range of (anti)neutrino luminosities for the merger and the first few milliseconds thereafter. We found that neutrino captures can increase the electron fraction beyond a critical threshold. Thus, strong neutrino irradiation inhibited the formation of heavy elements beyond the second r-process peak. This effect was partially reduced, as a shock wave from the central remnant passes through ejecta. Temporarily, electron captures decrease the electron fraction. Since the profile of the (anti)neutrino fluxes is likely anisotropic in simulations with a consistent neutrino treatment, we modulated the luminosities as a function of the polar angle. Here, we found the effects due to (anti)neutrino captures diminishing significantly. Therefore, we concluded that local luminosities are crucial to encode the influence of weak reactions on the nucleosynthesis.

We presented a comprehensive study of the neutrino-driven wind nucleosynthesis in the aftermath of a binary neutron star merger. We have focused on the initial phase where the remnant consists of a MNS surrounded by a massive accretion disk. The current nucleosynthesis study is based on the first three-dimensional simulation of such a wind [17], sampling the wind outflow by $\sim 17\,000$ tracer particles. The abundance distribution in the neutrino-driven wind is characterized by the production of lighter heavy elements ($A \lesssim 130$). We identified a time and angle dependency of the composition correlated with the electron fraction evolution. Elements heavier than $A > 130$ are produced only at early times, in an almost negligible amount and in the wind region that is closest to the disk. In contrast, matter ejected more perpendicular to the disk (bin 1: $0^\circ - 15^\circ$ in Fig. 4.16) produces only nuclei up to the first r-process peak ($A < 100$).

In all ejecta that we studied, the electron fraction is the key parameter to understand the characteristics of abundances. In the neutrino-driven wind, it covers a broad range from 0.1 to 0.4 with average values of $Y_\mathrm{e} \sim 0.33$. For the dynamic ejecta, there is a neutron-rich component with low electron fractions below $Y_\mathrm{e} = 0.1$. Due to neutrino irradiation these electron fractions can be increased to scatter with a broad range of $Y_\mathrm{e} = 0.1 - 0.5$. As noted already in earlier studies [13, 181, 220, 222], $Y_\mathrm{e} \approx 0.25$ is the threshold beyond which no more heavy r-process elements are formed. Since abundances depend strongly on Y_e, an accurate treatment of weak reactions is crucial and can be achieved by improving the neutrino transport and including more neutrino-matter reactions. For the neutrino-matter interactions, a small variation of Y_e can arise from a detailed inclusion of the (anti)neutrino absorption including weak magnetism and medium effects [288, 289].

The amount of ejecta also depends on angle and time. While we found that most material in the dynamic ejecta became unbound close to the orbital plane, shock-heating could drive the ejecta to higher latitudes. The neutrino-driven wind was preferentially driven out at relatively high latitudes. About 110 ms after the merger, a steady-state was reached in terms of mass loss. The total unbound mass depends crucially on the time when the MNS collapses to a black hole and if it survives for ~ 200 ms, as much as $9 \cdot 10^{-3} M_\odot$ can become unbound in the wind (i.e., $\sim 5\%$ of the initial mass of the accretion disk). This amount of matter rivals the dynamic ejecta that are typically found to be of order of $0.01 M_\odot$ ($1.3 \cdot 10^{-2} M_\odot$ for the specific case considered here). Other recent studies [15, 18, 144, 220] indicate that the wind switches off rapidly once a black hole forms. Approximately half of the neutrino luminosity is provided by the MNS. Therefore, when the black hole forms this contribution vanishes and the disk structure may significantly change. It is possible that general relativistic effects also have a non-negligible impact on the disk winds from a MNS and accretion disk system, as is the case for neutron star - black hole systems [290].

The angle dependency of the composition may have consequences for the mixing of the ejecta. Both dynamic and viscous ejecta contribute to the production of heavy r-process elements beyond the second peak ($A > 130$). If these ejection channels perfectly mix neutrino-driven wind material, its contribution may lead to variations for the lighter heavy elements (i.e., $A < 130$). This variation is indeed observed in stars with high enrichment of heavy r-process elements. In contrast, if the mixing is not perfect one could speculate that neutron star mergers with long-lived MNS may produce different abundance patterns including one with low enrichment of heavy r-process elements. This kind of pattern ("Honda-like pattern" [38, 291]) is observed in a few very old stars and its origin is still unknown. However, detailed mixing models following the late evolution of the three nucleosynthesis-relevant ejecta are required before concluding about the contribution of neutron star mergers to observed abundance patterns.

The initial separation of wind and dynamic ejecta allowed us to describe the individual contributions to the light curve of the electromagnetic transient due to the radioactive decay of neutron-rich nuclei. We used a semi-analytic radiation transport model to calculate the luminosities of the wind and dynamic ejecta. The light curve of the wind ejecta peaks after ~ 4 hours in the blue in contrast to the one of the dynamic ejecta that peaks few days after the merger in the infrared. The combined light curve significantly depends on the observing angle, as previously pointed out by Ref. [220]. The dynamic ejecta contain lanthanides and actinides that have high line expansion opacities of [110]. Hence, even small amounts of dynamic ejecta along the line of sight can completely obscure the blue transient from the wind. Since the morphology of dynamic ejecta is such that it leaves polar regions evacuated, it is far more likely to detect the blue component when the system is observed from the pole. The luminosity in the blue band exhibits a much higher dependency on the viewing angle compared to the luminosity in the infrared, in agreement with previous studies [220]. This significant anisotropy needs to be taken into account when assessing detectability of optical counterparts to neutron star mergers. Another interesting feature is the noticeable dependence of the position of optical peaks on the time of black hole formation. A longer collapse time leads to a later and more prolonged peak in both U+B and V+R bands, while this trend is washed out in the infrared. Although at this point it is difficult to draw any quantitative conclusions due to limitations of our model, our results suggest a possibility to use the position and duration of optical transients as proxies for the time of black hole formation (see also Ref. [223]). More work is needed to take into account additional channels of late-time ejecta production, and to improve radiation treatment.

Understanding the interplay of all ejecta from neutron star mergers is key to decode the diverse aspects of this astrophysical site. Further detailed simulations and complete nucleosynthesis studies will help to pin down the role of neutron star mergers for the origin of the heavy elements in the universe as well as to predict reliable electromagnetic counterparts for the detection of GWs. The obtained light curves can serve as an invaluable counterpart in the search for GWs.

Varying the nuclear physics input for r-process nucleosynthesis, we showed that detailed features of nuclear mass evolution toward the neutron drip line are critical to understand both the abundances and the origin of heavy elements in the r-process. Of utmost importance are the regions around magic numbers where separation energies vary rapidly due to spherical shell closures and shape changes. The systematic uncertainty band obtained within the deformed Skyrme-DFT approach exhibits significant variations with particle number. It is encouraging, however, that in certain mass regions the model error is fairly small; i.e., the intermodel consistency of our results can be high. The regions characterized by the broad uncertainty bands in Fig. 5.8 are indicative of model differences far from stability, where the theory relies on (sometimes extreme) extrapolations. To reduce the uncertainties, nuclear EDFs of spectroscopic quality need to be developed that are constrained by data on the most neutron-rich nuclei reachable in experiments. In this respect, the r-process abundance predictions presented in this work aim at assessing the current status of theoretical mass modeling at the limits of nuclear binding and also provide a useful benchmark for future improvements. It would be interesting to evaluate systematic uncertainty bands for other microscopic mass models based on effective interactions (or EDFs). In this context, we note that mass predictions performed within the covariant DFT [284] have provided separation-energy uncertainties remarkably similar to those from Skyrme-DFT [20]. In a next step, one can improve other microphysics input, such as fission yields and beta decay rates, as well as explore additional astrophysical environments.

With the bright prospects of further GW detections, it is only a matter of when GWs from a neutron star merger will be detected. Such a detection will not only help to pin down the physics of neutron-rich material, but it will also constrain the event rate at which neutron star mergers occur. This will shed a light on the galactical chemical evolution of our universe and probe the validity of neutron star mergers being the astrophysical host for the r-process.

In addition to the growing GW detector network, there will be more and high-quality observations of old metal-poor stars, due to the availability of improved telescopes. Upcoming large telescopes with high-resolution spectrographs, such as the European Extremely Large Telescope (E-ELT), will more deeply explore the blue wavelength region of stellar spectra. This is where the majority of the r-process elements exhibit their main absorption lines that observers measure.

From a nuclear physics perspective, there will be more measurements on neutron-rich nuclei. New-generation radioactive beam facilities, such as FAIR, FRIB, and RIKEN, will identify the properties of nuclei (e.g., nuclear masses and beta-decays) produced when r-process nuclei decay back to stability. These measurements directly help to improve the uncertainties that we found around the third r-process peak in our studies, since the theoretical predictions are very sensitive to properties of nuclei near the magic neutron number $N = 126$. Furthermore, the nucleosynthesis path of the neutrino-driven wind after a neutron star merger does not reach the heaviest nuclei. In some cases it even stops before $N = 82$. Thus, relevant nuclear physics input along the nucleosynthesis path will be measured in future generation facilities in the coming years to provide more reliable data.

Improved radiation transport models will be very important in at least two respects. They are employed for deriving stellar abundances and will thus reduce the uncertainties in observational results of r-process elements. At the same time, detailed radiation transport schemes are necessary to model the opacities in the aftermath of a neutron star merger. As the decay of the radioactive r-process nuclei powers subsequent kilonovae, our results on the morphology of the combined ejecta can be utilized for sophisticated predictions of kilonova light curves. These light curves will then serve as an electromagnetical counterpart in follow-up observations after GW detections from neutron star mergers.

Exascale computing will advance the theoretical modeling of both the nuclear properties and the astrophysical scenarios for the r-process. Indirectly, this will enhance the prediction of final r-process abundances, since the hydrodynamical conditions and the nuclear data serve as an input for nuclear reaction networks. Moreover, future high-resolution magneto-hydrodynamical simulations including an appropriate treatment of neutrino effects will provide tighter constraints on the exact properties of the outflowing material.

The future will see even greater collaborations to work along all of the above aspects. They will join forces to understand the rich physics in the invaluable laboratories provided by extreme environments, namely neutron star mergers and core-collapse supernovae.

Bibliography

[1] Dana Berry, SkyWorks Digitial, Inc. / Harvard-Smithsonian Center for Astrophysics, *Colliding neutron stars*, `https://www.cfa.harvard.edu/imagelist/2013-19`, accessed January 30, 2017, courtesy of Dana Berry May 31, 2017.

[2] Committee on the Physics of the Universe and National Research Council, *Connecting Quarks with the Cosmos: Eleven Science Questions for the New Century* (National Academies Press, 2003).

[3] E. M. Burbidge, G. R. Burbidge, W. A. Fowler, and F. Hoyle, Rev. Mod. Phys. **29**, 547 (1957).

[4] `https://www.ligo.caltech.edu/page/facts`, retrieved: 26.01.2017.

[5] B. P. Abbott *et al.*, Phys. Rev. Lett. **116**, 061102 (2016).

[6] L.-X. Li, and B. Paczyński, Astrophys. J. Lett. **507**, L59 (1998).

[7] E. Berger, W. Fong, and R. Chornock, Astrophys. J. Lett. **774**, L23 (2013).

[8] N. R. Tanvir, A. J. Levan, A. S. Fruchter, J. Hjorth, R. A. Hounsell, K. Wiersema, and R. L. Tunnicliffe, Nature **500**, 547 (2013).

[9] B. D. Metzger, G. Martínez-Pinedo, S. Darbha, E. Quataert, A. Arcones, D. Kasen, R. Thomas, P. Nugent, I. V. Panov, and N. T. Zinner, Mon. Not. R. Astron. Soc. **406**, 2650 (2010).

[10] M. Tanaka, and K. Hotokezaka, Astrophys. J. **775**, 113 (2013).

[11] C. Freiburghaus, S. Rosswog, and F.-K. Thielemann, Astrophys. J. Lett. **525**, L121 (1999).

[12] S. Goriely, A. Bauswein, and H.-T. Janka, Astrophys. J. Lett. **738**, L32 (2011).

[13] O. Korobkin, S. Rosswog, A. Arcones, and C. Winteler, Mon. Not. R. Astron. Soc. **426**, 1940 (2012).

[14] A. Bauswein, S. Goriely, and H.-T. Janka, Astrophys. J. **773**, 78 (2013).

[15] R. Fernández, and B. D. Metzger, Mon. Not. R. Astron. Soc. **435**, 502 (2013).

[16] M.-R. Wu, R. Fernández, G. Martínez-Pinedo, and B. D. Metzger, Mon. Not. R. Astron. Soc. **463**, 2323 (2016).

[17] A. Perego, S. Rosswog, R. M. Cabezón, O. Korobkin, R. Käppeli, A. Arcones, and M. Liebendörfer, Mon. Not. R. Astron. Soc. **443**, 3134 (2014).

[18] O. Just, A. Bauswein, R. A. Pulpillo, S. Goriely, and H.-T. Janka, Mon. Not. R. Astron. Soc. **448**, 541 (2015).

[19] `https://people.nscl.msu.edu/~thoennes/isotopes/`, retrieved: 12.12.2016.

[20] J. Erler, N. Birge, M. Kortelainen, W. Nazarewicz, E. Olsen, A. M. Perhac, and M. Stoitsov, Nature **486**, 509 (2012).

[21] J. Beringer *et al.* (Particle Data Group), Phys. Rev. D **86**, 010001 (2012).

[22] E. Anders, and N. Grevesse, Geochim. Cosmochim. Acta **53**, 197 (1989).

[23] K. Lodders, Astrophys. J. **591**, 1220 (2003).

[24] M. Arnould, S. Goriely, and K. Takahashi, Phys. Rep. **450**, 97 (2007).

[25] M. Busso, R. Gallino, and G. J. Wasserburg, Annu. Rev. Astron. Astrophy. **37**, 239 (1999).

[26] F. Käppeler, R. Gallino, S. Bisterzo, and W. Aoki, Rev. Mod. Phys. **83**, 157 (2011).

[27] K.-L. Kratz, K. Farouqi, and B. Pfeiffer, Prog. Part. Nucl. Phys. **59**, 147 (2007).

[28] K.-L. Kratz, J.-P. Bitouzet, F.-K. Thielemann, P. Moeller, and B. Pfeiffer, Astrophys. J. **403**, 216 (1993).

[29] C. Iliadis, *Nuclear Physics of Stars* (Wiley-VCH, 2007).

[30] W. Hillebrandt, Space Sci. Rev. **21**, 639 (1978).

[31] M. R. Mumpower, G. C. McLaughlin, R. Surman, and A. W. Steiner, ArXiv e-prints (2016), arXiv:1609.09858.

[32] D. N. Schramm, and W. A. Fowler, Nature **231**, 103 (1971).

[33] R. Surman, J. Engel, J. R. Bennett, and B. S. Meyer, Phys. Rev. Lett. **79**, 1809 (1997).

[34] M. R. Mumpower, G. C. McLaughlin, and R. Surman, Phys. Rev. C **85**, 045801 (2012).

[35] I. V. Panov, E. Kolbe, B. Pfeiffer, T. Rauscher, K.-L. Kratz, and F.-K. Thielemann, Nucl. Phys. A **747**, 633 (2005).

[36] S. Goriely, J.-L. Sida, J.-F. Lemaitre, S. Panebianco, N. Dubray, S. Hilaire, A. Bauswein, and H.-T. Janka, Phys. Rev. Lett. **111**, 242502 (2013).

[37] C. Sneden, J. J. Cowan, and R. Gallino, Annu. Rev. Astron. Astrophy. **46**, 241 (2008).

[38] S. Honda, W. Aoki, T. Kajino, H. Ando, T. C. Beers, H. Izumiura, K. Sadakane, and M. Takada-Hidai, Astrophys. J. **607**, 474 (2004).

[39] C. J. Hansen, F. Montes, and A. Arcones, Astrophys. J. **797**, 123 (2014).

[40] J. Simmerer, C. Sneden, J. J. Cowan, J. Collier, V. M. Woolf, and J. E. Lawler, Astrophys. J. **617**, 1091 (2004).

[41] C. Arlandini, F. Käppeler, K. Wisshak, R. Gallino, M. Lugaro, M. Busso, and O. Straniero, Astrophys. J. **525**, 886 (1999).

[42] Y.-Z. Qian, Astrophys. J. Lett. **534**, L67 (2000).

[43] D. Argast, M. Samland, F.-K. Thielemann, and Y.-Z. Qian, Astron. Astrophys. **416**, 997 (2004).

[44] A. Wallner *et al.*, Nat. Commun. **6**, 5956 (2015).

[45] A. P. Ji, A. Frebel, A. Chiti, and J. D. Simon, Nature **531**, 610 (2016).

[46] R. Kippenhahn, A. Weigert, and A. Weiss, *Stellar Structure and Evolution* (Springer Berlin Heidelberg, 2012).

[47] A. Burrows, Rev. Mod. Phys. **85**, 245 (2013).

[48] H.-T. Janka, K. Langanke, A. Marek, G. Martínez-Pinedo, and B. Müller, Phys. Rep. **442**, 38 (2007).

[49] H.-T. Janka, *Supernovae und kosmische Gammablitze: Ursachen und Folgen von Sternexplosionen* (Spektrum Akademischer Verlag, 2011).

[50] M. Reichert, *Reduced nuclear reaction network for hydrodynamical simulations*, Master thesis, TU Darmstadt (2016).

[51] A. Perego, R. M. Cabezón, and R. Käppeli, Astrophys. J. Suppl. Ser. **223**, 22 (2016).

[52] M. Rampp, and H.-T. Janka, Astron. Astrophys. **396**, 361 (2002).

[53] S. A. Colgate, and R. H. White, Astrophys. J. **143**, 626 (1966).

[54] H. A. Bethe, and J. R. Wilson, Astrophys. J. **295**, 14 (1985).

[55] T. Melson, H.-T. Janka, and A. Marek, Astrophys. J. Lett. **801**, L24 (2015).

[56] S. M. Couch, and C. D. Ott, Astrophys. J. **799**, 5 (2015).

[57] E. J. Lentz, S. W. Bruenn, W. R. Hix, A. Mezzacappa, O. E. B. Messer, E. Endeve, J. M. Blondin, J. A. Harris, P. Marronetti, and K. N. Yakunin, Astrophys. J. Lett. **807**, L31 (2015).

[58] H.-T. Janka, Annu. Rev. Nucl. Part. Sc. **62**, 407 (2012).

[59] M. Ugliano, H.-T. Janka, A. Marek, and A. Arcones, Astrophys. J. **757**, 69 (2012).

[60] T. Ertl, M. Ugliano, H.-T. Janka, A. Marek, and A. Arcones, Astrophys. J. **821**, 69 (2016).

[61] T. Ertl, H.-T. Janka, S. E. Woosley, T. Sukhbold, and M. Ugliano, Astrophys. J. **818**, 124 (2016).

[62] R. C. Duncan, S. L. Shapiro, and I. Wasserman, Astrophys. J. **309**, 141 (1986).

[63] A. Arcones, G. Martínez-Pinedo, E. O'Connor, A. Schwenk, H.-T. Janka, C. J. Horowitz, and K. Langanke, Phys. Rev. C **78**, 015806 (2008).

[64] S. E. Woosley, and R. D. Hoffman, Astrophys. J. **395**, 202 (1992).

[65] K. Takahashi, J. Witti, and H.-T. Janka, Astron. Astrophys. **286**, 857 (1994).

[66] B. S. Meyer, G. J. Mathews, W. M. Howard, S. E. Woosley, and R. D. Hoffman, Astrophys. J. **399**, 656 (1992).

[67] J. Witti, H.-T. Janka, and K. Takahashi, Astron. Astrophys. **286**, 841 (1994).

[68] Y.-Z. Qian, and S. E. Woosley, Astrophys. J. **471**, 331 (1996).

[69] A. Arcones, H.-T. Janka, and L. Scheck, Astron. Astrophys. **467**, 1227 (2007).

[70] L. Hüdepohl, B. Müller, H.-T. Janka, A. Marek, and G. G. Raffelt, Phys. Rev. Lett. **104**, 251101 (2010).

[71] L. F. Roberts, S. E. Woosley, and R. D. Hoffman, Astrophys. J. **722**, 954 (2010).

[72] T. Fischer, S. C. Whitehouse, A. Mezzacappa, F.-K. Thielemann, and M. Liebendörfer, Astron. Astrophys. **517**, A80 (2010).

[73] A. Arcones, and F. Montes, Astrophys. J. **731**, 5 (2011).

[74] F.-K. Thielemann *et al.*, Prog. Part. Nucl. Phys. **66**, 346 (2011).

[75] A. Arcones, and F.-K. Thielemann, J. Phys. G: Nucl. Phys. **40**, 013201 (2013).

[76] A. Arcones, and J. Bliss, J. Phys. G: Nucl. Phys. **41**, 044005 (2014).

[77] J. Bliss, A. Arcones, F. Montes, and J. Pereira, ArXiv e-prints (2016), arXiv:1612.02435.

[78] C. Fröhlich, G. Martínez-Pinedo, M. Liebendörfer, F.-K. Thielemann, E. Bravo, W. R. Hix, K. Langanke, and N. T. Zinner, Phys. Rev. Lett. **96**, 142502 (2006).

[79] S.-I. Fujimoto, K. Kotake, S. Yamada, M.-A. Hashimoto, and K. Sato, Astrophys. J. **644**, 1040 (2006).

[80] S.-I. Fujimoto, N. Nishimura, and M.-A. Hashimoto, Astrophys. J. **680**, 1350 (2008).

[81] C. Winteler, R. Käppeli, A. Perego, A. Arcones, N. Vasset, N. Nishimura, M. Liebendörfer, and F.-K. Thielemann, Astrophys. J. Lett. **750**, L22 (2012).

[82] P. Mösta, S. Richers, C. D. Ott, R. Haas, A. L. Piro, K. Boydstun, E. Abdikamalov, C. Reisswig, and E. Schnetter, Astrophys. J. Lett. **785**, L29 (2014).

[83] N. Nishimura, T. Takiwaki, and F.-K. Thielemann, Astrophys. J. **810**, 109 (2015).

[84] M. Obergaulinger, P. Cerdá-Durán, E. Müller, and M. A. Aloy, Astron. Astrophys. **498**, 241 (2009).

[85] P. Mösta, C. D. Ott, D. Radice, L. F. Roberts, E. Schnetter, and R. Haas, Nature **528**, 376 (2015).

[86] R. Y. Käppeli, *Numerical methods for 3D magneto-rotational core-collapse supernova simulation with jet formation*, dissertation, University of Basel (2013).

[87] R. Oechslin, H.-T. Janka, and A. Marek, Astron. Astrophys. **467**, 395 (2007).

[88] L. F. Roberts, D. Kasen, W. H. Lee, and E. Ramirez-Ruiz, Astrophys. J. Lett. **736**, L21 (2011).

[89] S. Wanajo, Y. Sekiguchi, N. Nishimura, K. Kiuchi, K. Kyutoku, and M. Shibata, Astrophys. J. Lett. **789**, L39 (2014).

[90] J. M. Lattimer, and D. N. Schramm, Astrophys. J. Lett. **192**, L145 (1974).

[91] J. M. Lattimer, and D. N. Schramm, Astrophys. J. **210**, 549 (1976).

[92] D. Eichler, M. Livio, T. Piran, and D. N. Schramm, Nature **340**, 126 (1989).

[93] F. Matteucci, D. Romano, A. Arcones, O. Korobkin, and S. Rosswog, Mon. Not. R. Astron. Soc. **438**, 2177 (2014).

[94] S. Shen, R. J. Cooke, E. Ramirez-Ruiz, P. Madau, L. Mayer, and J. Guedes, Astrophys. J. **807**, 115 (2015).

[95] F. van de Voort, E. Quataert, P. F. Hopkins, D. Keres, and C.-A. Faucher-Giguere, Mon. Not. R. Astron. Soc. **447**, 140 (2015).

[96] Y. Ishimaru, S. Wanajo, and N. Prantzos, Astrophys. J. Lett. **804**, L35 (2015).

[97] G. Cescutti, D. Romano, F. Matteucci, C. Chiappini, and R. Hirschi, Astron. Astrophys. **577**, A139 (2015).

[98] B. Wehmeyer, M. Pignatari, and F.-K. Thielemann, Mon. Not. R. Astron. Soc. **452**, 1970 (2015).

[99] M. Dominik, E. Berti, R. O'Shaughnessy, I. Mandel, K. Belczynski, C. Fryer, D. E. Holz, T. Bulik, and F. Pannarale, Astrophys. J. **806**, 263 (2015).

[100] B. P. Abbott *et al.*, Phys. Rev. Lett. **116**, 241103 (2016).

[101] V. Kalogera *et al.*, Astrophys. J. Lett. **601**, L179 (2004).

[102] V. Kalogera *et al.*, Astrophys. J. Lett. **614**, L137 (2004).

[103] J. Abadie *et al.*, Class. Quantum Grav. **27**, 173001 (2010).

[104] L. Rezzolla, B. Giacomazzo, L. Baiotti, J. Granot, C. Kouveliotou, and M. A. Aloy, Astrophys. J. Lett. **732**, L6 (2011).

[105] B. Yang, Z.-P. Jin, X. Li, S. Covino, X.-Z. Zheng, K. Hotokezaka, Y.-Z. Fan, T. Piran, and D.-M. Wei, Nat. Commun. **6**, 7323 (2015).

[106] Z.-P. Jin, K. Hotokezaka, X. Li, M. Tanaka, P. D'Avanzo, Y.-Z. Fan, S. Covino, D.-M. Wei, and T. Piran, Nat. Commun. **7**, 12898 (2016).

[107] S. R. Kulkarni, ArXiv Astrophysics e-prints (2005), astro-ph/0510256.

[108] B. D. Metzger, ArXiv e-prints (2016), arXiv:1610.09381.

[109] W. D. Arnett, Astrophys. J. **253**, 785 (1982).

[110] D. Kasen, N. R. Badnell, and J. Barnes, Astrophys. J. **774**, 25 (2013).

[111] J. Barnes, and D. Kasen, Astrophys. J. **775**, 18 (2013).

[112] D. Grossman, O. Korobkin, S. Rosswog, and T. Piran, Mon. Not. R. Astron. Soc. **439**, 757 (2014).

[113] S. Rosswog, T. Piran, and E. Nakar, Mon. Not. R. Astron. Soc. **430**, 2585 (2013).

[114] S. Rosswog, Int. J. Mod. Phys. A **24**, 1530012 (2015).

[115] B. D. Metzger, and E. Berger, Astrophys. J. **746**, 48 (2012).

[116] S. Nissanke, M. Kasliwal, and A. Georgieva, Astrophys. J. **767**, 124 (2013).

[117] T. Piran, E. Nakar, and S. Rosswog, Mon. Not. R. Astron. Soc. **430**, 2121 (2013).

[118] B. P. Abbott *et al.*, Astrophys. J. Lett. **826**, L13 (2016).

[119] J. M. Lattimer, and M. Prakash, Phys. Rev. Lett. **94**, 111101 (2005).

[120] J. M. Lattimer, *Observed Neutron Star Masses*, `https://stellarcollapse.org/nsmasses`, accessed December 16, 2016.

[121] R. Gold, S. Bernuzzi, M. Thierfelder, B. Brügmann, and F. Pretorius, Phys. Rev. D **86**, 121501 (2012).

[122] S. Rosswog, and M. Brüggen, *Introduction to High-Energy Astrophysics* (Cambridge University Press, 2007).

[123] M. Colpi, P. Casella, V. Gorini, U. Moschella, and A. Possenti, eds., *Physics of Relativistic Objects in Compact Binaries: from Birth to Coalescence* (Springer Science+Business Media B.V., 2009).

[124] M. Dominik, K. Belczynski, C. Fryer, D. E. Holz, E. Berti, T. Bulik, I. Mandel, and R. O'Shaughnessy, Astrophys. J. **759**, 52 (2012).

[125] D. R. Lorimer, Living Rev. Relat. **8**, 7 (2005).

[126] R. A. Hulse, and J. H. Taylor, Astrophys. J. Lett. **195**, L51 (1975).

[127] M. Burgay *et al.*, Nature **426**, 531 (2003).

[128] R. C. Tolman, Phys. Rev. **55**, 364 (1939).

[129] J. R. Oppenheimer, and G. M. Volkoff, Phys. Rev. **55**, 374 (1939).

[130] S. Rosswog, M. Liebendörfer, F.-K. Thielemann, M. B. Davies, W. Benz, and T. Piran, Astron. Astrophys. **341**, 499 (1999).

[131] K. Hotokezaka, K. Kiuchi, K. Kyutoku, T. Muranushi, Y. Sekiguchi, M. Shibata, and K. Taniguchi, Phys. Rev. D **88**, 044026 (2013).

[132] S. Rosswog, Phil. Trans. R. Soc. A **371**, 20272 (2013).

[133] S. Rosswog, O. Korobkin, A. Arcones, F.-K. Thielemann, and T. Piran, Mon. Not. R. Astron. Soc. **439**, 744 (2014).

[134] I. V. Panov, I. Y. Korneev, and F.-K. Thielemann, Astron. Lett. **34**, 189 (2008).

[135] I. Petermann, K. Langanke, G. Martínez-Pinedo, I. V. Panov, P.-G. Reinhard, and F.-K. Thielemann, Eur. Phys. J. A **48**, 122 (2012).

[136] S. Goriely, Eur. Phys. J. A **51**, 22 (2015).

[137] M. Eichler *et al.*, Astrophys. J. **808**, 30 (2015).

[138] A. Arcones, and G. Martínez-Pinedo, Phys. Rev. C **83**, 045809 (2011).

[139] A. Arcones, and G. F. Bertsch, Phys. Rev. Lett. **108**, 151101 (2012).

[140] J. d. J. Mendoza-Temis, M.-R. Wu, K. Langanke, G. Martínez-Pinedo, A. Bauswein, and H.-T. Janka, Phys. Rev. C **92**, 055805 (2015).

[141] M. Mumpower, R. Surman, G. McLaughlin, and A. Aprahamianan, Prog. Part. Nucl. Phys. **86**, 86 (2016).

[142] D. Martin, A. Arcones, W. Nazarewicz, and E. Olsen, Phys. Rev. Lett. **116**, 121101 (2016).

[143] K. Hotokezaka, K. Kyutoku, H. Okawa, M. Shibata, and K. Kiuchi, Phys. Rev. D **83**, 124008 (2011).

[144] Y. Sekiguchi, K. Kiuchi, K. Kyutoku, and M. Shibata, Phys. Rev. D **91**, 064059 (2015).

[145] S. Goriely, A. Bauswein, O. Just, E. Pllumbi, and H.-T. Janka, Mon. Not. R. Astron. Soc. **452**, 3894 (2015).

[146] M. Ruffert, H.-T. Janka, K. Takahashi, and G. Schaefer, Astron. Astrophys. **319**, 122 (1997).

[147] S. Rosswog, and E. Ramirez-Ruiz, Mon. Not. R. Astron. Soc. **336**, L7 (2002).

[148] L. Dessart, C. D. Ott, A. Burrows, S. Rosswog, and E. Livne, Astrophys. J. **690**, 1681 (2009).

[149] D. Martin, A. Perego, A. Arcones, F.-K. Thielemann, O. Korobkin, and S. Rosswog, Astrophys. J. **813**, 2 (2015).

[150] B. D. Metzger, A. L. Piro, and E. Quataert, Mon. Not. R. Astron. Soc. **390**, 781 (2008).

[151] A. M. Beloborodov, in *American Institute of Physics Conference Series*, American Institute of Physics Conference Series, Vol. 1054, edited by M. Axelsson (2008) pp. 51–70.

[152] W. H. Lee, E. Ramirez-Ruiz, and D. López-Cámara, Astrophys. J. Lett. **699**, L93 (2009).

[153] D. M. Siegel, R. Ciolfi, and L. Rezzolla, Astrophys. J. Lett. **785**, L6 (2014).

[154] D. M. Siegel, and R. Ciolfi, Astrophys. J. **819**, 14 (2016).

[155] D. M. Siegel, and R. Ciolfi, Astrophys. J. **819**, 15 (2016).

[156] A. Murguia-Berthier, G. Montes, E. Ramirez-Ruiz, F. De Colle, and W. H. Lee, Astrophys. J. Lett. **788**, L8 (2014).

[157] W. R. Hix, and F.-K. Thielemann, J. Comput. Appl. Math. **109**, 321 (1999).

[158] C. Winteler, *Light element production in the big bang and the synthesis of heavy elements in 3D MHD jets from core-collapse supernovae*, dissertation, University of Basel (2012).

[159] T. Mayer-Kuckuk, *Kernphysik* (Vieweg+Teubner Verlag, 2002).

[160] W. Hauser, and H. Feshbach, Phys. Rev. **87**, 366 (1952).

[161] E. Gadioli, and P. E. Hodgson, *Pre-Equilibrium Nuclear Reactions* (Clarendon Press, 1992).

[162] T. Rauscher, and F.-K. Thielemann, At. Data Nucl. Data Tables **75**, 1 (2000).

[163] T. Rauscher, Astrophys. J. Suppl. Ser. **147**, 403 (2003).

[164] P. Möller, J. R. Nix, W. D. Myers, and W. J. Swiatecki, At. Data Nucl. Data Tables **59**, 185 (1995).

[165] R. H. Cyburt *et al.*, Astrophys. J. Suppl. Ser. **189**, 240 (2010).

[166] A. J. Koning, S. Hilaire, and S. Goriely, *Talys 1.6 user manual*, `http://www.talys.eu/fileadmin/talys/user/docs/talys1.6.pdf` (2013).

[167] G. M. Fuller, W. A. Fowler, and M. J. Newman, Astrophys. J. **252**, 715 (1982).

[168] G. M. Fuller, W. A. Fowler, and M. J. Newman, Astrophys. J. Suppl. Ser. **48**, 279 (1982).

[169] G. M. Fuller, W. A. Fowler, and M. J. Newman, Astrophys. J. **293**, 1 (1985).

[170] K. Langanke, and G. Martínez-Pinedo, At. Data Nucl. Data Tables **79**, 1 (2001).

[171] P. Möller, B. Pfeiffer, and K.-L. Kratz, Phys. Rev. C **67**, 055802 (2003).

[172] F. X. Timmes, and F. D. Swesty, Astrophys. J. Suppl. Ser. **126**, 501 (2000).

[173] I. V. Panov, I. Y. Korneev, T. Rauscher, G. Martínez-Pinedo, A. Kelić-Heil, N. T. Zinner, and F.-K. Thielemann, Astron. Astrophys. **513**, A61 (2010).

[174] E. Mueller, Astron. Astrophys. **162**, 103 (1986).

[175] C. W. Gear, Commun. ACM **14**, 176 (1971).

[176] R. Longland, D. Martin, and J. José, Astron. Astrophys. **563**, A67 (2014).

[177] G. D. Byrne, and A. C. Hindmarsh, ACM Trans. Math. Soft. **1**, 71 (1975).

[178] Intel, *Intel MKL PARDISO*, `https://software.intel.com/en-us/node/470282` (2016).

[179] A. Juodagalvis, K. Langanke, W. R. Hix, G. Martínez-Pinedo, and J. M. Sampaio, Nucl. Phys. A **848**, 454 (2010).

[180] S. A. Bludman, and K. A. van Riper, Astrophys. J. **212**, 859 (1977).

[181] J. Lippuner, and L. F. Roberts, Astrophys. J. **815**, 82 (2015).

[182] A. Arcones, G. Martínez-Pinedo, L. F. Roberts, and S. E. Woosley, Astron. Astrophys. **522**, A25 (2010).

[183] E. Pllumbi, I. Tamborra, S. Wanajo, H.-T. Janka, and L. Hüdepohl, Astrophys. J. **808**, 188 (2015).

[184] C. J. Horowitz, and G. Li, Phys. Rev. Lett. **82**, 5198 (1999).

[185] S. Rosswog, and M. Liebendörfer, Mon. Not. R. Astron. Soc. **342**, 673 (2003).

[186] S. Rosswog, and M. B. Davies, Mon. Not. R. Astron. Soc. **334**, 481 (2002).

[187] S. Rosswog, Astrophys. J. **634**, 1202 (2005).

[188] Y. Sekiguchi, K. Kiuchi, K. Kyutoku, M. Shibata, and K. Taniguchi, Phys. Rev. D **93**, 124046 (2016).

[189] T. Nakamura, K. Oohara, and Y. Kojima, Progr. Theor. Exp. Phys. **90**, 1 (1987).

[190] M. Shibata, and T. Nakamura, Phys. Rev. D **52**, 5428 (1995).

[191] T. W. Baumgarte, and S. L. Shapiro, Phys. Rev. D **59**, 024007 (1999).

[192] D. Brown, P. Diener, O. Sarbach, E. Schnetter, and M. Tiglio, Phys. Rev. D **79**, 044023 (2009).

[193] F. Löffler *et al.*, Class. Quantum Grav. **29**, 115001 (2012).

[194] L. Rezzolla, and O. Zanotti, *Relativistic Hydrodynamics*, EBSCO ebook academic collection (OUP Oxford, 2013).

[195] D. Radice, L. Rezzolla, and F. Galeazzi, Mon. Not. R. Astron. Soc. **437**, L46 (2014).

[196] D. Radice, L. Rezzolla, and F. Galeazzi, Class. Quantum Grav. **31**, 075012 (2014).

[197] E. Schnetter, S. H. Hawley, and I. Hawke, Class. Quantum Grav. **21**, 1465 (2004).

[198] J. M. Lattimer, and F. D. Swesty, Nucl. Phys. A **535**, 331 (1991).

[199] F. Galeazzi, W. Kastaun, L. Rezzolla, and J. A. Font, Phys. Rev. D **88**, 064009 (2013).

[200] W. Kastaun, R. Ciolfi, and B. Giacomazzo, Phys. Rev. D **94**, 044060 (2016).

[201] V. Mewes, F. Galeazzi, J. A. Font, P. J. Montero, and N. Stergioulas, Mon. Not. R. Astron. Soc. **461**, 2480 (2016).

[202] W. Kastaun, and F. Galeazzi, Phys. Rev. D **91**, 064027 (2015).

[203] D. Radice, F. Galeazzi, J. Lippuner, L. F. Roberts, C. D. Ott, and L. Rezzolla, Mon. Not. R. Astron. Soc. **460**, 3255 (2016).

[204] F. Foucart, E. O'Connor, L. Roberts, M. D. Duez, R. Haas, L. E. Kidder, C. D. Ott, H. P. Pfeiffer, M. A. Scheel, and B. Szilagyi, Phys. Rev. D **91**, 124021 (2015).

[205] M. Ruffert, H.-T. Janka, and G. Schaefer, Astron. Astrophys. **311**, 532 (1996).

[206] O. Just, M. Obergaulinger, and H.-T. Janka, Mon. Not. R. Astron. Soc. **453**, 3386 (2015).

[207] E. O'Connor, Astrophys. J. Suppl. Ser. **219**, 24 (2015).

[208] W. Kastaun, R. Ciolfi, A. Endrizzi, and B. Giacomazzo, ArXiv e-prints (2016), arXiv:1612.03671.

[209] D. Alic, W. Kastaun, and L. Rezzolla, Phys. Rev. D **88**, 064049 (2013).

[210] G. Shen, C. J. Horowitz, and S. Teige, Phys. Rev. C **82**, 015806 (2010).

[211] G. Shen, C. J. Horowitz, and S. Teige, Phys. Rev. C **83**, 035802 (2011).

[212] R. Käppeli, S. C. Whitehouse, S. Scheidegger, U.-L. Pen, and M. Liebendörfer, Astrophys. J. Suppl. Ser. **195**, 20 (2011).

[213] G. A. Lalazissis, J. König, and P. Ring, Phys. Rev. C **55**, 540 (1997).

[214] `http://phys-merger.physik.unibas.ch/~hempel/eos.html`, retrieved: 23.01.2017.

[215] L. F. Roberts, J. Lippuner, M. D. Duez, J. A. Faber, F. Foucart, J. C. Lombardi, Jr., S. Ning, C. D. Ott, and M. Ponce, Mon. Not. R. Astron. Soc. **464**, 3907 (2017).

[216] M. Hempel, T. Fischer, J. Schaffner-Bielich, and M. Liebendörfer, Astrophys. J. **748**, 70 (2012).

[217] D. J. Price, and S. Rosswog, Science **312**, 719 (2006).

[218] D. Martin, A. Perego, A. Arcones, O. Korobkin, and F. K. Thielemann, in *XIII Nuclei in the Cosmos (NIC XIII)* (2014) p. 120.

[219] D. Neilsen, S. L. Liebling, M. Anderson, L. Lehner, E. O'Connor, and C. Palenzuela, Phys. Rev. D **89**, 104029 (2014).

[220] D. Kasen, R. Fernández, and B. D. Metzger, Mon. Not. R. Astron. Soc. **450**, 1777 (2015).

[221] R. D. Hoffman, S. E. Woosley, and Y.-Z. Qian, Astrophys. J. **482**, 951 (1997).

[222] C. Freiburghaus, J.-F. Rembges, T. Rauscher, E. Kolbe, F.-K. Thielemann, K.-L. Kratz, B. Pfeiffer, and J. J. Cowan, Astrophys. J. **516**, 381 (1999).

[223] B. D. Metzger, and R. Fernández, Mon. Not. R. Astron. Soc. **441**, 3444 (2014).

[224] R. Fernández, E. Quataert, J. Schwab, D. Kasen, and S. Rosswog, Mon. Not. R. Astron. Soc. **449**, 390 (2015).

[225] Y.-Z. Qian, and G. J. Wasserburg, Phys. Rep. **442**, 237 (2007).

[226] C. Sneden *et al.*, Astrophys. J. **591**, 936 (2003).

[227] G. Wallerstein, J. L. Greenstein, R. Parker, H. L. Helfer, and L. H. Aller, Astrophys. J. **137**, 280 (1963).

[228] S. Honda, W. Aoki, Y. Ishimaru, S. Wanajo, and S. G. Ryan, Astrophys. J. **643**, 1180 (2006).

[229] I. U. Roederer, J. J. Cowan, A. I. Karakas, K.-L. Kratz, M. Lugaro, J. Simmerer, K. Farouqi, and C. Sneden, Astrophys. J. **724**, 975 (2010).

[230] S. Rosswog, *priv. communication* (2015).

[231] B. Margalit, and T. Piran, Mon. Not. R. Astron. Soc. **452**, 3419 (2015).

[232] M. R. Mumpower, R. Surman, D.-L. Fang, M. Beard, P. Möller, T. Kawano, and A. Aprahamian, Phys. Rev. C **92**, 035807 (2015).

[233] M. Mumpower, R. Surman, D. L. Fang, M. Beard, and A. Aprahamian, J. Phys. G: Nucl. Phys. **42**, 034027 (2015).

[234] J. Kopecky, and M. Uhl, Phys. Rev. C **41**, 1941 (1990).

[235] W. M. Howard, S. Goriely, M. Rayet, and M. Arnould, Astrophys. J. **417**, 713 (1993).

[236] B. S. Meyer, and J. S. Brown, Astrophys. J. Suppl. Ser. **112**, 199 (1997).

[237] S. Wanajo, S. Goriely, M. Samyn, and N. Itoh, Astrophys. J. **606**, 1057 (2004).

[238] K. Farouqi, K.-L. Kratz, B. Pfeiffer, T. Rauscher, F.-K. Thielemann, and J. W. Truran, Astrophys. J. **712**, 1359 (2010).

[239] I. Dillmann *et al.*, Phys. Rev. Lett. **91**, 162503 (2003).

[240] R. Surman, and J. Engel, Phys. Rev. C **64**, 035801 (2001).

[241] P. Möller, A. J. Sierk, T. Ichikawa, and H. Sagawa, At. Data Nucl. Data Tables **109**, 1 (2016).

[242] J. Duflo, and A. P. Zuker, Phys. Rev. C **52**, R23 (1995).

[243] J. Pearson, R. Nayak, and S. Goriely, Phys. Lett. B **387**, 455 (1996).

[244] S. Goriely, M. Samyn, and J. M. Pearson, Phys. Rev. C **75**, 064312 (2007).

[245] S. Goriely, N. Chamel, and J. M. Pearson, Phys. Rev. C **88**, 024308 (2013).

[246] G. Audi, F. Kondev, M. Wang, B. Pfeiffer, X. Sun, J. Blachot, and M. MacCormick, Chin. Phys. C **36**, 1157 (2012).

[247] M. Wang, G. Audi, A. Wapstra, F. Kondev, M. MacCormick, X. Xu, and B. Pfeiffer, Chin. Phys. C **36**, 1603 (2012).

[248] S. N. Liddick *et al.*, Phys. Rev. Lett. **116**, 242502 (2016).

[249] P. Hosmer *et al.*, Phys. Rev. C **82**, 025806 (2010).

[250] M. Madurga *et al.*, Phys. Rev. Lett. **109**, 112501 (2012).

[251] H. Watanabe *et al.*, Phys. Rev. Lett. **111**, 152501 (2013).

[252] G. Lorusso *et al.*, Phys. Rev. Lett. **114**, 192501 (2015).

[253] D. Atanasov *et al.*, Phys. Rev. Lett. **115**, 232501 (2015).

[254] C. Mazzocchi *et al.*, Phys. Rev. C **92**, 054317 (2015).

[255] R. Caballero-Folch *et al.*, Phys. Rev. Lett. **117**, 012501 (2016).

[256] *Nuclear Physics: Exploring the Heart of Matter. Report of the Committee on the Assessment of and Outlook for Nuclear Physics* (The National Academies Press, 2012).

[257] *NuPECC Long Range Plan 2010: Perspectives of Nuclear Physics in Europe* (NuPECC Long Range Plan Report, 2010).

[258] *The 2015 Long Range Plan in Nuclear Science: Reaching for the Horizon* (NSAC Long Range Plan Report, 2015).

[259] A. B. Balantekin *et al.*, Mod. Phys. Lett. A **29**, 1430010-11 (2014).

[260] S. Bogner *et al.*, Comput. Phys. Commun. **184**, 2235 (2013).

[261] S. Binder, J. Langhammer, A. Calci, and R. Roth, Phys. Lett. B **736**, 119 (2014).

[262] T. A. Lähde, E. Epelbaum, H. Krebs, D. Lee, U.-G. Meißner, and G. Rupak, Phys. Lett. B **732**, 110 (2014).

[263] G. Hagen *et al.*, Nature Phys. **12**, 186 (2016).

[264] K. Hebeler, J. D. Holt, J. Menéndez, and A. Schwenk, Annu. Rev. Nucl. Part. Sc. **65**, 457 (2015).

[265] M. Bender, P.-H. Heenen, and P.-G. Reinhard, Rev. Mod. Phys. **75**, 121 (2003).

[266] J. Dobaczewski, W. Nazarewicz, and P.-G. Reinhard, J. Phys. G: Nucl. Phys. **41**, 074001 (2014).

[267] J. D. McDonnell, N. Schunck, D. Higdon, J. Sarich, S. M. Wild, and W. Nazarewicz, Phys. Rev. Lett. **114**, 122501 (2015).

[268] Y. Gao, J. Dobaczewski, M. Kortelainen, J. Toivanen, and D. Tarpanov, Phys. Rev. C **87**, 034324 (2013).

[269] M. Kortelainen, J. Erler, W. Nazarewicz, N. Birge, Y. Gao, and E. Olsen, Phys. Rev. C **88**, 031305 (2013).

[270] J. Bartel, P. Quentin, M. Brack, C. Guet, and H.-B. Håkansson, Nucl. Phys. A **386**, 79 (1982).

[271] J. Dobaczewski, H. Flocard, and J. Treiner, Nucl. Phys. A **422**, 103 (1984).

[272] E. Chabanat, P. Bonche, P. Haensel, J. Meyer, and R. Schaeffer, Nucl. Phys. A **635**, 231 (1998).

[273] P. Klüpfel, P.-G. Reinhard, T. J. Bürvenich, and J. A. Maruhn, Phys. Rev. C **79**, 034310 (2009).

[274] M. Kortelainen, T. Lesinski, J. Moré, W. Nazarewicz, J. Sarich, N. Schunck, M. V. Stoitsov, and S. Wild, Phys. Rev. C **82**, 024313 (2010).

[275] M. Kortelainen, J. McDonnell, W. Nazarewicz, P.-G. Reinhard, J. Sarich, N. Schunck, M. V. Stoitsov, and S. M. Wild, Phys. Rev. C **85**, 024304 (2012).

[276] `http://massexplorer.frib.msu.edu`.

[277] J. A. Holmes, S. E. Woosley, W. A. Fowler, and B. A. Zimmerman, At. Data Nucl. Data Tables **18**, 305 (1976).

[278] N. Nishimura, T. Kajino, G. J. Mathews, S. Nishimura, and T. Suzuki, Phys. Rev. C **85**, 048801 (2012).

[279] I. V. Panov, C. Freiburghaus, and F.-K. Thielemann, Nucl. Phys. A **688**, 587 (2001).

[280] J. Sadhukhan, W. Nazarewicz, and N. Schunck, Phys. Rev. C **93**, 011304 (2016).

[281] T. Kodama, and K. Takahashi, Nucl. Phys. A **239**, 489 (1975).

[282] A. Kelic, M. Valentina Ricciardi, and K.-H. Schmidt, ArXiv e-prints (2009), arXiv:0906.4193.

[283] S. Shibagaki, T. Kajino, G. J. Mathews, S. Chiba, S. Nishimura, and G. Lorusso, Astrophys. J. **816**, 79 (2016).

[284] A. V. Afanasjev, S. E. Agbemava, D. Ray, and P. Ring, Phys. Lett. B **726**, 680 (2013).

[285] E. Olsen, M. Pfützner, N. Birge, M. Brown, W. Nazarewicz, and A. Perhac, Phys. Rev. Lett. **110**, 222501 (2013).

[286] E. Olsen, M. Pfützner, N. Birge, M. Brown, W. Nazarewicz, and A. Perhac, Phys. Rev. Lett. **111**, 139903(E) (2013).

[287] K. Farouqi, K.-L. Kratz, L. I. Mashonkina, B. Pfeiffer, J. J. Cowan, F.-K. Thielemann, and J. W. Truran, Astrophys. J. Lett. **694**, L49 (2009).

[288] L. F. Roberts, S. Reddy, and G. Shen, Phys. Rev. C **86**, 065803 (2012).

[289] G. Martínez-Pinedo, T. Fischer, A. Lohs, and L. Huther, Phys. Rev. Lett. **109**, 251104 (2012).

[290] O. L. Caballero, R. Surman, and G. C. McLaughlin, *European Physical Journal Web of Conferences*, EPJ Web of Conferences, **93**, 03002 (2015).

[291] S. Honda, W. Aoki, Y. Ishimaru, and S. Wanajo, Astrophys. J. **666**, 1189 (2007).

Acknowledgements

Jede wissenschaftliche Arbeit ist nicht nur die Leistung einer einzelnen Person. Hier möchte ich mich bei allen bedanken, die durch ihre vielfältige Unterstützung, ihr Wissen oder ihre Motivation zu dieser Arbeit beigetragen haben.

An erster Stelle bedanke ich mich bei meiner Doktormutter Almudena Arcones für die bedingungslose Aufnahme als Doktorand in die Astro-Gruppe – trotz meiner Vorgeschichte als “Experimentalphysiker” –, für die Übertragung dieses hochinteressanten Forschungsthemas und den Aufbau mehrerer interdisziplinärer Kollaborationen. Danke für die vielen wertvollen Diskussionen zu jeder Zeit, für die fortwährende Unterstützung und für die motivierende Vorfreude auf die “bunten Bilder”. Ebenfalls möchte ich mich für die Möglichkeit der Teilnahme an zahlreichen Konferenzen, Summer/Winter Schools und Workshops bedanken.

Bei Herrn Prof. Dr. Wambach bedanke ich mich für die Übernahme des Zweitgutachtens sowie für die Zusammenarbeit bei den Vorlesungen zur Nuklearen Astrophysik II und zur Einführung in die allgemeine Relativitätstheorie.

Weiterhin danke ich allen derzeitigen und ehemaligen Mitgliedern der Arbeitsgruppe: Julia Bliss, Marius Eichler, Camilla Hansen, Takami Kuroda, Carlos Mattes, Paul Mekhedjian, Albino Perego, Moritz Reichert, Marcella Ugliano, Maximilian Witt, Hannah Yasin. Danke für die teils fachlichen teils unterhaltsamen Gespräche beim gemeinsamen Mittagessen und all die gemeinsamen Aktivitäten außerhalb der Arbeitszeit.

I would like to thank our collaborators Albino Perego, Oleg Korobkin, Stephan Rosswog, Friedrich-Karl “Friedel” Thielemann for our collaboration on the nuclesynthesis and its implications in neutrino-driven winds from neutron star mergers. Furthermore, I thank Witold Nazarewicz, Erik Olsen for our collaboration on the impact of nuclear masses. I gratefully acknowledge two more collaborations with Luke Bovard and Luciano Rezzolla as well as Wolfgang Kastaun, which focused on different aspects of the r-process nucleosynthesis in the dynamic ejecta.

Insbesondere möchte ich mich nochmal bei Albino bedanken, der nicht nur bei mehreren Kollaborationen wesentlich mitgewirkt hat, sondern auch meine Fragen geduldig beantwortet hat und sich stets Zeit für Diskussionen genommen hat.

Den Büros 1 und 302 danke ich für die produktive Arbeitsatmosphäre. Danke Julia, Hannah, Sandra, Moritz und Marc! Darüber hinaus danke ich noch den anderen “Braunies” Lukas und Martin für die abwechslungsreichen Gespräche in den Kaffeepausen.

Für das Korrekturlesen der Dissertation sowie für zahlreiche nützliche Kommentare danke ich Almudena, Camilla, Julia, Albino und Moritz. An dieser Stelle auch noch einmal ein riesiges Dankeschön an alle hier genannten für die Unterstützung kurz vor der Abgabe!

In der zweiten Hälfte meiner Zeit als Doktorand habe ich die Administration des Web- und Mail-Servers übernommen. Ich danke David Scheffler für die hervorragende Übergabe und auch die Verfügbarkeit für Rückfragen, gerade in den ersten Wochen. Für die sehr gute Zusammenarbeit bezüglich der IT im Institut bedanke ich mich bei Roland Wirth und Alexander Bartl.

Ein besonderer Dank geht an meine Freundin Bettina und meine Familie, insbesondere an meine Eltern Cornelia und Gerald sowie meine Schwester Corinna. Danke für die moralische Unterstützung, die Geduld und das Verständnis, das ihr mir entgegengebracht habt. Nicht zuletzt danke ich all meinen Freunden, die in der Freizeit für den Spaß und die nötige Zerstreuung gesorgt haben.

Teile dieser Arbeit wurden durch den Helmholtz-University Young Investigator Grant Nr. VH-NG-825 und den BMBF Grant Nr. 05P15RDFN1 unterstützt. Weiterhin war ich Mitglied der HGS-HIRe Graduiertenschule, über die ich finanzielle Unterstützung für Konferenzreisen erhalten habe und die mir die Teilnahme an sehr hilfreichen Softskill-Kursen ermöglicht hat. Darüber hinaus bedanke ich mich bei NAVI für die Unterstützung zur Teilnahme

an der Konferenz “Nuclear Physics in Astrophysics VII” und bei der Wilhelm-und-Else-Heraeus-Stiftung für die Bezuschussung der Teilnahmegebühren für die DPG Frühjahrstagungen.

Sämtliche Berechnungen der r-Prozess Nukleosynthese mit großen Mengen an Tracern sowie die parallelen Berechnungen von Reaktionsraten mithilfe von TALYS wurden auf dem alten Cluster “Prometheus” und auf dem neuen Cluster “Kronos” an der GSI durchgeführt.

Curriculum Vitae

Dirk Martin

May 3rd, 1989	Born in Rüsselsheim, Germany
June 4th, 2008	Abitur, Max-Planck-Schule Rüsselsheim, Germany
2009 – 2011	Bachelor studies, TU Darmstadt, Germany
October 6th, 2011	Bachelor’s degree, thesis title: ”Investigation of the reaction ^{144}Sm(p,p’) under extreme forward angles“
2011 – 2013	Master studies, TU Darmstadt, Germany
October 31st, 2013	Master’s degree, thesis title: ”Gamma Strength Function of ^{96}Mo: A test of the Axel-Brink hypothesis“
2014 – 2017	Doctoral studies and member of the scientific staff, TU Darmstadt, Germany

Erklärung zur Dissertation

Hiermit versichere ich, die vorliegende Dissertation ohne Hilfe Dritter nur mit den angegebenen Quellen und Hilfsmitteln angefertigt zu haben. Alle Stellen, die aus Quellen entnommen wurden, sind als solche kenntlich gemacht. Diese Arbeit hat in gleicher oder ähnlicher Form noch keiner Prüfungsbehörde vorgelegen. Eine Promotion wurde bisher noch nicht versucht.

Darmstadt, den 27. Juni 2017

(Dirk Martin)